

# Relativistic Laser Plasma Dynamics with Ultrathin Foils

vorgelegt von  
Dipl.-Phys. Julia Bränzel  
geb. in Lübben

von der Fakultät II - Mathematik und Naturwissenschaften  
der Technischen Universität Berlin  
zur Erlangung des akademischen Grades

Doktor der Naturwissenschaften  
– Dr. rer. nat. –

genehmigte Dissertation

## **Promotionsausschuss:**

Vorsitzender: Prof. Dr. Andreas Knorr  
Berichter: Prof. Dr. Stefan Eisebitt  
Prof. Dr. Jörg Schreiber  
Dr. Matthias Schnürer

**Tag der wissenschaftlichen Aussprache:** 28.11.2016

Berlin 2017



MAY YOU HAVE THAT FREEDOM.

*R. Feymann*



---

## Zusammenfassung

Diese Arbeit widmet sich den grundlegenden Wechselwirkungsprozesse von Laserpulsen relativistischer Intensität an dichten Plasmen. Unter Verwendung extrem dünner Folien wird die Beschleunigung von Ionen und Elektronen sowie die Emission hochenergetischer, kohärenter Strahlung in Hinblick auf ihre parametrischen Abhängigkeiten und eine Optimierung untersucht. Darüber hinaus wurden neue und bedeutende Effekte entdeckt.

Die Arbeit zeigt, inwiefern sich die Laserplasmawechselwirkung wesentlich für verschiedene Parameter unterscheidet. Dies betrifft die Stöchiometrie und Dicke des verwendeten Target, die Laserparameter und die Eigenschaften der Plasmagrenzfläche. Die resultierenden Auswirkungen auf die Ionen- und Elektronenbeschleunigung sowie auf die Emission von XUV Strahlung werden dargestellt, Korrelationen für unterschiedliche Parameterbereiche gefunden und Unterscheidungen in den unterliegenden Prozessen getroffen.

Durch das Verwenden von ultradünnen Folien aus schweren Elementen (Gold, Silber) wird ein neuer effizienter Beschleunigungsmechanismus für die schweren Ionen gezeigt, der es ermöglicht für Laserintensitäten von  $7 \times 10^{19} \text{ W/cm}^2$  diese bis auf eine kinetische Energie von bis zu  $1 \text{ MeV/u}^1$  zu beschleunigen. Im Folgenden wird eine detaillierte Analyse des Effekts und der zugrundeliegenden Skalierung zwischen der Ladung der Ionen und ihrer kinetischen Energie gegeben.

Darüberhinaus wurden experimentell prinzipielle theoretische Vorschläge getestet: Durch die Verwendung eines Doppeltargets wird die Emission von relativistischen Elektronen verstärkt und Umladungsprozesse in schnellen Ionen induziert. Es wird eine relativistische Rückstreuung eines zweiten Laserpulses an einem laserbeschleunigten Elektronenpaket untersucht. Es wird gezeigt, dass durch den Einsatz eines starken Vorpulses das Vorplasma gezielt und kontrollierbar manipuliert werden kann. Dies führt zu einer signifikanten Änderung in der Elektronendynamik, wodurch gezielt Prozesse der Laserplasmawechselwirkung unterdrückt und andere wiederum verstärkt werden können. Diese Experimente stellen neue Methoden vor, mit der die Emission von Ionen, Elektronen und hochenergetischer Strahlung kontrollierbar in ihren spektralen Eigenschaften geändert werden kann. Dies kann in Hinsicht auf zukünftige Applikationen der lasergetriebenen Beschleunigung, aber auch in Hinblick auf eine grundlegende Erforschung der Wechselwirkung zwischen extrem starken Lichtpulsen und einem Plasma von großem Nutzen sein.

---

<sup>1</sup> u ist die atomare Masseneinheit

## Abstract

This thesis investigated the fundamental interaction processes of laser pulses of relativistic intensity interacting with dense plasmas, created from ultrathin foils. These processes include, ion and electron acceleration and the emission of coherent, high energy XUV radiation. They were investigated with respect to their parametric dependencies and optimization, and important new effects arising out this work were examined.

This thesis shows how the laser-plasma interaction significantly differs for different experimental parameters, namely, the stoichiometry and thickness of the target, the laser parameters and the properties of the plasma boundary. The resulting impact on the ion and electron acceleration, as well as, on the emitted XUV radiation were measured and correlations for different parameter ranges were found from which differences in underlying mechanisms were obtained.

An unexpected acceleration of the heavy ions was discovered using ultrathin foils made of heavy elements, thus revealing a new acceleration mechanism. This mechanism enables an acceleration of heavy ions to kinetic energies of up to  $1 \text{ MeV/u}^2$  for a laser intensity of  $7 \times 10^{19} \text{ W/cm}^2$ . In this work, a detailed analysis and discussion of this effect and the underlying charge state to kinetic energy scaling is presented.

The experiments tested a number of theoretical suggestions: an enhancement of the relativistic electron emission and ion charge transfer processes with the use of double foil targets, and relativistic backscattering of a second laser pulse from a laser-accelerated electron bunch. This thesis also investigated how the pre-plasma can be manipulated in a controlled way by applying a strong pre-pulse. It will be shown that this changes the electron dynamics and this causes a significant suppression of certain laser-plasma processes, while other processes can be enhanced. These experiments introduce a novel techniques to change the spectral characteristics in controllable way. This could be of great value for future laser-plasma applications and for a further fundamental investigation of the interaction processes between light pulses and dense plasmas.

---

<sup>2</sup> u is the atomic mass unit

---

# Publications

- Publication that is used in the thesis presented here.

- 1 J. Braenzel, A. A. Andreev, K. Platonov, M. Klingsporn, L. Ehrentraut, W. Sandner, and M. Schnürer. “Coulomb-Driven Energy Boost of Heavy Ions for Laser-Plasma Acceleration”. In: *Physical Review Letters* **114** (2015), 124801. DOI: [10.1103/PhysRevLett.114.124801](https://doi.org/10.1103/PhysRevLett.114.124801)

- Publications that is not used in this work.

J. Braenzel, C. Pratsch, P. Hilz, C. Kreuzer, M. Schnürer, H. Stiel, and W. Sandner. “Note: Thickness determination of freestanding ultra-thin foils using a table top laboratory extreme ultraviolet source”. In: *Review of Scientific Instruments* **84** (2013), 84(5):056109. DOI: [10.1063/1.4807153](https://doi.org/10.1063/1.4807153)

J. Braenzel, A. Andreev, M. Schnürer, S. Steinke, K. Platonov, G. Priebe, and W. Sandner. “Sub-structure of laser generated harmonics reveals plasma dynamics of a relativistically oscillating mirror”. In: *Physics of Plasmas* **20** (2013), 083109. DOI: [10.1063/1.4817807](https://doi.org/10.1063/1.4817807)

F. Abicht, J. Braenzel, G. Priebe, C. Koschitzki, A. A. Andreev, P. V. Nickles, W. Sander, and M. Schnürer. “Tracing dynamics of laser-induced fields on ultrathin foils using complementary imaging with streak deflectionometry”. In: *Phys. Rev. Accel. Beams* **19** (9 Sept. 2016), 091302. DOI: [10.1103/PhysRevAccelBeams.19.091302](https://doi.org/10.1103/PhysRevAccelBeams.19.091302)

F. Mollica, L. Antonelli, A. Flacco, J. Braenzel, B. Vauzour, G. Folpini, G. Birindelli, M. Schnürer, D. Batani, and V. Malka. “Efficient laser production of energetic neutral beams”. In: *Plasma Physics and Controlled Fusion* **58** (2016), 034016. DOI: [10.1088/0741-3335/58/3/034016](https://doi.org/10.1088/0741-3335/58/3/034016)

S. K. Das, A. Andreev, H. Messaoudi, J. Braenzel, M. Schnürer, and R. Grunwald. “Highly periodic laser-induced nanostructures on thin Ti and Cu foils for potential application in laser ion acceleration”. In: *Journal of Applied Physics* **119**, 113101 (2016). DOI: <http://dx.doi.org/10.1063/1.4943636>

- S. Ter-Avetisyan, J. Braenzel, M. Schnürer, R. Prasad, M. Borghesi, S. Jequier, and V. Tikhonchuk. “New source of MeV negative ion and neutral atom beams”. In: *Review of Scientific Instruments* **87**, 02B134 (2016). DOI: [10.1063/1.4935234](https://doi.org/10.1063/1.4935234)
- A. Andreev, K. Platonov, J. Braenzel, A. Lübcke, S. Das, H. Messaoudi, R. Grunwald, C. Gray, E. McGlynn, and M. Schnürer. “Relativistic laser nano-plasmonics for effective fast particle production”. In: *Plasma Physics and Controlled Fusion* **58** (2016), 014038
- M. Kalashnikov, A. Andreev, K. Ivanov, A. Galkin, V. Korobkin, M. Romanovsky, O. Shiryaev, M. Schnürer, J. Braenzel, and V. Trofimov. “Diagnostics of peak laser intensity based on the measurement of energy of electrons emitted from laser focal region”. In: *Laser and Particle Beams* **33** (03 Sept. 2015), 361–366. DOI: [10.1017/S0263034615000403](https://doi.org/10.1017/S0263034615000403)
- F. Abicht, J. Braenzel, G. Priebe, C. Koschitzki, A. A. Andreev, P. V. Nickles, W. Sandner, and M. Schnürer. “Tracing ultrafast dynamics of strong fields at plasma-vacuum interfaces with longitudinal proton probing”. In: *Applied Physics Letters* **105** (2014), 034101. DOI: <http://dx.doi.org/10.1063/1.4891167>
- S. Steinke, P. Hilz, M. Schnürer, G. Priebe, J. Braenzel, F. Abicht, D. Kiefer, C. Kreuzer, T. Ostermayr, J. Schreiber, A. A. Andreev, T. P. Yu, A. Pukhov, and W. Sandner. “Stable laser-ion acceleration in the light sail regime”. In: *Physical Review ST: Acceleration and Beams* **16** (2013), 011303. DOI: [10.1103/PhysRevSTAB.16.011303](https://doi.org/10.1103/PhysRevSTAB.16.011303)
- R. Prasad, F. Abicht, M. Borghesi, J. Braenzel, P. V. Nickles, G. Priebe, M. Schnuerer, and S. Ter-Avetisyan. “Thomson spectrometer-microchannel plate assembly calibration for MeV range positive and negative ions, and neutral atoms”. In: *Review of Scientific Instruments* **84** (2013), 053302. DOI: [10.1063/1.4803670](https://doi.org/10.1063/1.4803670)
- F. Abicht, R. Prasad, G. Priebe, J. Braenzel, L. Ehrentraut, A. Andreev, P. V. Nickles, M. Schnürer, V. Tikhonchuk, and S. Ter-Avetisyan. “Energetic negative ion and neutral atom beam generation at passage of laser accelerated high energy positive ions through a liquid spray”. In: *SPIE Proceedings* **8779** (2013), 87790M. DOI: [10.1117/12.2019505](https://doi.org/10.1117/12.2019505)
- F. Abicht, M. Schnürer, J. Braenzel, G. Priebe, A. A. Andreev, C. Koschitzki, S. Steinke, T. Toncian, O. Willi, and W. Sandner. “Coaction of strong electrical fields in laser irradiated thin foils and its relation to field dynamics at the plasma-vacuum interface”. In: *SPIE Proceedings* **8779** (2013), 87790V. DOI: [10.1117/12.2017395](https://doi.org/10.1117/12.2017395)
- E. Schleifer, E. Nahum, S. Eisenmann, M. Botton, A. Baspaly, I. Pomerantz, F. Abicht, J. Braenzel, G. Priebe, S. Steinke, A. Andreev, M. Schnürer,

W. Sandner, D. Gordon, P. Sprangle, K. D. Ledingham, and A. Zigler. “Microstructured snow targets for high energy quasi-monoenergetic proton acceleration”. In: *SPIE Proceedings* **8779** (2013), 87791M. DOI: [10.1117/12.2019661](https://doi.org/10.1117/12.2019661)

M. Schnürer, F. Abicht, R. Prasad, M. Borghesi, G. Priebe, J. Braenzel, A. Andreev, P. V. Nickles, S. Jequier, V. Tikhonchuk, and S. Ter-Avetisyan. “Charge steering of laser plasma accelerated fast ions in a liquid spray - creation of MeV negative ion and neutral atom beams”. In: *Physics of Plasmas* **20**, 113105 (2013). DOI: <http://dx.doi.org/10.1063/1.4829005>

M. Schnürer, A. A. Andreev, F. Abicht, J. Braenzel, C. Koschitzki, K. Y. Platonov, G. Priebe, and W. Sandner. “The beat in laser-accelerated ion beams”. In: *Physics of Plasmas* **20** (2013), 103102. DOI: [10.1063/1.4824115](https://doi.org/10.1063/1.4824115)



# Contents

<b>Introduction</b>	<b>3</b>
<b>I THEORY</b>	<b>7</b>
<b>1 Fundamentals of Laser Particle Interaction</b>	<b>9</b>
1.1 An Ultra Short Laser Pulse . . . . .	9
1.2 Single Electron Laser Interaction . . . . .	10
1.3 Ponderomotive Force . . . . .	11
1.4 Laser Propagation in Plasma . . . . .	12
<b>2 Ionization and Plasma Absorption</b>	<b>15</b>
2.1 Ionization . . . . .	15
2.2 Absorption Processes in a Laser Plasma . . . . .	17
2.3 Energy Loss and Range Energy Relation of Ions in Matter . . . . .	19
<b>3 Laser Plasma Ion Acceleration</b>	<b>21</b>
3.1 Particle In Cell Simulation . . . . .	21
3.2 Target Normal Sheath Acceleration . . . . .	22
3.3 Radiation Pressure Acceleration . . . . .	23
3.4 Coloumb Explosion . . . . .	25
3.5 Shock Acceleration . . . . .	26
<b>4 High Harmonic Generation and Relativistic Backscattering</b>	<b>27</b>
4.1 Coherent Wake Emission . . . . .	27
4.2 Relativistic Oscillating Mirror Model . . . . .	28
4.3 Relativistic Backscattering . . . . .	29
<b>II EXPERIMENTAL METHODS</b>	<b>31</b>
<b>5 Laser System and Experimental Setup</b>	<b>33</b>
5.1 High Field Laser System . . . . .	33
5.2 Laser Contrast . . . . .	35
5.3 Single Laser Pulse Experiments . . . . .	37

5.4	Two Laser Pulse Experiments . . . . .	38
5.5	Ultrathin Foil Targets . . . . .	41
5.6	Detection devices . . . . .	44
<b>III RESULTS</b>		<b>49</b>
<b>6</b>	<b>Laser Ion Acceleration with Optimized Target Systems</b>	<b>51</b>
6.1	Dependency of the Ion Spectrum on the Laser Contrast . . . . .	53
6.2	Optimized Laser Ion Acceleration by Radiation Pressure . . . . .	55
6.3	Coulomb Boost for Heavy Ions . . . . .	58
6.4	Laser Transmission . . . . .	71
6.5	Ion Charge Transfer Processes . . . . .	73
6.6	Controlled Plasma Manipulation for Laser Ion Acceleration . . . . .	76
6.7	Conclusions on the Laser Ion Acceleration . . . . .	81
<b>7</b>	<b>Electron Spectrum from Laser Interaction with Ultrathin Foils</b>	<b>85</b>
7.1	Fast Electrons from Laser Plasmas . . . . .	86
7.2	Characterisation of the Fast Electron Spectrum . . . . .	88
7.3	An Amplified Electron Spectrum . . . . .	96
7.4	Electron Spectrum from a Two Laser Pulse Experiment . . . . .	102
7.5	Conclusions on the Fast Electron Spectrum . . . . .	107
<b>8</b>	<b>XUV Emission from Laser Interaction with Ultrathin Foils</b>	<b>111</b>
8.1	XUV Emission at Different Laser Contrast Conditions . . . . .	112
8.2	Relativistic Backscattering . . . . .	117
8.3	Enhanced High Harmonic Emission . . . . .	124
8.4	Conclusions on the XUV Emission . . . . .	129
<b>IV SUMMARY AND OUTLOOK</b>		<b>133</b>
<b>9</b>	<b>Summary and Perspective</b>	<b>135</b>
9.1	Laser Ion Acceleration . . . . .	135
9.2	Laser Electron Acceleration . . . . .	136
9.3	XUV Emission From Laser Plasma Interaction . . . . .	138
9.4	A Controlled Manipulation of Plasma Dynamics . . . . .	139
<b>A</b>	<b>Appendix</b>	<b>141</b>
A.1	Additional Material on Laser Ion Acceleration . . . . .	141
A.2	Additional Material on the Fast Electron Spectrum . . . . .	148
A.3	Additional Material on the XUV Emission . . . . .	157
<b>Bibliography</b>		<b>165</b>

## Introduction

The interaction between matter and photons remains one of the most interesting current research fields, as it continues to reveal fundamental physical processes. The following work examines this interaction in extreme conditions: a coherent light pulse with a relativistic intensity that interacts with an ultrathin plasma slab of solid state density and within an ultrashort time interval. These experiments create a setting in which the principle physical questions about the interplay between light and plasma can be examined. The laser field drives the electrons to relativistic oscillations and causes collective electron dynamics, namely, the ejection of fast electrons, the creation of high density plasmons, and a relativistically oscillating plasma boundary. At the same time, the charge separation between ions and electrons establishes an ultrastrong electric field at the plasma boundary that is capable of accelerating ions up to high velocities. The acceleration length in which either electrons or ions gain high kinetic energies (MeV) is on the order of some  $\mu\text{m}$ . In comparison, conventional linear particle accelerators require acceleration lengths on the order of hundreds of meters. This small acceleration length, suggests a potential for laser driven particle acceleration to complement the particle accelerator technology. Significant efforts have been undertaken in the scientific exploration of laser accelerated ions as a future ion source for medical and radiographic applications [1–3]. This is due to the desirable properties the laser accelerated ions can provide, e.g. a high pulsed particle flux at tunable kinetic energies and a narrow spatial emittance [1]. To date, the main research's focus on laser accelerated ions lies on the discovery of new acceleration models, and ways to optimize existing ones with regard to maximizing kinetic energy and achieving a narrow spectral emittance.

A concurrent process to the ion acceleration is the emission of coherent light bursts, as a consequence of the collective and relativistic electron oscillations. This phenomena is known as high harmonic emission from solid dense plasmas [4–6]. It describes the emission of a pulse train with equally spaced pulses, exhibiting pulse durations reaching the attosecond timescale, and a spectral bandwidth from the infra-red up to the eXtreme UltraViolet (XUV) range<sup>3</sup>. Since the amount and energy of the emitted photons, as well as, the pulse duration, scales with the gamma factor of the electrons and hence with intensity of the applied driving laser, the emitted radiation can provide a very high peak brilliance [7]. Today's research in biology, solid state physics and medicine drives a constantly growing demand for coherent light sources from the XUV up to the soft and hard X-ray range<sup>4</sup>. High harmonic radiation from laser-plasma sources are predicted to provide compact and brilliant light sources that could range between established and future ones, as e.g. LCLS (Linac Coherent Light Source), SACLA, the XFEL (X-Ray Free Electron Laser) and the optimized technology of high harmonic radiation from gases [8].

---

<sup>3</sup> in the energy range 1240 – 12.4 eV

<sup>4</sup> in the energy range 100 – 10<sup>4</sup> keV

The investigation of laser-plasma interaction is strongly connected to the progress in laser technology. For almost two decades, relativistic laser pulse intensities above  $10^{19}$  W/cm<sup>2</sup> have been available via the technology of Chirped Pulse Amplification. In the last few years, great improvement at the laser contrast has been achieved, enabling a steep intensity raise of up to 14 orders of magnitudes during few picoseconds and without pre-pulses. The laser contrast determines the properties of the pre-plasma and this has a significant impact on the involved plasma dynamics and subsequent processes. The improvement of the laser contrast revealed high harmonic emission from solid state targets and enabled the use of ultrathin foil targets in a thickness range of just a few nm, less than the skin depth of the laser. With these ultrathin foil targets, new ion acceleration regimes were recently discovered, e.g., acceleration by radiation pressure, which greatly improved the ions maximum kinetic energies and the acceleration efficiency. For both, high harmonic emission and ion acceleration, latest research found an interdependency between the laser parameters, the properties of the plasma and the target system. At specific conditions, a differentiation of the underlying laser-plasma dynamics becomes apparent and a significant improvement of the experimental results can be obtained. Until now, a systematic investigation of the inherent parameters controlling this effect has not been performed and motivates the ongoing research, including this thesis.

The thesis aimed to optimize the ion acceleration at the onset of the radiation pressure and investigated new concepts for the laser-plasma dynamics, by using ultrathin foil targets at different composition and configurations at ultra-high laser contrast. In order to reveal the underlying plasma dynamics and the interdependencies, the investigative approach was an experimental examination of simultaneous processes of ion, electron, incoherent and coherent XUV emission at a specific set of target and laser parameters. With the obtained results major dependencies are extracted, new effects are demonstrated, established scaling laws are extended, and the picture of concurrent physical models are joined and refined.

The impact of target thickness for laser ion acceleration was already studied using low density carbon foils [2, 9, 10]. From this starting point, this thesis focused on the influence on different target constituents. RPA influenced acceleration is demonstrated for hydrocarbon foils for a specific target thickness in Section 6.2. An efficient and unexpected acceleration of heavy ions (gold and silver) up to the energy range of MeV/u, was discovered by using ultrathin foils of heavy constituents and is presented in Section 6.3. Since the accelerated heavy ions were detected at multiple charge states, a new scaling of the kinetic energy with the charge to mass ratio is intensively analysed and discussed. The results deliver new insights, how and when the acceleration of heavy ions is affected by the presence of light ions. Arising questions on inherent charge transfer processes are further investigated by the use of a two foil target configuration and are discussed in Section 6.5.

The concurrent spectrum of ejected fast electrons was suggested to deliver

indirectly information about the laser-plasma interaction. This thesis aimed to find correlations between the fast electron spectrum and the concurrent ion acceleration or XUV emission in view of specific parameters and interdependencies, e.g. the laser contrast condition and the target thickness. The investigation is presented in Chapter 7 and approaches a classification of the fast electron spectra from ultrathin foil interaction. New and principle effects concerning the ejection of fast electron from the laser field are revealed and discussed in Sections 7.2 and 7.3.

The laser contrast condition determines the laser-plasma dynamic especially for few nanometer foil targets, which significantly alters the experimental results. A lower laser contrast pre-heats the target due to distinct pre-pulses and a long rise of the laser intensity. Since the laser contrast is an intrinsic parameter of the used laser system, the influence, in particular, usually remains undetermined. In view of interdependencies between target and laser parameters, it's impact is a crucial question for determining a principle differentiation in underlying plasma parameters. This is investigated in Sections 6.1, 7 and 8.1 with a experimental investigation examining the ion, electron and XUV emission at different laser contrast conditions. To understand the consequences of either pre-pulse or a specific rise of the intensity, the plasma was manipulated in a controlled way by applying at ultrahigh laser contrast a strong pre-pulse. In a basic approach, the experiment aimed for principle insights, how an enlarged raise of the plasma density or an expanded target foil affects the concurrent laser-plasma processes. Section 6.6 shows, how the strong pre-pulse inhibits the ion acceleration and changes the heavy ions' charge distribution. A remarkable improvement of the high harmonic emission is demonstrated by specific pre-heating of the ultrathin foil target in Section 8.3.

To complement the examination, a post-interaction of a strong, counter-propagating second laser pulse with an already emitted ion or electron distribution or the remaining plasma is investigated. Due to this method, new effects for the ion acceleration are presented in Section 6.6 and for the ejected fast electrons in Section 7.4. Regarding XUV emission, a principle question for relativistic laser-plasma physics was tested: Since the laser accelerates electron bunches at relativistic velocities, a second laser pulse can be backscattered from it. According to an idea of Einstein [11], the backscattered light can undergo a relativistic shift in frequency and should be detected at a significant different spectral range. This promising principle is known as relativistic backscattering and tested for a strong second laser pulse and the results are presented in Sections 8.2 and 8.3.



Part I  
THEORY



# 1 Fundamentals of Laser Particle Interaction

The first chapter provides the mathematical introduction to laser matter interactions at extreme laser intensities. It gives the theoretical description of a laser pulse with ultrashort pulse duration and explains how it influences the movement of a single electron. The propagation of a laser pulse in plasma is described. For a detailed study of the topic see [12–15].

## 1.1 An Ultra Short Laser Pulse

Today, the term ultrashort refers to laser pulse durations in the femtosecond ( $10^{-15}$  s) range. The mathematical description of an ultrashort laser pulse is bound to the Fourier transform, which delivers a bijective correspondence between the time and frequency domain representation of the pulse:

$$\mathbf{E}(\mathbf{r}, \omega) = F[\mathbf{E}(\mathbf{r}, t)] = \int_{-\infty}^{+\infty} \mathbf{E}(\mathbf{r}, t) e^{-i\omega t} dt \quad (1.1)$$

$$\mathbf{E}(\mathbf{r}, t) = F^{-1}[\mathbf{E}(\mathbf{r}, \omega)] = \frac{1}{2\pi} \int_{-\infty}^{+\infty} \mathbf{E}(\mathbf{r}, \omega) e^{i\omega t} d\omega \quad (1.2)$$

In the simplest case, the electric field  $E(t)$  of a wave packet is constructed by multiplication with the so called carrier envelope  $\xi(t)$

$$E(t) = \frac{1}{2} \xi(t) e^{i(\omega_L t + \phi(t) + \phi_0)} \quad (1.3)$$

where  $\tau_L$  is the laser pulse duration. The phase  $\phi(t)$  introduces a time dependent frequency change  $\omega(t) = \omega_L + \partial\phi(t)/\partial t$  and  $\phi_0$  describes a constant phase offset to the carrier envelope. In case of a Ti:Sapph laser  $\omega_L$  is about  $2.36 \times 10^{15}$  1/s and the carrier envelope is assumed to be a Gaussian distribution<sup>1</sup>. The spectral intensity (spectral power density), measurable with a spectrometer is then defined by:

$$S(\omega) = \frac{\epsilon_0 c n}{4\pi} |E(\omega - \omega_L)|^2 \quad (1.4)$$

<sup>1</sup>  $\xi(t) \sim \exp(-1.385(t/\tau_L)^2)$

with  $n$  the index of refraction. According to the Fourier transformation in Equation (1.1) ultrashort pulse durations are associated with a spectral bandwidth [12]:

$$\Delta\omega\tau_L \geq 2\pi C_B \quad (1.5)$$

whereas  $C_B$  is a constant determined by the carrier envelope. The propagation of the so constructed wave packet is given by the dispersion relation derived using the Maxwell equations:

$$\left(\Delta - \frac{1}{c^2} \frac{\partial^2}{\partial t^2}\right) \mathbf{E}(\mathbf{r}, t) = \mu_0 \frac{\partial^2}{\partial t^2} P(x, y, z, t) \quad (1.6)$$

here,  $\Delta$  is the Laplace operator,  $c = (\epsilon_0\mu_0)^{-1/2}$ ,  $\mu_0$  the magnetic permeability in vacuum and  $P(x, y, z, t)$  the polarizability which depends on the response of the involved medium. In order to fulfill equation (1.6) the ansatz:

$$\mathbf{E}(\mathbf{r}, t) = E(t)\xi^*(x, y, z)e^{-ik_L z} \quad (1.7)$$

is used, where  $E(t)$  is defined by Equation (1.3). The frequency dependent wave vector is denoted by  $k_L$  and  $\xi^*(x, y, z)$  is the spatial field distribution, which is usually determined by approximating the intensity profile of a focused laser pulse with a Gaussian distribution.

## 1.2 Single Electron Laser Interaction

Lets first consider how a laser field acts on a single charged particle (e.g. an electron), if the field is described by an oscillating standing electro-magnetic (E-M) wave and if spatial dependence is not considered. The motion of a charged particle is determined by the Lorentz force:

$$\vec{F}_L = q(\mathbf{E}(\mathbf{r}, t) + \mathbf{v}(\mathbf{r}, t) \times \mathbf{B}(\mathbf{r}, t)) \quad (1.8)$$

where  $q$  denotes the elemental charge,  $\mathbf{v}$  the electron's velocity. In the non relativistic case one can neglect the influence of the magnetic field  $\mathbf{B}(\mathbf{r}, t)$ , as it scales with  $\beta = v/c$  where  $c$  is the speed of light. In this case the electron oscillates periodically with the frequency  $\omega_L$  in the opposite direction to the electric field vector, assuming linear polarization. The definition of the dimensionless vector potential

$$a_0 = \frac{qE}{\omega_L m_e c} \quad (1.9)$$

normalizes the laser field strength  $|E|$  to the electron transverse movement in terms of  $m_e c$ ,  $m_e$  denotes the mass of the electron. When  $a_0$  reaches unity, a relativistic description of the electron motion is required and the intensity is referred to as relativistic. The electron kinetic energy is then given by

$$E_{kin} = m_e c^2 (\gamma - 1) \quad (1.10)$$

with the relativistic gamma factor

$$\gamma = 1/\sqrt{1 - \beta^2} = 1/\sqrt{1 - v^2/c^2} \quad (1.11)$$

The laser intensity  $I_L$  averaged in respect to  $\tau_L$  is expressed with respect to the dimensionless potential  $a_0$ :

$$I_L = \frac{a_0^2}{\lambda_L^2 [\mu m^2]} \cdot 1.37 \times 10^{18} [W/cm^2] \quad (1.12)$$

Rewriting the laser field according to Maxwell's equations  $\mathbf{E} = -\frac{\partial \mathbf{A}}{\partial t}$  and  $\mathbf{B} = \nabla \times \mathbf{A}$  and using the Lorentz Equation(1.8) one can derive the electron motion [13]

$$\begin{aligned} x &= \frac{-(1 - \delta^2)^{1/2} ca_0}{\omega} \cos(\phi) \\ y &= \frac{\delta ca_0}{\omega} \sin(\phi) \\ z &= \frac{ca_0^2}{4\omega} \left( \phi + \frac{2\delta^2 - 1}{2} \right) \sin(2\phi) \end{aligned} \quad (1.13)$$

where  $\delta = (\pm 1, 0)$  for the appropriate linear polarization of the field,  $\delta = \pm 1/\sqrt{2}$  gives circular polarization and  $\phi = (\omega t - kx)$  respectively. In case of linear polarized field in either the  $x$  or  $y$  direction and a propagation in the  $z$  direction, the  $v \times B$  contribution enables, for  $a_0 > 1$  an oscillation of the electron in the propagation direction of  $2 \times \omega$  which scales with  $a_0^2$ . This leads to the so called "figure 8" motion in the cycle averaged rest frame of the electron. Fig. 1.1 depicts the resulting two dimensional electron oscillation at different relativistic laser field strengths  $a_0$ . The kinetic energy  $E_{os}$  of the electron transverse oscillation ( $y$ ) with respect to one laser cycle  $T_L$  and Equation (1.10) can be approximated [13] with

$$\bar{\gamma}_0 = \sqrt{1 + \frac{a_0^2}{2}} \quad (1.14)$$

and Equation (1.10). The drift velocity in the laser propagation direction  $z$  can be approximated [13] with

$$\frac{v_{Drift}}{c} = \frac{a_0^2}{4 + a_0^2} \quad (1.15)$$

For an ideal electric field of finite duration and a gaussian pulse envelope, without any further boundary conditions, at the end of the interaction the electron comes to rest or has its initial velocity and does not gain energy from the laser field.

### 1.3 Ponderomotive Force

For a focused laser beam the spatial dependence of the field  $\mathbf{E}(\mathbf{r}, t)$  has to be taken into account, commonly a Gaussian field distribution is assumed. Due to

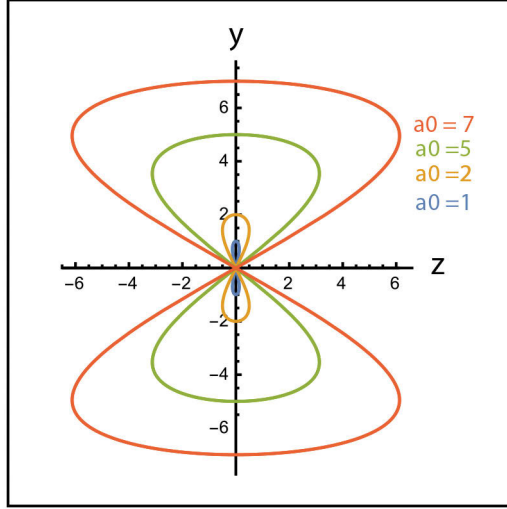


**Figure 1.1:** Figure 8 motion in the cycle averaged rest frame of the electron according to Equation (1.13) at different values of the normalized vector potential in the relativistic regime  $a_0 > 1$ . For the calculation, the electro-magnetic wave was considered to be linearly polarized in the  $y$  direction and propagating along  $z$ .

Equation (1.8) the electron undergoes an oscillatory movement and is driven out of the focal spot to a region of lower intensity by the ponderomotive force:

0.3cm

$$F_{Pond} = -\frac{q^2}{4\gamma m_e \omega_L^2} \nabla |\mathbf{E}^2(\mathbf{r}, t)| \quad (1.16)$$

The force points in the direction of the field gradient, if  $\nabla |\mathbf{E}^2(\mathbf{r}, t)| \neq 0$ , and enables a net gain of kinetic energy for the electron. Various models [1, 16, 17] assume the hot electron temperature,  $T_e$ , to be equal to this ponderomotive potential:

$$T_e = \int_{-\infty}^{+\infty} F_{Pond} d\mathbf{r} = m_e c^2 \left[ \sqrt{1 + \frac{a_0^2}{2}} - 1 \right] \quad (1.17)$$

and often refers to an mean energy similar to  $E_{os}$  in Equation (1.16).

## 1.4 Laser Propagation in Plasma

So far in this chapter, only the laser propagation in unionized matter has been considered (Equation (1.6)), i.e. the case of bound electrons. Therefore the impact of light is determined by the material's response, which was expressed with the polarizability  $P$ . For  $I_L > 10^{12}$  W/cm<sup>2</sup> the medium becomes ionized, hence the optical characteristics change remarkably. During the laser-plasma interaction this leads to a highly complex dispersion relation, because interdependent influences and nonlinear optic phenomena have to be considered. Namely, for the here applied intensity of  $I_L > 10^{19}$  W/cm<sup>2</sup>, the raising edge of the laser pulse or

the much weaker pre-pulse(s) are capable of efficiently pre-ionizing a foil target and thereby changing the optical properties, introducing a plasma density gradient and so on. Rewriting the polarizability of the medium,  $P$  of Equation (1.6), for a homogeneous and conductive medium, the dispersion relation in terms of collective free electron response using the current density  $\eta_e$  looks like<sup>2</sup>

$$\left([\Delta + \frac{\partial^2}{\partial t^2}] - \frac{1}{c^2}\eta_e \frac{\partial}{\partial t}\right)\mathbf{E}(\mathbf{r}, t) = 0 \quad (1.18)$$

Assuming collective electron oscillation against a stationary ion background allows the definition of the plasma frequency

$$\omega_p = \sqrt{\frac{n_e q^2}{\epsilon_0 m_e}} \quad (1.19)$$

, which scales with the electron density  $n_e$ , whereby  $\epsilon_0$  is the permittivity of vacuum. In the case of a fully ionized solid target  $n_e$  is in the order of  $10^{23}$  electrons/cm<sup>3</sup>. Neglecting further friction, the dispersion relation for a propagating EM-wave in plasma

$$\omega_L^2 = k_L^2 c^2 + \omega_p^2 \quad (1.20)$$

can be derived from Equation (1.18). The wave vector  $k_L$  becomes imaginary in the case of  $\omega_p \gg \omega_L$ , leading to an evanescent E-M-wave at the boundary of the plasma medium with a length of the skin depth<sup>3</sup>

$$l_s = \frac{c}{\sqrt{\omega_p^2 - \omega_L^2}} \quad (1.21)$$

. Hence the limit between opaque and transparent is marked by the critical density

$$n_c = \frac{\epsilon_0 \bar{\gamma} m_e \omega_L^2}{q^2} = \frac{1.11 \times 10^{21}}{\lambda^2 [\mu m^2]} \cdot \bar{\gamma} [cm^{-3}] \quad (1.22)$$

One has to distinguish between **underdense** plasma ( $n_e < n_c$ ) and **overdense** plasma ( $n_e > n_c$ ). Laser plasma experiments with ultrathin foils and ultrahigh intensities are necessarily associated with a highly ionized and therefore overcritical plasma, e.g.  $n_e/n_c > 200$  for a hydro-carbon foil. However, at  $I \gg 10^{16}$  W/cm<sup>2</sup> the evanescent wave is still strong enough to drive an efficient laser to plasma absorption, which is further described in Section 2.2.

Due to relativistic effects  $n_c$  increases when  $I_L$  overcomes the relativistic limit. For  $a_0 > 1$  this leads to the onset of relativistic transparency. The condition is fulfilled for

$$\omega_L > \frac{D\omega_p^2}{2ca_0} \quad (1.23)$$

<sup>2</sup> Known as the telegraphs equation. It uses the Lorentz gauge and by taking the local electric current density  $\mathbf{j} = -n_e q \mathbf{v}_e = \eta_e \mathbf{E}$ , with  $\vec{\nabla} \cdot \mathbf{E} = 4\pi \eta_e$  and  $\vec{\nabla} \cdot \mathbf{j} = \partial \eta_e / \partial t$

<sup>3</sup> at an incident angle of  $\theta = 0^\circ$ .

with respect to an adequate foil thickness  $D$  [18]. Such intensity driven change of the refractive index leads to **relativistic self-focusing**, which is similar to the Kerr lens effect [12]<sup>4</sup>.

---

<sup>4</sup>The Kerr effect is a second order effect by an expansion of the refractive index similar to  $n(E) \sim n_0 + S_1 E + S_2 E^2$ .

## 2 Ionization and Plasma Absorption

At ultrahigh laser intensity the ionization of the target's surface takes place before the laser intensity reaches its peak level. Efficient ionization is already established at intensities  $10^{-3}$  times smaller than peak level. The following chapter introduces the relevant theoretical models of laser ionization. For laser interaction with opaque overdense plasmas Section 2.2 gives an overview of the relevant plasma absorption mechanisms from a macroscopic point of view. The involved physical processes are still an ongoing field of research with a number of open questions that are characterized best with a quote of Gibbon [13]: "To date, there is no single model which can adequately describe all the main pieces of absorption physics, not to mention the numerous other effects - mass and energy transport, nonlinear propagation, fast particle generation, and so on - which can also take place."

### 2.1 Ionization

#### Tunnel Ionization

A fundamental principle of atomic physics states that a bound electron can be ionized by a photon when the photon energy overcomes the binding energy:  $h\nu \geq E_{bound}$ , where  $h$  denotes Planck's constant. In addition, it includes ionization by multi photon absorption:  $Nh\nu \geq E_{bound}$ , where  $N$  is the number of photons with energy  $h\nu$ . Quantum theory opens a further option for ionization in the high intensity regime: The influence of the electric field of a laser leads to a bending of the Coulomb potential of an atom. If the field is sufficiently strong, the distortion can be large enough to allow for a significant probability of the bound electron tunneling through the potential barrier [13], as shown in Fig. 2.1 a) and b). Depending on the phase between the electron oscillatory motion and electromagnetic field, the electron is accelerated away from the atom. When the sign of the field changes, it is accelerated back into to atom. Here, recombination with the atom, and second order effects like scattering processes and Auger electron creation take place, which, in consequence, can lead to further ionization processes like non-sequential ionization and radiative processes like the High Harmonic (HH) generation in gaseous media. The ionization rate is proportional to the electric field and the electron's binding energy, it can be calculated using the Ammosov-Delone-Krainov model [19].

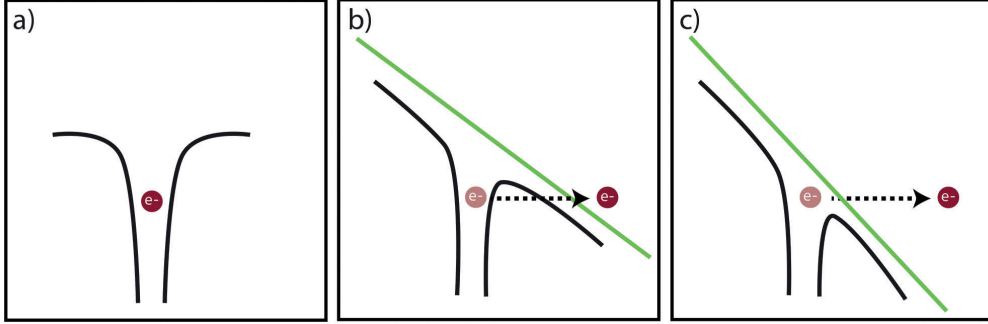


**Figure 2.1:** Schematic drawing of a bound electron in the Coulomb potential of an atom (a). The external electric field is bending the Coulomb barrier (b) enough to rise the probability for the electron to escape by tunneling. An higher external field is distorting the Coulomb barrier such, that the electron can leave the atom (c).

### Above the Barrier Ionization

At even higher intensities, the Coulomb barrier is distorted to such an extent that it reaches a value lower than the electron ionization threshold level. In consequence the electron can directly leave the potential well of the atom. Fig. 2.1 c) illustrates the basic principle of the process, valid for an intensity of  $I \gtrsim 10^{16}$  W/cm<sup>2</sup>. It is assumed to be one of the major ionization processes for ultrahigh intensity laser-plasma experiments.

### Collisional Ionization and Inverse Bremsstrahlung Absorption

For an intensity range  $I \times \lambda^2 \approx 10^{12-17}$  [W $\mu\text{m}^2$  /cm<sup>2</sup>], inverse Bremsstrahlung is the main absorption mechanism of laser light when considering ionization of the target beyond the skin depth  $l_s$ . In this process, energy from the laser pulse is partly absorbed by an electron when recombining with an atom. The recombination radiation can be strong enough to further ionize electrons. For free electrons with a thermal Temperature of  $T_e$  the process is determined by the electron-ion collision frequency [20]

$$\nu_{ei} = \frac{4(2\pi)^{1/2}}{3} \frac{n_e Z e^4}{m^2 v_T} \ln \Lambda = 2.91 \times 10^{-6} Z n_e T_e^{-3/2} \ln \Lambda [\text{s}^{-1}] \quad (2.1)$$

where the Coulomb logarithm,  $\ln \Lambda$ , depends on the electron-ion scattering cross-section. In an ionized multi-particle plasma, the Debye length is a measure for the length of the induced charge separation field

$$\lambda_D = \sqrt{\frac{\epsilon_0 T_e q}{q^2 n_e}} \quad (2.2)$$

With respect to  $\lambda_D$ ,  $\Lambda = \lambda_D \frac{T_e}{Z e^2}$  is found. It depends strongly on the laser intensity as this scales with  $T_e$ . For  $I_L = (10^{12} - 10^{14})$  W/cm<sup>2</sup> ionization by collision becomes dominant [13], including secondary processes such as three body interaction

and ionization by Bremsstrahlung due to recombination processes. Collisions become unlikely when the electrons have a high velocity and their free mean path becomes larger than  $\lambda_e = v_{Te}/\nu_{ei}$ , where the electron's thermal velocity  $v_{Te}$  [14]. This is the case for relativistic laser intensities and ultrathin foils discussed here. Thus, ionization via collisional processes plays a minor role and can be attributed to processes driven by the pre-pulse and the rising laser intensity level. Nevertheless, it becomes important when fast ions with charge  $Z$  pass through neutral or ionized matter. Depending on the ion velocity and material thickness, the ion can either catch or strip electrons. This effect is used at conventional particle accelerators e.g. by the so called "stripper" foil [21]. Recharging processes for laser accelerated ion beams passing through matter are a focus of current research, and will be further described in Section 2.3.

## 2.2 Absorption Processes in a Laser Plasma

The laser to plasma absorption mechanisms for an ultraintense laser and an ultradense plasma are currently a topic of complex and intense discussion [17]. In the experiments presented in this thesis, extreme laser parameters such as ultrahigh intensity, ultrashort pulse duration and ultrahigh laser contrast were applied. In this extreme parameter range, the plasma expansion can become almost negligible. Thus, the laser interacts with a sharp step like plasma boundary or steeply rising plasma density on the order of  $L(\nabla n_e) = 0.01-0.1\lambda_L$ , where  $\lambda_L$  is the wavelength of the laser. The following paragraphs will give a brief overview of the main absorption models. A more in depth description on this topic can be found in [17, 20, 22, 23].

### Collisional Absorption

The impact of collisional absorption due to electron-ion collisions depends on the collision rate, which is a function of the scattering cross-section, and can be expressed by the collisional frequency  $\nu_{ei}$  of Equation (2.1). A reduction of collision rate is seen when the electron quiver velocity overcomes the thermal velocity. To account for this effect, an effective collective collisional frequency [13]  $\nu_{eff} \sim \nu_{ei}v_{Te}/(v_{os}^2 + v_{Te}^2)^{3/2}$  is introduced. For ultrahigh laser intensity, it follows that, according Equation (1.14),  $v_{os} \gg v_{Te}$  leading to a long electron free mean path. Therefore collisional heating can be excluded as the main absorption process and collision-less absorption mechanisms have to be taken into account.

### Resonance Absorption

A resonant plasma wave<sup>1</sup> can be driven when the electrical field of the laser is parallel to a long ( $\leq \mu\text{m}$ ) scale length of the plasma density gradient  $L(\nabla n_e)$ . The absorption is resonant when  $\omega_L$  equals  $\omega_p(z)$ , corresponding to the condition  $n_e(z) = n_c$ , where  $z$  is the laser propagation direction. The absorption efficiency

<sup>1</sup> electron density wave, plasmon

depends on the incident angle of the laser on target surface. For a laser target geometry at an incident angle of  $\alpha_L > 0^\circ$ , the point of reflection for the laser is reduced to  $n_c \cos^2 \alpha_L$ , and the evanescent field can trigger a strong plasma wave [13, 14]. Resonance absorption is significantly decreased for steep plasma gradients and when the incident laser is normal on the target surface [13].

### Vacuum Heating - Brunel Absorption

For a steeper rise of the plasma density,  $L(\nabla n_e) \leq \lambda_L$ , incident angles  $\alpha_L \geq 0^\circ$  and p-polarized electrical fields, electrons are accelerated into vacuum and then accelerated back into the plasma gradient due to the oscillating electric field. In terms of a collective electron oscillation, this can be understood as an electron bunch entering the overdense plasma boundary and passing inside the target. The electrons excursion length  $z_e$  in vacuum [24] can be calculated by

$$\frac{z_e}{\lambda_L} = \frac{a_0}{2\pi\sqrt{1+a_0}} \quad (2.3)$$

The mechanism is efficient when  $z_e$  exceeds  $L(\nabla n_e)$ . If the incident angle  $\alpha_L = 0^\circ$ , then this absorption process can only occur when additional situations, such as e.g., a spatial intensity distribution or target denting and/or the  $v \times \mathbf{B}$  movement, are considered.

### Anomalous Skin Effect

At intensities  $I_L > 10^{19} \text{W/cm}^2$ , according to Equations (2.3), (1.15) and (1.17), the electron excursion length overcomes the skin depth  $l_s$  of Equation (1.21). This induces a nonlocal current in the plasma that enables laser to plasma absorption. It is expressed with an enlarged skin layer  $l_a$  [13]

$$l_a = \left(\frac{2}{\pi}\right)^{1/6} \left(\frac{c^2 v_{os}}{\omega_L \omega_p}\right)^{1/3} \quad (2.4)$$

For  $I_L = 5 \times 10^{19} \text{W/cm}^2$ , an electron drift velocity of 1 MeV and overcritical plasma density of  $n_e/n_c = 300$  the absorbed fraction [13] can be calculated with

$$\eta_{ASE} = \frac{8\omega_L l_a}{3\sqrt{3}c} \quad (2.5)$$

For the above mentioned parameters it is approximately 11%.

### $\mathbf{j} \times \mathbf{B}$ Heating

The  $v \times \mathbf{B}$  term of the Lorentz force (Equation (1.8)) accelerates electrons under specific conditions (relativistic intensity, p-polarized laser field) in the laser propagation direction with frequency of  $2\omega_L$ . If one connects the single particle picture here with a collective electron movement it can result in absorption similar to Brunel and Anomalous Skin Effect mechanisms, for the incident laser normal to the target geometry.

## Ponderomotive Plasma Heating

In addition, the influence of the ponderomotive force (Equation (1.16)) has to be considered. In the relativistic intensity regime, this influence becomes significant and enables a net energy gain for electrons oscillating in a spatial intensity distribution. Hence, electrons can be accelerated into the plasma with velocity of up to  $T_e$  given by Equation (1.17).

In principle, multiple absorption mechanisms can occur simultaneously. In view of the aforementioned extreme laser conditions these are:  $j \times B$  heating for normal incidence and p-polarized laser, absorption driven by ponderomotive effects and the anomalous skin effect.

## 2.3 Energy Loss and Range Energy Relation of Ions in Matter

Simply speaking, the cross-sections for the propagation of charged particles in matter determine processes like scattering, energy loss and charge transfer<sup>2</sup>. For the transfer matter this introduces secondary processes, as excitation, electron ejection, recombination, Auger effect and further scattering processes. Charged particles with a kinetic energy of  $E_{kin}$  travelling in matter lose subsequent energy with scattering and collision processes, known as the theory of stopping power. The stopping power is defined as the energy loss,  $E_{loss}$ , per unit of path length,  $z$ . It is determined by various relevant velocity dependent scattering cross-sections,  $\sigma_i$ , (e.g. electron-electron, electron-ion, and ion-ion); the properties of the stopping material and of the charged particle. The Bethe-Bloch theory gives the following relation for the stopping power for ions [25]:

$$\frac{-\partial E_{loss}}{\partial z} = \frac{Z^2}{m_p A} f(v) \quad (2.6)$$

where  $m_p$  is the mass of a proton,  $Z$  the charge and  $A$  the mass number of the projectile ion. The function  $f(v)$  depends primarily on the projectile velocity and on the stopping material, and secondarily considers specific dependencies e.g. relativistic contributions, charge state and so on.

The Bethe-Bloch equation becomes invalid when  $v_{ion}$  equals the orbit velocity of a bound electron. Then successive electron capture (EC) occur and cause a neutralization of the projectile ion [25]. For the projectile ion an effective charge  $Z^*$  has to be taken into account [26]:

$$Z^*(v) = \eta_Z(v) Z_0 \quad (2.7)$$

Initially the projectile ion has a charge state of  $Z_0$  that is decreased in dependency on the ion velocity with  $0 < \eta_Z < 1$ . The EC process can be assumed to occur for ions at  $E_{kin} > 0.5 \text{ MeV/u}$  in solid dense matter [25, 26]. Note, that given different

---

<sup>2</sup> ionization and electron capture

parameters, such as, higher velocities, the transfer matter density and negative charge states of the projectile ion, ionization (electron loss) of the projectile ion can occur [27]. This process is well known and used in acceleration physics by the application of so called stripper foils.

---

## 3 Laser Plasma Ion Acceleration

Due to their mass, and in contrast to the electrons, direct acceleration of ions in the laser field does not reach the MeV/u range for the laser intensities discussed in this thesis. However, ions are accelerated into the MeV/u kinetic energy regime in a secondary process: The laser driven electron dynamics cause a charge separation, which enables ion acceleration in the associated Coulomb field. In conventional models describing this process, laser-matter-interaction and plasma evolution are viewed from a macroscopic perspective, as the involved physics include highly nonlinear multi-particle and field dynamics. A high complexity arises from the co-parametric dependencies between laser and target parameters and different simultaneously occurring processes. Hence, direct comparison between theoretically predicted scaling laws and experimental results is still challenging. Thus, the experimental situation is often explained with the help of multi-particle computer simulations. To date, the research focuses on how do the acceleration processes depend on the various involved parameters, and aims for maximizing ion velocities. In the following sections, the most relevant ion acceleration models are introduced.

### 3.1 Particle In Cell Simulation

The detailed theoretical description of laser-plasma dynamics is based on the electrodynamics of a multi-particle system interacting with a relativistic electromagnetic field and in dependence of a spatial and temporal evolution. The basic description starts from the electrodynamics with the Maxwell and Boltzmann equations [15], and includes the dispersion relation in the plasma with the Helmholtz equations [13, 14]. To account for either collisionless or collisional interaction the involved magneto-fluid dynamics are calculated using the Vlasov or Fokker-Planck equations, respectively. Furthermore, atomic processes (ionization, recombination) and even nuclear physics (scattering cross-sections, fission and fusion) can be considered. The models in detail are beyond the scope of this work, but need to be mentioned, since they base the algorithms of computer simulations that are usually used to confirm real laser-plasma experiments and to find an analytical description of the involved dynamics. The experimental conditions are simulated by so called Particle in Cell calculations (PIC). Here a number of particles are merged in a cell. The cells motion is evaluated by solving e.g. the Helmholtz-Vlasov equations numerically.

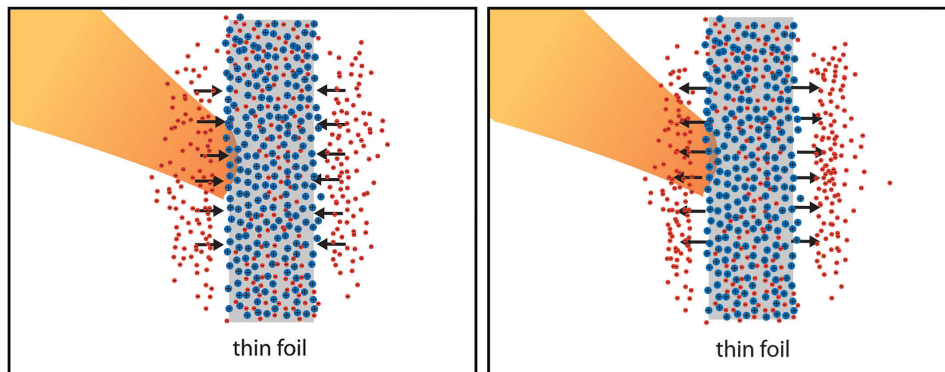


**Figure 3.1:** A laser pulse is focused on a thin foil target at  $\theta_L = 45^\circ$  and ionizes it to a overcritical plasma density. Fast electrons are created at the front side, passing the target. At the target boundary they build up an accelerating electrical field due to the charge separation to the ion background.

### 3.2 Target Normal Sheath Acceleration

The **Target Normal Sheath Acceleration** [16, 28, 29] is the first and most important model describing ion acceleration with thin ( $\mu\text{m}$ ) foils irradiated by a laser pulse with an intensity in the range of  $10^{18}$ – $10^{20}$   $\text{W}/\text{cm}^2$ . In this model, the target remains opaque to the laser light and each laser cycle, fast electrons are accelerated by the laser field and are driven through the target. The kinetic energy of the electrons is assumed to be  $E_{kin} \geq E_{os}$  according to Equation (1.14) or (1.17) and is often called hot electron temperature  $T_e$  [16]. These fast electrons can leave the plasma at the target boundary, where they either escape into vacuum, or reenter the plasma due to the restoring force of the ions and they oscillatory motion with the laser field. In the cycle averaged picture this process causes a quasi stationary charge separation at the plasma boundaries capable of building up a strong electrical field

$$\mathbf{E}_{\text{Sheath}} = \sqrt{\frac{8\pi}{e_N} n_e T_e} \quad (3.1)$$

which starts to expand into vacuum pulling the ions behind it [23, 28, 30]. Thus  $E_{\text{sheath}}$  depends on the ponderomotive potential, which, according to Equation (1.17) scales with the laser field strength and the electron density of the plasma. The electron density is often assumed to be some orders of magnitude lower than solid state density  $10^{23}$   $\text{electrons}/\text{cm}^3$ . This is reasoned by an averaged degree of ionization in the target, the electrons' divergence along the target and to the fraction of electrons, which escaped into vacuum [29].

The expected maximum ion kinetic energy  $E_{kin}^{max}$  is dependent on the acceleration time  $\tau_{acc}$ , which is assumed to be longer than the actual laser pulse duration [28, 31, 32]. In the case of laser pulse durations in the range of pico- or

some hundred femtoseconds, with a standard laser contrast<sup>1</sup> and laser intensities above  $10^{18}$  W/cm<sup>2</sup> the ions maximum kinetic energy can be approximated by [1, 28]:

$$E_{kin}^{max} = 2ZT_e[\ln(\eta + \sqrt{\eta^2 + 1})]^2 \quad (3.2)$$

with  $\eta = \tau_{acc}\tau_L\omega_{pi}$  and the ion plasma frequency is

$$\omega_{pi} = \sqrt{\frac{n_i Z^2 q^2}{\epsilon_0 m_p A}} \quad (3.3)$$

Here  $n_i$  denotes the ion density,  $Z$  the charge state and  $A$  the mass number. The laser to fast electron conversion is assumed to be in the range of approximately 5–10% and to scale with the laser intensity as  $\sim I^{3/4}$  [1]. From an experimental point of view the TNSA acceleration exhibits the following characteristic features:

- The ions spectra have a quasi thermal and thus Maxwellian distribution [1, 29]
- The electron sheath is symmetrically established both at the target rear and front side [33, 34], leading to efficient ion acceleration normal to the target. The most effective laser-plasma absorption was found at an angle of incidence of  $45^\circ$  giving the best results for the TNSA process when the ions are detected in target normal direction [33].
- The contamination layer of the target is accelerated. It consists of light ions like hydrogen (H), carbon (C), oxygen (O) and nitrogen (N). For heavy ion acceleration (A *ge16*) the light ions have to be removed by heating processes [35].

The detailed description of the TNSA process is complex, since it considers a spatial and momentum distribution of the electrons, the target thickness, the laser energy absorption processes and specific models for the expansion process [1, 31, 32, 36]. With respect to different ion species, the expansion of the accelerating field and additional screening effects have to be considered. For ultrashort laser pulses and ultrathin targets, the plasma dynamics changes significantly [1, 36] and will be described in the next section. This has to be taken into account when comparing results of different laser systems operating at the same intensity but at different laser energies and pulse durations.

### 3.3 Radiation Pressure Acceleration

In the 1960s Marx [37] introduced the science fiction idea of accelerating a spacecraft by the pressure of light using a strong laser. Marx's idea involved the use

<sup>1</sup> Common laser contrast means a basic laser contrast level of  $10^{-(6-8)}$  relative to the laser peak intensity, with additional weaker prepulses on ns to ps timescale, furthermore a raising edge of the intensity is in 100 ps range [1].

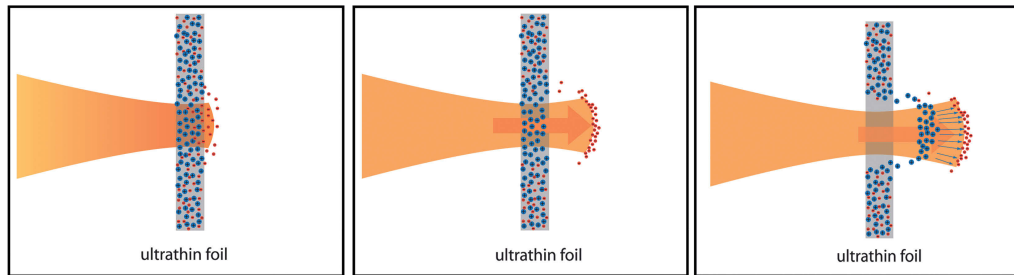


**Figure 3.2:** Schematic representation of the RPA mechanism: laser hits an ultrathin foil target, a dense electron bunch is formed and accelerated to the target rear side. The target remains transparent for the laser light. The overcritical and thus highly reflecting electron bunch is further pushed by the pressure of light. When the restoring force of the ions is high enough to prevent the electrons escape, the ions are pulled to high velocities by this electron bunch.

of a highly reflective mirror in order to enable efficient momentum transfer between the photons and the spaceship. The amount of reflected light determines the radiation pressure

$$P_I = \frac{I_L R}{c} \quad (3.4)$$

where  $R$  is the fraction of the reflected light. In order to transfer this idea to laser-plasma based particle acceleration, one needs a sufficient dense but thin enough target: ideally fully ionized with all electrons forming a dense electron bunch ( $n_e \gg n_c$  see Section 1.4). The photons' momentum transfer to this highly reflecting electron sheath [38] is given by

$$\frac{\partial \mathbf{p}}{\partial t} = R \frac{I_0(t - x(t)/c)}{2\pi n_e D} \frac{\sqrt{p^2 + m_e^2 c^2} - p}{\sqrt{p^2 + m_e^2 c^2} + p} \quad (3.5)$$

where  $p = mv$  is the momentum of the electron sheath. At sufficient laser intensity, the radiation pressure pushes the irradiated area into the target. The process is called hole boring (HB) [36] and can introduce spatial denting and shockwaves into the target.

Similar to the TNSA model, for radiation pressure influenced laser-ion acceleration, during the laser-plasma interaction a dense electron sheath is established at the target rear side. For thin or less dense target foils, a part of the laser light can pass through the target and further accelerate this electron sheath. If the ions are still bound to it by a sufficient high restoring force, radiation pressure can enhance the ion acceleration as depicted in Fig. 3.4. Thus, radiation pressure acceleration depends for a given laser intensity on a specific target thickness and density. A lower limit in terms of target thickness is given by the so called **electron blow out**: electrons can overcome the Coulomb-attraction to ion background with  $k_L = \omega_L/c$  for a target thickness [39] of

$$D \ll \frac{a_0 n_c}{k_L n_e} \quad (3.6)$$

In the ideal case, all electrons are assumed to be pulled out to form the electron sheath, thus enabling a high reflectivity for the pushing laser light. For the ion acceleration a balance between radiation pressure and the restoring force to the ions has to be maintained. This condition is fulfilled for an optimum target thickness that was obtained from multi-parametric PIC simulations by Ref. [39] at

$$D_{\text{opt}} = 3 + 0.4 \times a_0 \lambda_L \frac{n_c}{n_e} \quad (3.7)$$

Since this condition is a function of the electron density  $n_e$ , it often refers to an optimal areal density  $\sigma_{\text{op}} = n_e D / n_c \lambda_L \sim a_0$ . In principle, the condition corresponds to the inset of relativistic transparency described by Equation (1.23) [1]. An increase of the RPA efficiency was suggested for circular laser polarization, since  $j \times \mathbf{B}$  heating is inhibited and fewer electrons can escape the potential well (cf. Section 2.2). Ions that follow the electron sheath are found at the same velocity. Therefore, pure RPA accelerated ions are expected to have a bandwidth limited energy distribution. At the optimum target thickness and density for  $Z/A = 0.5$ , maximum ion energies are predicted [36] at

$$E_{\text{kin}}^{\text{max}} = \frac{m_e^2 c^2}{8m_p} a_0^2 \left(\frac{\tau_L}{T_L}\right)^2 \sim 2.3 \text{MeV} \times \frac{I \tau_L^2}{[10^{-6} \text{Jscm}^{-2}]} \quad (3.8)$$

Experimental results for a RPA influenced acceleration have shown a remarkable increase of the ion energies by optimizing the foil thickness to the laser intensity [2, 40]. Currently available laser systems reach intensities  $I_L \sim 5 \times 10^{20}$  which is sufficient to see the onset of the RPA. Therefore, in literature considering experimental result, the ion acceleration scheme is often referred to a mixture of TNSA and RPA-like acceleration or modified similar scenarios, e.g leaky-light sail [41].

### 3.4 Coloumb Explosion

In the introduced acceleration models, ions are pulled by an electron sheath and their acceleration depends on their charge to mass ratio ( $Z/A$ ). The acceleration can be viewed as an ion accelerating in an expanding and moving capacitor. Assuming a shared starting point in time and space, ions with different  $Z/A$  numbers separate during the acceleration. Additionally, light ions co-propagating with the electron sheath screen the accelerating electrical field for heavier ones [35, 42]. If the lack of electrons in the ion background is not compensated, a repulsive Coulomb field is established. In the case of a highly dense, highly charged and slower ion background, it can become an additional strong acceleration field for a (few) particle(s) in front of it. For an ultrathin foil thickness, the majority electrons are considered to leave the target with the accelerating sheath<sup>2</sup>. Therein, theoretical works predicted an enhancement of the kinetic energies of light ions,

<sup>2</sup> Ionization of the target depends on amount of particles and on ionization levels of the used materials.

because the repelling Coulomb field of the slower heavy ions ( $A \geq 12$ ) pushes them from behind [39, 42, 43]. An efficient acceleration via Coulomb explosion for highly mass limited, cluster targets is discussed in [1].

### 3.5 Shock Acceleration

Laser driven plasma acceleration is often and in respect to PIC simulations described on the basis of electro-magnetic fluid dynamics. In general shock waves are excited by a disturbance in the density of a medium, e.g. by a projectile propagating through plasma. Shock waves are density pressure waves and travel with the sound velocity  $v_s$  through the medium. In plasma, a shock front is formed when e.g. ion densities (bunches) meet at significant different velocities. The condition introduces an acceleration of ions by the shockfront at  $v_s = Mc_s$  with

$$c_s = \left( \frac{ZT_e}{Am_p} \right)^{1/2} \quad (3.9)$$

The model predicts, for ions reflected from the potential of the shockfront, a quasi mono energetic spectrum up to  $2v_s$ , for Mach numbers  $M > 1$  [36]. Simulations have shown efficient ion acceleration at the onset of relativistic transparency, by a shock wave in plasma [44, 45]. Particles from the target front side are accelerated by e.g. radiation pressure to higher velocities,  $v_s$ , than the particles that are accelerated by a TNSA like sheath at the rear side of the target. This process was already mentioned as hole boring in Section 3.3. The shock velocity resulting from the pressure of light can be approximated, according to Equation (3.8) [16] with:

$$\frac{v_{sRPA}}{c} \sim \sqrt{\frac{Zm_e n_c}{2Am_i n_e}} \times a_0 \quad (3.10)$$

## 4 High Harmonic Generation and Relativistic Backscattering

For an ultrahigh laser contrast, the laser interacts with a steep dense plasma boundary. This interaction drives collective electron oscillations at the target boundary that causes a coherent emission of an attosecond pulse once per laser cycle, known as High Harmonic (HH) generation from over dense plasma. The phenomenon is in the focus of latest scientific research, since it is a promising coherent source of XUV radiation. Moreover, the HH emission reveals, indirectly, information about the ultrafast and collective electron dynamics of the laser-plasma interaction [24, 46, 47].

High harmonic radiation is named after the characteristic feature of the attosecond pulse's spectral intensity distribution, which exhibits successive peaks at multiples of the fundamental frequency

$$\omega_N = N \times \omega_L \quad (4.1)$$

where  $N \in \mathbb{N}$  denotes the harmonic number. Hence, the detected harmonic intensity spectrum consists of a sequence of consecutive harmonic lines up to  $N_{max}$ . In the time domain, HH emission has to be understood as an pulse train with equally spaced ultrashort pulses. Each single pulse is emitted at a time difference of one laser cycle, with a pulse duration of less than  $10^{-16}$  s [48]. The separation of single pulses from a pulse train is still challenging and recently, the first successful approaches were reported in Refs. [49–51].

There are two basic models explaining HH generation from ultraintense laser pulses interaction with solid state targets. They are introduced in the following sections, for a more detailed review Ref. [24] is recommended. Another option to obtain ultrashort, coherent radiation is predicted due to a relativistic backscattering process and is discussed in the final section of this chapter.

### 4.1 Coherent Wake Emission

In the Brunel absorption process (cf. Chapter 2) for a laser on target incidence angle of  $\alpha_L > 0^\circ$ , a dense electron bunch is accelerated into the plasma boundary once per laser cycle. For a steep rise of the plasma density ( $L(\nabla n_e) \sim \lambda_L/10$ ), this electron bunch excites plasmons (electron density waves) in its wake. These plasma waves can decay via linear mode conversion into coherent radiation [5,

[24]. This radiation is called Coherent Wake Emission (CWE). When the plasmon passes through a the local density of  $n_e(z) = N \times n_c$  it decays into the corresponding harmonic emission  $N \times \omega_L$ . Hence, radiation in multiples of  $\omega_L$  is emitted within one laser cycle. The CWE model has been developed with the aid of PIC simulations [24] and the emission direction has to fulfil a conservation between the wave vector of the emitted light and the plasmon. The maximum cutoff frequency of the emitted radiation is given by the maximum electron density [5, 24, 52]:

$$N_{max} \sim \sqrt{\frac{n_e^{max}}{n_c}} \quad (4.2)$$

For  $n_e/n_c = 400$ , which is a reasonable approximation for carbon or glass bulk targets and  $\lambda_L = 800$  nm, this results in a CWE harmonic cutoff of  $N_{max} = 20$ . This scaling was confirmed in earlier experiments at the MBI laser system in Refs. [47, 53] regarding to bulk targets and a XUV detection in the reflection direction with a laser on the target incidence angle of  $45^\circ$ . The CWE emission process is predicted to commence for laser intensities below the relativistic onset [5].

In principle, the Brunel absorption mechanism is reliant on a laser to target incidence angle of  $\alpha_L > 0^\circ$ . For a setup with the laser normally incident on an ultrathin foil, another mechanism is required and the laser driven electron oscillations relate in the relativistic case to the figure 8 motion at the plasma boundary of Section 1.2 of Equation (1.1). CWE harmonics emitted from of an ultrathin foil have been discussed theoretically in [54], with the help of PIC simulations, for laser to target setup at  $> 45^\circ$ .

## 4.2 Relativistic Oscillating Mirror Model

Albert Einstein introduced the model of a relativistic oscillating mirror [11] from which light is reflected. Due to the relativistic movement, a relativistic doppler shift changes the frequency of the reflected light to

$$\omega' = \omega_L \frac{1 + \beta}{1 - \beta} \quad (4.3)$$

The relativistic oscillations of electrons at a sharp plasma boundary with kinetic energy up to  $E_{os}$ , can serve as such a relativistic oscillating electron mirror. This is the idea of the Relativistic Mirror Model (ROM) that describes the emission of HH radiation from overdense plasma surfaces in the interaction with laser pulses at relativistic intensities  $a_0 > 1$ . Detected in the reflection direction, ROM harmonics are emitted once per laser cycle from a relativistically oscillating plasma surface. In particular, for a linear polarized light field  $\mathbf{A}(\mathbf{z}, \mathbf{t})$  normally incident on an oscillatory plasma boundary, the reflected electrical field [4] reads

$$E_R(z, t) = \frac{\omega_P}{\omega_L} \mathbf{A}(t_{ret}) = A_0 \sin(\omega_L t + k_L z - \omega_L X(t)/c) \quad (4.4)$$

where the surface movement  $X(t)$  denotes, to first approximation  $X^1(t) = -X_s \sin(2\omega_L t)$  and the retarded time in the rest frame of the observer

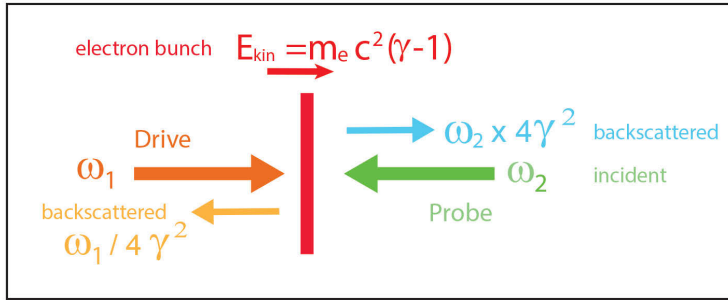


**Figure 4.1:** Illustration of relativistic backscattering for two counter-propagating laser pulses and a foil target. The drive pulse accelerates an electron bunch to relativistic velocity upon which the second pulse is reflected in the backward direction. Due to the double relativistic doppler shift, the backscattered pulse experiences a frequency shift of up to  $\omega \times 4\gamma^2$ .

is  $t_{ret} = (t - X(t_{ret})/c + z/c)$ . With respect to  $X(t)$ , the reflection introduces an upshift in frequency and occurs in a time range that is significant smaller than half of the laser period. For successive laser cycles, it corresponds to the emission of a pulse train, with single pulse durations  $> \tau_L/\gamma^2$  [4, 55], where  $\gamma$  denotes the velocity of the plasma surface. For a reflection when the laser pulse is at normal incidence angle on the target, only odd harmonic numbers result. An obvious difference to the CWE mechanism is found in the frequency cutoff: For ROM it scales with electrons' oscillatory movement, thus it scales with  $a_0$ . The highest harmonic number is predicted at

$$N_{max} = 4\gamma^2 \quad (4.5)$$

For  $a_0 = 5$  and a velocity of the surface according to Equation (1.14), one can calculate  $N_{max} = 54$ . For HH emission in laser propagation direction and incident angle  $\alpha_L = 0^\circ$ , this model is not directly applicable due to the reflection direction. Modified models will be discussed in more detail with the presented results.

### 4.3 Relativistic Backscattering

Einstein's relativistic mirror model can be also approached by a direct relativistic backscattering. Theoretically, this was suggested for two laser pulses in a counter-propagating setup. One laser creates a relativistic electron bunch e.g. by the use of an ultrathin foil target, from which the second laser pulse is reflected [39]. The backscattered pulse is shifted to a higher frequency in accordance with Equation (4.3). The principle is depicted in Fig. 4.1 and is dependent on the electron bunch velocity. If the second laser has an intensity high enough to drive HH emission itself, theoretically one expects an enhanced harmonic frequency cutoff at  $\lambda/(N_{max} \times 4\gamma^2)$  [39]. The efficiency of the process is determined by the reflectivity,  $R$ , of the relativistic mirror, and therefore connected to the density and spectral bandwidth of the electron bunch. The ideal case of collective electron

motion at one velocity with high reflectivity is looked by the theoretical models. It delivers promising results, but is a simplification. The electron bunch is expected to be accelerated within a certain spectral bandwidth, and, for ultrathin foils, with a density much lower than the solid state density [56]. In addition, PIC simulations demonstrate that the emission of electron bunches once per laser cycle has to be taken into account [57]. The reflectivity from such an electron bunch can be described within classical electro-dynamics by relativistic Thomson scattering [56, 58, 59]. In the approximation of [56],  $R$  scales with the electron scattering cross-section

$$\sigma_T = 6.65 \times 10^{-29} \text{m}^2 \quad (4.6)$$

and by the number of scattering electrons  $N_e$  per area  $A_F$

$$R_T = \sigma_T \sqrt{\pi} \frac{N_e}{A_F} f(q, \gamma) \quad (4.7)$$

where  $f(q, \gamma) < 1$  is a function of the form factor and spectral condition of the electron bunch. For ultrathin foils a few nm thick,  $R$  is limited by particle numbers and is estimated to be below  $10^{-5}$  for all electrons of a  $\sim 10$  nm foil. In the case of coherent scattering Equation (4.7) is predicted to scale with  $N_e^2$  [56], which, could enhance the efficiency remarkably.

## Part II

# EXPERIMENTAL METHODS



## 5 Laser System and Experimental Setup

All experimental data presented in this work has been obtained using the High Field Laser at the Max Born Institute (MBI). Section 5.1 gives a summary of the design of the laser system and Section 5.2 a characterization of the resulting laser contrast. The basic setup used in experiments for ion, electron acceleration and XUV radiation is introduced, along with the inherent diagnostics, in Section 5.3. How the setup was modified for a two counter-propagating laser pulse experiment is described in Section 5.4. It includes the used diagnostics and definitions of the overlap in time and space between both laser pulses. The used target foils are characterized in Section 5.5, followed by a description of the applied spectral detection devices for ions, electrons and XUV radiation in Section 5.6.

### 5.1 High Field Laser System

The High Field Laser at the MBI is a 80/100 TW Ti:Sapphire Chirped Pulse Amplification (CPA) laser system. It consists of two synchronized laser arms, with each arm delivering a different laser contrast, pulse energy and pulse duration. All experiments presented in this work, were single laser pulse measurements, and were performed with Arm I (80 TW). Substantial improvements of the laser system were achieved with respect to the pulse duration and laser contrast. Both laser arms share the same frontend, a commercial Kerr-Lens mode locked oscillator followed by a XPW (Cross Polarized Wave) module. The pulse repetition rate of the oscillator is decreased from 85 MHz to 10 Hz by a pulse picker<sup>1</sup>. The XPW frontend [60] increases the initial laser contrast before subsequent amplification by reducing the Amplified Spontaneous Emission (ASE) level in a nonlinear optical cross polarized wave mixing process [12, 61]. The polarization of a laser pulse can be changed in an anisotropic crystal (e.g. CaF<sub>2</sub>), where the change is dependent on the impinging light intensity. The process corresponds to a temporal polarization filter, which switches the polarization dependent on the applied intensity. Afterwards a second polarizer filters the signal, allowing low and high intense laser radiation to be separated. Therefore, for Arm I, the relative laser contrast ratio of  $> 10^{-10}$  is obtained on the picosecond time scale and with respect to the main peak intensity at full laser power.

<sup>1</sup> A Pockels cell is an electro-optical device, capable of switching its polarity dependent refractive index by applying high voltage. A pockels cell operates on ns to ps range.

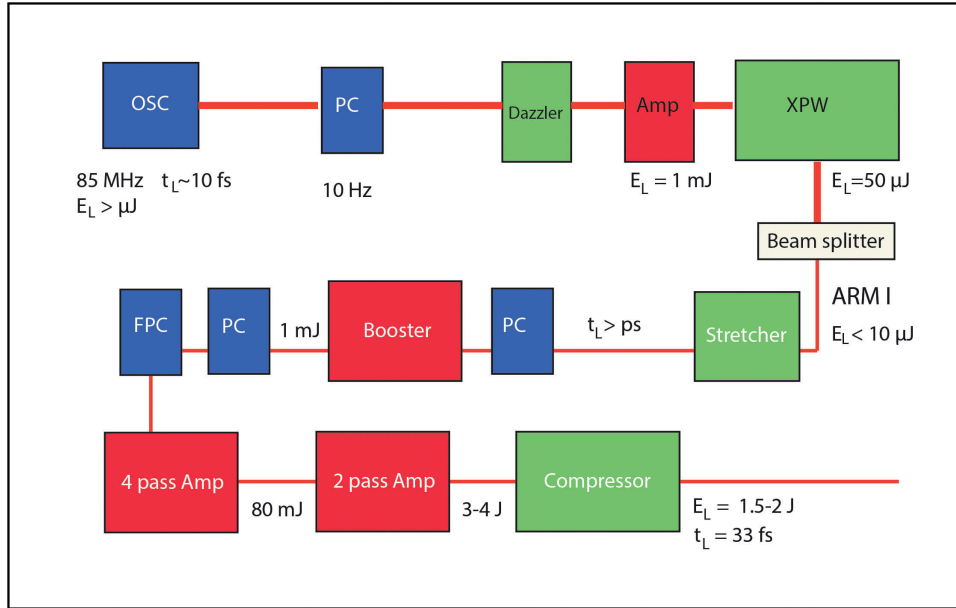


**Figure 5.1:** Schematic setup of laser Arm I, which is a Chirped Pulse Amplification system. The system bases on a common Kerr-Lens mode locked oscillator in combination with a XPW frontend, behind which the beam is split into Arm I and Arm II. The laser pulse of Arm I is first stretched by temporally elongation using an Öffner stretcher, and cleaned of pre-pulses by two pockel cells (PC). Then, the pulse is further amplified by the "booster", which contains an acoustic-optic spectral phase modulation module (Dazzler) to compensate phase distortions introduced by the amplification process. The pulse contrast is enhanced by a fast pockel cell (FPC) operating in the hundred picosecond range and further amplified by two following multi-pass amplifiers. In the last stage, the pulse is compressed and guided in vacuum to the experimental chamber. Single shots are selected manually using a manual shutter.

Prior published work with the same laser system [32] used a 5-way multi-pass amplifier [10] in the amplification chain. This was replaced in the year 2013 by a "booster-amplifier" consisting of a 2-pass amplifier that enabled a higher amplification efficiency. The method takes advantage of a configuration, where the laser incidence on crystal is at Brewster's angle<sup>2</sup>. The reduction in the number of the amplification passes shortens the optical path length in the crystal. This optimized the laser's contrast in terms of ASE and reduced reflections from the amplifying crystal surface, which otherwise lead to pre-pulses in the common multi-pass geometry. The booster was equipped with a Dazzler<sup>3</sup>, which allows one to manipulate and compensate for higher order spectral pulse phase distortions, which are introduced by the amplification process [62]. It was used to achieve pulse duration close to the Fourier limit. The laser Arm I reached for a single

<sup>2</sup> Brewster angle: incident angle at which the transmission of light is maximal. It depends on optical characteristics of the material and the laser polarization

<sup>3</sup> Acousto Optic Programmable Dispersive Filter to manipulate the spectral phase and the carrier envelope of a laser pulse.

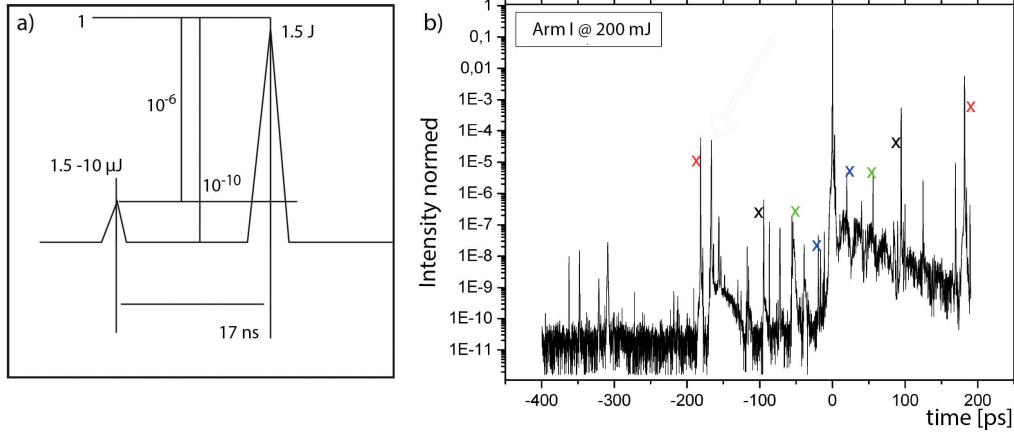


**Figure 5.2:** a): Pre-pulse levels of the high laser contrast condition measured with a fast diode on a nanosecond timescale. b): Third order autocorrelation measurement shows the laser at high contrast condition on a picosecond time scale. Peaks marked with "x" are ghost lines caused by internal reflections of the measurement instrument.

laser pulse an energy of up to  $E_L = 2.3$  J after the pulse compression on the target, with a pulse duration of  $\tau_L = 35$  fs<sup>4</sup>. Adaptive optics were used to perform laser wavefront corrections on a daily basis.

## 5.2 Laser Contrast

### 5.2.1 High Laser Contrast

The laser contrast was measured on the nanosecond and picosecond time scales and is shown in Fig. 5.2. Due to reflections in the third laser amplifier, a pre-pulse appears 17 ns before the main peak of the laser pulse with an energy content in the minor  $\mu$ J range. The pre-pulse intensity was dependent on the daily laser alignment and therefore could be up to 30% smaller as in Fig. 2 a). Assuming a compressed pre-pulse with a duration in the range of 60 – 90 fs and a focus diameter similar to the value of the focused main laser pulse, the pre-pulse could reach an intensity of about maximal  $10^{13}$  W/cm<sup>2</sup>. A third order autocorrelation measurement of the laser intensity on the picosecond time scale is shown in Fig. 5.2 b). The basic laser contrast level was about  $\sim 10^{-10}$  relative to the laser's peak intensity and several weak pre-pulses are present. The strongest pre-pulse was detected 180 ps before the main peak with an intensity about  $2 \times 10^{-5}$  lower than the pulse peak level. It was followed by pre-pulses at a relative contrast difference of  $10^6$ . If applied, this laser contrast condition will be named in the following **high laser contrast** or **HC**.

According to the theory of laser induced target ionization and absorption introduced in Chapter 2, pre-ionization of the target occurs for these laser contrast

<sup>4</sup>The pulse duration was measured via spectral phase interferometry for direct electric field reconstruction (SPIDER).

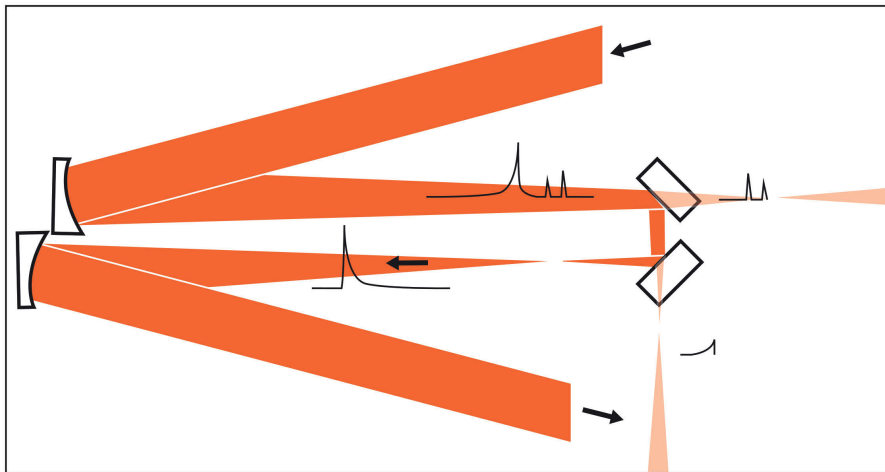


**Figure 5.3:** The double plasma mirror (DPM) setup consists of two anti-reflection coated, polished glass substrates and a focusing unit. Light is transmitted until the rising intensity or pre-pulses ionizes the substrate's surface to an extent, that plasma with overcritical density is created, which switches the optical property to reflection in accordance to Equation (1.22).

parameters. Additional plasma heating is expected from the rising pulse edge for an intensity above  $10^{16}$  W/cm<sup>2</sup> a few picoseconds before the pulse peak arrives. Pre-pulses and this rising intensity level determine the scale length of the plasma density gradient, which has a substantial influence on the plasma dynamics when the interaction with the main laser pulse takes place. Currently, there is no analytical model that provides a detailed description of the influence of short pre-pulses on the evolving plasma dynamics, if the pre-pulses have different intensity levels and act on different time scales. Therefore, this question is usually addressed to PIC simulations, for an adequate long time interval [63–65].

## 5.2.2 Ultrahigh Laser Contrast

If the incident laser intensity is high enough on a solid state surface, it is ionized and transformed into plasma with an electron density higher than the critical density  $n_c$  (cf. Equation (1.22)). According to the dispersion relation in Section 1.4, this process change the optical properties of the surface from transparent to highly reflective. The laser contrast can benefit from this basic principle by using it as a irreversible single shot device, known as plasma mirror [52, 66]. It consists of one or a set of glass substrates with high quality surfaces on which the laser is slightly focused. The light arriving at the surfaces in form of pre-pulses, is transmitted until the rising edge of the main intensity peak ionizes the surface to such an extent that the optical properties of the medium is changed, and a highly reflecting surface is created - a plasma mirror. For the experiments presented in this thesis, **ultrahigh laser contrast/ (UHC)** was achieved by applying a Double Plasma Mirror (DPM) setup, which was described in detail in Ref. [67] and is illustrated

in Fig. 5.3. The used glass substrates improve the filtering process by means of a high quality anti-reflection coating with a high surface quality of  $\lambda_L/10$ . The resulting laser contrast enhancement was approximately four orders of magnitude. In comparison to Fig. 5.2, this led to a contrast ratio, with respect to the main peak level, of  $10^{-14}$ . This value is based on calculations in Refs. [10, 68, 69] and measurements for comparable designs [40]. In the framework of this thesis, the DPM setup was modified in comparison to the setup of Ref. [10]. By applying a higher intensity on the second substrate, the performance of the DPM was optimized with regards to the stability of the laser wavefront, and the absorption efficiency of the pre-pulses. The DPM delivered a laser energy transmission of up to 80%. The resulting beam profile, energy transmission and the pre-pulse level were monitored in each measurement. The diagnostics used are described in the following section.

### 5.3 Single Laser Pulse Experiments

The basic setup used for laser driven ion and electron experiments with thin and ultrathin foil targets is shown in Fig. 5.4. The laser pulse was focused by a  $f/2$  Off Axis Parabola (OAP) to a focus diameter FWHM of 4–6  $\mu\text{m}$ . The energy content in the FWHM of the focus is up to  $(19 \pm 3)\%$ . For a pulse energy of 4.0 J before compression and a beam line transmission of  $\sim 63\%$ , an laser intensity up to  $I_L = 1 \times 10^{20} \text{ W/cm}^2$  could be obtained at high laser contrast condition, if averaged over the focus area. In the case of ultrahigh laser contrast, with the use of the DPM, an intensity up to  $I_L = 8 \times 10^{19} \text{ W/cm}^2$  could be reached. The laser intensity was dependent on daily parameters such as the quality of the laser focal spot and the applied laser energy. In order to monitor relative shot to shot fluctuations of the laser energy, the transmitted laser light was measured behind a highly reflective beamline mirror (**E** in Fig. 5.4). This diagnostic recorded the spatial intensity distribution of the beam profile and provided additional information about e.g. instabilities in the laser wave front arising from the DPM's surfaces, or flow marks by thermal air movements in the laser room. A fast diode (**D** in Fig. 5.4) measured the pre-pulse level on a nanosecond time scale for every laser shot.

Throughout this work, the laser illuminated the target at normal incidence. The detection direction of the accelerated ions, electrons and XUV radiation was always in the direction of the laser propagation (**B, F, G** in Fig. 5.4). Back reflected laser light from the target was imaged by a Roper Scientific PIXIS 512B cooled camera (**C** in Fig. 5.4). It provided an image of the intensity distribution of the laser focal plane on the target and enabled an alignment of the laser focal position with an accuracy of  $\pm 10 \mu\text{m}$ . This diagnostic is named BRFX in the following. With the help of a broad white light source in the experimental chamber, the same diagnostic was applied for imaging the target's surface with a magnification factor of  $\times 35$ . This enabled monitoring of the target surface and identification of damaged foils, as shown in Fig. 5.4.

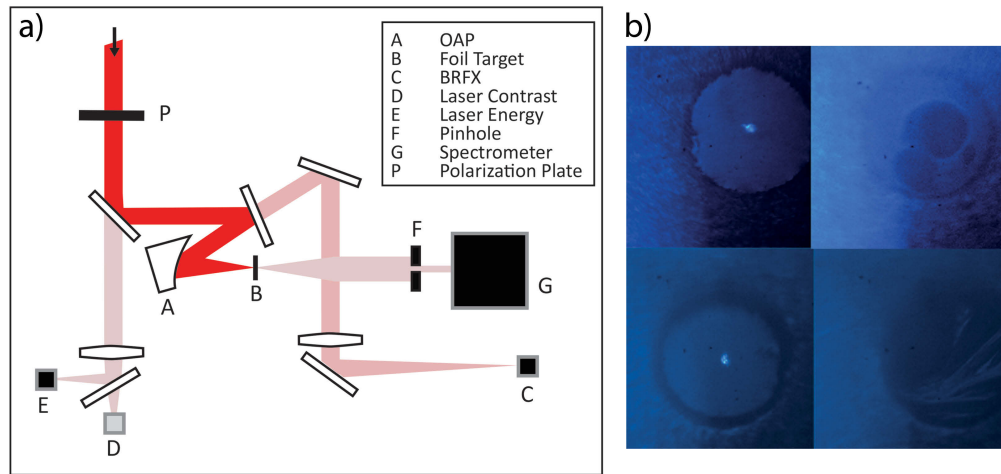


**Figure 5.4:** a): Schematic of setup used in laser-plasma particle acceleration experiments for an interaction of a single laser pulse with a foil. Here, OAP stands for Off Axis Parabola, and BRFX for back reflex diagnostic. The laser beam is illustrated in red and transmitted light in pink. b): Target surfaces of various damaged or undamaged foils imaged by the BRFX diagnostic.

## 5.4 Two Laser Pulse Experiments

In order to apply two laser pulses on the target foil, the experimental setup of Fig. 5.4 was modified. Fig. 5.5 shows the basic setup for two laser pulses in a counter-propagating geometry. The laser pulse was passed through a beam splitter (**I** in Fig. 5.5) with a reflection to transmission ratio of 73/27. For convenience, the reflected part is called the "**drive pulse**" in the following, while the transmitted part refers to the "**second laser pulse**" or the **P2** pulse. Due to the beamsplitter, the maximal available intensity of the drive pulse is decreased to  $I_L \leq 6 \times 10^{19} \text{ W/cm}^2$  at ultrahigh and  $I_L = 7 \times 10^{19} \text{ W/cm}^2$  at high laser contrast. The drive beam was focused by the  $f/2$  OAP (**A – 1** in Fig. 5.5), as in the previous setup, P2 was passed along a delay stage (**H** in Fig. 5.5), focused using a  $90^\circ$ ,  $f/5.4$  OAP (**A – 2** in Fig. 5.5). P2 propagated in the opposite direction to the drive pulse. In respect to the beam splitter<sup>5</sup> the transmitted pulse was assumed to be temporally elongated to a duration of  $\tau_P = 70 \text{ fs}$  [32]. A focal diameter of P2 was experimentally determined with a value of approximately for the FWHM of about  $15 \mu\text{m}$ . In respect to the beam splitter transmission values and a longer pulse duration, a maximum intensity of the P2 pulse of  $I_P \leq 2 \times 10^{18} \text{ W/cm}^2$  was calculated. A lower intensity  $I_P$  could be applied by either limiting the beam in diameter with an aperture or by a displacement of the focusing optic in the target normal direction<sup>6</sup>. In the center of this focusing optic, a tunnel was located with  $0.5 \text{ mm}$  in diameter, through which radiation and particles could pass. With this

<sup>5</sup> 25 mm silicon oxid irradiated at incident angle of  $45^\circ$

<sup>6</sup> The later option corresponds to defocused position of P2 on the target foil.

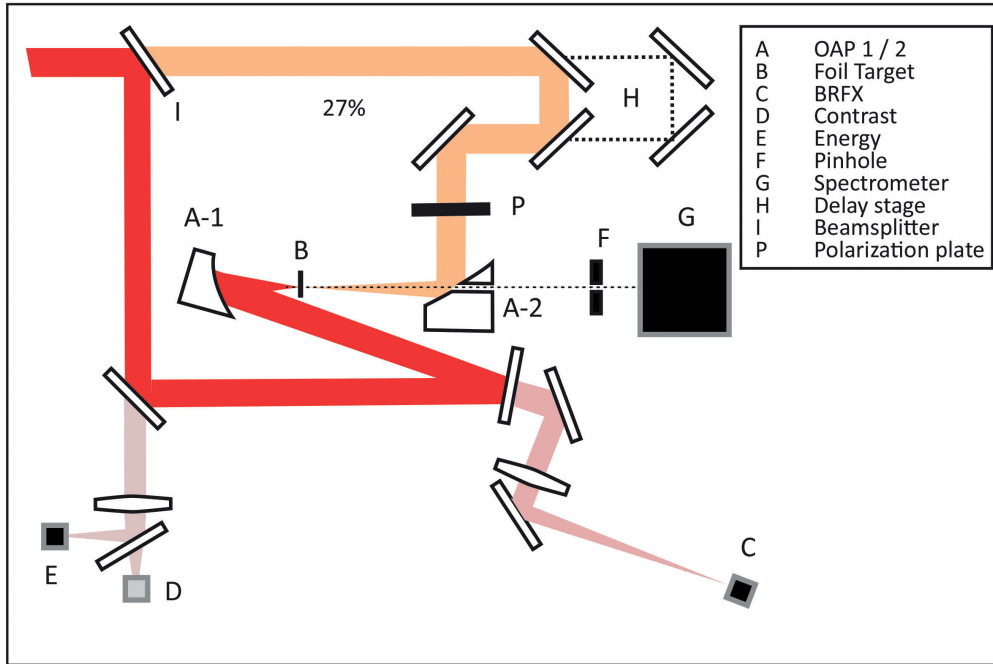


**Figure 5.5:** Experimental setup for the irradiation of a target using two laser pulses propagating in opposite directions. The beam splitter placed at **I** separates the laser beam into two parts. The weaker, transmitted laser light (orange) is guided over a delay stage (**H**) to a second focusing optic at **A-2**. The setup enables the propagation of both pulses on the same axis, in opposite directions respectively. Further details are provided in the main text.

counter-propagating setup, particles were detected in the propagation direction of the drive pulse and the detection units were placed behind the focusing optic of the second laser pulse (**F** and **G** in Fig. 5.5). Moreover, both pulses shared the same propagation axis, but in opposite directions. The alignment ensured an angular deviation between drive and P2 pulse of about  $0.5^\circ$ .

### Overlap in Time and Space

The two laser pulse experiment requires an overlap of both pulses in time and space. Spatial overlap of both focal planes on the target was monitored with a double microscope setup, one imaging the focal plane of the drive pulse, the other imaging the focal plane of the P2 pulse. In order to determine a relative distance between both focal planes, an immovable mesh of 40 lines per mm at the position of the target was imaged from both sides. Since the distance between the microscopes was fixed, this method ensured a spatial overlap with an accuracy of  $\pm 100 \mu\text{m}$  in the laser propagation direction ( $z$ ) and of less than  $10 \mu\text{m}$  in the  $x$  and the  $y$  direction. Spatial displacements of both focal planes in  $x - y$  plane due to pointing fluctuations of the laser were about  $10 \mu\text{m}$ . The BRF diagnostic, as introduced before, imaged the intensity profile of the drive pulse on the target to

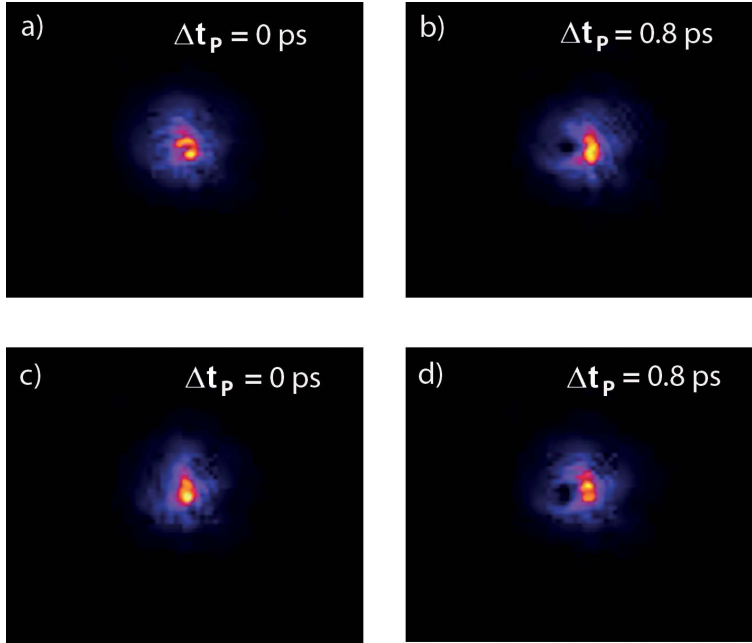


**Figure 5.6:** Images of the shadowgraphy measurement at different delay times using the BRFX diagnostic (see **C** in Fig. 5.5). a): Temporal and spatial overlap between drive and P2 pulse. It corresponds to the onset of the plasma channel created by the drive pulse in the case of a spatial overlap between both focal positions. b): Shadow of plasma channel in the profile of P2 pulse at an applied delay of 0.8 ps, using the delay stage. c), d): Alternatively, a temporal delay is introduced by moving the focusing optic of the P2 pulse along the propagation axis. c): Without displacement at the temporal overlap. d): 240  $\mu\text{m}$  displacement in the direction of its focusing optic, which corresponds to a delay of 0.8 ps.

within an accuracy of 10  $\mu\text{m}$ . By removing the target from its designated position, the intensity profile of P2 at this particular position could be imaged with the same diagnostic. Thus, this method was used to improve the spatial overlap of both focal planes in the coordinate  $z$ .

In order to enable and determine the temporal overlap of both laser pulses at the focal plane of the drive pulse, a shadowgraphy imaging method was applied [32]: For laser energies in the  $\mu\text{J}$  range, the drive pulse was capable of ionizing gas at the focal plane. Due to laser self-focusing [12], this drove a plasma channel in air or gas, which became visible in the form of a spark. It existed for a lifetime of some 100s of ps, much longer than the actual pulse duration  $\tau_L$ . When the second laser pulse, at an even lower intensity, now passed through the plasma channel, a shadowed area appeared in its profile, due to a changed refraction index in the plasma channel. In order to obtain a shadowgraph of the created plasma channel, the beam profile of the second laser pulse was imaged using the back reflected light diagnostic (BRFX) (cf. Fig. 5.5 **C**). Fig. 5.6 shows shadowgraphs for various delay and displacements of the focal plane of the P2 pulse. If the P2 pulse had arrived before the formation of a plasma spark by the drive pulse, then

no shadow was seen in the intensity profile. If the P2 pulse arrived after the drive pulse, then a shadowed area appeared.

The temporal overlap between drive and P2 pulse was defined in the following way: Firstly, the temporal overlap  $\Delta t_P = 0$  always referred to the moment in time when the drive pulse impinged on the target. The drive pulse was fixed in time and space<sup>7</sup>, while the P2 pulse was delayed and/or displaced relative to it. Secondly, the temporal overlap was determined by the time, when the plasma channel of the drive pulse just appeared as a shadowgraph in the image of the focal profile of the P2 pulse. In order to measure the temporal delay as precisely as possible, a careful time scan was performed on a daily basis at a chamber pressure of 100 mbar (nitrogen). This procedure minimized additional contributions due to dispersion at different path lengths. The overlap of both pulses at the target position was determined with an accuracy of  $\Delta t_0 = (0.0 \pm 0.2)$  ps. By the limited accuracy of this method, the temporal overlap is assumed to be at an almost fixed time within this time interval. Fluctuations due to spatial beampointing were assumed to be below 50 fs. The uncertainty of the temporal overlap could correspond to a constant offset for the delay time applied, if the same experimental run is considered. The temporal overlap was aligned for each experimental run and this leads to possible different offsets considering  $\Delta t_0 = 0$  for each experimental run. Hence, a direct comparison for measurements at different delay times was restricted to the same experimental run. In addition, for the shadowgraphic measurement both pulses were passed through identically designed beams shutter windows, which additionally might have introduced aberrations on the order of a few  $\mu\text{m}$ . The associated temporal overlap was therefore assumed to lie within an time interval of  $\pm 0.3$  ps. Relatively a delay of P2 could be applied with a stepsize of 0.1 ps, either by increasing the path length with the delay stage, or by a displacement of the focusing optic of the P2 pulse.

## 5.5 Ultrathin Foil Targets

Current research on laser ion acceleration (cf. Chapter 3) focuses on an optimization of the target thickness for the given laser parameters to increase the kinetic energy of the ions. In contribution, this work included the development of methods for ultrathin foil production and characterization, which was published in Ref. [70]. The performed experiments used foils with a thin ( $< 5 \mu\text{m}$ ) and ultrathin ( $< 200 \text{ nm}$ ) thickness. These foils were freestanding over the holes of a steel plate with diameters of either 300/600/2000  $\mu\text{m}$ .

### 5.5.1 Polyvinylformal Foils

Polyvinylformal (PVF) is a common hydrocarbon material with the stoichiometry  $[\text{C}_5\text{H}_7\text{O}_2]_n$  and a density of 1.23–1.25  $\text{g}/\text{cm}^3$ . The foils were produced by means of a spin coating process, using 1, 2-Dichlorethane as solute with a concentration

<sup>7</sup> within the given accuracy of its alignment

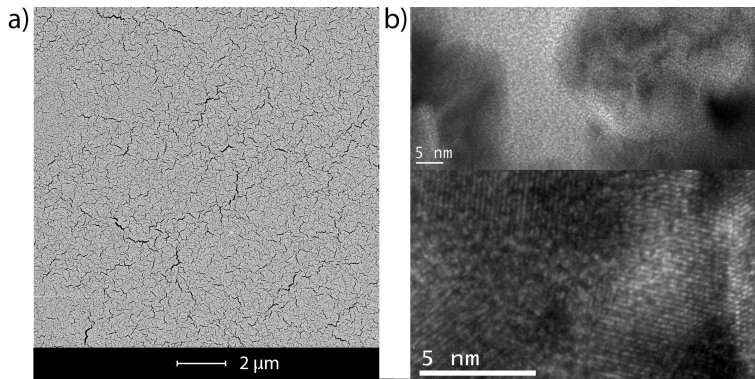


**Figure 5.7:** a): Characterization of a freestanding gold foil with a thickness of several nm: the reflection electron microscope measurement shows a crack like structure in the gold layer of sub  $\mu\text{m}$  range and reveals rests of the parting agent of lighter material (grey color gold, black color carbon like elements) b): the high resolution electron transmission microscopy measurement revealed a poly-crystalline surface substructure of few nm.

of PVF in the range of 0.1% – 10%. Due to the high thermal evaporation pressure of the solute, after spin coating an ultrathin membrane is left on the substrate. The foils were separated from the substrate by submerging it until the membrane floated on the surface [71]. Then it was placed on a suitable steel hole plate. The method achieved a minimum thickness of  $(7 \pm 1)$  nm for freestanding foils. Compared to commercially available foils like Diamond like Carbon (DLC), the hydrocarbon foils are robust in terms of gas pressure [72] and hence, easy to handle with a small defect rate.

### 5.5.2 Coated Polyvinylformal and Freestanding Metal Foils

PVF foils were coated with an ultrathin metal layer, e.g., gold or silver, in a thickness range from 2 nm up to 6 nm by thermal evaporation at  $10^{-6}$  mbar and a deposition rate of 0.2 nm/s. Further increase of the metal layer thickness was found to damage the foils due to high surface tension and melting. A similar method enabled the production of freestanding metal foils with thicknesses from  $(6 \pm 2)$  nm of up to  $(100 \pm 10)$  nm by vapour depositing and with the help of the parting agent Victawet [73]. Characterization of the foil's stoichiometry and surface roughness was done<sup>8</sup> and the details were published in Ref. [74]. Therein, a freestanding gold foil at a thickness of  $(12 \pm 2)$  nm was measured with state of the art energy dispersive X-Ray spectroscopy and found it to consist of 96% gold, 2% carbon, < 2% oxygen and some hydrogen<sup>9</sup>. A  $\mu\text{m}$  crack like structure was observed by reflection electron microscopy and is shown in Fig. 5.7 a). The black areas correspond to light elements such as, e.g. carbon, while the grey areas to gold. Hence, the gold seemed to be attached to a layer, which can be identified as rests of the used parting agent. Considering the whole area, the cracks

<sup>8</sup> by M. Klingsporn

<sup>9</sup> Hydrogen was not attainable within the used method.

covered up to 10%. For thicker gold foils no such measurements exist and hence it is not known, if this cracklike structure is still valid for them. High resolution transmission electron microscopy measurements revealed a poly-crystalline surface structure, depicted in Fig. 5.7 b).

### 5.5.3 Thickness Determination by XUV Transmission

The foil thickness is usually determined with height sensitive methods, as e.g. using atomic force or near field microscopy. Both methods demand a step like boundary between substrate and foil, as they are relative measurements. For ultrathin foils, the boundary has to be introduced by a cut with the foil placed on a substrate, which becomes inaccurate in the range of few nm. Ellipsometry is an alternative method to measure on a substrate the overlaying foil thickness with the help of the optical properties of the foil and the substrate. However, it requires additional information, as e.g. the substrates refraction index, exact stoichiometry, density and the roughness of the substrate surface. Hence, an alternative and easy way was developed to determine the thickness of a free-standing foil by measuring the transmission values for energetic radiation. Here a laser driven Mo XUV plasma source, similar to Ref. [75] was used. It delivered incoherent radiation with an wavelength of 18.9 nm and a high photon flux. With this radiation the foil's transmission values were obtained relative to the detected signal without a foil. By using optical standard tables [76] and the foil density, the foil thickness was calculated according to the law of absorption [77]. A cross calibration with standard height based measurements validated the method for considered assumptions, such as e.g. the target density. Since the setup allowed a determination of the transmission to within an accuracy of 0.5%, the method was very accurate for ultrathin foils of up to 500 nm. Details about the applied method, results, setup and the XUV source used were published in Ref. [70]. The same method was used to determine the thickness of the gold foils. The surface of these foils exhibited in Fig. 5.7 a crack like structure, which could affect the measurement. This structure covers up to < 10% of the surface for which a higher transmission has to be assumed. If it is assumed to be 100%, then, according the theoretical values of Ref. [76], this would increase the thickness of a prior 10 nm gold foil of about 3 nm. Since the cracks belong to a hydrocarbon layer, which was left from the parting agent, this difference is even smaller<sup>10</sup>. In the following the thickness of pure gold foils corresponds to the calculation for a pure gold foil.

---

<sup>10</sup>The density for this layer is unknown, for hydrocarbon layer a value between 1.5 – 2.0 g/cm<sup>3</sup> is reasonable.

## 5.6 Detection devices

### 5.6.1 Ion Detection

The velocity of accelerated ions ( $v_{ion}$ ) were detected with a traditional Thomson spectrometer. It consisted of a static magnet with magnetic field  $B_y$  and a pair of electric field plates between which a potential of up to 9 kV was applied. Passing particles were deflected according to their charge to mass number  $Z/A$  and kinetic energy, leading to charge separated, momentum dispersive traces on the detector plane, according to

$$x = \frac{qZlLB_y}{m_p A v_{ion}} \quad y = \frac{qZlLE_y}{m_p A v_{ion}^2} \quad (5.1)$$

where  $l$  is the length of magnet in the propagation direction  $z$  and the  $L$  is the distance between magnet and detector. By identifying the ions' species at specific charge states, the particles' velocities can be derived solely using the magnetic deflection. Vice versa using both Equations of (5.1), the  $Z/A$  numbers can be evaluated according to theoretical parabolic traces on the detector image. Particles passed through an entrance pinhole prior to detection, within  $1 \times 10^{-7}$  sr (cf. Fig. 5.4 F). A Hamamatsu Multi Channel Plate (MCP) 100 mm in diameter served as the detector. The MCP consisted of a multi-electron channel plate and a phosphor screen, between which a high field strength was applied. Ions hit the electron channel plate and expel electrons. These are further amplified and accelerated into the phosphor screen, which then emits light. Raw data images of the phosphor screen were taken with a camera with high resolution and dynamic range. In the experiments either a AVT Stingray 145B or 504 camera was used. The detector system was calibrated in regard to particle number with the help of alpha particles emitted by a calibrated  $\text{Am}_{204}$  radioactive source.

### 5.6.2 Electron Detection

#### Magnetic spectrometer

The electron spectrometer consisted of a 250 mm long static magnet, which provided a low and homogeneous magnetic field. A schematic sketch of the construction is depicted in Fig. 5.8. Electrons entering the spectrometer entrance pinhole are bent into circles proportional to their velocity. Their trajectories hit a detection screen placed at a distance of  $x_0$  from the entrance axis. Their kinetic energy can be calculated using

$$E_{kin}^{e^-} = m_e c^2 \sqrt{\left( (qB_x)^2 \frac{y^2 + y_0^2}{2y_0} \right)^2} \quad (5.2)$$

in the case of a static and constant magnetic field. The measurement of the magnetic field, see Fig. 5.8 b), shows it to be a function of the propagation coordinate  $z$ . Hence, for the purpose of an accurate energy calibration, the measured magnetic field map was implemented in calculations of a particle tracer simulation,

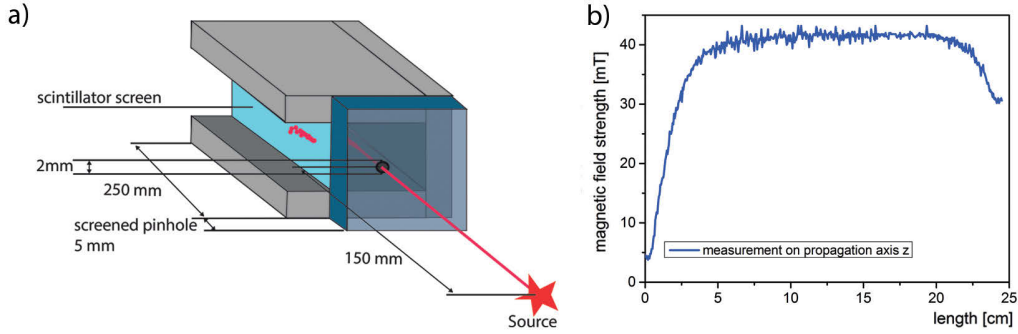


**Figure 5.8:** a): A schematic of the electron spectrometer. b): Measurement of the magnetic field of the spectrometer magnet along its length in the laser propagation direction and with the applied screening apertures.

performed by Ref. [78]. This spectrometer enabled high resolution electron detection in the kinetic energy range of 0.1–10 MeV. It was used at different configurations corresponding to modification of the gap length. The electrons' trajectories showed a significant influence by the decaying magnetic field at the spectrometer entrance and therefore,  $\mu$ -metal apertures were implemented to avoid a deflection outside the spectrometer. This decreased the magnetic field at the entrance pinhole to a value below 3 mT. In order to avoid other secondary effects, such as e.g. low energetic highly divergent electrons created by particles impinging next to entrance pinhole or high energetic Bremsstrahlung radiation, a 3 mm led pinhole was used, which significantly reduces background noise on the screen. Along the spectrometer's width and length, an ovate constant magnetic field of 0.04 T was measured and is shown Fig. 5.8 b) with respect to the particle propagation axis. In the following, this configuration is named configuration III<sup>11</sup>.

The spectrometer was used with a modified magnetic gap length to account for a wider spectral range. The resulting magnetic field strength was then about 0.07 T and is named configuration II. In both configurations the distance between the detection screen and the propagation axis, ( $x_0$  in Equation (5.2)), was set at  $(25 \pm 1)$  mm, which excluded detection of particles with less than 0.1 MeV kinetic energy for configuration III and 0.2 MeV for configuration II, respectively. The distance between the spectrometer and the electron emission source was about 140 mm to enable a high particle flux and a capturing half angle of  $1^\circ$ .

The spectrometer was equipped with standard scintillation screens: either Kodak LanexFast (front) or Kodak BioMaxMS [79]. While the BioMaxMS is a highly sensitive screen, the Kodak LanexFast saturates at one order of magnitude higher amount of charge. Both screens consist of a few  $\mu\text{m}$  poly-hydrocarbon protection skin, and an up to one mm thick composite layer of phosphor and other elements (C,H,Y,O,N). This is followed by a  $> 100 \mu\text{m}$  thick reflecting plastic layer. The screen was calibrated in particle number according to [79, 80] by using

<sup>11</sup>The numbering scheme of the experimental configurations corresponds to that of the documentation of the performed experiments for ease and clarity of reference.

a tritium light source. The calibration implied a systematic, constant uncertainty given by the unknown life time of the Tritium source, which is assumed to be up to 20%. Moreover, the calibration is only valid for electron kinetic energies of  $\geq 1$  MeV, since there is no reference for the screen's conversion efficiency in the lower energy range. The detection screen was shielded from radiation with a 15  $\mu\text{m}$  aluminium foil. In order to account for the electrons spatial and spectral distribution, a multi-pinhole construction could be applied. It collected particles at half angles of  $0^\circ$ ,  $\pm 4^\circ$  and  $\pm 8^\circ$  from target.

In the two laser pulse experiments (cf. Section 5.4), electrons were detected using a different spectrometer configuration. In the following, this setup will be referenced as configuration IV. Equipped with the BioMaxMS screen and a stronger, smaller magnet of 0.22 T, it enabled a detection range of 0.5–4 MeV. In this setup, electrons are detected after having passed through the tunnel of the second focusing Parabola (**G** in Fig. 5.5). The spectrometer was placed at a total distance of 530 mm from the target. In consequence, and compared to the formerly introduced configurations, this configuration had a significantly lower dynamic range and energy resolution. This configuration was not calibrated in terms of particle numbers.

## Image Plates

To account for the full electron beam divergence and the total electron number ( $N_e$ ), an alternative measurement method was applied by using dose sensitive Image Plates (IP). IPs are widely used in medical applications for radiography. The method replaced common X-ray photo-films, because it can be read out directly after exposition. In principle, IP consists of chemical constituents which enable phosphorescence emission after being excited due to an exposition to energetic radiation or energy deposit by particle radiation. In the experiments, the IP was screened from ions and XUV radiation with the help of 30  $\mu\text{m}$  aluminium foil and a 1 mm acryl plastic plate. The distance from the target was about  $(100 \pm 5)$  mm. An additional hole in the center of the IP enabled a simultaneous measurement with the magnetic spectrometer (configuration III). IP detected electrons above 0.3 MeV [81] and this kind of measurement is not dispersive in energy. In order to account for the electron number, and in accordance with Ref. [81, 82], the energy deposition by electrons on the IP was assumed to be similar for all kinetic energies.

### 5.6.3 XUV Radiation Detection

On the laser propagation axis a spectrometer for detecting the emitted XUV radiation was installed. It is schematically depicted within the experimental setup for single laser pulse interaction in Fig. 5.9. A gold transmission grating with  $G = 1900$  lines/mm was placed behind the electron spectrometer (cf. Section 5.6.2). Hence, the setup enabled detection of XUV radiation and electrons at the same time. In addition, deflection of charged particles led to a remarkable reduction

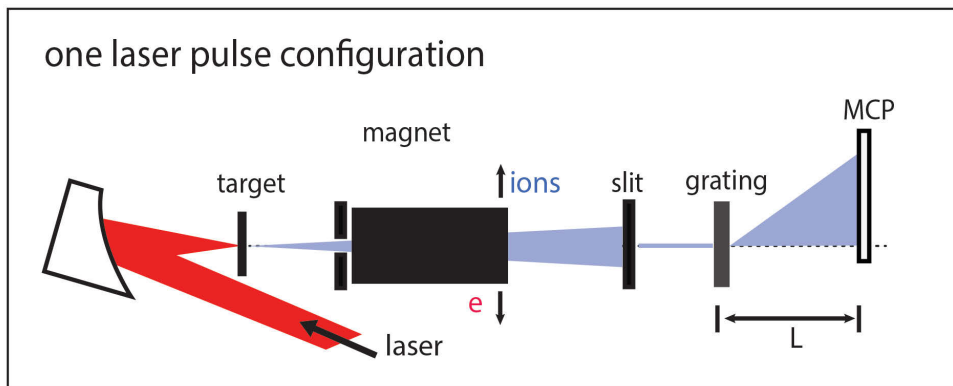


**Figure 5.9:** A schematic of the XUV spectrometer for single laser pulse and ultra-thin foil experiments. It detects XUV radiation by laser-plasma interaction in the laser propagation direction. The spectrometer's entrance slit was placed after the electron spectrometer in configuration III (Section 5.6.2).

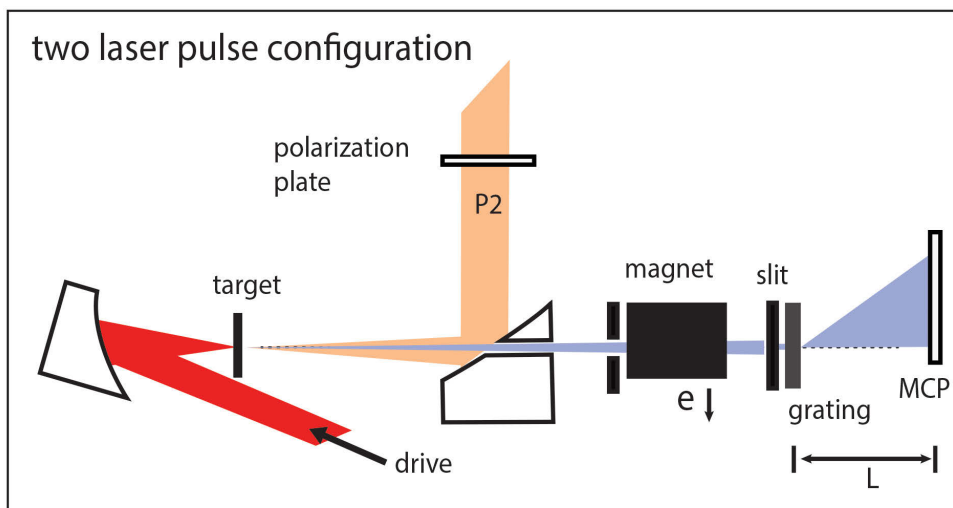


**Figure 5.10:** A schematic of the XUV spectrometer setup for the two laser pulse experiment. XUV radiation from the laser-plasma interaction is detected in the propagation direction of the drive pulse. The detection device was placed after the electron spectrometer in configuration IV.

of the background noise on the detector. A common slit aperture with a width of  $\sim 300 \mu\text{m}$  was inserted at a distance of 410 mm from target for the single laser pulse setup. In the two laser pulse experiments (cf. Section 5.4), the same spectrometer was placed at a distance of 795 mm from the target position. As depicted in Fig. 5.10, XUV radiation in the propagation direction of the drive pulse was detected, after it has passed through the tunnel of the focusing optic of the P2 pulse. In both configurations, the diffracted radiation was amplified by a Hamamatsu MCP with a 100 mm diameter, and its phosphor screen was imaged

by an AVT Stingray (145 or 504) camera. The spectral evaluation considered the first order diffraction relation

$$\lambda = \frac{1}{G} \sin \alpha \quad (5.3)$$

where  $\alpha = \arctan(y/L)$  is the diffraction angle,  $y$  the amount of deflection and  $L$  the distance between grating and detector. In order to account for different spectral ranges in the energy range of 1 nm to 210 nm, the spectrometer was used at different distances to the detector. The measurement obtained the spectral intensity  $S(\omega^*)$  with a resolution better than  $\Delta\lambda = 2$  nm.

#### 5.6.4 Laser Radiation Detection

To account for the amount of transmitted laser light in experiments on ultrathin foils, the XUV spectrometer of Fig. 5.9 was used with a grating operating in the optical spectral range. The grating constant counted 300 lines per inch and was made of SiN. The diffracted signal passes through a vacuum window (BK7) and illuminated a white paper, which was then imaged by an AVT Stingray 145B camera. The measurements accounted for relative transmission values  $T$ , allowing the integrated spectral intensity of the specific bandwidth,  $\Delta\lambda_L = 700\text{--}900$  nm, to be compared for single shot events with and without using a target foil.

Part III

RESULTS



## 6 Laser Ion Acceleration with Optimized Target Systems

Laser plasma ion acceleration has been investigated for over two decades [1, 36]. The research still aims to increase the ion velocities and to lower the ion spectral bandwidth. The fundamental questions of this research field are related to the inherent acceleration dynamics and to the interplay between different acceleration schemes. For laser systems at relativistic intensity an ultrahigh laser contrast became possible through the development of the plasma mirror technology (cf. Section 5.2.2). This laser contrast condition enabled the use of ultrathin foil targets and provided a laser interaction with a steep plasma boundary. This led to discovery of novel and more efficient acceleration schemes, such as the acceleration by the pressure of light (RPA) (cf. Section 3.3). In the first place, this has moved the focus of investigation to an interdependency between the target thickness/density and the laser field strength (cf. Equation(3.7)), to achieve the highest ion kinetic energies [2, 36, 38–40, 42, 83]. Furthermore, different laser contrast conditions revealed an impact of the plasma density gradient and the properties of the pre-plasma on the laser ion acceleration [64, 84]. This thesis investigated new ways how the laser ion acceleration can be optimized with different target systems. The experiments performed here, extend the latest discussions with a detailed examination of different target parameters, such as, target thickness, target material constituents, two layer foils, separated foil system and a direct manipulation of the ion acceleration due to an additional second laser pulse before and after the actual laser-plasma interaction. With respect to these different parameters, new and important insights into the interplay between the acceleration schemes RPA and TNSA for a multi-ion species plasma are presented.

The significant influence that the laser contrast and the target thickness has on the ion acceleration efficiency, is presented in Section 6.1. Pre-pulses and the rising intensity level are inherent parameters of the laser system and lead to a pre-heating of the target. It is shown, that this produces a remarkable change in the detected maximum kinetic energies and the ion charge distribution.

In the laser ion acceleration models, ions are accelerated by a dense electron sheath, which is established during the laser to plasma interaction close to the target boundary (cf. TNSA scheme in Section 3.2). Additional acceleration of this electron sheath can be achieved due to radiation pressure (cf. Section 3.3), when the target thickness and density enables a partial transmission of the laser

light [2, 10, 39, 40, 69, 83]. Section 6.2 presents that the maximum kinetic ion energies can be significantly enhanced when a specific foil thickness and density is used. The experiments improve upon previous results obtained the Max Born Institute [2, 10, 69].

Section 6.3 presents an unexpected and highly efficient acceleration of the heavy ions with the help of ultrathin foils that consisted of heavy elements. Gold ions were detected at high kinetic energies, of up to the MeV/u range, even in the presence of a  $> 10$  nm thick hydrocarbon layer. These results stand in contrast to former published experiments, where light ions always suppressed the acceleration of the heavy material [35, 85]. How the heavy ions can gain this high kinetic energy is explained by a model by A. A. Andreev and K. Platanov, which is introduced briefly. The heavy ions spectra exhibited successive charge states and a characteristic charge dependent spectral distribution. The spectral characteristics and the charge to maximum kinetic energy scaling will be examined in detail. This section investigates also how the presence of light material can affect the acceleration of the heavy ions by using two layer targets and different ratios between gold and hydrocarbon material. With the help of two different spatial arrangements of these layers an interesting difference in the heavy ion spectra is obtained. The observations are discussed with respect to the latest acceleration models and give new insights into the acceleration dynamics for a multi-ion species plasma.

Closely linked to the question of the ion acceleration for different charge to mass ratios, are inherent or induced charge transfer processes. Laser plasma accelerated ions passing through gaseous or liquid media were demonstrated to capture electrons and lead to neutral or even negative states of charge. This topic is a focus of recent research, since, up to now, its fundamentals are not fully resolved [86–88]. Section 6.5 presents recharge processes for accelerated ions in solid state dense matter with the help of a double foil target system. The investigation examines the resulting ion charge states and determines the change in the corresponding spectral distributions.

The properties of the pre-plasma manifest in significant differences in the obtainable ion kinetic energies. Section 6.6 investigates how a controlled manipulation of the pre-plasma affects the laser ion acceleration. By the help of a strong pre-pulse the plasma is pre-heated and the rise of its density at the plasma boundary or even the density itself can be expanded. It will be shown how this affects the maximum kinetic energies of light ions and the charge distribution of heavy ions. In addition, an interaction shortly after the actual laser ion acceleration with a second, strong laser pulse changes the spectral distribution of the ions.

All experiments were performed with the laser on target at normal incidence, in single shot measurements and used the setups described in Section 5.3 and 5.4. The diagnostic used was introduced in Section 5.6.1.

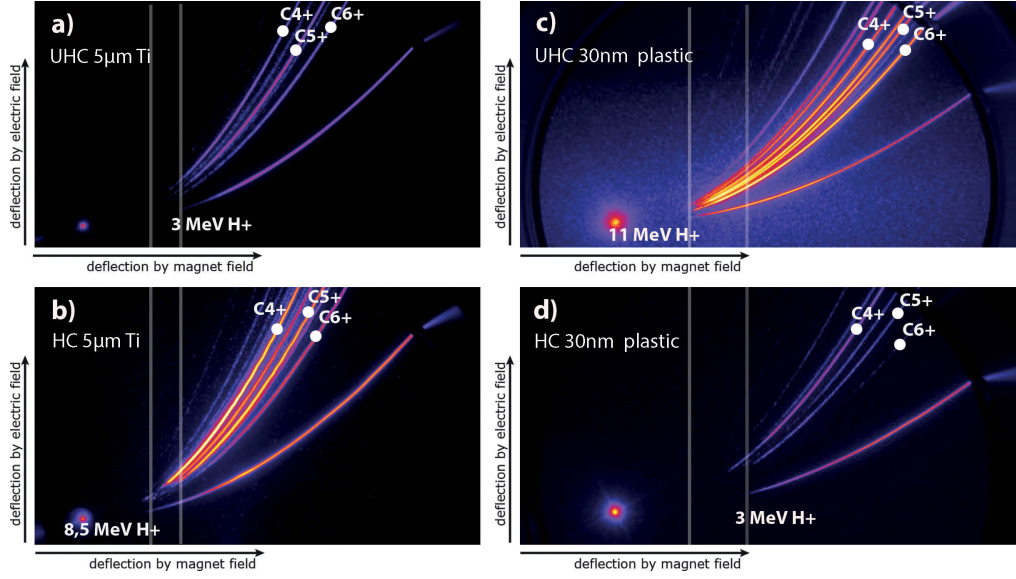


**Figure 6.1:** Ion spectra obtained with either high or ultrahigh laser contrast condition shown for two different target foils: Ion traces on detector from a 5  $\mu\text{m}$  Ti foil and laser at UHC a:) and HC b:) under same experimental conditions and same colour scaling. The same comparison is shown for a used ( $30 \pm 2$ ) nm thick PVF foil in c:) obtained at UHC and d:) at HC.

## 6.1 Dependency of the Ion Spectrum on the Laser Contrast

Laser pre-pulses on the nanosecond, picosecond timescale and the laser's raising intensity level are characteristic for the contrast of a laser system. They can significantly change the plasma boundary by pre-ionizing, heating and pre-expanding the target. Pre-expansion determines the scale length of the plasma density gradient [64, 68], and also the plasma density, in the case of ultrathin target foils. According to Section 2.2, the scale length of the plasma density gradient determines the laser to plasma absorption processes and with it, the laser driven electron dynamics, and as one consequence, the ion acceleration [84]. Up to now, a measurement method or model to obtain the pre-plasma property and its influence is not fully derived and is often obtained from complex simulations [63–65, 68]. In consequence, the comparison between experimental results measured at different laser systems, with different laser contrast conditions is often hindered due to effects from different, and often unknown, pre-plasmas properties.

Two examples for ion spectra at different laser contrast conditions are given to illustrate well known observations. Laser ion acceleration was performed at the MBI's laser system with high (HC) and ultrahigh (UHC) laser contrast conditions (cf. Section 5.2) and at a laser field strength of  $a_0 \sim 6.5$  and  $a_0 = 5.5$  respectively. The detected ion spectra are shown in Fig. 6.1, for either a 30 nm hydrocarbon (PVF) foil, or a 5  $\mu\text{m}$  metal (Ti) foil. The HC condition delivered higher kinetic

ion energies and a higher particle number for the thick Ti target, in comparison to the case of UHC. Opposite results were obtained from the ultrathin hydrocarbon foil. At HC, a limit for efficient ion acceleration was found at a foil thickness  $30 \text{ nm}$ <sup>1</sup>. This limit indirectly reflects a significant change in the ion acceleration due to the difference in the pre-plasma properties. Such observations can give important indirect information for the comparison of results obtained at different laser systems with different laser contrast conditions. Moreover, the example illustrates why the parameter target thickness/density is so important.

A further distinction was observed in the detected ion charge distribution. At HC and for an ultrathin PVF foil, the dominant carbon ion species was detected at charge states  $C^{4+}$ , while it was  $C^{5+}$  and  $C^{6+}$  at UHC. In the case of the thicker target, the dominant charge distribution at the UHC condition was reduced to  $C^{5+}$  and was at  $C^{4+}$  and  $C^{5+}$  for the HC condition. This comparison shows that there is a relation between the dominant charge state and the foil thickness and the laser contrast. Here, the ions were detected in the laser propagation direction and it is assumed that they were accelerated from the target rear side. A lower charge state for thicker targets might be explained by a lower degree of ionization, due to an increased target thickness. However, for the HC the dominant charge state is detected lower than for the UHC. Since the laser parameters are comparable, one can assume a similar ionization of the target for both laser contrast conditions and hence a similar charge distribution. Smaller charge states could be explained by recharge processes, namely an electron capture (EC), during or after the laser-plasma interaction. EC processes become probable for fast ions travelling through matter or, e.g., an extended plasma (cf. Section 2.3). Inherent recharge processes have been hardly discussed for the laser ion acceleration and could interfere the acceleration efficiency. Ion recharge processes are further investigated in Section 6.5.

Moreover, for both contrast conditions, ions were detected down to a minimum charge to mass ratio of  $\leq 0.25$ . In the case of the Ti target, no Ti ions were observed. This is an important observation regarding the  $Z/A$  scaling in the laser-plasma acceleration. This will further be examined in Section 6.3, where the use of ultrathin heavy material foils caused an acceleration for heavy ions with significantly smaller  $Z/A$  ratios.

Concluding briefly, different optimum conditions are experimentally derived for  $E_{kin}^{max}$ , the particle number and the dominant charge state for each laser contrast. At the UHC condition, the ion acceleration becomes inefficient for a target thickness exceeding the skin depth,  $l_s$  (cf. Equation (1.21)), with approximately two orders of magnitude. At this foil thickness, the lower laser contrast delivers a higher particle number and higher maximum ion energies. In general, one assumes for lower laser contrast, a TNSA like acceleration (cf. Section 3.2), while at UHC and with using ultrathin targets, the onset of RPA is reached [10, 69] (cf. Section 3.3). It was demonstrated in Ref. [2, 40, 69, 83], that the RPA

<sup>1</sup>For a slightly thicker PVF foil target, HC and similar experimental conditions, proton energies up to 12 MeV and  $E_{kin}^{max}(C^{4+}) \sim 30 \text{ MeV}$  were detected.

scheme leads to remarkably higher ion energies than the TNSA for the same laser intensity. How a specific target thickness optimizes the ion kinetic energies for a RPA influenced acceleration is presented in the next section.

The significant influence of the laser contrast on the experimental results trigger the question, how the resulting pre-plasma condition affects the ion acceleration efficiency? The influence of pre-pulses is further examined in Section 6.6 by a controlled manipulation of the pre-plasma with a second laser pulse.

## 6.2 Optimized Laser Ion Acceleration by Radiation Pressure

### 6.2.1 Optimal Target Thickness

According to the RPA model in Section 3.3, the highest kinetic ion energies are predicted for an optimum target thickness  $D_{\text{opt}}$ . For this thickness the theoretical models assume a displacement of most of the electrons at the targets rear side that leads a reflection of the transmitted laser pulse from these electrons. This causes an additional acceleration due to the radiation pressure. For even thinner foils (too thin foils), the radiation pressure can overcome the restoring force between the ions and electrons, leading to the so called electron blow out. In this case, all electrons are assumed to leave the ions and are accelerated by RPA to higher velocities [56]. In consequence, the ions are accelerated less efficiently, either due to a much shorter acceleration time and/or a pure Coulomb explosion [39, 41, 89–91].

The onset of radiation pressure acceleration was demonstrated experimentally amongst others in Refs. [2, 40, 69, 83]. The highest kinetic energies for ion species  $\text{H}^+$  and  $\text{C}^{6+}$  were found only at a specific target thickness. This optimal thickness depends on the target density/material and  $a_0$ . Therefore, it is often summarized in an areal density  $\sigma_{\text{opt}} \sim n_e/n_c D$  (cf. Section 3.3 and Equation (3.7)). Its theoretical scaling to  $a_0$  was discussed by various authors [9, 39, 41, 69, 89–91]. Their prediction for  $D_{\text{opt}}(a_0, n_e)$  differs, which is illustrated in Fig. 6.2. According to three different theoretical predictions, in a),  $D_{\text{opt}}$  is plotted as a function of  $a_0$  for fully ionized PVF and, for gold with an averaged degree of ionization of  $\text{Au}^{15+}$ . The calculations considered a relativistic correction of  $n_c^2$ . In addition to the uncertainty in theoretical predictions, the effective number  $n_e$  (cf. Chapter 3) in the laser-plasma interaction can only be approximated. This is the reason why, from an experimental point of view, a scan of the target thickness becomes necessary for each laser system and target composition.

One objective of this thesis was the investigation of the dependency of  $E_{\text{kin}}^{\text{max}}$  on the foil thickness for a low density, hydrocarbon material, namely PVF. The experiments are a continuation of past research using Diamond Like Carbon (DLC) foils [2, 10]. The characterization of the foils used was described in Section 5.5. Compared to DLC, the PVF material reduces  $n_e$  by about  $\times 1.5$ , with respect to

<sup>2</sup>The relativistic correction of  $n_c$  for the laser parameter used is  $\leq 4$

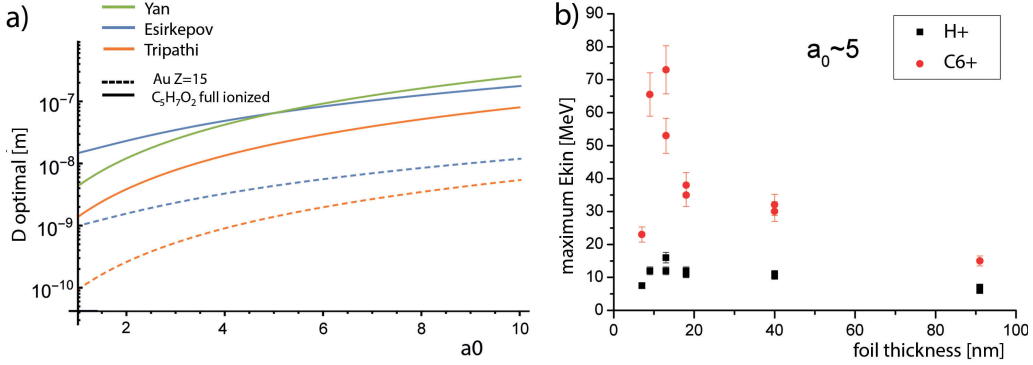


**Figure 6.2:** a): Theoretical  $D_{\text{opt}}$  calculated as a function of  $a_0$ , according to equations from publications of Yan, Esirkepov and Tripathi [39, 89, 90] and using a relativistic correction of  $n_c$  (cf. Equation (1.22)) for different values of  $n_e$ , according to different foil materials. b): Dependency on the PVF foil thickness of the maximum kinetic energies of  $H^+$  and  $C^{6+}$  ions detected. The applied laser field strength was about  $a_0 = 5$  at ultrahigh laser contrast.

full ionization. Therefore, and according to Equation (3.7), the optimal thickness can be reached at  $\geq 50$  nm for  $a_0 \sim 5$ <sup>3</sup>. This relaxes the demands of the target preparation. Experiments on ion acceleration with PVF foils were performed by scanning a range of foil thicknesses between 7 nm and 90 nm at the UHC condition, using a linearly polarized laser with a normalized laser field strength of  $a_0 = 5$ . Fig. 6.2 b) shows detected  $E_{\text{kin}}^{\text{max}}$  for  $H^+$  and  $C^{6+}$ , with respect to the foil thickness. The results were obtained from different experimental runs and could be confirmed on a regular basis, since similar scans were used to diagnose changes in the laser contrast condition. The best results were obtained at  $(12 \pm 2)$  nm, which is in good agreement with the prediction of  $D_{\text{opt}}$  out from the model of Ref. [89]. At this foil thickness,  $E_{\text{kin}}^{\text{max}}(H^+) = 16$  MeV and  $E_{\text{kin}}^{\text{max}}(C^{6+}) = 75$  MeV was reached with 1.2 J of laser energy on the target. For a foil thickness below  $< 10$  nm,  $E_{\text{kin}}^{\text{max}}$  decreased, as expected for too thin foils [2, 39, 69].

### 6.2.2 Ion Spectra at Optimized Target Parameters

Typical ion spectra detected in the optimal target thickness range are shown in Fig. 6.3. The target material was PVF at an thickness of 12 nm and  $a_0 = 5$ . On the detector image in a), a separated high energetic tail appeared in the proton and  $C^{6+}$  ion traces. The particle number for this high energy tail is rather small (cf. Fig. 6.3 b). The separation in the trace appeared at different velocities: 5 MeV/u for protons and 1.3 MeV/u for  $C^{6+}$ . In a wide range, protons and  $C^{6+}$  ions were detected at the same velocity. These spectral features only appear in the ion spectrum for an optimal foil thickness and were observed in 9 experimental runs and in total 23 measurements for similar parameters. According to the RPA model, during the acceleration the ions move with the displaced electron

<sup>3</sup> with the relativistic correction of  $n_c$ .

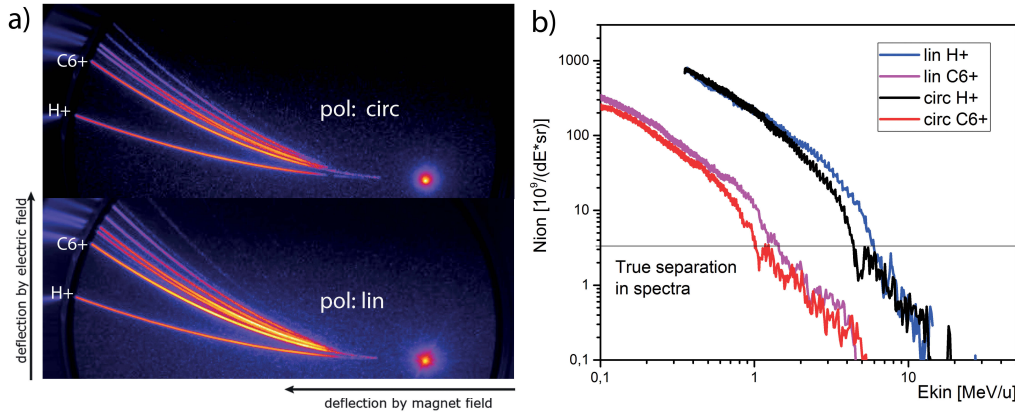


**Figure 6.3:** a): The on detector image for two different laser polarizations at ultra-high laser contrast and an (optimum) target thickness of 12 nm. b): The corresponding evaluated ion spectra.

sheath at the same velocity. For different ion species an averaged areal mass density,  $\sigma_D = (m_p A_1 Z_1 n_1 + m_p A_2 Z_2 n_2)D$ , is often assumed rather than single constituents and different  $Z/A$  numbers [38, 41, 92]. In consequence, pure RPA acceleration predicts a quasi mono-energetic ion spectrum [38, 39, 41]. This raises the question, when and how the ions separate according to their  $Z/A$  number during the interaction. The detected separation in Fig. 6.3 in the ion traces of proton and carbon is comparable in particle number, but differs in velocity. This can indicate a shared origin, as e.g., RPA/hole-boring for all ion species, which then is followed by a second acceleration that scales proportional to  $Z/A$  and leads to a separation of the ions. The last condition can be fulfilled within the TNSA model [1, 28, 38] (cf. Equation (3.2)). After the laser interaction, ions are further accelerated, since the accelerating electron sheath is maintained longer than the laser pulse duration in the timescale of up to ps. The strength of the accelerating field decreases within the total acceleration time and its impact on the ion acceleration is a complex process [32]. Simplified, this post-acceleration is similar to an acceleration of ions at different  $Z/A$  numbers in an expanding and moving capacitor. Hence, a mixed acceleration scheme could explain the separation found in the proton and carbon spectrum at different velocities. Similar spectral modulations were reported in [2, 10, 69, 93] and were explained by a mixed acceleration scheme involving both RPA and TNSA [41, 92].

### 6.2.3 Dependence on Laser Polarization

According to the theory of RPA, the best results are expected for circular laser polarization, since this is predicted to reduce the amount of fast electrons that escape from the laser plasma interaction (cf. Sections 3.3, 2.2) [2, 38, 39, 91]. In a direct comparison between linear and circular polarization in Fig. 6.3 a) and

b), no major differences in  $E_{kin}^{max}$  or particle numbers were observed<sup>4</sup>. Hence, no significant dependency of the acceleration efficiency on the laser polarization was found. This result is in agreement with Refs. [40, 83] that demonstrated an efficient RPA like ion acceleration with linear laser polarization.

### 6.3 Coulomb Boost for Heavy Ions

So far, the target optimization only considered a low density material and helped to enlarge the suitable foil thickness range for optimized ion acceleration at UHC condition and a fixed laser intensity. In a refined version of the RPA model, heavy material ( $A > 100$ ) target constituents were suggested in order to optimize the laser ion acceleration [41–43, 92, 94]. According to RPA, the ideal target has to be thin enough to displace all the electrons out of the target. The remaining ion background stays transparent to the laser light (cf. Chapter 1.4) enabling a further acceleration of these electrons by the pressure of light. At the same time, a balance between the radiation pressure and the restoring force to the ions has to be maintained to inhibit the electron escape. According to Equation (3.6), this balance is determined by  $n_c$ ,  $a_0$  and the areal density  $n_e D$ . When ultrathin, few nm thick foils are used, one has to consider that a limited number of electrons (and ions) can be provided. By Equation (4.7), the number of electrons determine the reflectivity for the (transmitted) laser light and hence it determines the momentum transfer of photons to the electron sheath. This motivated the use of few nm layers of heavy material constituents ( $A > 100$ ) in two ways:

- Increase of  $n_e$  while simultaneously maintaining the RPA regime at the same time, with additional electrons donated from heavy material, due to a fast separation of the ion species with  $Z/A$  [41, 92, 94]
- Additional acceleration of light ions by a Coulomb explosion of the highly charged ion background, as suggested in [39, 41–43]

Although solid state materials with high atomic numbers, e.g.  $A > 100$ , can provide a large number of electrons,  $n_e$  is still dependent on the degree of ionization and amount of material. For the laser parameters used, the charge state of heavy ions is assumed to be far from full ionization [39]. In consequence, as shown in Fig. 6.2 a), the condition for the optimal foil thickness can be fulfilled, even for heavy material foils.

Experiments were performed with few nm gold foils at a normalized laser potential of  $a_0 = 5.5$  and the UHC condition. The gold foils used are characterized in Section 5.5.2. The results obtained, answered the question, if an ultrathin heavy material layer can enhance acceleration of light ions with "no", but discovered

<sup>4</sup> Circular polarization was introduced with the help of a polarization plate. Without losses and according to Ref. [13] the laser field strength is decreased about  $1/\sqrt{2}$ . Hence, circular polarization delivered similar results with a reduced field strength. But the effect is small and was not found to be significant.

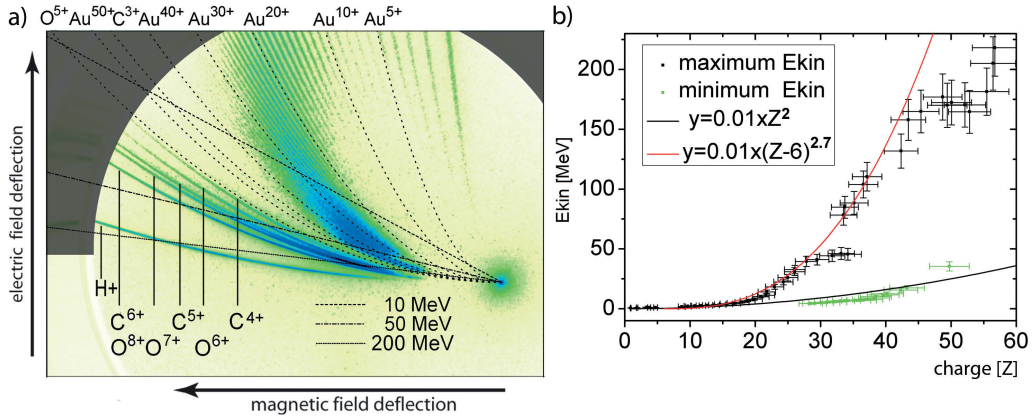


**Figure 6.4:** Ion spectrum from a  $(12 \pm 3)$  nm gold foil and laser interaction at the UHC condition. a): An image of the detector screen after ions have passed through the Thomson spectrometer. The overlay plots mark theoretical parabolas to various charge states of gold, and lines of constant kinetic energy for  $A = 197$ . b): Evaluation of the maximum and minimum detected kinetic energy of gold ions, as a function of the charge state, for the measurement in a). The analytical scaling for  $Z$  to  $E_{kin}^{max}$  and  $Z$  to minimum kinetic energy  $E_{kin}^{min}$  is shown. Pictures are taken from the corresponding publication [74].

an efficient acceleration of heavy ions instead. The experiments demonstrated for the first time, a laser-plasma acceleration of highly charged heavy ions into the kinetic energy range of 1 MeV/u, in the presence of a contamination layer of light ions. The following findings base on an experimental campaign consisting of 18 experimental runs and in total 104 measurements with using gold/silver coated plastic or pure gold targets. The main results were published in [74] and are briefly summarized in the following Sections 6.3.1 and 6.3.2. Additionally, a detailed evaluation of the characteristic features of the heavy ion spectra is given in Sections 6.3.3 and 6.3.4. These sections examine the charge to maximum and minimum kinetic energy scaling and their parametric dependencies, such as, e.g., the target thickness, laser energy and how the presence of several nm hydro-carbon material affects the acceleration. Section 6.3.5 focuses on a modified target arrangement: With the gold layer facing towards the illuminating laser, fast gold ions originating from the target front side were detected in the laser propagation direction.

### 6.3.1 Accelerated Heavy Ions

Experiments at ultrahigh laser contrast using free standing gold foils within an thickness range from 13 nm to 50 nm revealed an efficient acceleration of highly charged gold ions. An image of the detector screen of the Thomson spectrometer is shown in Fig. 6.4 for laser interaction at  $a_0 = 5.5$  with a 12 nm gold foil. Next to the ion traces corresponding to hydrogen, carbon and oxygen, a multiplet of ion traces with  $Z/A \leq 0.25$  appeared. The traces are identified as successive Thomson parabolas of gold at charge states from Au<sup>1+</sup> to Au<sup>48+</sup>. A maximum

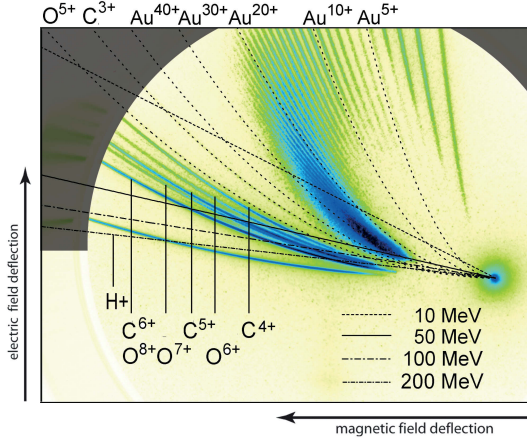


**Figure 6.5:** The image of the detector shows ion traces from laser interaction with a double layer target. It consists of a  $(40 \pm 2)$  nm thick PVF foil and a  $(6 \pm 2)$  nm gold coating at the foil's rear side. Overlay plots depict theoretical Thomson parabolas at different  $Z/A$  ratios and lines of constant energy for the fixed mass number  $A = 197$ . The picture was published in the supplement of [74]

kinetic energy of  $\leq 200$  MeV was reached for gold ions at the maximum charge state. This high value of  $E_{kin}^{max}$  is valid only for few particles, as illustrated by the overlay in Fig. 6.4. This overlay marks constant velocities<sup>5</sup>, in accordance with Equation (5.1), at the particular intersection points with Thomson parabolas of various charge to mass ratios. This shows that the majority of the gold particles was detected in the kinetic energy range below 50 MeV. The spectral distribution of the detected gold ions exhibits a remarkably limited bandwidth. Fig. 6.4 b) presents evaluated  $E_{kin}^{max}$  and  $E_{kin}^{min}$  against charge for gold ions for the same measurement. From the experimental data, a charge to maximum kinetic energy scaling of

$$E_{kin}^{max} \sim 0.01 \times (Z - 6)^{2.7} \quad (6.1)$$

was extracted. The constant displacement of  $(Z - 6)$  in the scaling reflects to the observed high and almost constant detected velocities of gold ions at charge states  $Z \leq 6+$ . This observation is further investigated and discussed in the following sections.

Light ions were obtained in the experiments with similar  $E_{kin}^{max}$  values as in the case of using a pure PVF foil with a thickness of  $\sim 20$  nm (cf. Fig. 6.2 in Section 6.2): for  $H^+ \leq 10$  MeV/u and  $\leq 3.3$  MeV/u for  $C^{6+}$ . The light ions originate from the target contamination, which was confirmed by the stoichiometric characterization in Section 5.5.

Heavy ions were also accelerated from gold coated PVF foils. These two layer foils consisted of few nm thick gold layers on PVF foils within a thickness range of 10–80 nm. In the measurements with these targets, the gold ion spectra was detected with comparable spectral characteristics as in the case of pure gold foils,

<sup>5</sup> constant kinetic energy for a fixed  $A$

but exhibited a somewhat lower maximum kinetic energy. Fig. 6.5 shows a raw ion spectrum obtained from such a gold coated PVF target. The target consisted of 40 nm PVF and a 6 nm gold coating on its rear side. In direct comparison to the spectrum obtained from the pure 12 nm gold foil in Fig. 6.4, the layer target delivered similar results, e.g., ion traces of successive gold charge states from  $Z = 1+$  to  $Z = 45+$  were detected with a similar spectral distribution. A maximum kinetic energy of about  $\geq 100$  MeV was reached for the maximum charge state. This value is lower than in the case of the 4 times thinner pure gold foil. This result can be addressed to a thickness dependent scaling similar to Section 6.2. Still, this measurement demonstrates that the acceleration mechanism for heavy ions is almost independent of the light material with an areal density of at least  $1 \times 10^{-7}$  g/cm<sup>2</sup> and when the heavy material was placed at the rear side of the target. For PVF foils with a thickness  $\geq 30$  nm and the gold layer at the target front side, the obtained spectra were significantly different. This and additional observations in the gold ion spectra for gold coated plastic foils are further evaluated in Section 6.3.3.

The ultrahigh laser contrast was found to be necessary for the acceleration of heavy ions. At high laser contrast and for either pure gold foils or gold coated plastic foils with a thickness of 12–50 nm, no gold ions have been detected at all. An example is given in the Appendix in Fig. A.2. Since former experiments could accelerate heavy ions from  $\mu\text{m}$  thick foils only by removing the contamination layer [35], the here obtained findings reveal a significant difference in the laser-plasma dynamics that is determined by the laser contrast condition and the target thickness.

### 6.3.2 Heavy Ion Acceleration Theory

The observed high charge state of gold ions, e.g.  $Z > 15+$ , was explained by A.A. Andreev using the Ammasov-Delone-Krainov model [19]. 1D PIC simulation was performed using a gold foil target at a comparable thickness and are shown in [74]<sup>6</sup>. The simulation revealed a spatial dependency to the charge distribution of gold ions in the direction normal to the target. This introduces a higher degree of ionization at the target boundaries (front and rear side), as illustrated in Fig. 6.6.

From the PIC simulation, a spatial dependence for the heavy ions charge state along the target normal of

$$Z(z) = 23 \times \left[ \frac{2c}{\omega_L r_D} \frac{\partial n_e}{\partial z} \right]^{0.4} \quad (6.2)$$

was derived. In comparison to an average charge state of  $\text{Au}^{15+}$ , this remarkably enhances the charge state and the acceleration field  $E_{acc}$  at the target boundaries. The difference can be seen in Fig. 6.6 by the means of a simulated and theoretically calculated  $E_{acc}$ , which exhibit a two times higher field strength at the target

<sup>6</sup>by A. Andreev and K. Platanov

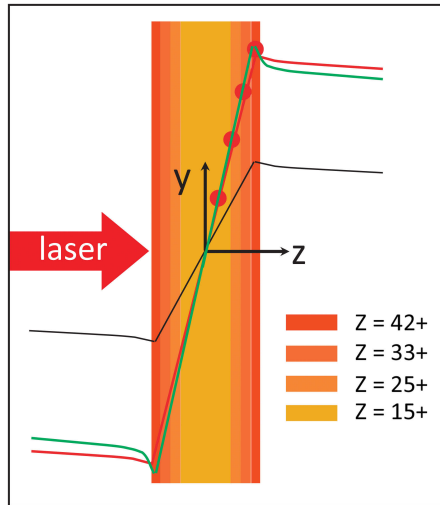


**Figure 6.6:** The spatial dependency of the gold ions' charge states in the direction normal to the target. The maximum charge state is at the foil boundaries. The black curve shows the calculated accelerating field,  $E_{acc}(z)$ , for a constant charge distribution of  $Z = 15+$ . The calculated  $E_{acc}(z)$  for the spatial dependency of the charge distribution, according to the schematic, is shown by green curve. Red shows  $E_{acc}(z)$  obtained from the 1D PIC simulation. The calculation and simulation were done by A.A. Andreev and K. Platanov. The picture is taken from the corresponding publication [74].

boundary than in the case of an average charge state. By using Equation (6.2) in a laser ion acceleration model for ultrathin foils [74], a charge to kinetic energy scaling of  $E_{kin}^{max}(Z) \sim Z^3$  [74] for the heavy ions could be extracted. This exceeds the TNSA scaling of  $Z^2$  [29, 31] and is in good agreement with the results of the experimental observations and the performed 2D PIC simulation. Details of the analytical model and the 2D PIC simulations are described in [74].

### 6.3.3 Detailed Characterization of Heavy Ion Spectra

Ultrathin PVF foils with a few nm gold layer were used to test the influence of different ratios between heavy and light elements on the heavy ion acceleration. The spectral distribution from pure gold foil targets was detected comparable to the one obtained from a double layer target, when a sufficient gold layer was provided and placed at the target's back side. This was already demonstrated in the comparison of Fig. 6.4 and Fig. 6.5. The ion spectrum originating from a rear or front side heavy material coating differed in the heavy particle charge state population and in the maximum kinetic energies in dependency on the substrate's foil thickness. A comparison of heavy ion spectra detected from different layer thicknesses and spatial arrangements of the gold coating, is given with the help of detector images in Fig. 6.7. In the following a characterisation of the observed differences is given and obviously, one has to distinguish between two kinds of gold ion spectra:

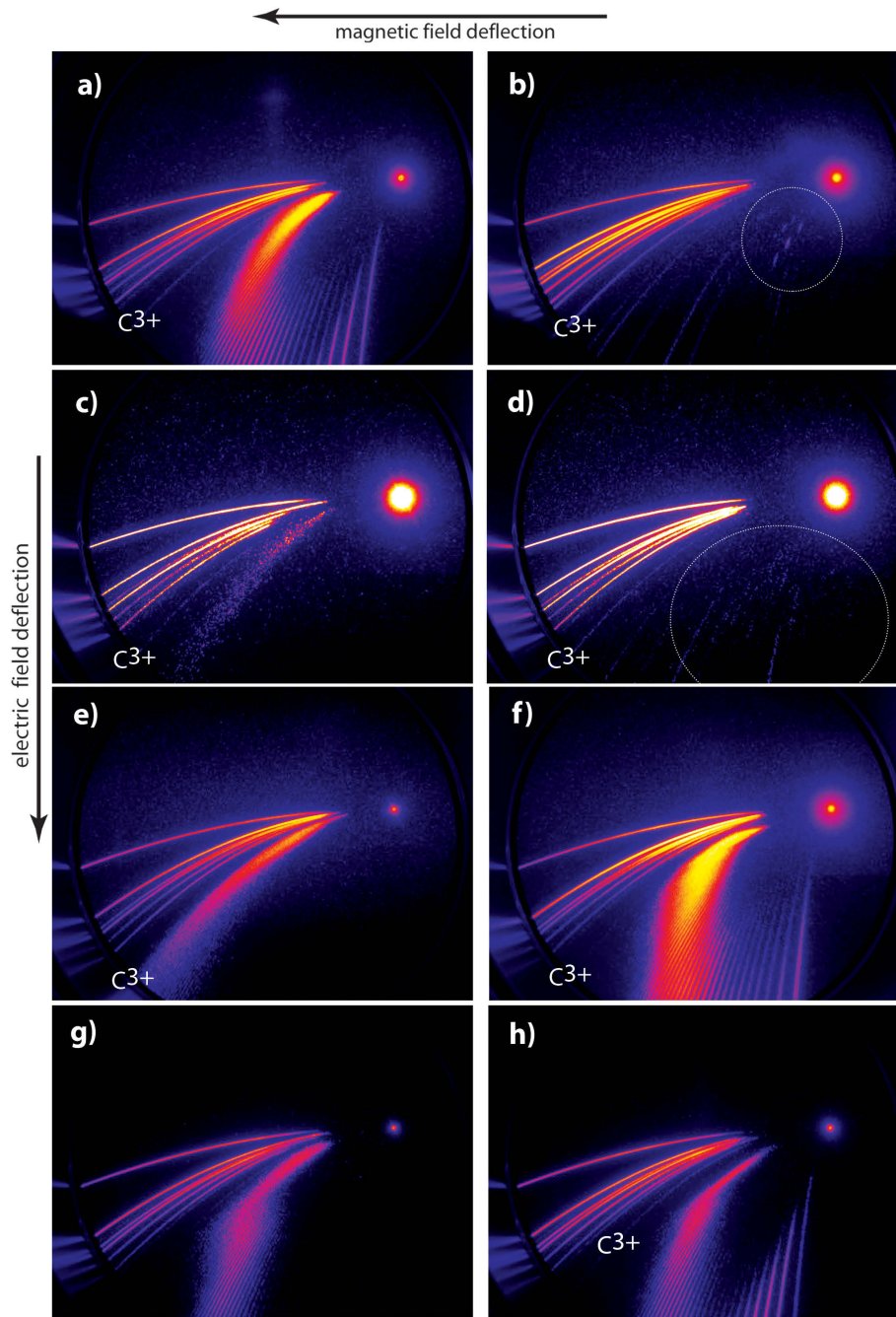


**Figure 6.7:** Ion traces on the detector after having passed through the Thomson spectrometer for different experimental parameters. a): Gold coating of  $(2 \pm 1)$  nm thickness on a  $(31 \pm 1)$  nm thick PVF foil. The laser illuminated the PVF foil, the gold coating was placed at the target rear side. b): The same target with the coating at the target front side. Colour scaling is enhanced to make the gold ion traces visible. c) and d):  $(7 \pm 2)$  nm thick gold layer on a  $(75 \pm 3)$  nm PVF foil. c): Gold layer placed at the target rear side, d:) at the target front side. The signal strength of gold ions is in the range of the detector's threshold, colour scaling is enhanced to illustrate their presence. e) and f):  $(7 \pm 2)$  nm gold coating on back e) and front f) of a  $(9 \pm 1)$  nm thick PVF foil. g) and h): Same target as e) and f) with reduced laser energy of about 66%.

- One spectra is reminiscent of falling star drag at the  $Z/A$  ratio of  $C^{3+}$ . A typical example can be seen in Fig. 6.7 e). In general, with the UHC condition and ultrathin foils, carbon ions were only accelerated down to down to a minimum charge to mass ratio of  $C^{3+}$  (see Section 6.1) and heavy ions were missing at all. In Fig. 6.7 e) and g) the heavy ion spectra adhered closely to this number. In the detected velocity range, gold ions are found at charge states between  $Au^{50+}$  and  $Au^{33+}$ . Lower charge states are missing, except from  $Au^{1+}$  to  $Au^{5+}$ . The gold ions' spectral distribution is broad and without a minimum kinetic energy cutoff within the detection range. This kind of spectrum was observed for the thinnest PVF substrates of 7–10 nm and a sufficiently thick gold coating of 4–6 nm on the target rear side.

By using a 10 nm PVF foil with a 3 nm silver coating, the same characteristics features were observed in the silver detected ion spectra. A maximum silver charge state of about  $Ag^{38+}$  was achieved. This equals the charge to mass ratio of  $C^{4+}$  and the maximum velocity was detected with  $E_{kin}^{max}(Ag)/u \geq 1.23 \text{ MeV}/u$ . The corresponding measurement is shown in the Appendix A.1 in Fig. A.1.

- In the second typical spectrum, gold ion traces were observed at consecutive charge states from  $Au^{1+}$  to  $Au^{50+}$ . The maximum kinetic energy cutoffs of gold ions followed proportional to their charge state with a lemniscate like symmetry <sup>7</sup>. Typical examples can be found in Fig. 6.7 a), f) and h). This characteristic feature was detected from either pure gold foils in a thickness range of 10–50 nm, or backside gold coated PVF foils of up to a PVF thickness of 20 nm, or front side coated PVF foils with a thickness  $\leq 10$  nm. In contrast to the above described spectra, ions with charge states between  $Z = 5+$  and  $Z = 15+$  exhibited a strong increase in the charge to maximum velocity scaling (cf. Fig. 6.4 b)). This introduces a remarkable "turning" in the traces' cutoffs on the detector. The spectral distribution of the heavy ions was limited in bandwidth, exhibiting a minimum kinetic energy with a similar lemniscate like symmetry regarding successive charge states.
- Fig. 6.7 g) depicts an ion spectrum showing a crossover between the two introduced classifications.
- The maximum detectable gold ion charge state depends on the thickness of the substrate and the applied laser energy.  $E_{kin}^{max}$  scales with the charge state, the substrate, and the applied laser energy. Hence, the higher the maximum detected gold ion charge state, the higher  $E_{kin}^{max}$ . The best results were achieved for the thinnest targets, within the optimized thickness range  $D_{opt} \leq 12$  nm for the used laser intensity (cf. Section 6.2) and a back or front side gold coating of up to 7 nm (Fig. 6.7 e), f)). The maximum charge

<sup>7</sup> Lemniscate function by Bernoulli:  $r = a\sqrt{2|\cos(2\varphi)|}$  [95]

state depends on the applied laser energy: The ratio of detected  $Z^{max}$  at full laser energy to  $Z^{max}$  for a 66% decreased laser energy, determined from Fig. 6.7 g), h), is about 1 : 0.7. In addition, in Fig. 6.7 c) and d) a reduction of the maximum charge state and the detected particle number was observed for targets with a thicker PVF substrate, e.g. 75 nm.

- For circular laser polarization, the heavy ion spectrum exhibited all of the named characteristics, such as, e.g., a falling star drag like spectra or a the lemniscate like symmetry for  $E_{kin}^{max}(Z)$  and  $E_{kin}^{max}(Z)$ . Examples are depicted in the Appendix A.1 in Fig. A.3.

### 6.3.4 Symmetry in the Heavy Ion Spectrum

The remarkable symmetry, seen on the detector screen in the spectral cutoff position of heavy ions, reflects a distinct relation between the maximum velocity and charge. The large range of successive charge states enabled a study on the  $Z/A$  to velocity scaling. The gold ion spectra revealed in Section 6.3.1 and Section 6.3.2 new effects for the acceleration dynamics with respect to different  $Z/A$  ratios, which were so far not predicted within the theoretical models [35, 42, 43, 94]. In addition, the limitation of the spectral bandwidth is in contradiction to the TNSA model prediction, and understanding this feature is one of the most important objectives for field of laser ion acceleration. The following evaluation refines the charge to kinetic energy scaling derived in Section 6.3.1 for the low charge states, e.g.  $Z \leq 15+$ . As already indicated in the last section, gold ions at charge states between  $1+ \leq Z \leq 12+$  were detected with a almost constant velocity. According to the spectrometer function, for a constant maximum velocity, the spectral cutoffs of successive charge states follow a straight line on the detector. This was observed for the lower charge states and can be seen in Fig. 6.7 a), f), h), Fig. 6.4 a) and Fig. 6.5. In the determined  $Z$  to  $E_{kin}^{max}$  scaling in Equation (6.1), this was considered with the constant charge offset.

The evaluation and transfer from the detector image to a  $E_{kin}^{max}$  to  $Z$  diagram, as it was done in in Fig. 6.4 b), suffered from inaccuracies given by the selection of data points and the merge of ion traces for high charge states. Hence, this motivated an approach to derive a more detailed scaling directly on the detector image, accounting for all heavy ion charge states and reflecting the observed symmetry. This was done with the help of a parametric function  $f(v^{max}(Z,A))$ , which delivers for the parameters  $Z$  and  $A$  discrete intersection points with a set of Thomson parabolas on the detector according to the spectrometer function of Equation (5.1). For an intuitive interpretation, one has to understand for functional dependencies of  $v^{max}(Z,A)$  the resulting projection of  $f(v^{max}(Z,A))$  on the detector: A constant velocity for all charge states ( $v(Z/A) = v_0$ ), transfers the cutoff position for all ion species on the detector to a line with an origin at the zero point. While a  $v \propto Z/A$  scaling projects each cutoff onto the same vertical deflection, a  $v \propto Z^2$  leads to a parabolic function for the cutoff of the ions. Let

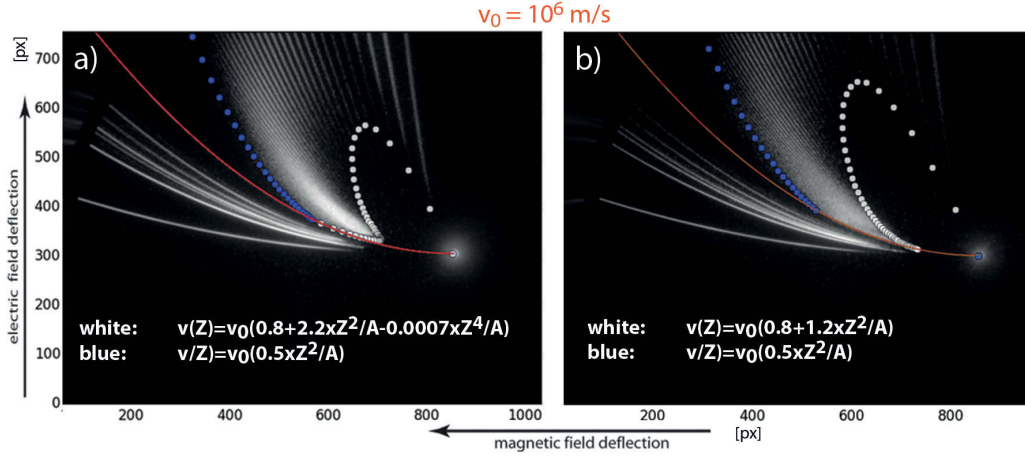


**Figure 6.8:** A reconstruction of  $E_{kin}^{max}(Z,Au)$  and  $E_{kin}^{min}(Z,Au)$  on the image of the detector. The charge to energy scaling used the Equation (6.3) and the spectrometer function according to Equation (5.1). The coefficients used for the reconstruction plot (dots) are given in the pictures. The scaling function gives discrete interception points with the detected cutoff for each charge state. The red line is a plot of the theoretical Thomson parabola for  $Z/A = 0.244$  for the same spectrometer function. a): The gold ion spectrum from a  $(35 \pm 2)$  nm PVF foil and a  $(2 \pm 1)$  nm thick gold coating. The gold was placed at the target rear side. b): The ion spectrum obtained from a  $(12 \pm 3)$  nm pure gold foil.

us consider an expansion of the velocity with respect to the ion charge  $Z$ :

$$v = \sum_{i=0}^n C_i \frac{Z^i}{A} \quad i \in \mathbb{Z} \quad (6.3)$$

where  $C_k$  is a scaling coefficient. An expansion of  $v^{max}$  to  $Z$  scaling is reasonable for low polynomial orders and opens up the possibility of identifying an acceleration model. Only positive acceleration was assumed, and the coefficients were determined by variation. A reconstruction of the gold ion cutoffs, using the expansion of velocity of Equation (6.3) and the spectrometer function (5.1), is shown in Fig. 6.8 for two different experimentally obtained detector images. The lemniscate like symmetry found in the cutoff position of gold ions on the detector could only be reconstructed for terms  $i = 0$ , to which higher orders with  $i \leq 1$  were added. By using the orders  $i = 0$  and  $i = 2$ , the reconstruction delivered discrete values of  $E_{kin}^{max}(Z)$  and  $E_{kin}^{min}(Z)$  already in remarkably good agreement with the detected results. For most of the lemniscate like symmetric spectra, a superposition of  $v(Z) = C_0 Z^0/A + C_2 Z^2/A$  reproduced the basic charge to maximum velocity scaling on the detector. The method accounted for a summarized description of a wide range of charge states and even small deviations became apparent.

Out of various shot series, for gold ion spectra exhibiting the lemniscate like symmetry, the reconstruction delivered a constant velocity of  $v_0 = (8 \pm 2) \times 10^5$  m/s in superposition with  $v^{max} = C_2 Z^2/A$  with  $C_2 = (1.0 \pm 0.5) \times 10^6$  m/s. Deviations

to the reconstruction were observed in the gold ion spectra for higher charge states with  $Z \geq 30+$ , as e.g., in Fig. 6.8 a). These can be attributed to a repulsive force affecting the highest charge states. With a negative higher order coefficient e.g.  $i = 4$ , the reconstruction could be refined. Here, as an interpretation, a repelling Coulomb field is conceivable, which arises from light material moving ahead and affects the heavy ions that follow the closest [41, 92]. This idea is supported by the carbon and oxygen spectrum in Fig. 6.8 a), where a decreased particle number was observed in the same velocity range.

A charge independent, constant velocity has to origin from a charge independent force, which, in terms of an electro dynamic model, would be contradictory. This apparent contradiction can be resolved by considering a shock acceleration model that assumes an acceleration of the whole foil, regardless of the ion species, to a same velocity, as already discussed in Section 6.2 [39, 41, 92]. For shock acceleration, like the hole-boring process (see Section 3.5), and with respect to a multi-ion species target, according to Equation (3.10), a small dependence on the ion charge remains and could be refined by an averaged ion charge and mass number. Assuming  $a_0 = 6$ , an ion charge to mass number of  $Z/A = 20/197$ , and a density of  $n_e/nc = 300$ , a velocity of  $v_{shock} \sim 0.002c$  is calculated from Equation (3.10). These assumptions reflect a collective movement, and the derived value,  $v_{shock}$ , is in agreement with the velocity contribution,  $v_0$ , which was obtained from the reconstruction of the experimental data. This is supporting evidence for an shock acceleration model. Higher velocities for higher charge states, and hence, higher order terms for the used velocity expansion,  $v^{max}(Z,A)$ , reflect a relation to additional acceleration schemes, as e.g. vacuum expansion (TNSA like). For the high charge states of gold ions, a remarkably high velocity scaling of about  $v^{max} \sim Z^2$  was derived. This high scaling was explained by a higher charge state at the plasma boundary in Section 6.3.1. Altogether, this leads to the following simplified acceleration scheme: During laser-plasma interaction, the laser accelerates the whole foil (or a fraction of it) via the hole boring boring process up to the found constant velocity. Meanwhile, or shortly after, the interaction a TNSA like acceleration sets in, which is determined by a higher accelerating field, due to the spatial distribution of the gold ion charge states along the target. Since in comparison to pure hydrocarbon foils no significant difference in the maximum velocities of hydrogen or carbon is observed, a fast separation between the light material and the heavy material seems to be a reasonable explanation.

Furthermore, the gold ion spectra exhibited a limited spectral bandwidth from which a charge to the minimum kinetic energies scaling of about  $v^{min}(Z) \propto Z^2$  was obtained, as shown in Fig. 6.8. This finding, shows a complex interplay in a staged acceleration scheme. The shock acceleration could deliver ions with a constant velocity  $v_0$  with a narrow spectral bandwidth that are then further accelerated by a charge dependent force. Here, the important question arises, how are the initial heavy ion charge states distributed? And how can the acceleration dynamic for different charge states be described in detail? For example, if the vacuum expansion of ions and electrons considers one electron sheath or if a separation of

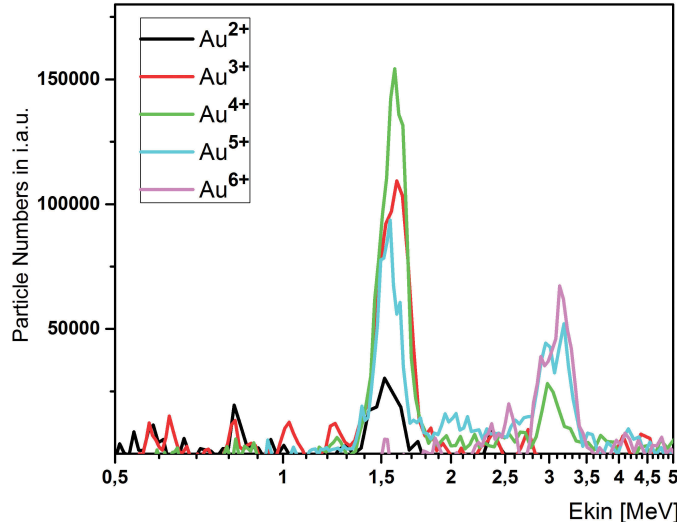


**Figure 6.9:** The evaluated spectral distribution of gold ion traces of the spectra from Fig. 6.7 b), detected from a target front side gold coating of 2 nm on a 35 nm PVF foil substrate. For gold ions from  $Z = 2+$  to  $Z = 5+$  a narrow spectral distribution was detected with a bandwidth FWHM of  $\Delta E/E = 0.1$  at the same energy of  $E_{kin} = (1.6 \pm 0.1)$  MeV. In the spectrum of gold ions at charge states of  $Z = 4+, 5+, 6+$ , a second peak at  $E_{kin} = (3.2 \pm 0.1)$  MeV with  $\Delta E_{kin}/E_{kin} = 0.2$  was observed.

ion and electron interfaces that follow each other have to be taken into account. Since, two different types of gold ion spectra were detected, as characterized in Section 6.3.3, one with successive gold ion charges states and one with a few but very high charge states, an additional interpretation has to be discussed: Charge transfer processes, occurring for ions passing through a dense medium, during the acceleration. Depending on the projectile ion's charge, the velocity and density of the transfer material, ions catch or lose electrons, as described in Section 2.3. Efficient electron capture (EC) has been demonstrated in recent publications for laser accelerated ions in the MeV kinetic energy range passing through gaseous and liquid media in [86, 87, 96, 97] or even ionized matter [98] leading to neutralization or even negatively charged ions. In this sense, a gold ion bunch at a high charge state and with a specific velocity distribution could undergo successive ECs. This would result, if no significant change in the velocity is assumed, to an ion spectrum at successive charge states and with a similar velocity distribution. This idea is supported for those heavy ion spectra that were observed only at high charge states in Fig. 6.7. The important question about inherent charge transfer processes will be further discussed in the following section and is directly examined in Section 6.5.

### 6.3.5 Target Front Side Acceleration of Heavy Ions

In the TNSA model (see Section 3.2), particles are accelerated symmetrically normal to the target [32]. As ion movement inside the target is very small, one

assumes that the accelerated ions originate from each target boundary. This is different for RPA or the hole-boring process, which includes a preference for an acceleration in the laser propagation direction [39] (cf. Section 3.5). Nevertheless, up to now, no experimental observation of pure RPA acceleration has been reported. In order to understand the interplay of the TNSA and RPA schemes, one fundamental question is, if the whole foil is accelerated in the laser propagation direction.

In the experiment performed gold coated plastic foils were used. The gold layer was either placed at the target front or rear side. In the case of rear side coated PVF foils, accelerated gold ions originated from target rear side. In the case of front side coated PVF foils of up to a specific thickness, gold ions were also detected in the laser propagation direction. Hence, these gold ions were accelerated from the target front side. This was observed for the targets with different gold and plastic layers, shown in Fig. 6.7. The gold ion spectra from thinner PVF substrate foils, in the range of 7–10 nm, exhibited similar spectra for front side and back side gold coatings. For these ultrathin substrate foils, the direct comparison between back and front side coatings, finds the  $Z^{max}$  to  $E_{kin}^{max}$  dependency somewhat higher for the case of the backside coating. But considering the lemniscate like gold ion spectra, no significant difference in the charge states, spectral characteristics or particle number was observed.

On the contrary, for an increased thickness of the substrate layer, a significant reduction in the particle number of gold ions and in the observed maximum charge state commenced. This can be seen in Fig. 6.7 b) and d) for plastic substrates with a thickness of 35 nm or 75 nm and the gold layer facing the laser illuminated target side. Only low charge states of up to  $Z = 6+$  are detected, while a narrowing in the bandwidth of their spectral distributions appeared. With a comparable spectral feature, an additional ion spectrum is shown in Fig. 6.9, for a 35 nm PVF foil with a 2 nm front side gold coating. Gold ions at  $Z = 2+$  to  $Z = 5+$  were detected at a constant kinetic energy of  $(1.6 \pm 0.1)$  MeV and with a remarkably narrow spectral bandwidth of about  $\Delta E_{kin}/E_{kin} = 0.1$ . For the charge states  $Z = 4+$  to  $Z = 6+$  a second, quasi mono energetic peak appears, at double the kinetic energy of the first.

Out of these findings, one can derive the following: heavy ions facing the laser illuminated foil were accelerated in the laser propagation direction, unless the PVF foil was too thick. The experiments observed this limit for a substrate foil thickness of about  $\geq 35$  nm resulting in a significant reduction of the detected number of gold ions and charge states. This can be interpreted in terms of RPA or the hole-boring process and means that the whole foil was accelerated in the laser propagation direction. The reduction the maximum charge states that commences with an increasing PVF foil thickness, points towards recharging processes: One can assume the charge state of gold ions at either front or rear side to be comparable [74] or even higher at the laser illuminated foil side. Hence, for thicker PVF foils, gold ions originating from the target front side might have passed through a remaining plasma to be detected in the laser propagation direction. By passing

the material, ions can capture electrons at a rate dependent on their velocity, material density and thickness, as introduced in Section 2.3. The maximum gold ion charge state was found to be dependent on the PVF thickness. This indicates that a longer travel length of the projectile ion in the medium leads to successive EC, when a high degree of gold ionization at the target front side is assumed. Successive EC is probable when the velocities of the ion and the electron are comparable [25, 87, 88]. In addition, a shock front acceleration that occurs at the target front side could explain the double kinetic energy value, since this model includes two velocities, at  $v_s$  and  $2v_s$  (cf. Section 3.5). Sections 6.5 and 6.6 will examine recharge processes for laser ion acceleration in different approaches. It will be shown that the process can have a strong effect on the ion spectral distribution.

### 6.3.6 Discussion of the Heavy Ion Spectra

The charge state to kinetic energy relation of the accelerated heavy ions is a demonstrative example to examine scaling laws and staged accelerations models. Little was reported on laser accelerated heavy ions, since usually their acceleration is inhibited (see Section 6.1). The examination here found a new and unexpected mechanism that enabled an efficient acceleration of heavy ions and revealed an heavy ion spectrum with distinct spectral characteristics that were not reported before [35, 41–43, 93, 94]. With the help of the ultrahigh laser contrast condition and heavy material foils with a thickness that is close to the laser skin depth, an efficient acceleration of heavy ions became possible, even in the presence of light elements. This finding stands in contrast to former observations [99] and theoretical predictions [39, 41, 42], since it is assumed that the light elements separate early from the heavy ions due to their higher charge to mass ratio and leave the heavy quasi immovable behind. Therefore, without removal of the light elements [35, 99], a limit in the charge to mass ratio is usually observed up to which the ions are accelerated (cf. Section 6.1). With the parameters used here (UHC, ultrathin heavy material foils), this limit can be overcome. This became possible due to a high gold ion charge state, which could be explained with the ADK model by A. A. Andreev. For either pure gold foils or a gold layer at the target's backside, no influence by the light elements was observed and the fastest heavy ions adhered the light in velocity and charge to mass number. This is valid up to a specific ratio between the heavy and light material in a target that was found to be significantly higher than the contamination layer of the target. The high ion charge states were dependent on the laser energy and the thickness of the contamination layer. Gold ions with the lowest charge states were detected with a constant and charge independent velocity. This and the prior results revealed a complex interplay between different acceleration schemes. From these findings the following preliminary scenario is suggested: Shock acceleration of the foil by hole boring process at the target frontside from which a charge independent velocity of up to  $10^5$  m/s is obtained. Then a second acceleration that is similar to the TNSA and proportional to the ions charge to mass ratio. However, the detected

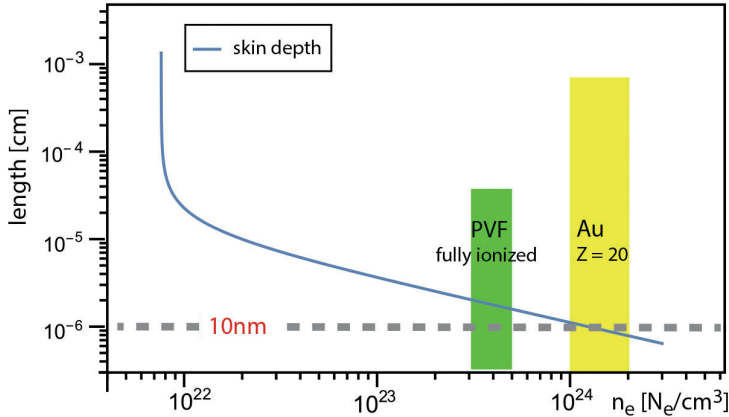


**Figure 6.10:** The laser skin depth  $l_s$  as a function of the electron density  $n_e$  according to Equation (1.21) and a normalized laser field strength of  $a_0 = 5$ . PVF material at full ionization and gold with an average ionization of  $Z = 20+$  is shown.

charge to maximum velocity scaling of  $v_{max}(Z) \sim Z^2$  is higher than predicted from the TNSA model. This was explained by an enhanced field strength at the target boundary due to a spatial dependency of the gold ions charge distribution and enabled the significantly high maximum kinetic energies for the heavy ions. The results showed that this did not affect lighter elements, which can be a consequence of their fast separation from the plasma. This finding stands in contrast to similar staged acceleration schemes or an additional acceleration from the highly charged heavy ion background that had been proposed to enhance the proton acceleration for a multi-ion species plasma in Refs. [41–43, 92, 94]. Two different kinds of gold ion spectra were detected, one that only consisted of high gold ion charge states and a broad spectrum and one that exhibited successive charge states with a limited spectral bandwidth. For the latter a minimum kinetic energy a scaling similar to  $v_{min}(Au) \propto Z^2$  was obtained. These findings and the observations of accelerated gold ions from the laser illuminated target side in the laser propagation direction, raise the important question, if ion charge transfer processes during the acceleration could affect the heavy ion charge distribution and spectral distribution. In conclusion, a refined model is required that includes the heavy ion acceleration discovered here, and which considers the following questions: How do the ions at different charge to mass ratios separate during or after the laser-plasma interaction and what additional effects have to be considered, such as e.g. recharge processes and repulsive potentials between ion bunches of different charge to mass ratios.

## 6.4 Laser Transmission

Although for ultrathin targets, full ionization and hence an overcritical opaque plasma boundary is expected, for high laser intensity the onset of relativistic transparency has to be considered, in accordance with Equation (1.23). A small

Target material	thickness	contrast	T	$I_L$
C <sub>5</sub> H <sub>7</sub> O <sub>2</sub>	90 nm	HC	9%	$7 \times 10^{19}$ W/cm <sup>2</sup>
C <sub>5</sub> H <sub>7</sub> O <sub>2</sub>	85 nm	UHC	2%	$5 \times 10^{19}$ W/cm <sup>2</sup>
C <sub>5</sub> H <sub>7</sub> O <sub>2</sub>	2 × 100 nm (two foil setup)	HC	3%	$7 \times 10^{19}$ W/cm <sup>2</sup>
Au	10 nm	UHC	1%	$5 \times 10^{19}$ W/cm <sup>2</sup>

**Table 6.1:** Relative transmission values, T, of laser light in the spectral range  $750 < \lambda < 950$  nm detected from laser target interaction on the laser propagation axis. Transmission values obtained at high laser contrast (HC) and ultrahigh laser contrast (UHC) at various foil thickness and material. By inserting a second foil at distance of  $w = 500$   $\mu\text{m}$  (cf. Section 6.5) transmission values are given for high contrast.

transmittance of the laser light through the ionized target foil occurs if the laser skin depth  $l_s$  exceeds the target thickness:  $l_s > D$ . In Fig. 6.10  $l_s$  is plotted as a function of  $n_e$ , for  $a_0 = 5$  and according to Equation (1.21). The calculation considered a relativistic correction. The function is compared to  $n_e$  from solid state PVF and gold, at a reasonable degree of ionization. The condition  $l_s > D$  is fulfilled for a target thickness of 10 nm and PVF targets with full ionization or for gold foils with an averaged ionization degree of  $Z = 20+$ .

Relative measurements of the laser transmission during the laser target interaction were performed for PVF and gold foil targets. The experimental setup is described in Section 5.6.4. This measurement complements the investigation of the previous sections following the question, how much laser light is transmitted through the ultrathin foils? Table 6.1 collects the detected transmission values in the spectral range of 700–900 nm for different laser contrast conditions (HC, UHC). The transmission values are given relative to the integrated spectral intensity, which was measured without a target in the same experimental run. With the UHC condition, the measurement exhibited a transmission value of  $T = 2\%$  for a  $(85 \pm 3)$  nm PVF foil and  $T = 1\%$  for a  $(10 \pm 2)$  nm gold foil. The optimal foil thickness with respect to ion acceleration was found at a thickness of 12 nm in Section 6.2 for a PVF target. Theoretically, for the applied laser intensity,  $l_s$  is about 20 nm, hence, much smaller than the PVF foil thickness of Table 6.1. Therefore, smaller T values were expected and relatively higher values for the much thinner gold foil [18]. The obtained transmission value is in fair agreement with the calculations in [10].

On the contrary, for the HC condition, the experiment delivered significantly higher transmission values. For the same target (85 nm, PVF), a value of up to  $T = 9\%$  was obtained. The difference of about 20% in the applied  $I_L$  between the two laser contrast conditions is not sufficient to derive a equivalent longer skin depth or to reach a significant higher onset of relativistic transparency. Hence, the high laser transmission values might be attributable to a decreased foil density due to an expansion of the target that is introduced by pre-pulses or the rising intensity level.

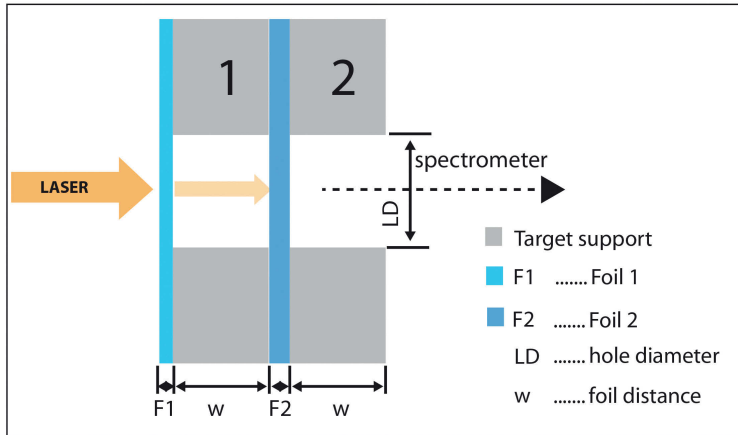


**Figure 6.11:** A schematic of the two foil target setup. The distance  $w$  was either introduced by place holders between the foils or the target support itself. Note, in order to enable a direct comparison to the single foil configuration, the second foil was removed but the same target support construction was used.

## 6.5 Ion Charge Transfer Processes

Charge transfer processes, in particular electron capture (EC) for laser accelerated ions, were objectives of recent investigations of experimental campaigns next to this thesis [86, 87, 96]. In principle, electron capture (EC) or electron loss is expected for a projectile ion passing through transfer matter with a dependency on its charge and velocity (cf. Section 2.3). The cross-sections for a laser accelerated ion beam passing through transfer matter are yet not covered by theoretical models [98]. The examination of the EC processes in the laser-plasma ion acceleration was motivated by experiments performed using gaseous [87] or liquid mediums [86, 96]. Moreover, charge transfer processes have to be viewed as possible inherent processes during the laser ion acceleration. Indications of this were already discussed with regard to the spectra of accelerated gold ions (cf. Section 6.3.5) and the differences in the charge distributions obtained at different laser contrast conditions (cf. Section 6.1). In order to complement the investigation and discussion, experiments examined charge transfer processes for ultrathin solid state matter with the help of a double foil target configuration, as depicted in Fig. 6.11. Such a target system opens up the possibility to tailor the ion energy distribution, since the second foil inhibits the passing of slower ions to a degree determined by its stopping range (cf. Section 2.3). A similar method was suggested for accelerated protons in Ref. [100] without taking a charge transfer process into account.

In the configuration used, the second foil was placed at a distance of  $w = 500 \mu\text{m}$ , through which accelerated electrons, ions, the transmitted laser light and the emitted XUV radiation pass before detection. The experiments were performed with PVF foils at various thicknesses  $\leq 90 \text{ nm}$  in 5 experimental runs and in total 21 measurements. As expected, for this small foil thickness and ion

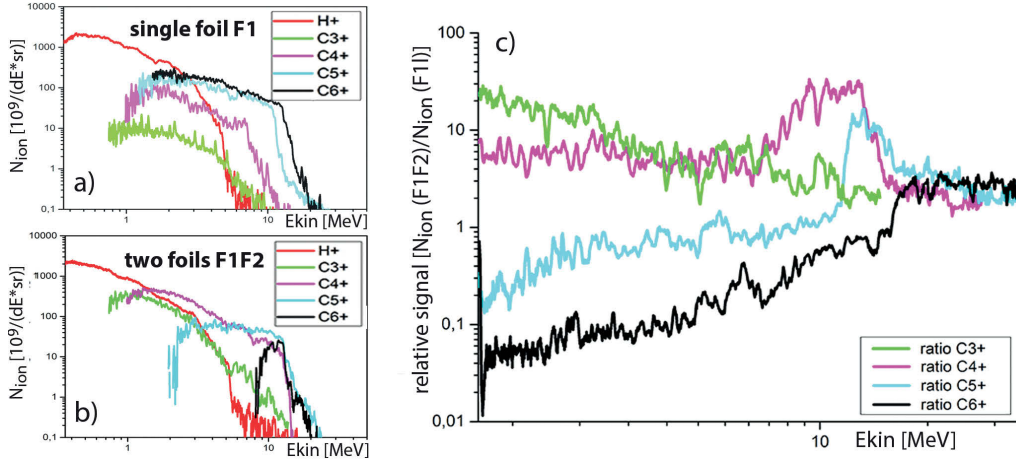


**Figure 6.12:** Change in the ion particle numbers and spectrum by using a two foil target setup with first foil F1 at thickness  $(14 \pm 1)$  nm and second foil F2 at  $(35 \pm 2)$  nm. The foils are distanced about 500  $\mu$ m. a): The ion spectrum obtained from the laser interacting with a single foil b): the spectrum obtained for the two foil setup. The background signal has been removed for both evaluations, the low energetic end of the spectrum corresponds to the end of detection range. c): The relative change in the spectrum between the two foil and single foil setup with the data of a) and b), to illustrate qualitatively the charge transfer. No subtraction of the background signal was done here to avoid a significant noise ratio and/or falsification by additional filtering.

velocity, the second foil did not affect the spectrum of  $H^+$  [101]. On contrary, for heavier ions, e.g. carbon and oxygen, electron capture was observed and for each charge state, a significant change in the spectrum. Fig. 6.12 shows the charge transfer for the carbon ions in a direct comparison. The measurements were obtained for the ultrahigh laser contrast condition and are taken out of the same experimental run. The ion spectra detected from the single foil with a thickness 14 nm, F1, is compared to the spectra obtained in presence of second 35 nm thick foil, (F2). Both foils are of PVF material with a density of  $\rho = 1.23$  g/cm<sup>3</sup>, which corresponds to a density normed travelling length of  $x_D = 43 \times 10^{-4}$  mg/cm<sup>2</sup>. The comparison shows that the charge transfer has influenced all carbon ion species. Even  $C^{2+}$  ions at very small particle numbers appeared in the spectrum, which were not observed without the second foil (not shown). An increase in the maximum kinetic energies of  $C^{5+}$  and  $C^{4+}$  was detected (cf. Fig. 6.12 a) and b)), reaching up to the maximum kinetic energy of  $C^{6+}$ . This shows that a single and double electron capture of fast  $C^{6+}$  ions must have taken place. The second foil affected the spectrum of  $C^{6+}$  in a similar manner to a bandpass filter and remarkably reduced its spectral bandwidth.  $C^{6+}$  ions were detected with a limited spectral bandwidth in the high energy range. This shows, that the cross section for EC increases the smaller the ion velocity is.

In order to illustrate charge transfer in the carbon ion population, Fig. 6.12 c) demonstrates the relative change in particle number  $N_{ion}(Z)$  per kinetic energy to the single foil case. It exhibits a rise in the particle number of the  $C^{3+}$  and  $C^{4+}$

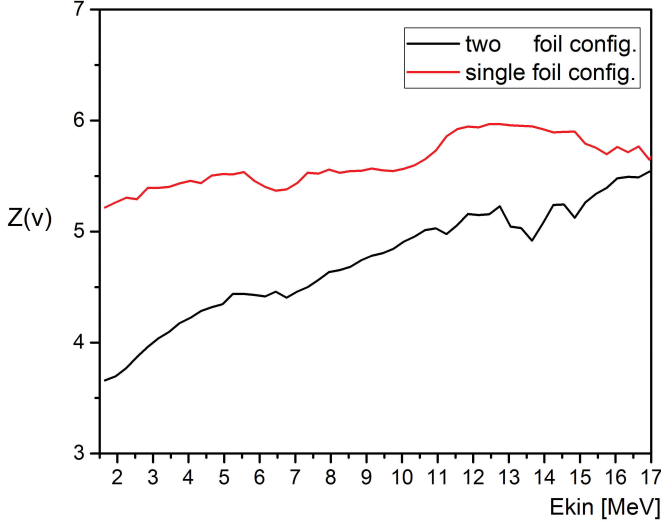


**Figure 6.13:** Comparison of the mean charge  $Z(v)$  according to Equation (6.4) and the measurement of Fig. 6.12 with respect to the single and two foil configurations. Note that the scaling is linear in both axis.

populations, while in the same energy range, the particle numbers of  $C^{6+}$  and  $C^{5+}$  are reduced about a comparable amount. Hence, in the presence of the second foil, particle numbers of both species were decreased dependent on their kinetic energy for  $E_{kin} \leq 15$  MeV in the case of  $C^{6+}$  and  $\leq 11$  MeV for  $C^{5+}$ . The difference in these values corresponds to the ratio between their  $Z/A$  numbers of  $0.81 \pm 0.2$ . In the detection range, the deviation in the overall integrated particle number for carbon species from  $C^{6+}$  to  $C^{3+}$  between single and two foil configuration was below 5%. A similar transfer from the dominant carbon ion species  $C^{5+}$  to  $C^{4+}$  was detected for a double foil target at the HC condition (cf. Fig. A.4 in Appendix Section A.1).

In Ref. [98] recharging processes were demonstrated for laser accelerated ions passing through warm and cold dense matter at velocities of up to 0.8 MeV/u. The authors evaluated, in a calibrated measurement and for all detectable ion populations, a velocity dependent mean charge state  $Z_{mean}$ :

$$Z_{mean}(v) = \frac{\sum_i [Z_i n_i(Z_i, v)]}{\sum_i n_i} \quad (6.4)$$

considering an ion beam with a charge and velocity dependent distribution  $n_i(Z^i, v)$ , where  $i$  stands for the numerator of the particular ion charge state.  $Z_{mean}$  refers to the effective charge  $Z^*$  of Equation (2.7), but considers the integrated ion beam density with all charge states. The experiment in Ref. [98] found an EC for ions having passed through a foil. They showed that  $Z_{mean}$  increases with the ion beam velocity, independent of eV heated or unheated material. Fig.6.13 shows an evaluation in accordance to Equation (6.4) for the measurements in single and two foil configurations of Fig.6.12. In comparison to Ref. [98], the measurements

in Fig. 6.13 reveals an efficient EC for ions at higher charge states. Contrary to transfer matters, such as liquid [88] or gas [87] media, the ultrathin foil target did not affect the ion beam divergence. This can be seen in the comparison between the detector images in Fig. A.4 in Appendix Section A.1 and Ref. [87].

In view of future applications, the two foil configuration showed an easy way to produce bandwidth limited ion spectra. A detailed examination of the underlying process with respect to foil thickness, sufficient statistics, and the comparison to different theoretical models requires further investigation and is examined in an ongoing cooperation with D. Casas.

## 6.6 Controlled Plasma Manipulation for Laser Ion Acceleration

Pre-pulses and the rising intensity level of the laser pulse characterize the HC condition and introduce pre-ionization, pre-heating and pre-expansion of the target. For few nm foil targets, this can decrease the target density. In comparing experimental results obtained at two different laser contrast configurations in Sections 6.1 and 6.4 important differences in the resulting ion spectra and laser transmission values were already demonstrated. These differences indicated a significant change of the target density and the scale length of the plasma density gradient when the target was pre-heated due to the lower laser contrast condition. How the pre-plasma condition differ between the two laser contrast conditions is an open question, since it can not be easily measured and usually is obtained from PIC simulations [63–65, 68]. The impact that a longer rise of the plasma density at the target boundary has on the electron dynamics is a scope of recent investigations [17, 22, 64, 68, 84] and is not fully resolved yet. The scale length of the plasma density gradient,  $L(\nabla n_e)$ , determines the laser to plasma absorption (cf. Section 2.2) and leads to higher electron temperature that can reduce the ion acceleration efficiency [64, 84]. In order to test how a defined pre-pulse influences the ion acceleration, for ultrahigh laser contrast, a second laser pulse, P2, was applied. The aim was to determine the delay time of the P2 pulse in which the ion acceleration is inhibited. Since the acceleration of ions is considered to be longer than the laser pulse duration in the TNSA model [1, 32], the experiment further tested if a post-interaction with a second counter-propagating laser pulse can affect the ion spectra.

P2 was applied at an intensity  $I_P \sim 1 \times 10^{18} \text{ W/cm}^2$  and at a delay time  $\Delta t_P$ . It propagated in the opposite direction of the stronger drive pulse which had an intensity of about  $5.5 \times 10^{19} \text{ W/cm}^2$ . A sketch of the counter-propagating setup is shown in Fig. 6.14, details of inherent parameters, definitions and methods are described in Section 5.4. The temporal overlap was determined to be in an time interval of  $\pm 0.3 \text{ ps}$ . Fluctuations are assumed to be below 50 fs and thus, the temporal overlap is considered to be at an almost fixed time within this time interval. In consequence, for the same experimental run a constant offset up to  $\pm 0.3 \text{ ps}$  for the delay times is possible. The polarizations of the two pulses were

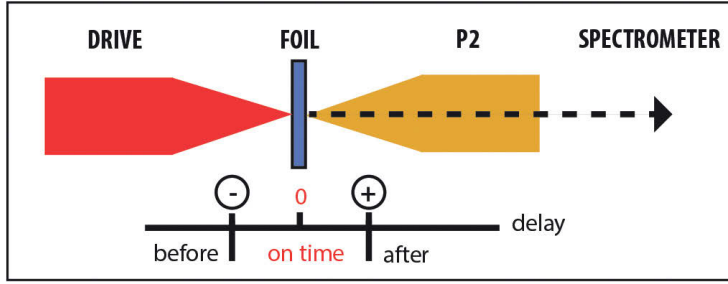


**Figure 6.14:** Sketch of the counter-propagating setup for examining the influence of a second laser pulse (P2) on the ion acceleration. Ions were detected at  $0^\circ$  from the target in the propagation direction of the drive pulse after they have passed through a hole of the focusing optic of the probe pulse. At negative delay time  $\Delta t_P$ , the P2 pulse interacts with the foil before the drive pulse, while at positive delay P2 hits the plasma and accelerates particles after the interaction with the drive pulse has taken place.

chosen linear and parallel to each other. Accelerated ions were detected in the propagation direction of the drive pulse, after having passed through a hole in the second laser pulse focusing parabola. A Thomson spectrometer captured the particles on the propagation axis within a half angle of  $0.0012^\circ$ .

### 6.6.1 Ultrathin Hydrocarbon Foils

The experiments were performed for a single PVF foil target at a thickness of 34 nm. The P2 pulse was applied at different delay times in the range  $-5 < \Delta t_P < +3$  ps. The detected maximum ion kinetic energies are compared to a reference measurement without using the P2 pulse. A significant decline in  $E_{kin}^{max}$  for all ion populations was observed, which scaled with the applied negative delay time. The results are summarized in Fig. 6.15 and show the reduction in  $E_{kin}^{max}$  relatively to the reference measurement and dependent on the delay. A statistical shot to shot variation about  $\delta E_{kin}^{max} = 8\%$  was assumed. When the pre-pulse had pre-heated the target  $\leq -3$  ps before the drive pulse interacted with it, the maximum ion kinetic energies were reduced to a  $> 50\%$  smaller value. Hence, pre-heating of the plasma significantly interferes with the laser to ion acceleration either due to longer scale length of the plasma density or a reduction of the target density. The reduction did not further increase for earlier delays ( $\leq -3$  ps). This observation is in agreement with the results of Ref. [64] that found no further decrease of ion energies for  $L(\nabla n_e) \sim 5 \mu\text{m}$  for different laser and target parameters.

At positive delay times, the second laser pulse arrives after the drive pulse has already interacted with the target. In this case,  $E_{kin}^{max}$  of the carbon ions remained almost unaffected, while  $E_{kin}^{max}$  was slightly reduced for the protons (cf. Fig. 6.15). Since  $\Delta t_P > 0$  corresponds to an interaction of the P2 pulse with already accelerated particles behind the target, it could affect the the co-moving electron sheath and hence the post-acceleration of ions (TNSA). The P2 pulse is strong enough to drive electrons, which approach with kinetic energies of few

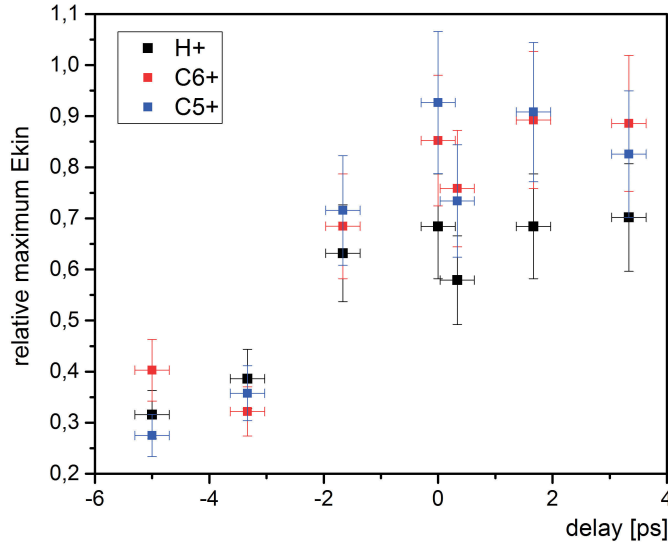


**Figure 6.15:** A significant energy loss of the maximum kinetic energies of  $\text{H}^+$ ,  $\text{C}^{6+}$  and  $\text{C}^{5+}$  was detected for negative delay times of the second laser pulse. Maximum kinetic energies are given relative to a reference measurement without the second laser pulse. Both measurements are from a  $(34 \pm 2)$  nm thick PVF foil, at ultrahigh laser contrast, and refer to the same experimental run.

keV, to turn backwards.  $\text{C}^{5+}$  and  $\text{C}^{6+}$  ion spectra are shown in Fig. 6.16 for different positive delay times. A direct comparison to a corresponding reference measurement without the P2 pulse is given for two different foil thickness (PVF, 34 nm and 14 nm). In the carbon spectrum, a significant suppression in the particle number was observed for the low energy range. The effect occurs only for a specific charge state that depends on the delay time of the second laser pulse. In the delay range of  $0 < \Delta t_P < +1.7$  ps for the 34 nm foil, a strong reduction in the particle number of the  $\text{C}^{5+}$  population was detected, for kinetic energies below 2 MeV. At longer delay times,  $\Delta t_P > +3.3$  ps, the spectral distribution of  $\text{C}^{5+}$  is again comparable to the one obtained without the P2 pulse. For the delays 0 ps, +1.7 ps and +3.3 ps, the  $\text{C}^{6+}$  population exhibited a higher particle number, in direct comparison to reference measurement, while the spectral distribution remained similar. At a shorter delay time of +0.2 ps, a decline in the particle number was observed for kinetic energies below 4 MeV for  $\text{C}^{6+}$ . It is depicted in Fig. 6.16 d) for a 14 nm thick PVF foil. For the same delay in the  $\text{C}^{5+}$  spectrum a higher particle number at kinetic energies above 2 MeV appeared. For later delay times such as  $> +0.3$  ps, the ion population of  $\text{C}^{6+}$  is comparable to the one obtained from the measurement without the P2 pulse, while the decline in particle number now commences for  $\text{C}^{5+}$  and kinetic energies below 2 MeV. This basic approach revealed, that second laser pulse operates like a spectral filter on a specific charge state. The ion spectra gave an indication that the mechanism is similar to the electron capture process found in experiments with double foil targets in Section 6.5.

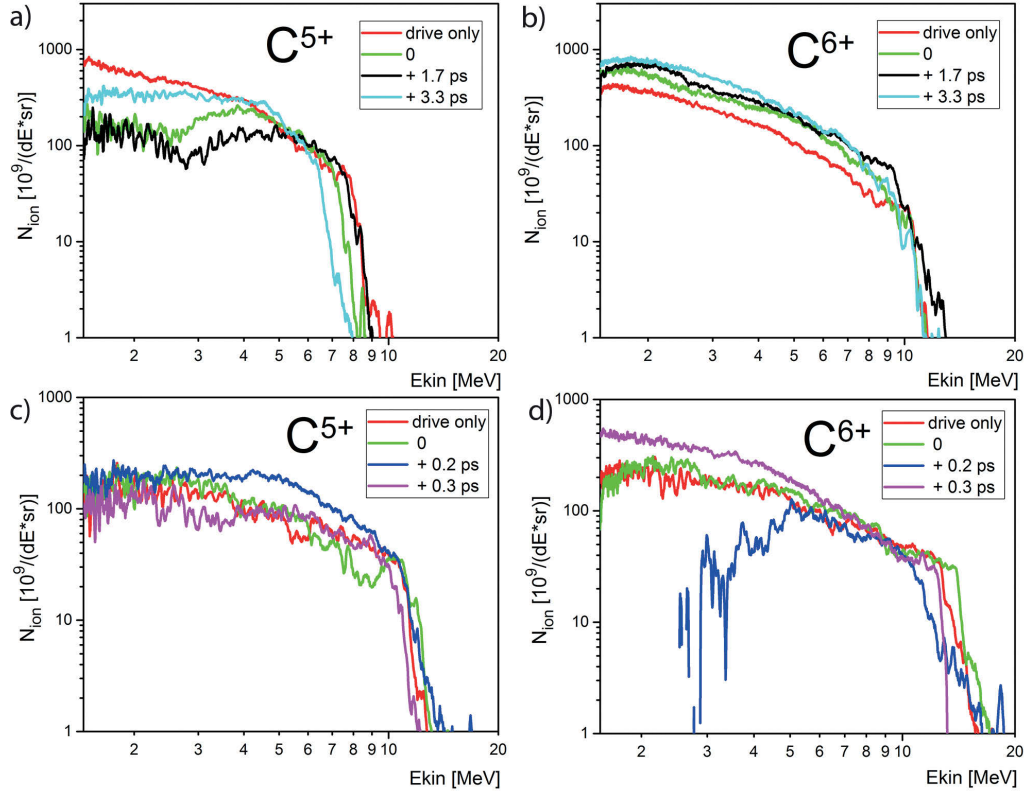


**Figure 6.16:** Ion spectra for selected ion species  $C^{6+}$ ,  $C^{5+}$  at positive delay times of the second laser pulse and at ultrahigh laser contrast. a) and b): Detected spectra using a  $(34 \pm 2)$  nm PVF foil target, c) and d): from a  $(14 \pm 2)$  nm PVF foil.

### 6.6.2 Heavy Material Foils

The same experiment was performed using a 50 nm gold foil. Fig. 6.17 a) compares detector images of the detected ion spectra for a measurement without the P2 pulse and an for the P2 pulse at a delay of  $-0.7$  ps. The intensity of the P2 pulse was about  $I_P = 9 \times 10^{17}$  W/cm<sup>2</sup>. In both cases, the gold ion spectra exhibit comparable spectral characteristics as discussed earlier for thinner gold foils in Section 6.3.3, but, with a decline of the maximum gold charge state for negative delay times. Fig. 6.17 b) shows the maximum detected gold charge state in relation to different delay times of the P2 pulse. Out of these measurements, a linear decrease in  $Z_{Au}^{max}$  for  $-2 < \Delta t_P < 0$  ps was extracted:

$$Z_{Au}^{max}(\Delta t_P) = Z_{Au}^{max}(0) + 14 \times \Delta t_P \text{ [ps]} \quad (6.5)$$

The decline saturates for an delay time below  $\Delta t_P < -2$  ps. Here,  $Z_{Au}^{max}(0) = (47 \pm 2)$  and corresponds to the maximum charge state obtained by solely using the drive pulse.

In addition, the interaction of the P2 pulse at minor negative delay ( $\sim -1$  ps), reproducibly increased the detected particle number of all ion species in the de-

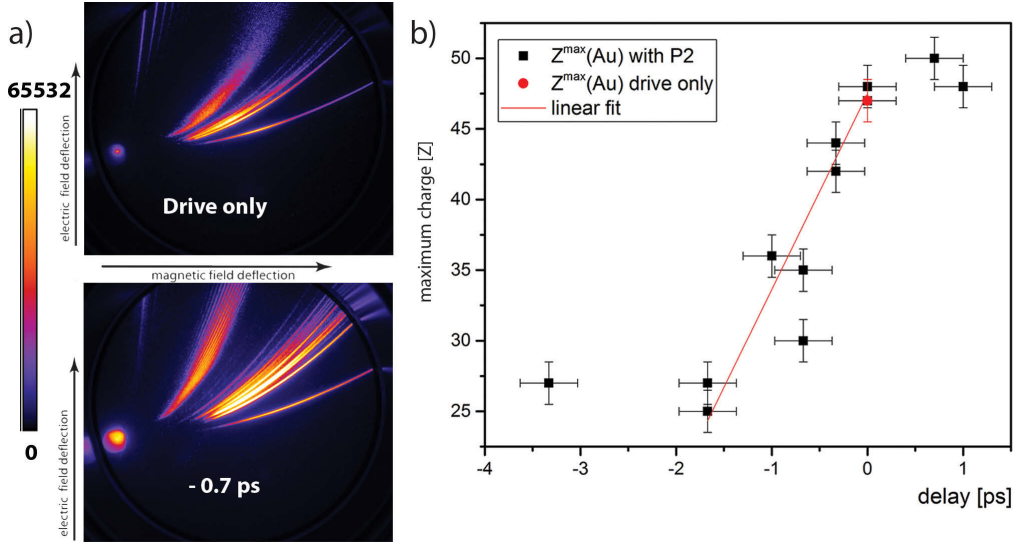


**Figure 6.17:** a): Detector images displaying ion spectra from a Thomson spectrometer, obtained from a measurement with a  $(50 \pm 4)$  nm gold foil and the P2 pulse at a delay of  $-0.7$  ps and without it (drive only). Both images have the same colour scaling, at same spectrometer configuration and exposure conditions. b): Detected maximum gold charge state at different delays of the P2 pulse. Linear fit (red) corresponds to Equation (6.5).

tection range. The corresponding evaluated spectra of  $\text{H}^+$  and  $\text{C}^{6+}$  and its dependency on the applied delay time can be found in the Appendix Section A.1. At  $\Delta t_P = -0.7$  ps, the integrated particle number, in the detection range, of  $\text{C}^{6+}$  and  $\text{H}^+$  had a 30% higher yield than obtained from the single laser pulse interaction. As already demonstrated for the hydrocarbon foils, negative delay times cause a reduction of the maximum kinetic energies. The investigation revealed a novel method to increase the ion acceleration efficiency with respect to the particle number.

At negative delay times, ion traces at  $Z/A$  numbers, which are not observed in case of a positive delay times or measurements without the P2 pulse, appeared on the detector in Fig. 6.17 a). A detailed evaluation with respect to isotopes, gold and ions of light elements up to period 4 is discussed in the Appendix Section A.1. The ion traces at this charge to mass ratios could not be definitely identified and remain as an interesting topic of further investigation.

## Discussion on the Two Laser Pulse Experiments

In a basic approach, the experiments with two laser pulses provided important insights and revealed novel effects: First, an inhibition for an efficient laser ion acceleration was observed when a strong pre-pulse has pre-heated the target few ( $< -2$  ps) before the drive laser pulse interacts with it. The experiments showed that a smaller ion acceleration efficiency regarding to  $E_{kin}^{max}$  is a consequence of pre-plasma condition, namely the rise of the plasma density and target density. The decrease of the acceleration efficiency seen in the case of a pre-heated plasma

boundary confirms the investigation for the TNSA model in Ref. [64, 84].

With using heavy material targets, pre-heating the foil raised the overall detected particle number. This correlates to the high particle number obtained from thick metal foils when the HC condition was applied (see Section 6.1). Hence, although a pre-expanded target does not reach the highest maximum ion kinetic energies, it can raise the acceleration efficiency in terms of particle numbers. At the same time a reduction of the maximum heavy ion charge state was shown. The reduction was found to scale proportional with the negative delay time of the pre-pulse. This gives an evidence that the pre-plasma condition determines the charge states of the heavy ions, and hence, could suppress their acceleration. This can explain why no heavy ions were detected in the case of a lower laser contrast condition (cf. Section 6.3).

Experiments presented here, showed that a post-interaction of laser accelerated ions with a second counter-propagating laser pulse affects the ion spectrum. The results revealed an influence on carbon ions at a specific charge state that was dependent on the delay time. In case of the  $C^{6+}$  and  $C^{5+}$ , a decline in the particle number for a particular spectral range commences at a certain delay time. The resulting ion spectrum is strongly reminiscent of the ion spectra obtained in the two foil target setup of the previous section. Accordingly, charge transfer processes are a possible interpretation, but appear, if introduced by the post-interaction with a second laser pulse, dependent on the applied delay time for a certain charge state. In Sections 6.2 and 6.3 the ion acceleration with using ultrathin foils and ultrahigh laser contrast was discussed with respect to a mixture of the acceleration models RPA and TNSA (cf. Chapter 3). This included a discussion about the separation of the accelerated ion species and the accelerating electron sheath within and after the pulse duration  $\tau_L$ . In this context, a second counter-propagating laser pulse could accelerate electrons in the backward direction when they expand into the vacuum. This could introduce charge transfer processes on the one hand, as an interruption of the late TNSA acceleration (vacuum expansion) on the other hand. This scenario could explain the observed decline in the ion particle number in the low energy range, for different charge states at different delay times, when either an separation of the ions due to their charge to mass ratio or a charge dependent cross-sections are considered.

## 6.7 Conclusions on the Laser Ion Acceleration

The dependency of laser driven ion acceleration on a range of parameters was investigated: laser contrast, target thickness, target composition, and single and double foil target configurations. Furthermore, the influence of a counter-propagating laser pulse at positive and negative delay times and an intensity of  $\sim 10^{18}$  W/cm<sup>2</sup> was examined. The results revealed different new ways to manipulate the spectral bandwidth, particle number and kinetic energies of laser accelerated ions.

## The Optimum Regime for Ion Acceleration

For the RPA model, optimization of maximum ion kinetic energies with respect to target thickness for a low density hydrocarbon material was investigated. An optimum target thickness of 12 nm for hydrocarbon material (PVF) and at  $a_0 = 5$  and UHC contrast condition was found. RPA and a subsequent TNSA like acceleration delivered a maximum proton energy of 16 MeV and maximum carbon energies of 70 MeV. The results confirmed and improved prior benchmarks and relaxed the demands on target preparation [2, 69]. This optimal ion acceleration was obtained almost independently of the laser polarization used, which is similar to the findings of [40, 83, 102].

## Heavy Ion Acceleration

With the use of ultrathin heavy material targets the experiments revealed an unpredicted efficient acceleration of heavy ions at ultrahigh laser contrast. Heavy ions (gold and silver) were detected at successive charge states up to  $Z \leq 50+$ , reaching kinetic energies of up to 1 MeV/u. In comparison to previous experiments, the heavy material was accelerated in the presence of light elements [35, 85, 99]. This was demonstrated and investigated in detail for gold coated hydrocarbon foils at various ratios of layer thicknesses. The significant high kinetic energies detected for heavy ions are a consequence of their high charge state in combination with a spatial dependence of their charge distribution within the target [74]. This acceleration scheme was obtained PIC simulations and a theoretical model by A. A. Andreev and K. Platanov. A detailed analysis of the heavy ion spectrum revealed a distinct charge to maximum and minimum kinetic energy scaling, which was found to be higher than predicted by previous theoretical models [31]: A superposition of a constant velocity  $v_0 \sim 10^5$  m/s and a  $v \propto Z^2$  was determined, capable of reconstructing the experimentally obtained heavy ion spectra for almost all measured ion charge states with good agreement. The results gave important insights into the ion acceleration processes from a multi-ion species target in terms of the overall spectral scaling with  $Z/A$  and the charge distribution of the heavy ions. A staged acceleration scheme between a shock like acceleration and a followed TNSA like acceleration was discussed to explain the spectral characteristics of the gold ion spectra, as e.g., the charge to kinetic energy scaling and the narrow spectral bandwidth.

Furthermore, the experiments revealed an acceleration of heavy material from the target front side. This gave evidence for a shock acceleration of ions from the laser illuminated target side, similar to the model the hole boring process [16]. The acceleration of heavy ions was found to be limited by the target thickness, since for  $\mu\text{m}$  thick Ti foils and similar experimental conditions, no Ti ions were detected. A significant reduction in the heavy ion charge states, particle numbers and kinetic energies was detected when the heavy ions were accelerated from the target front side dependent on the used target thickness. Together with the charge transfer processes demonstrated for double foil targets, this gives an indication that similar processes have to be considered for the heavy ion acceleration.

The laser contrast condition is the second parameter that affects the heavy ion acceleration, since no heavy ions were detected at lower laser contrast. Hence, the influence of a manipulated plasma boundary was investigated for the heavy ion acceleration, with the help of using a short and strong pre-pulse. The pre-pulse lead to a decrease of the maximum detected charge state of the heavy ions and this was found to be proportional the applied negative delay time. This showed a dependency on the heavy ion charge state on the property of the pre-plasma and correlates to an inhibition of the heavy ion acceleration for lower laser contrast conditions. For the pre-heated plasma, a significant enhancement in the ion particle number, regardless of the ion species was detected. Hence, the inclusion of heavy material in the target suggests a method to optimize the acceleration efficiency in terms of particle number if combined with laser pre-pulses.

### **An Energy and Charge Selective Filter for Ions**

Electron capture processes were investigated for a laser accelerated projectile ion beam in solid state dense matter. Ions, accelerated from an ultrathin hydrocarbon foil, passed through a second ultrathin solid density foil, placed at a distance of 500  $\mu\text{m}$ . The efficiency of the electron capture was found to depend on the charge state of the projectile ion and to rise indirect proportional to the ions' velocity. For the highest charge state, particles were detected only at high kinetic energies and in a narrow spectral range. In consequence, a spectral filtering for ions at high charge states resulted. The findings disclose an easy method for a bandwidth limited ion spectrum. Due to the small thickness of the stopping foils used, the loss of the ion energy is negligible, while the electron capture was found to be significant. The method requires further investigations in order to test if a controllability of the spectral bandwidth and energy range can be achieved by a dependency on the target thickness and/or density of the transfer matter.

In the case of a laser and single foil interaction, the main population of accelerated carbon ions was always detected at a lower charge state at high laser contrast as compared to ultrahigh laser contrast. Since this effect is observed for comparable laser and target parameter, the difference has to be attributed to the properties of the pre-plasma between both laser contrast conditions. It was also shown, that pre-heating of the plasma decreases significantly the maximum heavy ion charge state. Here, the question raises, if a pre-expanded or pre-heated plasma causes charge transfer processes during or shortly after the acceleration. In this context, the characteristics in the charge states and spectra from frontside accelerated gold ions, gave indications to underlie a similar mechanism. Inherent charge transfer processes have not been discussed for laser-ion acceleration schemes. The presented results showed, that a validation of these processes is required. The underlying cross-sections in plasma and the deviation from classical theoretical models, are a hot topic of debate [87, 88, 96, 98, 103–105]. The results will be further investigated theoretically in cooperation with D. Casas.

## The Influence of Controlled Laser Pre-pulses on Ion Acceleration

To date, experimental results obtained using different laser systems are difficult to compare, since in addition to the laser energy, pulse duration and target thickness, the laser contrast has a significant influence [1, 64, 84]. Section 6.1 showed how the laser contrast influences the efficiency of the laser-ion acceleration. In order to test the influence of laser pre-pulses on the picosecond time scale, a second counter-propagating laser pulse was applied at different delay times and ultrahigh laser contrast (cf. Section 6.6). Target pre-heating by the second laser pulse at  $I_P \sim 10^{18}$  W/cm<sup>2</sup> revealed the time interval in which this pre-pulse significantly inhibited an efficient ion acceleration. In the sub 5 ps range, the maximum kinetic energies were demonstrated to decline significantly with the applied delay time. The findings can give important information, e.g. for diagnostic purposes, on the laser contrast. Here, the target thickness/density and laser field strength have to be considered as additional parameters.

## The Influence of a Controlled Ion Post-Interaction

The post-interaction of accelerated ions with a second strong laser pulse opens a new and direct way to change the ion spectra. The duration of ion acceleration takes longer than the pulse duration and is determined the vacuum expansion between electrons and ions [32]. The experiments showed that this can be manipulated by a second, strong and counter-propagating laser pulse. The post-interaction with the second laser pulse led to suppression of the particle number of carbon ions. A reduced particle number was detected in the low energetic part of the carbon ion spectrum ( $< 0.5$  MeV/u) for a specific charge state that is dependent on the positive delay time. In consequence, a bandwidth limited spectrum of one charge state resulted. Either by recharging processes, or an inhibition of the ions' post-acceleration, the method operates like a charge selective spectral filter. Further investigations with higher intensities and smaller delay times of the second laser pulse are required in order test if this method could controllable suppress specific kinetic energy ranges.

## 7 Electron Spectrum from Laser Interaction at Ultrathin Foils

All models concerning the ion acceleration and the emission of high energetic radiation from laser-plasma interaction, assume an electron temperature and density for its evolution in time. It has been suggested that the fast electron spectrum, with kinetic energies above 0.1 MeV, can shed light on the involved plasma parameters, such as the hot electron temperature or the ponderomotive potential (cf. Sections 1.3 and 3.2). From the electron spectra one can derive differentiations for the laser-plasma interaction regarding different parameters [13, 17, 56, 106, 107]. The exact mechanism through which the electrons gain kinetic energy from the laser pulse and plasma interaction is an open question [17, 56, 65, 107, 108] and motivated the investigation in this chapter. The experiments attempted to determine, if the fast electrons could be used as a novel diagnostic of the ion acceleration and XUV emission. In this context, the experiments made the first steps towards a characterization of the fast electron spectrum. Additionally, important theoretical hypotheses were tested and revealed new effects.

Section 7.1 gives a summary on the electron dynamics and the emission process of fast electrons in the laser-plasma interaction where the laser is of relativistic intensity and the plasma has an overdense plasma boundary. The section introduces the complex of problems viewed by different models, e.g. the dynamics in the picture of a single electron in an ultrastrong laser field and in the picture of multi-particle dynamics at a plasma boundary, a possible post-acceleration in the transient laser field. The section summarizes briefly how these models have been combined to explain the emission of coherent XUV and fast ions.

Section 7.2 presents the basic spectral characteristics and the quantity of fast electrons that are emitted from the laser interaction with single ultrathin foil targets. Laser contrast dependent features in the electron spectrum were found that correlate to the results for ion and XUV detection in Sections 6.1 and 8.1. The investigation will show that the electrons' spectral distribution and their number are dependent on a variety of experimental parameters.

According to Section 4.3 the laser-plasma interaction with ultrathin foils allows for the possibility of backscattering a second laser pulse from a laser accelerated relativistic electron bunch. The efficiency of such a backscattering process is connected to the electron number of this electron bunch (cf. Equation (4.7)).

Since the number of fast electrons is small [56], new methods are needed to enhance the emission process. In this context, the fundamental questions are: Does the transient laser field further accelerate and decelerate the electrons, and if so how? It was suggested in Ref. [109], that the use of a second separated foil would decouple the transmitted laser light from the electrons and hence inhibit deceleration due to the decay of the laser field. Section 7.3 presents a new effect: an amplification of the electron number,  $N_e$ , by the use of such a two foil target system. Investigation into the underlying physical mechanism of this effect motivated further experimental work, using two laser pulses, to test the role played by pre-ionization. Results of this work are presented in Section 7.4.

## 7.1 Fast Electrons from Laser Plasmas

The kinematics of a single electron interacting with a relativistic laser pulse are, on their own, complex, since the laser introduces oscillations both the parallel and the perpendicular direction of the electrical field (cf. Section 1.2). The description of the collective electron dynamics for a laser pulse interacting with an overdense plasma is directly related to the absorption mechanisms involved [13, 17]. A brief summary was given in Section 2.2, which discussed the inherent plasmon excitation and the dependency on the laser intensity and incidence angle. Modelling the laser-plasma interaction requires the use of a collective electronic motion model to describe the highly complex dynamics of the multi-particle system. In order to reduce the complexity of the problem, simplified models are used: A model similar to the single particle picture to explain, for example, the high harmonic generation in the ROM model (cf. Section 4.2), macroscopic models, such as, e.g. an electron sheath close to the plasma boundary in the RPA and TNSA model (cf. Sections 3.3, 3.2), or such as, electron bunches entering and passing through the plasma, which can lead to high harmonic emission via the CWE model (cf. Section 4.1). A summary and classification of the relevant publications is given in Refs. [17, 106, 107], where various published theoretical models are compared and contrasted. A limited number of experimental publications on this topic exists for the fast electron spectrum from the interaction of intense laser pulses and ultrathin foils [56, 57]. These will be discussed, along with the experimental results obtained here, in the following section.

The oscillations of the electrons with the laser field leads to kinetic energies up to  $E_{os}$ , as given by Equation (1.14), in the direction of the electric field and during the laser cycle. For the relativistic case and for a linear laser polarization, electrons are accelerated by the  $v \times B$  force in direction of the laser propagation and results in a second oscillation with  $2\omega_L$ . During this oscillation they can reach a velocity of up to  $v_D$  (cf. Equation (1.15)) [13]. The superposition of both types of motion lead to a figure 8 like trajectory in the cycle averaged rest frame of the electron (cf. Fig.1.1 in Chapter 1.1). In the ROM model, this or a similar motion is used to derive the collective relativistic electron oscillations at the plasma boundary from which the incident laser light is reflected. Considering

the interaction of an electron of constant velocity or at rest with an ideal laser field in free space, without further given boundary conditions, the electron can not gain a net energy. It comes to rest or to its initial velocity after the interaction (cf. Section 1.2). The underlying fundamentals are described by the principles that are similar to the Woodward Lawson Theorem [108, 110] for focused laser pulses. The Woodward Lawson Theorem has to be violated to cause an acceleration of the electron in a laser field. This becomes possible, for example, by a spatial gradient of the laser intensity or if the interaction takes place at or in a medium or when the electron has a velocity that is not constant due to other external forces (cf. Section 1.3).

When the laser is focused its intensity has a spatial gradient and this introduces the ponderomotive force. Therefore, the electrons can be scattered out of regions with the highest intensity during the interaction with the laser field (cf. Equation (1.17)). This can lead to high kinetic energies of  $\geq E_{os}$  and the electron's trajectory is then determined by the gradient of the laser intensity [107]. According to this equation and the here used laser parameters,  $E_{os}$  lies between 2 MeV and 4 MeV,  $v_D$  to a kinetic energy  $E_D$  of  $\sim 0.8$  MeV. One expects the fast electrons to be accelerated of up to the named kinetic energy, if they could escape from the laser field. In the literature this process is often identified to create the hot/fast electrons that are emitted from the laser-plasma interaction [13, 17, 57, 65, 107] and they are predicted to have a Maxwellian spectral distribution [13, 17, 107]. Even higher kinetic energies can be achieved via the process of vacuum laser acceleration (VLA). This mechanism is predicted to cause under certain boundary conditions a continuous acceleration of the electrons during the laser pulse. They can gain high kinetic energies when they are ejected before the laser field strength decays [107].

In the laser-plasma interaction, the laser field interacts with an opaque plasma boundary and the electrons feel the restoring force to the ions. This gives an even more complex interplay and the interaction is described by macroscopic models [13, 22, 111]. In this context, the laser-plasma absorption models (cf. Section 2.2) are discussed and the dispersion of the laser field in the density gradient of the plasma has to be considered (cf. Section 1.4). The interaction between the laser field and oscillating electrons at the plasma boundary is determined by the incidence angle of the laser [13, 17, 22, 24, 111] and the scale length of the plasma density gradient. Subsequent processes, e.g. resonant excitation of plasmons, take place due to the energy disposal of the laser field in the plasma skin layer,  $l_s$  (cf. Equation (1.21)) [13, 17]. In addition, electron bunches entering the target can be caused by the electrons that are accelerated by the laser field close to the plasma boundary [24, 111]. These processes create electron bunches that pass through the plasma and can decay at specific plasma densities into a coherent and highly energetic radiation (CWE) [5, 24]. Under certain conditions [17], the electrons can be ejected from the laser field and the plasma potential and are then detected at high kinetic energies in the range of  $\geq E_{os}$  [13, 17, 56].

At the same time, all these processes find some quantity of electrons bound

to plasma boundary by the restoring force to the ions. For ultrathin foil targets with the laser normally incident, both the figure 8 trajectories and the restoring force of the ions are thought to cause ejected electrons to recirculate, periodically returning to the target boundaries [17, 112, 113]. This and similar models create a strong electrostatic potential at the target boundaries and is used in the ion acceleration models [17, 23]<sup>1</sup>. These electrons are considered to co-propagate with the ions during and after the laser pulse interaction [1, 69, 92]. For a 10 MeV/u ion this corresponds to an electron with a kinetic energy of  $\sim 5$  keV, which is out of the detection range of the commonly used spectrometers.

Hence, only electrons capable of escaping the potential well at the plasma boundary represent the detectable electron distribution in this work. Furthermore, the post-acceleration of ejected electrons in the transmitted laser field has to be considered since ultrathin targets are partly transparent (cf. Section 6.4) [109]. In experiments presented here, electrons were detected in an energy range from 200 keV to 30 MeV.

## 7.2 Characterisation of the Fast Electron Spectrum

All experiments were performed with the setup described in Chapter 5.3 and the detection methods according Section 5.6.2. The experiments were restricted to the case of the laser at normal incidence angle on the target and detected the electrons in the laser propagation direction. The fast electrons' spectral distribution and their number exhibited interdependencies on different parameters. This is presented in the following with the help of typical examples. If not otherwise stated, in a direct comparison, the measurement always refers to the same experimental run. In total observation were obtained from 37 experimental runs with more than 133 measurements using single foil targets where the setup of the spectrometer was changed to access different parts of the spectral range. Only the fundamental features of the spectra are discussed. The electron spectra are presented in an energy binning that corresponds to the accuracy of the spectrometer (cf. Section 5.6.2).

### 7.2.1 Electron Spectrum and Laser Contrast

The laser contrast determines the properties of the pre-plasma and of the plasma boundary. The plasma boundary and in particular the scale length of the plasma density gradient, is a key parameter for the laser driven electron dynamics and introduces significant difference in all subsequent processes. This has been found in PIC simulations when a certain scale length of the plasma density was introduced into the simulations [17, 22, 24, 107]. In an indirect way, the impact of the pre-plasma condition was studied in experiments from solid state targets with using different laser contrast conditions [63, 68] or very recently with applying

<sup>1</sup>In the TNSA model, the electron sheath direction is normal to the target, regardless of the laser incidence angle.

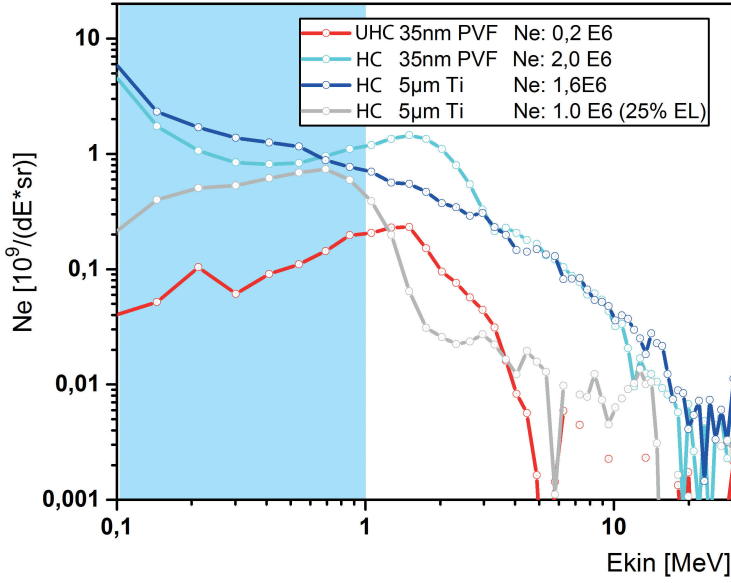


**Figure 7.1:** The Spectra of fast electrons emitted in the laser propagation direction for different laser contrast and target conditions. Blue shaded area indicates energy range for which the detector screen is not calibrated. The measurements from a  $(35 \pm 2)$  nm PVF foil are shown for UHC (red) with  $E_L = 1.6$  J, for HC (light blue) condition with  $E_L = 2.0$  J, and for a  $5 \mu\text{m}$  Ti foil and HC condition with either  $E_L = 2.0$  J (dark blue) or  $E_L = 0.6$  J (grey). Total electron numbers  $N_e$  are given for the full detection range (0.1 – 20 MeV). All measurements were taken at the same position of the focal plane on the target.

a weak pre-pulse ( $10^{14}$  W/cm<sup>2</sup>) [65]. These experiments demonstrated, that the efficiency of the coherent XUV radiation and is highly dependent on the scale length on the plasma gradient in a range of  $L(\nabla n_e) < \lambda_L/2$ . This will be further investigated in Section 8.1. In Section 6.1 and Ref. [64] it was already shown that the laser contrast and hence the pre-plasma condition determines the efficiency of the ion acceleration. Hence, the laser driven electron dynamics at the plasma boundary are highly sensitive to the pre-plasma and change the efficiency of simultaneously occurring processes. How pre-plasma and hence an induced difference in the electron dynamics at the plasma boundary affect the fast electron emission in particular is not fully explained yet and a topic of the latest publications [17, 65].

In Fig. 7.1, the spectrometer<sup>2</sup> detected electrons within a kinetic energy range of 0.1–30 MeV in a capturing half angle of  $1^\circ$  on the laser propagation axis. The laser illuminated either a thick  $5 \mu\text{m}$  Ti or a 35 nm PVF foil with a laser field strength of  $a_0 \sim 5.5, 6.5$  at ultrahigh (UHC) and high (HC) laser contrast condition, respectively. For the full detection range the integrated number of electrons is about  $N_e = 1.6 \times 10^6$  for the Ti and  $N_e = 2.1 \times 10^6$  for the PVF target with the laser at HC condition.

<sup>2</sup> configuration II

The total electron number scales with the laser energy: A measurement where  $E_L$  was reduced to approximately 25%, led to a  $\sim 60\%$  smaller value for  $N_e$  from the PVF target in Fig. 7.1. Note, that although no calibration for the scintillation screen exists for an energy range below 1 MeV, the experiments did not observe any significant indication of a decreased detection efficiency down to 0.2 MeV<sup>3</sup>.

For the UHC condition and the PVF target, the integrated electron number is about  $N_e = 0.2 \times 10^6$ , which is one order of magnitude smaller than the number obtained from the HC condition. This discrepancy was observed in all experimental runs. The difference in the laser energy between both laser contrast conditions was approximately about 20% (cf. Section 5.2.2) and hence, the scaling of  $N_e$  with  $E_L$  from above can not explain this high discrepancy in  $N_e$ . The findings show a significant difference in the number of emitted electrons for different laser contrast conditions, which can be interpreted in a similar manner to the corresponding results of the ion acceleration in Section 6.1: The higher laser contrast enables a steeper rise of the plasma density that significantly changes the emission process of fast electrons and enables a more efficient ion acceleration for the foil thickness below 200 nm. The significantly smaller number of fast electrons state a restricted ejection from the steeper plasma boundary, which correlates to an enhancement of the electron to ion acceleration and to a smaller transmission of the laser through the target (see Section 6.1). In contrast to the total electron number, the spectral characteristics, e.g.  $f(E_{kin})^{max}$ , were similar for both laser contrast conditions. This interesting result shows that in spite of the differences in the pre-plasma induced by the different contrast conditions there is little difference in the emitted spectral distribution.

### 7.2.2 Interdependencies of the Spectral Distribution

The spectral distribution of the fast electrons,  $f(E_{kin})$ , and in particular the position of the global maximum is expected to give indirect information about the laser-plasma interaction and the kinetic energy gain of the electrons in the laser field [56, 65, 107].

#### Dependency on the Laser Energy

In the example shown in Fig. 7.1, the Ti target and the laser at HC condition delivered a broad spectral distribution, while a distinct peak  $f(E_{kin})^{max}$  appeared at 1.7 MeV with a bandwidth FWHM of  $\Delta E/E \geq 1$  for both laser contrast conditions when using the much thinner PVF target.  $f(E_{kin})^{max}$  lies between the theoretical calculated  $E_{Drift}$  in accordance with Equation (1.15) and the ponderomotive electron ejection with  $E_{os}$  of Equation (1.14). In Ref. [56] similar peaks were observed for a comparable experimental setup using different laser systems and various target thicknesses. They could not conclude definitely that  $f(E_{kin})^{max}$  corresponds to the ponderomotive potential.

<sup>3</sup>The calibration is pending, peaks at 0.3 MeV appeared when using the Kodak LanexFast screen, which can be seen in Fig. 7.7 and Fig. 7.8, while the total electron numbers  $N_e$  achieve a similar number obtained at other measurements.

In Fig. 7.1, for HC contrast condition  $f(E_{kin})^{max}$  and  $N_e$  scaled with the applied laser energy (grey line). When the laser energy was reduced to 25% for the Ti target a spectral peak was detected at a kinetic energy of 0.8 MeV, corresponding to  $\sim 50\%$  of the kinetic energy obtained at full laser energy from the PVF target. Theoretically,  $E_{os}$  scales with  $\sqrt{E_L}$ , which would be in agreement with this example. A similar scaling can be seen in the spectra obtained at different laser contrast conditions, which differed in  $E_L$  by about 20% in Fig. 7.1. But, in the experimental runs the electron spectrum was strongly influenced by additional parameters, which hindered a simple interpretation of the results as being attributable to the ponderomotive potential. These were:

- A dependency of  $N_e$  and the spectral distribution on small deviations of the focal plane's position on the target, such as, e.g., the peak position, the high energy tail and additional modulations in the spectrum.
- The spectral distribution is influenced by the target thickness or an interdependency between the target thickness and the laser parameters
- No spatial dependency of the electron spectrum
- An indication that  $f(E_{kin})^{max}$  was influenced by the hole diameter of the target holder construction

An overview for the dependency of  $N_e$  on  $E_L$  and on the target thickness is depicted in Fig. 7.2 a) and refers to different experimental runs. The integrated electron number is depicted for measurements within a displacement of the laser's focal plane on the target of about  $\pm 10 \mu\text{m}$  for different foil thicknesses. Obviously,  $N_e$  differs for the same laser energy and hence, further parametric dependencies have to be considered.

### Dependency on the Displacement of the Focal Plane

Fig. 7.2 b) shows the electron spectra for the HC condition and for some small displacements of the focal plane on a 38 nm PVF target. These electron spectra were measured with spectrometer configuration III (cf. Section 5.6.2) and for a laser field strength of  $a_0 = 6$ , at maximum. A displacement of  $\pm 20 \mu\text{m}$  decreases  $I_L$  by about  $< 20\%$ , due to the divergence of the laser beam. According to Equation (1.3), this should affect the ponderomotive potential and thus, the position of  $f(E_{kin})^{max}$ . In Fig. 7.2 b), a shift of  $f(E_{kin})^{max}$  with the displacement of the focal plane can be observed. The value of this displacement was not consistent across different experimental runs (shown in the Appendix Section A.2). This can be attributed to small variations of the spatial intensity distribution in the focal volume, or other small fluctuations to which the electron spectra is sensitive. Similar assumptions were made in Ref. [56]. With respect to different positions of the focal plane in a range of  $\pm 20 \mu\text{m}$  in Fig. 7.2 b), the electron spectra exhibit a difference in  $N_e$  of up to 30%. In light of this observation, a quantitative description for the scaling of  $f(E_{kin})^{max}$  and  $N_e$  with  $I_L$  can not be extracted

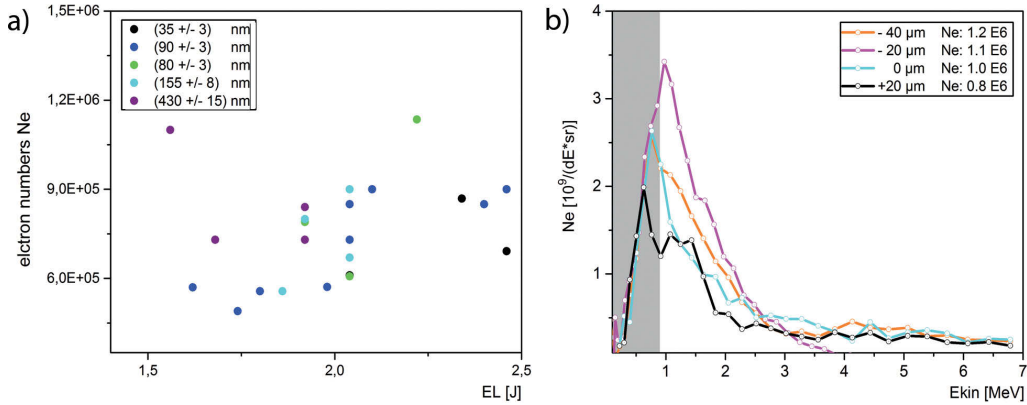


**Figure 7.2:** a): Integrated  $N_e$  from the single foil configuration for various PVF foil thicknesses and different laser energies. The data points are taken from different experimental runs, using the HC condition, the foils were free standing over a hole diameter of 0.6 mm. All measurements used the spectrometer configuration III at a detection range 0.2–7.5 MeV and the accuracy of the laser focus on the target was considered to be within  $\pm 10 \mu m$ . b): The electron spectra for different positions of the laser’s focal plane on a  $(38 \pm 2)$  nm PVF foil, at the HC condition. Corresponding images of the detector are shown in the Appendix Section A.2 in Fig. A.6. Note, the scaling of the y-axis was chosen to be linear.

from the 37 experimental runs (each run compared at least 2 different positions of the focal plane). Nevertheless, considering just one experimental run, the same focal position on the target and the same laser energy, a deviation of  $f(E_{kin})^{max}$  of up to  $\pm 0.2$  MeV was observed (cf. Section A.2) and  $N_e$  was reproducible to within 10%. In the following, and for previous sections if not explicitly stated otherwise, a direct comparison is only given for one experimental run and for the same displacement position of the focal plane on the target.

### Dependency on the Target Thickness

For thicker target foils ( $\geq 400$  nm) the spectral distribution of fast electrons showed different features. Either the spectrum was broadened or a redistribution of electrons kinetic energies was observed. This can be seen in Fig. 7.1 for a  $5 \mu m$  Ti foil and is shown in Fig. 7.8 for a 430 nm PVF foil. Thicker target foils introduced a shift of  $f(E_{kin})^{max}$  to a significantly lower energy range. This observation is based on 4 experimental runs with 8 measurements using the Ti foil and 5 measurements for the 430 nm PVF foil.

The only experimental report so far of a spectral redistribution in  $f(E_{kin})^{max}$  was for the case when the target thickness entered the electron blown out regime in Ref. [56]. In this case, a high laser transmission through the target is achieved, enabling an additional acceleration of ejected electrons, which introduces a high energy peak in the electron spectra. In Ref. [56] no shift of  $f(E_{kin})^{max}$  to a lower kinetic energy was observed for DLC foils with a thickness of up to  $15 \mu m$ . This difference remains an open question.

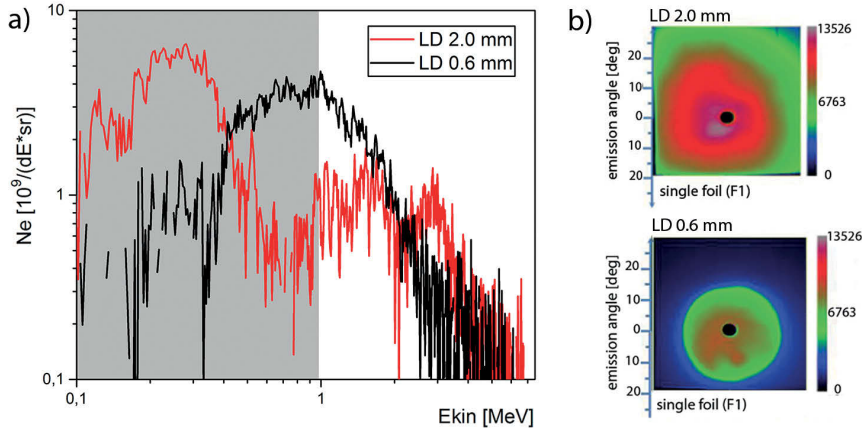


**Figure 7.3:** a:) The electron spectra for different hole diameters ( $LD$ ) of the target support plate for the HC condition. The measurement is taken from different experimental runs, but at comparable parameters, as e.g. laser energy, target thickness (PVF ( $95 \pm 5$ ) nm), position of focal plane. The integrated electron number is for a target hole diameter of 2.0 mm about  $N_e = 1.2 \times 10^6$  and for an diameter of 0.6 mm about  $N_e = 0.9 \times 10^6$ . Note, that the spectra are given in the raw energy binning. b:) The IP measurement measured the dose of the electron beam for two different target hole diameters and comparable PVF foils ( $85 \pm 3$  nm).  $N_e = 0.7 \times 10^9$  for the case of a 0.6 mm and  $N_e = 1.3 \times 10^9$  for the 2.0 mm hole diameter. A hole was introduced in the middle of the IP, to enable simultaneous measurement with the magnetic spectrometer.

For a foil thickness range of  $\leq 500$  nm, see Fig. 7.2 b), a small increase of  $N_e$  with the target thickness was observed. However, in the comparison between a 35 nm PVF and a 5  $\mu$ m Ti target in Fig. 7.1, a simple proportionality relationship between  $N_e$  and the target thickness was not seen, pointing to co-parametric dependency such as, e.g. laser intensity and target thickness. At the UHC condition and with a foil thickness range close to that required to be in the optimized RPA regime, the experiments did not find correlations in the electron spectra to an increase of the ion kinetic energies for smaller foil thicknesses (cf. Section 6.2). This result is in agreement with Ref. [56] and is shown for PVF foils in the optimized thickness range for the ion acceleration (cf. Section 6.2) in Appendix Section A.2 in a comparison to previous measurements using the MBI laser system as it was in the year 2010 [56].

### Dependency on the Diameter of Freestanding Foils

An unexpected influence of the spectral distribution due to the target holder diameter was observed. The electron spectra obtained from two different target hole diameters (0.6 mm and 2 mm) are shown in Fig. 7.3 and exhibit a significant difference in the position of  $f(E_{kin})^{max}$ . For a laser focal diameter of  $< 5$   $\mu$ m, one usually assumes that there is no influence from a charge transfer with the target holder. For either small variations of  $E_L$ , small displacements of the focal plane ( $\leq 40$   $\mu$ m) or for different target thicknesses ( $\leq 200$  nm),  $f(E_{kin})^{max}$  was always

detected at a kinetic energy above 0.7 MeV when a target holder with 0.6 mm diameter holes was used. This can be seen in various examples provided in this chapter or the additional material in the Appendix in Section A.2. In contrast, when using hole diameters of 2.0 mm and otherwise comparable parameters ( $E_L$ , the position of focal plane, the target thickness, the laser contrast) in all of the 5 experimental runs (22 measurements in total),  $f(E_{kin})^{max}$  was always observed to be shifted down in energy by a significant amount, into the kinetic energy range from 0.1 MeV to 0.4 MeV, while no decrease in  $N_e$  was seen. This is shown in Fig. 7.3 for two different measurements from a laser interaction with  $a_0 \sim 6$  and an ultrathin PVF foil. Both measurements are taken at the same position of the focal plane in different experimental runs.

With an alternative measurement method, the electron number and the electrons' divergence was measured using IP<sup>4</sup> (cf. Section 5.6.2). The IP plates accumulated the electron dose according to Ref. [81, 82] for kinetic energies above 0.4 MeV<sup>5</sup> in the direction of the laser propagation. Fig. 7.3 b) compares two measurements for comparable PVF foils and target hole diameters of either 0.6 mm or 2.0 mm. The measurements refer to two different experimental runs, with comparable laser energy (2.0 J). On the IP a homogeneous dose distribution can be seen, but the beam profile diameter significantly differs for each hole diameter. In the case of the smaller hole diameter, the electron beam profile is confined by a sharp aperture due to the target holder construction<sup>6</sup>. The integrated particle number is about  $N_e = 7 \times 10^8$  for a diameter of 0.6 mm and about  $N_e = 1.3 \times 10^9$  for the 2.0 mm one, with an error of 15%. The obtained value is in fair agreement with the one obtained from the magnetic spectrometer when its capturing angle is taken into account.

An unexpected influence of the target hole diameter on the fast electron kinetic energies and the electron divergence was observed. The experiments performed so far have been unable to determine the underlying physics of this effect and further investigation is needed in order to understand the peak in the electron spectrum. It is important to note that, due to restrictions in foil manufacture, it is common to use target holders with even smaller hole diameters [56], and usually no mention is made of this parameter.

### 7.2.3 Discussion of the Fast Electron Spectrum

In Ref. [56] electron spectra from different laser systems and from ultrathin foils were compared and significant differences were found, which could not be attributed to a specific experimental parameter. The experiments presented here

<sup>4</sup>Experiments were performed by M. Schnuerer and D. Sommer

<sup>5</sup>Calculated with NIST database *estab* [101]: In order to reach the IP, electrons had to pass a 30  $\mu\text{m}$  Al foil and a 1 mm plastic acryl plate. This is possible for electrons with kinetic energies above 0.3 MeV. To account for the particle number, the detection efficiency of the IP plate was assumed to be independent of the particles energy, in accordance to Ref. [81, 82].

<sup>6</sup>The measurement used a target holder consisting of two steel hole-plates with a width of 0.5 mm each. The foils were placed at the front of the first plate, hence electrons emitted from there had to pass through a tunnel of 1.0 mm.

made progress towards the classification of the parametric dependencies of the electron spectra, but further investigation and theoretical discussion is needed to explain some ambiguities in the results and to extract the emission process.

The electron spectrum is affected by various parameters. The effects are seen either in  $N_e$  or  $f(E_{kin})$ . In order of importance: the laser energy and the laser contrast; the influence of the laser intensity due to small displacements of the focal plane on the target; the target thickness; and the influence of the target holder.

A scaling of  $N_e$  and  $f(E_{kin})^{max}$  with the laser energy was shown for otherwise fixed parameters, which in a rough approximation is  $\propto \sqrt{E_L}$  and hence, similar to the scaling from the ponderomotive potential and the electrons' quiver velocity. However, this interpretation can not be definitely concluded upon, since the spectral distribution seems to be manipulated by the target hole diameter. This observation was an unexpected result, which needs further investigation, since it hinders interpretation of the emission process and the construction of the theoretical models. In addition, the emission by the ponderomotive force predicts a change in the particle number and kinetic energy dependent on the detection angle, since the force is related to the spatial gradient of the laser intensity. In agreement with the investigation in [56], no spatial dependency of the fast electron spectral distribution was found (cf. Fig. 7.3 and in the following). This stands in contrast to the electron spectra obtained in the specular direction with an oblique laser incidence angle in Ref. [65, 107] and shows that there is a difference in the underlying mechanism. Furthermore, in Ref. [107], a peaked spectral distribution was seen for fast electrons that were detected in the laser reflection direction, where the laser was at an oblique angle of incidence to solid state targets. In that work, a much higher kinetic energy, with respect the laser parameter used, was obtained for  $f(E_{kin})^{max}$  than the ones here and in Ref. [56]. It was attributed to the VLA process (cf. Section 7.1) and exhibited a distinct spatial dependence. Hence, the VLA process can not explain the spectral distribution obtained here.

A clear dependence of  $N_e$  on the laser contrast was found, with significantly less fast electrons emitted for the ultrahigh laser contrast condition. In contrast, no significant dependence of the fast electron spectral distribution on the laser contrast was seen. Since the laser transmission through the target is different for both contrast conditions (cf. Section 6.4), it was expected to find an affect on the kinetic energies of the electrons [17, 56, 65, 109]. In consideration of the fundamental processes of the electron acceleration from dense laser-plasmas in the laser propagation direction, an interesting observation was made: The difference in the plasma properties induced by the laser contrast restricts the ejection of fast electrons but provide a similar gain for the kinetic energies. This finding can not be explained by the single particle picture and has to be discussed using macroscopic laser-plasma models. In Ref. [65] an enhancement of the number of fast electrons was just recently reported for the case of a longer rise of the plasma density. The experiments detected electrons in the specular direction with an oblique incidence angle on a thick solid state target. A longer scale length of the plasma density gradient was introduced with the help of a low intensity pre-pulse.

The effect was confirmed in PIC simulations, and although a similar method was applied to increase the electron number in Ref. [107], the underlying mechanism is yet not fully derived. Summarizing Ref. [17, 65] briefly, the emission of fast electrons from the laser field and the plasma potential is considered to occur in the skin depth,  $l_s$  (cf. Sections 1.4, 2.2 and 6.4), at the plasma boundary, in an interplay between the laser field and the potential coming from the restoring force of the ions. In the PIC simulations in Ref. [17] this interplay induces anharmonic plasmon excitations in the skin layer of the plasma, which leads, among other things, to the ejection of electrons. The efficiency of the ejection is found to be highly dependent to the length of the plasma density gradient, since it can fulfil resonance conditions between the laser field and the plasma frequency. Both publications refer to an oblique incidence angle and this situation is difficult to transfer to the case discussed here, since the laser field is parallel to the plasma boundary (in Section 2.2). More work is needed to develop an analytical model that can explain this process in detail and that can be applied to the case of a laser interaction at thin foils and electron emission in the laser propagation direction.

The investigation further showed that the electrons' spectral distribution changes little over a large range of the target thicknesses. A change to lower kinetic energies only set in for significantly thicker targets ( $D > 10 \times l_s$ ). This indicates, at first glance, a connection between the gain of kinetic energy and the laser transmission through the target (cf. Section 6.1), but contradicts the following results: Firstly, no differences in the electron spectra, corresponding to changes in the position of the spectral peak, appeared if the optimum regime for the RPA-like ion acceleration is entered in agreement to Ref. [56]. Secondly, in spite of the change in the total electron number, comparable spectral characteristics resulted for the lower contrast condition and therefore for the case of a pre-heated target that enabled a higher laser transmission. Whether energy loss processes in the plasma need to be considered for thicker targets and if a strong transient laser field induces a higher probability of ejecting the electrons at high kinetic energies remain topics for further investigation.

### 7.3 An Amplified Electron Spectrum

Recent theoretical publications [109, 114] suggested the use of a target system consisting of two ultrathin foils (F1 and F2) separated by a distance of  $w$ . This method was predicted to enhance the amount of emitted fast electrons in the following way: A single electron interacting with an ideal laser pulse comes to rest or its initial velocity after the decay of the pulse envelope (cf. Section 1.2). It does not gain energy from the interaction, unless additional conditions such as, e.g., a spatial gradient of the laser pulse intensity, are fulfilled. For a two foil target system, consisting of ultrathin foils, and small values of  $w$ , the transmitted laser light is strong enough to ionize the second foil. If, due to this ionization, the electron density reaches  $n_e(\text{F2}) > n_c$  during the laser pulse duration, the second foil is opaque for the laser light (cf. Section 1.4), while the target remains transparent

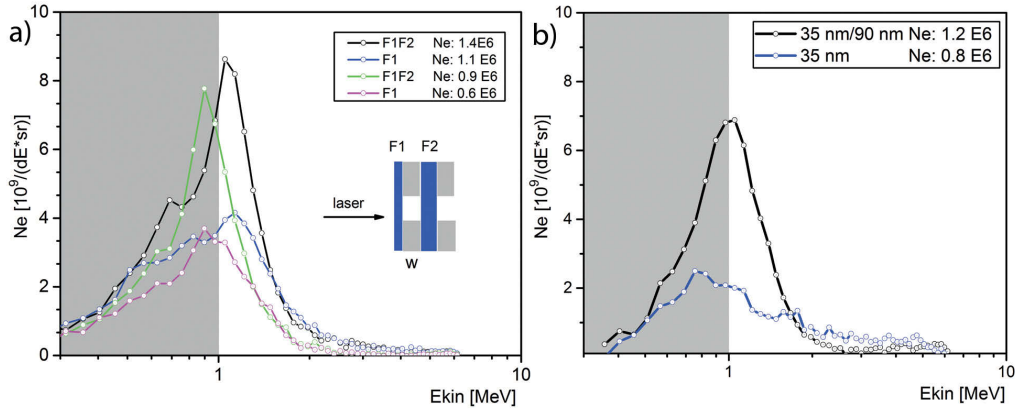


**Figure 7.4:** Comparison of electron spectra detected for single and two foil configurations. The grey shaded area indicates the uncalibrated, with respect to  $N_e$ , part of the spectral range of the detector screen. a): For comparable foil thickness and two different values of  $E_L$ : F1 and F2 a  $(95 \pm 5)$  nm PVF foil. The black and blue curve corresponds to  $E_L = 1.8$  J, the green and pink curve to  $E_L = 1.4$  J. The two foil experimental setup is illustrated in the insert. b): Electron spectra from the double foil configuration with the first foil of  $(35 \pm 2)$  nm and a second foil of  $(90 \pm 3)$  nm, with  $E_L = 1.7$  J.

to fast electrons. This can cause the electrons to become decoupled from the transmitted laser field that would otherwise decelerate the electrons when the field envelope declines [108]. These conditions could be fulfilled for those electrons that leave the first foil with a kinetic energy of a few MeV, which are then overtaken by transmitted laser pulse and reach the second foil before the end of the laser pulse. This would allow electrons to escape the decaying laser field envelope and therefore keep the energy gained from the field. From simple kinematic consideration, with the foil separation used here and no further acceleration of the electrons, only electrons from the early laser cycles reach the second foil while the transmitted light pulse is still there. The laser transmission values obtained in Chapter 6.4 for the laser at the HC condition, reached of up to 8%, enabling an intensity of  $\sim 10^{16}$  W/cm<sup>2</sup> on a second foil at a distance of  $w = 500 \mu\text{m}$  from the first foil. This is high enough to efficiently ionize it. The two foil target configuration used is depicted in Fig. 6.11 and Fig. 7.4. In the experiments, electrons were detected using the spectrometer configuration III and an applied laser field strength of  $a_0 \sim 6$  at HC condition.

Comparison of electron spectra measured for the single foil (F1) and the two foil (F1F2) configurations shows an amplification of the electron number,  $A(N_e)$ , with the addition of the second foil. Certain general patterns were observed in the comparison between single and double foil measurements over the 22 experimental runs and in total 167 measurements. The double foil target configuration always led to a similar change in the spectral distribution and the integrated electron number,  $N_e$ , was higher in 80% of the cases and as high in the rest. In the detection range of  $(0.1 - 7.5)$  MeV,  $A(N_e)$  reached up to a factor of  $\sim 1.5$ . Two basic examples are presented in Fig. 7.4. It can be seen that both single and

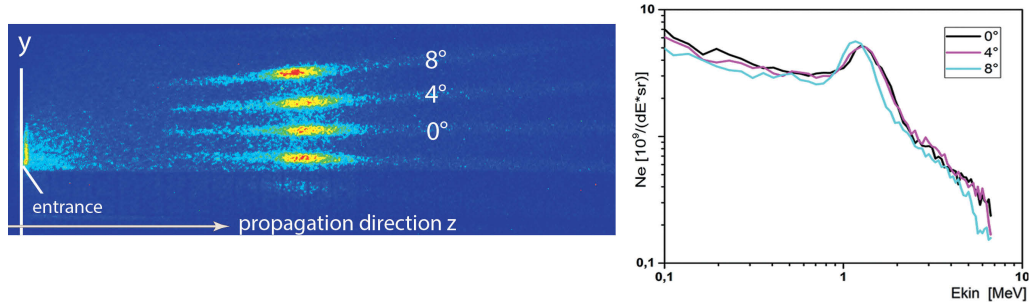


**Figure 7.5:** Raw image of the detector screen of the electron spectrometer with the multi-pinhole setup. The deflection in the  $y$  direction is in agreement with the emission angle from the target. Corresponding evaluated spectra for traces are shown for  $0^\circ$ ,  $+4^\circ$  and  $+8^\circ$ . Note, no subtraction of the background signal was performed, leading to the high signal in the low energetic part of the spectra.

double foil spectra show qualitatively similar distributions, however, a significant enhancement is seen in the vicinity of the peak structure with the addition of the second foil.  $A_{N_e}$  in respect to the full detection range reaches a factor of 1.3 for both foils at a thickness of  $\sim 100$  nm. The amplified spectral distribution exhibits a FWHM  $\Delta E/E = 0.4$  at  $f(E_{kin})^{max} = 1.1$  MeV, which in the case of the single foil configuration is about  $f(E_{kin})^{max} = 1.1$  MeV with a FWHM  $\Delta E/E = 1.2$ . Note, that the scale of the  $y$ -axis in Fig. 7.4 was chosen to be linear in order to reveal the details.  $A_{N_e}$  was about a factor of 1.5, when using a 35 nm plastic foil for F1 and a 90 nm for F2, as shown in Fig. 7.4 b). In conclusion, a separated second foil, placed at a distance of 500  $\mu\text{m}$ , remarkably enhanced the number of electrons in a small spectral range.

### 7.3.1 Momentum dependent Focusing

To exclude strong magnetic lensing in the electron beam due to fringe fields from the spectrometer magnet (cf. Section 5.8) or the target holder, or even from the interaction of the electron with the second foil, a multi-pinhole was introduced into the setup. A raw image of the electron detector screen and the corresponding evaluated spectra is shown for the two foil configuration in Fig. 7.5. The pinholes collected particles at  $0^\circ$ ,  $4^\circ$  and  $8^\circ$  half angles from the target normal. The detection angle from the target was well reproduced by the deflection of each trace. The integrated electron signal showed, for each detection angle, an amplification of  $N_e$  with the addition of the second foil, comparable in amount, spectral range and deflection direction. The detected enhancement of the electron numbers is spectrally comparable for all detection angles and hence, did not indicate a momentum dependent focusing due to spatial gradients of magnetic fields, nor a spatial dependency of the electron spectrum <sup>7</sup>.

<sup>7</sup>This is also valid for the electron spectra obtained from a single foil, which was tested in the same configuration, but is not shown here.

### 7.3.2 Areal Dose and Divergence of the Electron Beam

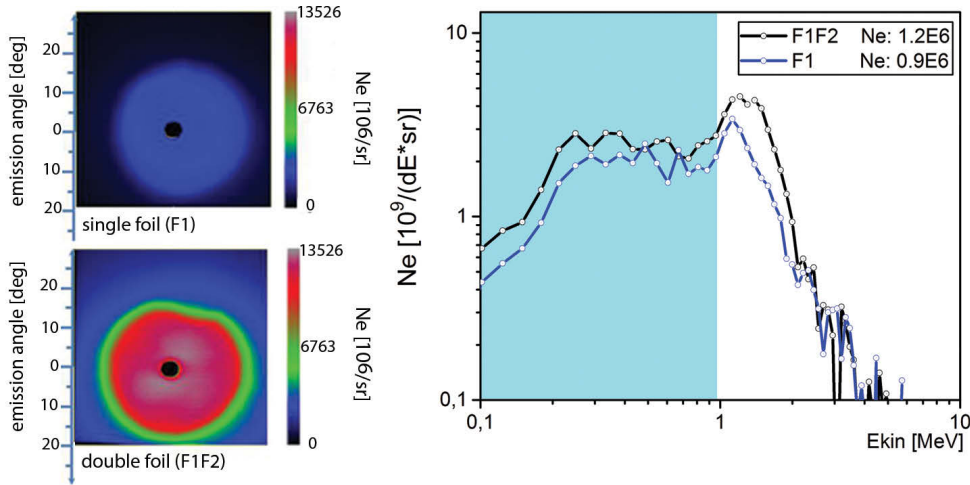


**Figure 7.6:** The raw image of the IP plate after being exposed to electrons from laser interaction with a target hole diameter of 0.6 mm for the single and two foil target configurations. Both PVF foils had a thickness of  $(87 \pm 4)$  nm. The corresponding spectral distribution from the magnetic spectrometer is shown. The light blue shaded area indicates the uncalibrated spectral range of the detector screen.

The double foil configuration was investigated with the IP measurement method. This method was introduced in the previous section and described in (cf. Section 5.6.2). A hole in the IP, 6 mm in diameter, on the laser propagation axis enabled a concurrent measurement with the magnetic spectrometer in configuration III. The following results are based on 4 experimental runs and in total 10 measurements and aimed to test the electron enhancement effect as a matter of principle. The results for a single and double foil target are compared in Fig. 7.6. The laser was applied at an field strength of  $a_0 = 6.5$  (2 J on target, HC), the target hole diameter was about 0.6 mm and both foil thickness were 87 nm. From the single foil measurement the IP detected an integrated dose of  $N_e = 0.6 \times 10^9$ <sup>8</sup>. The number is within 30% in agreement with the corresponding results obtained from the magnetic spectrometer with respect to its capturing angle. In the presence of the second foil, small inhomogeneities appeared in the electron profile and the integrated signal reached a significantly higher dose of about  $N_e = 1.7 \times 10^9$ . In comparison to the single foil, an amplification of about  $A(N_e) > 2.5$  was obtained, while the concurrent measurement of the magnetic spectrometer detected a much smaller value of about  $A(N_e) = 1.3$ . Although up to here, a comparison between the detection efficiencies of both methods is unknown and requires further investigation, the IP measurement confirmed an amplification in dose for a two foil target configuration.

In the previous section, the confinement of the electron beam for this size of hole diameter was found. To exclude beam focusing effects, e.g. by strong fields

<sup>8</sup>The error of the measurement is assumed to be 15%.

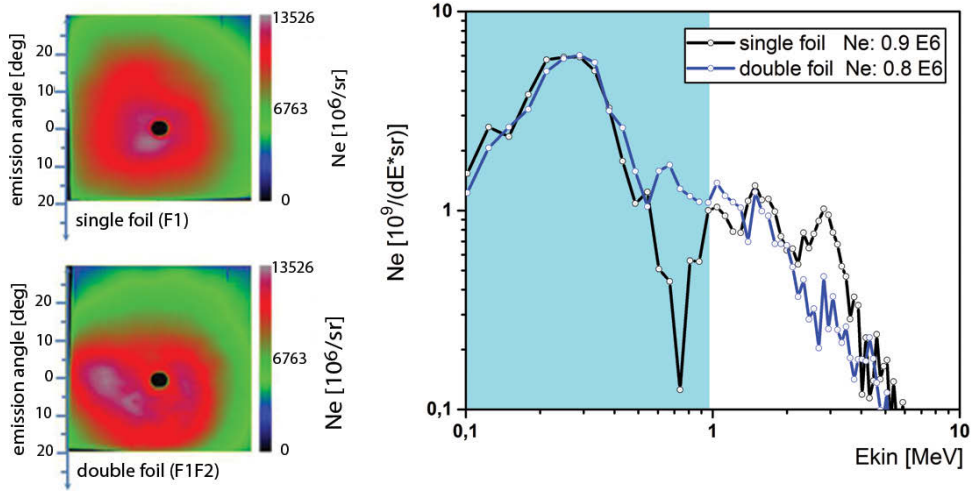


**Figure 7.7:** The raw image of the IP plate after being exposed to electrons from laser interaction with a target hole diameter of 2.0 mm for the single and two foil target configurations. Both PVF foils had a thickness of  $(84 \pm 4)$  nm. The corresponding spectral distribution from the magnetic spectrometer is shown. The light blue shaded area indicates the uncalibrated spectral range of the detector screen.

on the hole boundary, the experiment was repeated using a target holder with holes 2.0 mm in diameter. The measurement (at HC condition,  $E_L = 2$  J and two 84 nm PVF foils) is shown in Fig. 7.7. The integrated signal from the IP delivered a smaller amplification of  $A(N_e) = 1.6$  with the addition of the second foil. The difference in the spectral distribution in comparison to Fig. 7.6, was already discussed in the previous section and caused by the holder's diameter. No amplification was detected from the concurrent spectrum recorded by the magnetic spectrometer for this measurement. A closer look at the spatial profile and the region where the magnetic spectrometers was located indicates that the spatially inhomogeneous distribution might have lead to this result.

### 7.3.3 Target Thickness and Spectral Distribution

It was shown in the previous section that the addition of a second foil enhances the number of electrons detected in a spectral region around the maximum,  $f(E_{kin})^{max}$ , of the spectral distribution obtained from a single foil. The question that naturally arises is, does the spectral distribution from the first foil determine the spectral the double foil spectral distribution? In the previous section, e.g. Fig. 7.1, the spectral distribution of emitted electrons changed with the use of thicker target foils. This can be seen Fig. 7.8, where a remarkable change of  $f(E_{kin})^{max}$  towards the low energy range is seen, for the electrons detected from a PVF foil thickness of 430 nm. The applied laser field strength was about  $a_0 = 6.5$ . The distribution maximum is seen at 0.3 MeV from the 430 nm foil, and at 1.7 MeV for the 90 nm foil in the same experimental run. The integrated

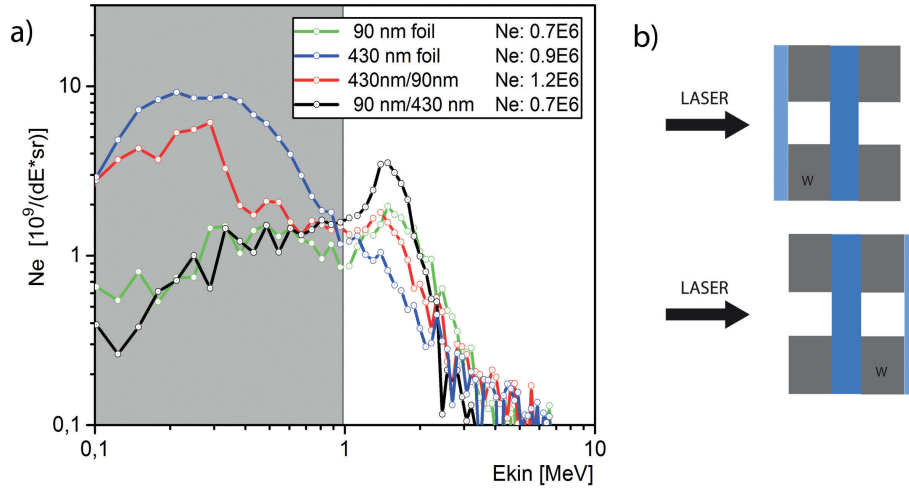


**Figure 7.8:** a) Electron spectra detected for the single and two foil configurations with PVF foil thicknesses of  $F1 = (90 \pm 3)$  nm and  $F2 = (430 \pm 20)$  nm using a target hole diameter of 0.6 mm. The foil order in the two foil setup was reversed by turning the target. The difference this introduces in terms of the target holder construction is schematically illustrated in b). The grey shaded area indicates with respect to  $N_e$  the uncalibrated, with respect to  $N_e$ , spectral range of the detector screen.

electron number is higher for the thicker foil:  $N_e = 0.7 \times 10^7$  for the single foil and  $N_e = 1.2 \times 10^7$  from the double foil. The direct comparison between the two foil arrangements was enabled by turning the target and is shown in Fig. 7.8 b).

In the double foil measurement with the arrangement,  $D(F1) = 90$  nm and  $D(F2) = 430$  nm, in Fig. 7.8 the spectral maximum of the corresponding single foil measurement is strongly enhanced, while the particle number of high energy electrons above 2 MeV declines. The same number of electrons was obtained as from the single foil configuration, but with a difference in the spectral distribution. For reversed arrangement, a strong enhancement of the distribution maximum at 0.3 MeV is detected, while particle numbers above 0.9 MeV decline. In comparison to the number obtained from the single foil configuration, the relative increase is about  $A_{N_e} = 1.3$ .

In both cases with the second foil, more electrons are detected in the spectral range that corresponds to the spectral maximum of the electron distribution from the first foil. When the electrons passed through the thicker second foil,  $A_{N_e}$  is smaller compared to the case of passing through a thinner second foil. These observations are based on in total 11 measurements and at least each combination was measured two times. It has to be mentioned, that turning the target changes the travelling length through the target holder from 1 mm to 0.5 mm for the electrons that originated from the first foil. In the last section, the electron beam was found to be spectrally shifted by the target hole diameter. Hence, it was tested, if different the target holder arrangement lead to the spectral redistribution observed here. This was done in additional experiments and no difference in the electron spectra with turning the target was found. Corresponding measurements

are shown in Appendix Section [A.2](#) and [A.2](#).

### 7.3.4 Discussion of the Electron Amplification

A target configuration consisting of two separated foils revealed a new effect: An enhancement in the quantity of the fast electrons emitted. These enhanced electron spectra are comparable in the divergence, in the spatial spectral distribution and in the spectral characteristics to the one measured with the single foil configuration. This excluded a momentum dependent focusing as a source of the effect in the spectral range discussed. The higher quantity of electrons was detected in a spectral range that corresponds approximately to the spectral maximum of the electron spectrum emitted from the first foil. This could be an indication that the higher electron number detected for a double foil configuration is not emitted from the second foil and originates from the first foil. This interpretation is close to the one suggested by the model in Ref. [109], which explained an enhanced electron ejection from the transient laser field by the addition of the second foil, since the second foil inhibits the deceleration of the electrons by the declining laser field envelope. The amplification effect, as well as, the fast electron emission process is complex regarding to the kinematics of emitted electrons by interaction the transmitted laser pulse. The decoupling between laser field and electrons has to be discussed in a sub laser cycle model, with regards to the question of how it affects the deceleration process for an electron distribution that consists of electrons with different velocities, emission times and phase relations to the laser field. This is the subject of the ongoing cooperation with A. A. Andreev and recently performed PIC simulations. The next step (prompted by the theoretical suggestions of Ref. [109]) was to see if this amplification effect is related on the optical properties of the second foil, which then gives a connection to the transmitted laser light. This is presented in the next section, where a counter-propagating laser pulse was used to pre-ionize the second foil.

## 7.4 Electron Spectrum from a Two Laser Pulse Experiment

In the previous Section [7.3](#) an amplification in electron number ( $A_{Ne}$ ) was detected by using a two foil target and the laser at HC condition. In Chapter [6.4](#) the transmitted laser light by the interaction with a single foil F1 was detected, which is intense enough to ionize a second foil F2 even at a distance of 500  $\mu\text{m}$ . If the discovered amplification effect, as suggested in Ref. [109], is a consequence of the decoupling between the transient laser field, the effect should be determined by the optical properties of the second foil. In order to test, in a basic approach, if this effect can be attributed to a transient laser field, first, an experiment was performed, which investigated how the electron spectrum was influenced if there was a second laser pulse simultaneously at the target's backside with an intensity similar to the transmitted laser light. Second, it was tested if the amplification

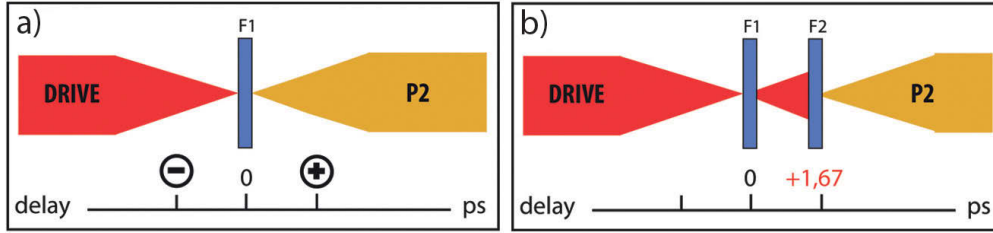


**Figure 7.9:** a) and b): Definition of the delay time between drive and second laser pulse (P2) in respect to the single and two foil configuration.

effect for a double foil configuration can be further enhanced by pre-heating and pre-ionization of the second foil with the help of a second laser pulse.

The experiments used a two laser pulse setup in a counter-propagating arrangement, which is illustrated in Fig. 7.9 a) and b) for a single and two foil configuration, respectively. The corresponding setup refers to Fig. 5.5, the characterization and inherent properties are described in detail in Section 5.4. In this setup, the drive pulse had an intensity of  $I_L = 7 \times 10^{19} \text{ W/cm}^2$ , and the second pulse (P2) of up to  $I_P < 1 \times 10^{18} \text{ W/cm}^2$ . The drive and the P2 pulse were linearly polarized and the P2 pulse was chosen to be perpendicular to the drive pulse. This polarization was chosen to support a simultaneous measurement of the backscattered XUV spectrum, which is presented in Section 8.2.1. The temporal overlap between the two laser pulses measured with an uncertainty of about  $\pm 0.3 \text{ ps}$ , while a delay with step size of  $0.1 \text{ ps}$  could be set. The actual temporal overlap was assumed to be at a fixed time within the given uncertainty, which could lead to a constant offset for the delay values for each experimental run. Electrons were detected within a capturing angle of  $6 \times 10^{-6} \text{ sr}$  in the propagation direction of the drive pulse. Details about the spectrometer used (configuration IV) are described in Section 5.6.2. Compared to the previous spectrometer configurations, this one had a lower spectral range, resolution and dynamic range. The spectrometer remained uncalibrated with respect to the electron number. All measurements used the HC condition, since the number of emitted electrons from UHC condition was too low for the spectrometer's dynamic range (cf. Section 7.2.1). Owing to the high complexity of the experiment, the results shown are based on relatively poor statistics: 7 experimental runs and in total 63 measurements for the various parameters: single and double foil configuration, single and two laser pulse interaction at different delay times and different intensity levels for the P2 pulse. They have to be considered as a first approach.

#### 7.4.1 Single Foil and Two Laser Pulse Interaction

The experiment tested the following situation: the P2 pulse is propagating in the opposite direction to the electrons that are accelerated by the drive pulse. The P2 pulse is focused on the foil's back side with an intensity that is assumed to be equivalent to that of the laser transmission for the drive pulse (cf. Section 6.1).

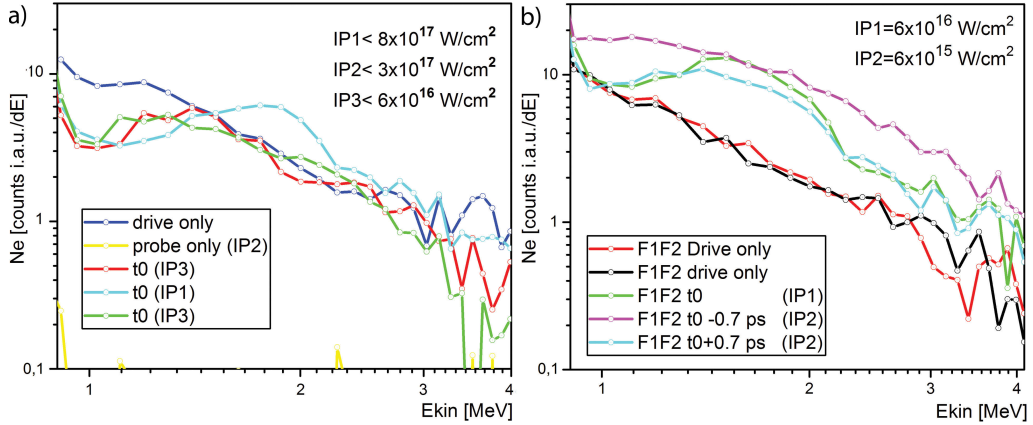


**Figure 7.10:** a): Electron spectrum detected in the counter-propagating two laser pulse experiment by using single PVF foil targets with a thickness of  $(85 \pm 4)$  nm at different intensity levels  $I_P$  of the P2 pulse. b): Electron spectra detected from the two foil setup at different delay times and intensities of the second counter-propagating laser pulse. Foils F1 and F2 were from PVF and each had a thickness of  $(85 \pm 4)$  nm. The second foil was placed at a distance of  $500 \mu\text{m}$  and the target hole diameter was about  $0.6$  mm. Two double foil reference measurements, without using P2 pulse, are shown. Electron numbers are given in arbitrary numbers and are comparable in a), b) and are taken from the same experimental run.

A complex interplay is expected due to the interaction of the P2 pulse with both the ejected electrons and the transmitted laser pulse. All possible scenarios are strongly connected to the intensity of the P2 pulse and the temporal relation between transmitted laser pulse and electrons. Due to the divergence, this intensity differs significantly in the range of  $100 \mu\text{m}$ . With the uncertainty for the temporal overlap, pre-, simultaneous or post-acceleration can not be clearly differentiated. Nevertheless, in order to test this principle and to complement the following results for a two laser pulse and double foil interaction, the experiments investigated, if and how a second laser pulse influences the electron spectrum for a single foil target interaction close to the temporal overlap.

No electrons were detected in the propagation direction of the drive pulse with the sole application of the P2 pulse in an intensity range of  $10^{16} < I_P < 1 \times 10^{18} \text{ W/cm}^2$ . An example is shown in Fig. 7.10 a) and shows no electrons in the detection range from  $0.9 \text{ MeV}$  to  $4.1 \text{ MeV}$ . For the two laser pulse interaction, the P2 pulse introduced a redistribution in the kinetic energies of the electrons, while the number of electrons in the spectral range of this spectrometer did not differ significantly. This can be seen for different intensity levels of the P2 pulse in Fig. 7.10 a). Here, a target holder construction with  $0.6$  mm diameter holes and a PVF foil thickness of  $85 \text{ nm}$  was used. For all values of  $I_P$ ,  $N_e$  exhibited a decreased particle number for kinetic energies below  $1.5 \text{ MeV}$ , and a peak in the electron spectrum at slightly higher kinetic energies. Dependent on the applied intensity of the P2 pulse, this peak was observed at different kinetic energies. Due to the uncertainty in the temporal overlap, this effect can either be introduced by

pre-heating of the target, a two laser pulse interaction at the temporal overlap or a post-interaction of the electrons with the second laser pulse. Redistributions in the kinetic energy and a small reduction of  $N_e$  were found in all of the 15 measurements in total, obtained in 7 experimental runs, for different delay times and values of  $I_P$ . The effect on the electron spectrum is complex, which can be seen by additional examples for different delay times in the Appendix Section [A.12](#).

The method hold promise as an interesting experimental technique to examine the influence of de- and acceleration of fast electrons in a transient laser field. For the double foil experiments, a minor influence on the particle number and a smaller effect on the spectral distribution might be expected for the P2 pulse interacting with the second foil and with electrons arriving there from the first foil.

#### 7.4.2 Double Foil Target and Two Laser Pulse Interaction

In the same experiment, measurements using a double foil target were performed to answer the question, can the found enhancement of the fast electrons from a double foil target be further maximized by pre-heating and pre-ionizing the second foil shortly before the emitted electrons and the transmitted laser pulse arrive. Fig. [7.10](#) b) depicts electron spectra from a two foil configuration for different applied delay times and different values of  $I_P$ , which consisted of two 85 nm PVF foils, which were separated about  $w = 500 \mu\text{m}$ . In comparison to the reference measurement (drive pulse only, double foil), in the presence of the second laser pulse, a significant increase of  $N_e$  commenced. In Fig. [7.10](#) this can be seen for delay times of  $\Delta t_P = -0.7 \text{ ps}$ ,  $0 \text{ ps}$  and  $+0.7 \text{ ps}$  and for an intensity range from  $I_P = 6 \times 10^{15} \text{ W/cm}^2$  to  $8 \times 10^{17} \text{ W/cm}^2$ . With respect to the travelling time of light for the distance  $w$ , for all of these delay times, the P2 pulse pre-heated the second foil. A additional measurements from the same experimental run are given in the Appendix Section [A.12](#).

In Section [7.3](#),  $A_{N_e}$  described the relative amplification of the integrated electron number between the double foil and single foil target configuration and for a single laser pulse interaction. In the following, all results concerning the integrated (over the full detection range) electron signal are given relative to a measurement using the single laser pulse on a double foil configuration. The relative value will be called  $A_{N_e}^*$ . Evaluated values of  $A_{N_e}^*$  for various delay times and intensity levels of the P2 pulse are summarized in Fig. [7.11](#). It combines measurements of 5 experimental runs and gives a basic impression of how much the second laser pulse influences the amplification effect. Up to  $A_{N_e}^* \sim 3$  was obtained when the P2 pulse illuminated the second foil with an intensity range from  $I_P \sim 1 \times 10^{16} \text{ W/cm}^2$  to  $I_P = 1 \times 10^{18} \text{ W/cm}^2$ , several ps before the drive pulse arrived at the first foil. For  $I_P = 6 \times 10^{16} \text{ W/cm}^2$  an amplification of the electron numbers was observed when the second foil was pre-heated in the time interval between the interaction of the drive pulse with the first foil, until the transmitted light arrived at the second foil. Higher values of  $I_P$  did not lead to a higher electron number for this time interval. By applying P2 at an intensity of  $I_P \sim 10^{18} \text{ W/cm}^2$  at the time when the transmitted light of the drive pulse

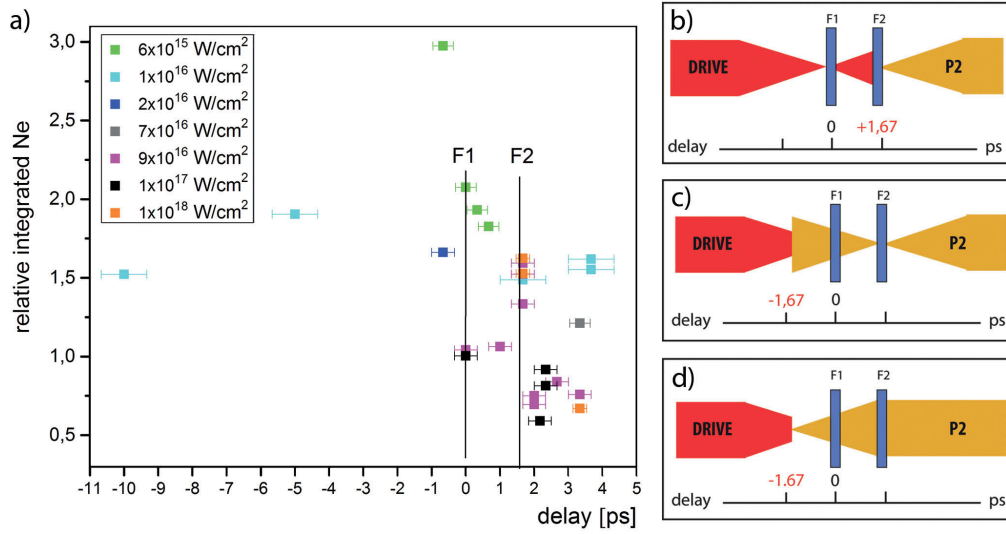


**Figure 7.11:** a): Relative detected amplification of the electron numbers  $A_{N_e}^*$  from a two foil setup ( $D(F1)=D(F2)=77$  nm) with respect to the delay  $\Delta t_P$  of the counter-propagating second laser pulse at different intensities  $I_P$ .  $A_{N_e}^*$  is given relative to the integrated  $N_e$  detected from the drive pulse and two foil target configuration, using the same experimental conditions. Black vertical lines corresponds to the travelling time of light for the distance between foils F1 and F2. Different intensities  $I_P$  of the probe pulse are indicated by different colours and are given in respect to F2. b): Schematic sketches illustrate the relation between target position and the definition of the probe pulse delay in time.  $\Delta t_P = 0$  is defined as the virtual overlap of drive and P2 pulse on target F1. With F2 placed at 500  $\mu\text{m}$  behind F1, at  $\Delta t_P = 0$  the probe pulse has already interacted for 1.7 ps with F2, before the transmitted light from the drive pulse arrives at F2. A smaller delay (c) pre-ionizes F2 even earlier. At  $\Delta t_P = +1.67$  ps the transmitted light from the drive pulse is coincident with the P2 pulse on F2 (b). Longer delay times means P2 arrives after the interaction of the drive pulse on F2. Note, that the "transmitted" laser light for the P2 pulse is only shown for an intuitive understanding of the relation between the two pulses.

arrived, an amplification of up to  $A_{N_e}^* = 1.6$  was measured. The same result was obtained for the interaction of the P2 pulse with F2 some ps seconds after the transmitted light had already reached F2, if  $I_P$  was smaller than  $6 \times 10^{16}$  W/cm<sup>2</sup>. For the P2 pulse at a higher intensity and at a time after the transmitted light of the drive pulse had interacted with the second foil ( $\Delta t_P > 1.7$  ps), a relative reduction in  $N_e$  commenced. This result indicates that either a de-acceleration or deflection of the emitted electrons by the P2 pulse takes place.

### 7.4.3 Discussion of the Electron Spectra from a Two Laser Pulse Experiment

The experiment showed that the increase in the electron number emitted from a double foil target could significantly raised if the second foil was pre-heated by a weaker pre-pulse ( $I_P < 10^{17}$  W/cm<sup>2</sup>). Comparing the electron number detected

for the single laser pulse and the single foil interaction with the case of a two laser pulse and two foil interaction, one can derive an amplification of  $A_{Ne} * A_{Ne}^* > 5 \times N_e$  with respect to the detection range used here. The spectral distribution of the enhanced electron spectra exhibited different spectral features dependent on the applied delay time and intensity of the second laser pulse. A redistribution of the electrons' kinetic energies was observed for a single foil and two counter-propagating laser pulse interaction when the second laser pulse interacted close to the temporal overlap. The details of the interplay between both pulses and the ejected electrons require further investigation in order to determine if the redistribution effect can be attributed to a strongly pre-heated plasma boundary or a simultaneous interaction of the two laser pulses at each plasma boundary or post-acceleration processes.

Nevertheless, the results from the pre-heated double foil configuration gave strong evidence that the underlying mechanism of the electron amplification effect is determined by the properties of the second foil. Pre-heating of the target leads to ionization, but as well to pre-heating of the electron temperature and an expansion of either the whole target or the scale length of the plasma density gradient. Whether this effect can be fixed to the optical properties of the second target and thus, can be explained by a decoupling between ejected electrons and the transient laser field, according to [109], is the objective of an ongoing investigation with A. A. Andreev.

## 7.5 Conclusions on the Fast Electron Spectrum

### Characterization of the Fast Electron Spectrum

This section studied the fast electrons emitted from a relativistic laser-plasma interaction with ultrathin foils in the laser propagation direction. The electron spectrum was found to be sensitive to small variations of the experimental parameters. The results examined dependencies of the electrons' spectral distribution and their particle number on various involved parameters, such as the laser contrast, the laser energy and intensity, the target thickness and the target hole diameter. The spectral distribution of fast electrons detected from ultrathin foils exhibited a maximum in the kinetic energy range of 0.8–1.7 MeV. The value is close to the theoretical calculation of ponderomotive potential for the laser parameters used. A strong dependency on the applied laser energy of the amount of emitted electrons and of the position of the electrons' spectral maximum was shown. For otherwise fixed parameters and in a rough approximation, the kinetic energy of the spectral maximum scales with  $\propto \sqrt{E_L}$ , which would be in agreement to the scaling for an emission by the ponderomotive force. But, the experiments also found indications that this spectral maximum is dependent on the target thickness and the hole diameter of the target support used. Hence, these findings hinder a simple interpretation and further interdependencies have to be taken into account. Nevertheless, a significant difference in  $N_e$  with change of the laser contrast condition was demonstrated in a comparison between high and ultra-

high laser contrast at otherwise fixed parameters. An one order of magnitude smaller electron number was detected for the ultrahigh laser contrast than for the lower contrast condition. The similarity of the spectral distribution for both laser contrast conditions is one of the most interesting findings. The property of the plasma boundary makes a difference for the efficiency of the fast electron emission process, but the maximum strength of the acceleration is independent of it. The smaller quantity of fast electrons obtained with the ultrahigh laser contrast correlates to a more efficient ion acceleration (cf. Section 6.2) for the parameter range discussed and in comparison to the lower contrast condition for a corresponding target thickness. From this one could conclude: The higher laser contrast, and hence, a steeper and unheated plasma boundary, inhibits significantly the electrons escape from the laser and plasma potential and enables a more efficient ion acceleration. Overall, the investigation showed that the fast electron spectra is a highly sensitive indicator for various parameters. Since the experimental results in general, and the electron spectra in particular, differ significantly when obtained using different laser systems, the spectrum of fast electrons discloses a potential to become a new method to complement and to refine existing methods for the comparison of laser parameters, as e.g. the laser energy/intensity, the pulse duration and the basic laser contrast. Further comparative measurements are necessary to derive a scaling, and a more detailed understanding of how the features found in the electron spectra correlate to the related parametric interdependencies. In addition, the discussion of the results with respect to recent publications [17, 56, 65, 107] illustrated that the fundamental problem of how the electrons are ejected from the laser field and the plasma potential needs further experimental and theoretical investigation.

### **Manipulation of the Fast Electron Spectrum**

The experiments investigated, how does the interaction of two counter-propagating laser pulses at a single foil affect the fast electron spectrum. A second laser pulse was applied with an intensity range from  $6 \times 10^{16} \text{ W/cm}^2$  to  $8 \times 10^{17} \text{ W/cm}^2$  and propagated in the opposite direction to the foil. In a first basic approach, the experiment found indications that the spectral distribution of the fast electrons could be changed when the the second laser pulse was applied close to the temporal overlap. Since the influence of a transmitted laser pulse on the fast electrons, is a fundamental question [17, 56, 109], this setup could be used for further investigations regarding the affect of a pre-heated target, a post-acceleration or deceleration in transient laser fields.

### **Amplification of the Fast Electrons Emission**

An amplification of up to a relative value of 1.5 of the total electron numbers in an energy range of 0.1–7 MeV was revealed by applying a second separated target foil at a distance of 500  $\mu\text{m}$ . Further investigation examined the effect and aimed to find evidences on whether the underlying mechanism is an emission process at the second foil, or, as suggested by Ref. [109], a consequence of a decoupling between

transient laser field and ejected electrons from the first foil that would otherwise suffer from deceleration. First it was shown that the spectral distribution from the double foil interaction is enhanced in a specific spectral range, which is determined by spectral characteristics of the electrons emitted from the first foil. Second, this amplification effect was significantly maximized by a pre-heating of the second foil with an additional pre-pulse at the foil's back side. This demonstrated that a higher amount of detected fast electrons has to be attributed to the properties of the second foil and indicates that they originate from the first foil. Further investigation is required to resolve why this effects leads to more electrons in the energy range that corresponds to the maximum of the electron spectra detected from laser and single foil interaction. This question can not be answered from the experimental observations and needs a confirmation by either PIC simulations or an analytical model that describes in detail the electron ejection and acceleration. For the spectral range of 0.9–4.5 MeV an amplification of approximately 5 in  $N_e$  relative to the number obtained from the single foil interaction was reached for the laser at the high contrast condition and a double foil target that was pre-heated with the help of the second laser pulse.



---

## 8 XUV Emission from Laser Interaction with Ultrathin Foils

In this chapter the XUV radiation emitted from laser interaction with ultrathin foils is investigated and complements the examination of concurrent laser-plasma processes. The investigation demonstrates how to correlate the results of the ion and electron acceleration, presented in Chapter 6 and 7, to features in the detected XUV spectrum. The collective electron dynamics are imprinted on the XUV spectrum, allowing one to distinguish between incoherent and coherent radiation emission, and to determine the laser to plasma energy conversion and the plasma temperature.

The coherent XUV radiation corresponds, in this context, to the high harmonic radiation (HH) and is emitted when a ultraintense laser pulse interacts with a steep plasma boundary. The HH emission from dense laser-plasmas is a promising brilliant light source, since its maximum frequency and the number of photons emitted scale with the laser intensity [4, 6]. This was a subject of intense investigation over the last few years [24, 47, 68, 112, 115–118]. These studies focussed on HH radiation emitted from bulk targets and detected in the laser reflection direction. However, the spectral characteristics of the HH radiation emitted from ultrathin foil targets in the direction of the laser propagation differ. Little has been reported about this particular case [40, 63, 112, 119], the underlying emission process is not fully understood and needs further investigation. The approach taken here was to investigate how a manipulation of the plasma pre-condition affects the high harmonic emission process. The manipulation was performed with the aid of a controlled pre-pulse. In addition, an alternative way to obtain brilliant, coherent XUV radiation from relativistic laser-plasma interaction was investigated: In a two laser pulse interaction at ultrathin foil targets, the principle of laser backscattering from a relativistic electron bunch was tested [55, 57, 120].

Chapters 6 and 7, demonstrated that the laser-plasma dynamics were highly dependent on the properties of the plasma boundary, which in turn was affected by the laser contrast condition, leading to significant differences between experimental results for ion and electron acceleration. Complementary, the XUV radiation, that is emitted in the laser propagation direction, is characterized in Section 8.1 for a single laser pulse interaction for different laser contrast conditions.

Section 8.1.2 gives a summary between the models, which describe the high harmonic emission process in connection to the experimental results.

The experiments tested relativistic backscattering for a strong laser pulse from laser accelerated fast electrons, as suggested in the relativistic mirror model in Section 4.3. A relativistic electron bunch can be accelerated by the interaction of a laser at relativistic intensity with an ultrathin foil target and can serve as a reflecting mirror for a second laser pulse that propagates in the opposite direction. The reflected light is predicted to be significantly changed in frequency [120] due to a relativistic doppler shift [37] and promises a new mechanism to obtain brilliant XUV pulses. The experiment tested if this idea is realizable for the parameter range provided by the experimental setup used for this work. Section 8.2 shows how the XUV spectra is affected when two laser pulses, in a counter-propagating setting, interact at the same time with an ultrathin foil.

Section 8.3 investigates how a controlled pre-pulse and hence, a concerted manipulation of the pre-plasma, affects the HH emission from ultrathin foils. The target density and the length of the plasma density gradient significantly determines the efficiency of HH emission [5, 24, 68] and with this method a significant enhancement is demonstrated. The experiments examine the parametric dependencies for this effect and reveal a new and promising controllability of the high harmonic emission efficiency.

## 8.1 XUV Emission at Different Laser Contrast Conditions

The laser contrast is the fundamental parameter determining the characteristics of the XUV radiation emitted from the laser-plasma interaction. This is explained by the well known dependency of the HH emission process on a rather steep ( $< \mu\text{m}$ ) and specific rise of the plasma density [4, 24, 55, 116]. A steep plasma boundary is not fulfilled for the lower laser contrast condition (HC), as already discussed in the results for ion and electron acceleration in Sections 6.1 and 7.2. In the following, the models for the HH emission process from ultrathin foils are discussed with respect to the experimental results and with reference to the laser contrast. The findings are based on 17 experimental runs.

### 8.1.1 The Incoherent XUV Spectrum

The XUV radiation from the laser interaction with a single foil target was detected in the laser propagation direction ( $\alpha_L = 0^\circ$ ) at HC and UHC conditions with the help of a transmission spectrometer (cf. Section 5.6.3). Typical XUV spectra are shown in Fig. 8.1 for an applied laser field strength of  $a_0 = 6.5, 5.5$  and for the HC and UHC, respectively. With the lower laser contrast, the detected spectrum consists of an incoherent Bremsstrahlung radiation and some discrete lines of plasma radiation [121] that are dependent on the target material used [75]<sup>1</sup>.

<sup>1</sup> A more detailed classification considering oxygen and carbon line radiation can be found in [53].

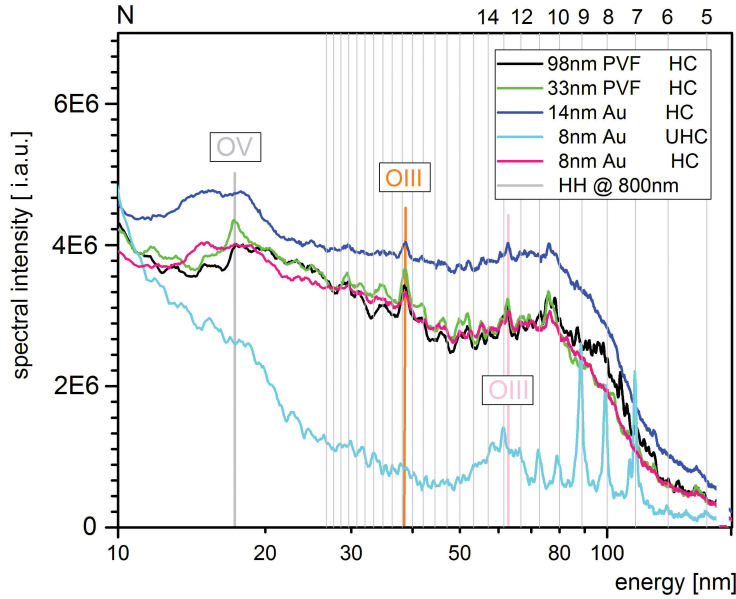


**Figure 8.1:** The XUV radiation detected in the laser propagation direction by a single laser pulse interaction with single foil targets of different compositions and for the laser at either high (HC) and ultrahigh (UHC) contrast condition. Some plasma lines are identified. In the case of the UHC condition, high harmonic radiation appears up to an order of  $N = 14$ .

No harmonic emission was observed for this laser contrast condition. Pre-heating of the foil by the pre-pulses and the rising laser intensity level (cf. Section 5.2.1) disturbs the HH emission due to a longer scale length of the plasma density gradient [24] and possibly due to a higher electron temperature. The incoherent radiation is assumed to be emitted on a timescale longer than the laser-plasma interaction, due to recombination processes. A high photon flux makes this radiation suitable, for example, the XUV transmission spectroscopy. In particular, similar radiation (20 nm incoherent XUV radiation) is used to characterize the target foil thickness, as described in Section 5.5 and Ref. [70]. In contrast, for the UHC condition, the broad, incoherent XUV radiation was detected with a significantly decreased intensity in the spectral range between 20–90 nm. This reflects a difference in the plasma dynamics involved for a steeper rise of the plasma density, enabling the emission of HH radiation. This significant lower intensity of the incoherent XUV radiation correlates with the results in Chapter 7, where a significantly lower number of fast electrons were detected with the laser at UHC than at HC condition. In the same comparison, this correlates as well, to a more efficient ion acceleration and a lower laser transmission through the target (cf. Section 6.1 and Section 6.4).

### 8.1.2 High Harmonic Radiation from Ultrathin Foils

In the following, HH radiation in the forward direction and from laser and ultrathin foil interaction is presented. For this particular case, the underlying mechanism has not been fully explained yet and few experimental results have been reported. Hence, first, a summary of the recent discussion is given and second, the basic characteristics of the detected HH radiation are determined and discussed.

#### The High Harmonic Radiation Emission Process

The CWE and ROM model are widely investigated and discussed for HH emission, detected in the reflection direction, from thick solid state targets with a laser on the target incidence angle of  $45^\circ$  [4, 5, 24, 55, 68, 116](cf. Chapter 4). HH emission detected in the laser propagation direction from ultrathin foils and with an laser incidence angle of  $0^\circ$  displays different spectral characteristics and the underlying mechanism still is under discussion [18, 54, 57, 63, 112, 119]. The reason for the ongoing discussion lies in the restrictions of the CWE and ROM model and in the observed differences in the spectral characteristics. A well known observation<sup>2</sup> is that for a relativistic laser intensity the HH cutoff,  $N_{max}$ , is much higher for HH emission detected in the reflection direction from thick bulk targets than for the case of HH emission in the laser propagation direction from thin and ultrathin foils.

As introduced in Section 4.1, the CWE model is based on a plasmonic radiative decay inside the plasma, which is caused by a relativistic electron bunch entering the plasma boundary. The generation of the fast electron bunch is directly connected to the Brunel absorption mechanism, which was excluded for the laser at normal incidence (cf. Section 2.2). A similar electron bunch might be established for the electrons' movement in the target normal direction by the ponderomotive force in Equation (1.16) or the figure 8 trajectories in Equation (1.13), however, here with a periodicity of  $2\omega_L$ . According to Equation (4.2), in the CWE model,  $N_{max}$  is determined by the maximum plasma density,  $n_e$ . Ref. [119] explained HH radiation from ultrathin foils by the CWE model, since the experimental results found a connection between  $N_{max}$  and  $n_e$  as a function of the target thickness. It is difficult to justify the use of the simplified version of the ROM model for the HH emission in the laser propagation direction, since one has to consider a "reflection" of the laser in forward direction (compare Section 4.2). If it is used, as done in Ref. [54, 63], it leads, by symmetry reasons, to only odd harmonic numbers in accordance to Equation (4.4). In the ROM model  $N_{max}$  scales with the  $\gamma$  factor of the electrons' oscillatory movement at the plasma boundary (cf. Equation (4.5)). Hence, the CWE and ROM HH generation can be definitely distinguished when  $N_{max}$  exceeds the CWE limit. For both processes the emission efficiency is dependent on a distinct scale length of the plasma gradient [5, 24]. The CWE mechanism requires a steeper rise of the plasma density than the emission process of the ROM mechanism. The properties of the plasma bound-

<sup>2</sup>compare [47, 63, 68, 112, 116] and the results in this Section

ary are determined by the applied laser contrast. As discussed before, the scale length of the plasma density gradient is difficult to be measured (cf. Section 5.2) and usually approximated by the use of a complex PIC simulation [63, 68] or is derived from the experiments by the use of model dependent considerations [119].

Recent publications [112, 118] suggested a new model to explain the HH emission from ultrathin foils in the forward direction with a harmonic cutoff frequency that was detected much higher than the CWE limit: Coherent Synchrotron Emission (CSE). Similar to synchrotron radiation from electrons in an undulator<sup>3</sup> [77, 122], the model connects the emission directly to the electrons and the Bremsstrahlung radiation they emit in their relativistic oscillatory motion. Due to the "figure 8" like trajectories of the electron bunches at (and through) the plasma boundary (cf. Fig. 1.1), highly energetic photons are emitted at the points of return. The CSE model concludes that the emitted radiation has an ultra short pulse duration, coherence and a spectral distribution exhibiting multiples of the driving frequency due to the periodicity of the emission process. Hence, the spectral characteristics of this radiation (e.g.  $N_{max}$ ) are similar to that of the ROM model, and the difference lies only in the intensity scaling for different harmonic orders [112].

### The Spectrum of the High Harmonic Radiation

The experiments presented here used ultrathin ( $\leq 85$  nm) PVF and gold foils and detected the HH radiation for a laser incidence angle normal on the target. The laser was linearly polarized, at UHC condition, and the laser field strength was approximately  $a_0 = 5$ . The following conclusions and examples were obtained from a measurement campaign consisting of 10 experimental runs, where each took at least 2 measurements for the discussed parameters. In the measurements, HH emission was observed with even and odd harmonic numbers, as depicted in a typical example in Fig. 8.2. In some experimental runs, even harmonic lines were observed with a reduced signal strength. A suppression of even harmonic numbers has been reported in all publications on HH from ultrathin foils and for the discussed detection direction [57, 63, 112, 119].

The intensity of harmonic lines  $N \leq 7$  were suppressed/reduced, independent of the PVF foil thickness, for either 12 nm, 35 nm or 85 nm. Similar results were reported in Ref. [54, 63, 112] and concluded that the HH radiation is emitted from the target front side. The emission was explained by either the ROM or the CSE model, since the detected values for  $N_{max}$  exceeded the CWE cutoff frequency. According to Equation (1.22),  $n_c$  stands for the optical properties of the plasma and scales with  $\sim 1/\lambda^2$ . The plasma is opaque until a frequency is reached where the condition  $n_e/n_c \sim 1$  is satisfied. This can explain the suppression of the high harmonic radiation up to a certain order  $N_c$ . For fully ionized PVF and  $\lambda = 800$  nm one approximates  $n_e/n_c = 220$ . With respect to  $\lambda = 114$  nm, which corresponds to the first detected intense harmonic line  $N_c = 7$  (Fig. 8.1 and

<sup>3</sup>Undulator is a alternating magnetic field. The device is used to force the electrons for a specific velocity to oscillate.

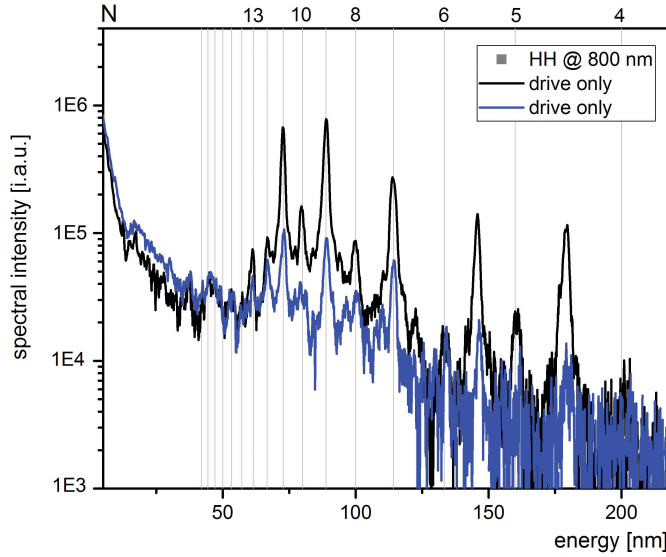


**Figure 8.2:** The different intensity levels for detected high harmonic radiation measured in the same experimental run. The laser interacted with a  $(35 \pm 2)$  nm PVF foil and the applied laser field strength was about  $a_0 = 5$ .

Fig.8.2), the ratio of  $n_e/n_c$  is about  $\sim 4$ . When the relativistic correction of  $\bar{\gamma}n_c$  is considered, for this wavelength the condition  $n_e = n_c$  is fulfilled, for which a significant higher transmittance is expected. Hence, the intensity of HH radiation that is emitted from the target front side is spectrally filtered due to transmission through the dense plasma.

Throughout the experimental campaign, in the same experimental run and under the same experimental conditions, the HH radiation was detected with a strongly fluctuating intensity level. An extreme example is shown in Fig. 8.2 for a measurement using a 35 nm PVF foil target, obtained in the same experimental run and for the same experimental parameters (position of the focal plane on the target, laser energy).

No particular dependence of  $N_{max}$  on the target thickness was found.  $N_{max}$  reached up to  $(15 \pm 2)$  for the applied laser field strength of  $a_0 = 5$  and for PVF foils in the range from 12 nm to 85 nm. This can be seen in the following and in Fig. A.13 the Appendix Section A.3. According to Equation (4.2) the cutoff frequency in the CWE model is limited by the maximum electron density. It is predicted to be about  $N_{max}(CWE) = 15$  for full ionized PVF material. In consequence, higher numbers are expected for a higher target density, such as, e.g., gold foils. However, the HH cutoff frequency did not change for ultrathin gold foils or DLC material, as depicted in Fig. 8.1 for a gold foil. Note, that the determination of the HH cutoff is hindered by the XUV background signal that possibly could cover higher orders. An dependency of  $N_{max}$  on the target thickness was found Ref. [119] for DLC foils in the foil thickness range from 5 nm to 17 nm. In that work it was explained by a reduction of the maximum electron

density for ultrathin foil targets due to a small expansion at the beginning of the interaction. In Ref. [112] a dependency of  $N_{max}$  on the foil thickness was explained within the CSE model by a low particle number and hence, a too low target density for too thin foils. The effect is not further described, but could be attributed to an similar interdependency between the laser intensity, the target thickness and the laser contrast as in the RPA model in Section 6.1. Both seems to be not the case for the results presented here. No change of  $N_{max}$  with either the target thickness or target density was not observed. Through examination of the published results for HH emission from ultrathin foils, it becomes apparent that experiments using laser systems with short pulse durations and the highest laser contrast have measured much smaller values of  $N_{max}$ , than the ones using high energy laser systems with longer pulse durations [57, 112]. In Ref. [63] a direct comparison between HH emission from the front and back side of a target foil was shown and revealed a significant smaller cutoff frequency for the backside emitted HH. However, the experimental situation used is difficult to be compared to the here discussed one, since the HH emission has a spatial dependency [24, 123]. In that experiment, the laser incidence was oblique and the detection directions were at an oblique angle that did not correspond to the specular or the laser propagation direction.

In the experiments performed here, for a PVF foil thickness  $> 30$  nm and for the spectral range  $\lambda > 120$  nm, HH emission was observed at half integers  $\lambda(N) = 2\lambda_L/N$  (cf. Fig. 8.2). This effect has not been reported for this experimental situation before. For HH radiation detected from bulk targets in the laser's reflection direction, a splitting in the HH lines into doublet or triplet lines, was reported in [46, 47]. The effect was explained by a small movement of the plasma boundary during the HH emission process and affected all harmonic lines. The harmonic line splitting corresponded to harmonic lines of different fundamental frequencies, from which the velocity of the emitting surface can be calculated. The observation of the half integer emission seen here raises the following questions: Why does the experiment coincidentally fulfill the conditions for half integer emission exactly, and why does it only occur in a specific low energy range, a range where the plasma is assumed to be opaque? Note, that in Fig. 8.2 the intensity level of harmonics lines at half integers is higher than the one for integers. Here, an emission from plasma waves might be considered, since radiation emitted  $3/2\omega_L$  has been only reported so far due to a two plasmon decay instability [124].

In conclusion, although the experiments found evidence that the detected HH emission had to pass through a medium/plasma, a definite conclusion on the underlying generation mechanism can not be made. For either the ROM, CSE or CWE definite characteristics were not seen in the HH spectra.

## 8.2 Relativistic Backscattering

According to Section 4.3, a significant frequency upshift can occur when a laser is reflected from a relativistically moving mirror. As was previously introduced, this

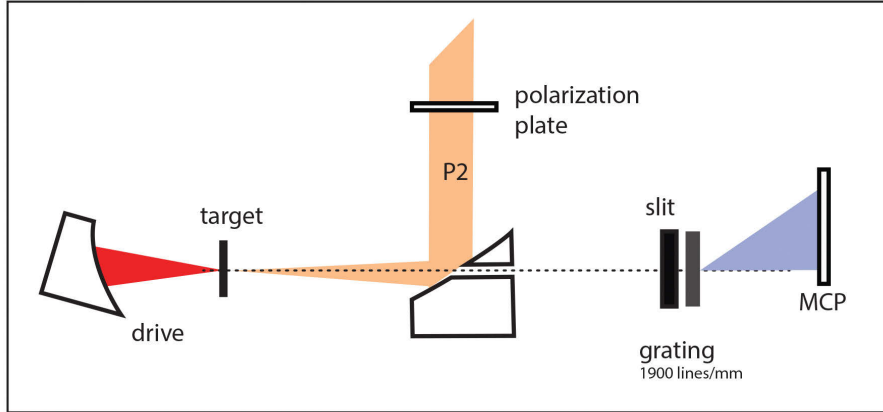


**Figure 8.3:** A schematic for the experimental setup to detect the XUV radiation in an experiment with two counter-propagating laser pulses. Radiation is detected in the propagation direction of the drive pulse.

scenario could be possible for a two counter-propagating laser pulse experiment. Here, a dense electron sheath/bunch, accelerated to relativistic velocities by the first (strong) laser pulse, serves as the mirror that reflects the second laser pulse. The reflectivity of the electron bunch depends on its density, as given by Equation 4.7. In Section 7, the fast electrons emitted from a laser and ultrathin foil interaction exhibited a maximum in the spectral distribution at  $E_{kin} \leq 2$  MeV. According to Equation (4.3), backscattering at this kinetic energy could shift the frequency of the scattered laser pulse from 800 nm up to  $\geq 10$  nm.

Experiments at HC and UHC contrast condition tested relativistic backscattering with two laser pulses using ultrathin foil targets. A schematic of the experimental setup used is depicted in Fig. 8.3. The detailed description of the setup, detection devices and inherent diagnostics can be found in Section 5.4. The spectrometer was not calibrated with regard to photon number and spectral efficiency. The definition of the temporal overlap between both laser pulses  $\Delta t_P = 0$  is illustrated in Fig. 8.4. The diagnostics determined it to be within an interval of  $\pm 0.3$  ps. It was assumed that the exact temporal overlap was at a fixed time within this time interval for the same experimental run. Hence, the here named delay times can have a constant offset,  $\pm 0.3$  ps at maximum. A minimum delay step size of about 0.1 ps could be applied.

### 8.2.1 Backscattering at High Laser Contrast

The results of Sections 7.2.1 and 7.3 found a high number of fast electrons for the laser at HC condition, especially in the case of a double foil target. With a detected electron number of  $N_e > 10^9$  and an electron beam divergence determined to be  $10^\circ$  (cf. Fig. 7.6), an electron bunch density of  $\sigma_{n(e)}(F2) \sim 10^{14}/\text{cm}^2$  can be calculated at the position of the second foil. According to Equation (4.7), a high reflectivity is therefore not reached. But, with respect to the divergence of

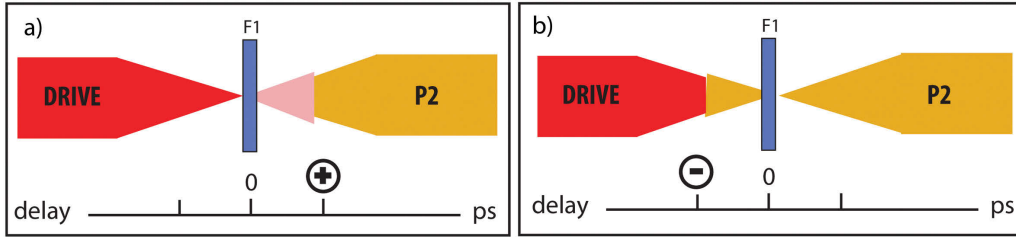


**Figure 8.4:** Schematic illustrates the definition of the delay time  $\Delta t_P$  between the two laser pulses (drive and P2). The transmitted light of the P2 pulse is sketched only for the purpose of an intuitive understanding. The positive delay time in a), corresponds to the case, when the drive pulse interacts with the target before the P2 pulse arrives it. For negative delay time in b), the situation is vice versa.

the electron beam, the possibility of having a significant higher electron density close to the back of the first foil exists. This motivated a testing of the backscattering for single foil targets. In addition, for a coherent scattering or, as suggested in [57], a coherent multi-bunch scattering, a higher scattering efficiency can be reached. This promising principle was tested in experiments at HC condition.

In the experiment, the target configuration consisted of two foils separated with  $w = 500 \text{ }\mu\text{m}$ , depicted in the insert of Fig. 8.5. In the case of a single foil, the same target holder construction was used with a priorly removed second foil. P2 illuminated either foil one (F1) or foil two (F2) at  $I_P \geq 1 \times 10^{16} \text{ W/cm}^2$ , while the intensity of the drive pulse was about  $I_L = 7 \times 10^{19} \text{ W/cm}^2$ . Ultrathin foil PVF targets with a thickness in the range between 12 nm and 85 nm were used. The experiment was performed in 8 experimental runs and in total  $\geq 67$  measurements were taken for different foil thicknesses, delay times, pre-pulse intensity levels and laser polarizations. A selection of results that illustrate the essential features are shown in Fig. 8.5 and compares measurements obtained in a single experimental run. Both laser pulses were linearly polarized, which was set to be parallel to each other. No indication was found for an expected backscattered and a thereby frequency shifted signal. The recorded XUV radiation only differs in the intensity and not in the spectral distribution for different delay times and in both the single or two foil target configurations. This can be seen in a direct comparison between the XUV radiation obtained with and without the second laser pulse P2 in Fig. 8.5. For the single laser pulse interaction, a significant enhancement of the overall XUV intensity between the single and two foil configuration was detected. The spectral distribution remained comparable, and the enhancement has to be attributed to radiation caused by the interaction of fast particles with the second foil. An overall increase of the signal was observed for the case of a single foil target with the presence of P2. It is shown for the temporal overlap of both pulses in Fig. 8.5 a). The higher XUV signal can be explained by an additional plasma heating by the P2 pulse. For the double foil target configuration, the spectrum remained almost unaffected in the presence of the P2 pulse and for a delay range of some picoseconds, as depicted in Fig. 8.5 b). A small increase of the intensity

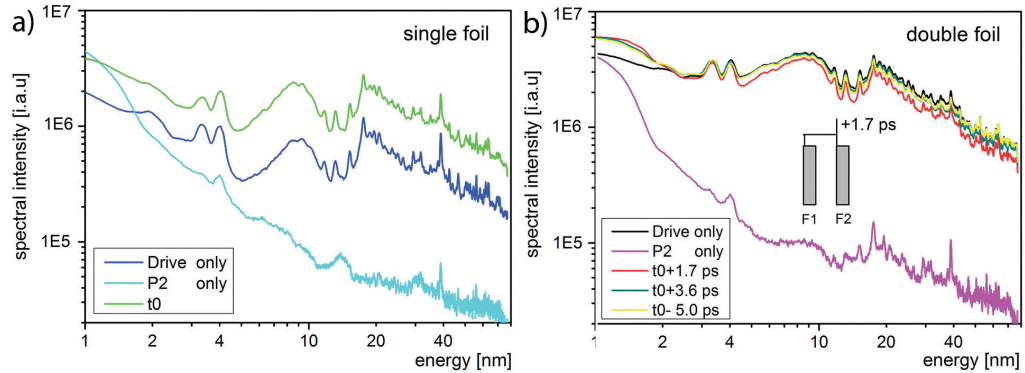


**Figure 8.5:** XUV spectra detected from laser interaction with either a single a) or a double foil target b). The laser was applied at HC contrast condition and the spectra are compared for the case of either a single (drive or P2) or a two laser pulse interaction. The thickness of both PVF foils, F1 and F2, was about  $(85 \pm 3)$  nm. In the double foil target configuration, the foils were separated about  $w = 500 \mu\text{m}$ . The distance corresponds, according to the travelling time of light, to a delay of about  $+1.7$  ps. The P2 pulse illuminated the foil's backside with an intensity of  $I_P \geq 1 \times 10^{16} \text{ W/cm}^2$ .

for the spectral range of  $< 2$  nm was detected for longer positive and negative delay times. Since this effect was found comparable for significant different delay times, any relation to the relativistic mirror model can be excluded. The small enhancement in the high energy range might be explained by a superposition of separately obtained spectral intensities of the drive and P2 pulse.

## 8.2.2 Backscattering at Ultrahigh Laser Contrast

Section 8.1 demonstrated that the interaction of a laser pulse at the UHC contrast condition with an ultrathin plasma slab enables HH emission in the laser propagation direction. Hence, with regard to backscattering from laser accelerated electron bunches at this setting, one expects a more complex spectral distribution for the reflected radiation [120]. On the one hand, a shift of the frequency occurs, as before, when the pulse is reflected from a relativistically moving electron mirror (cf. Fig. 4.1). On the other hand, the drive pulse excites relativistic oscillations on the plasma boundary which can comprise the whole plasma slab for ultrathin foils. In consequence, the condition for HH emission via the ROM model is fulfilled and the reflected radiation is found at multiple integers of its frequency. Furthermore, if the reflected pulse has a high field strength it can decelerate the electron bunch, excite oscillations at the plasma boundary or even lead to HH emission itself [120]. A first approach to test the fundamentals of this promising idea was reported in Ref. [57]. The present work aimed to pursue this investigation by performing a comparable experiment, but in a different parameter range.

According to Section 7.2 the detected number of fast electrons was significantly lower for the UHC than for the HC contrast condition. One has to keep in mind that the detailed description of the electron emission with regard to the time of emission and the velocity distribution is not known and is in the fo-

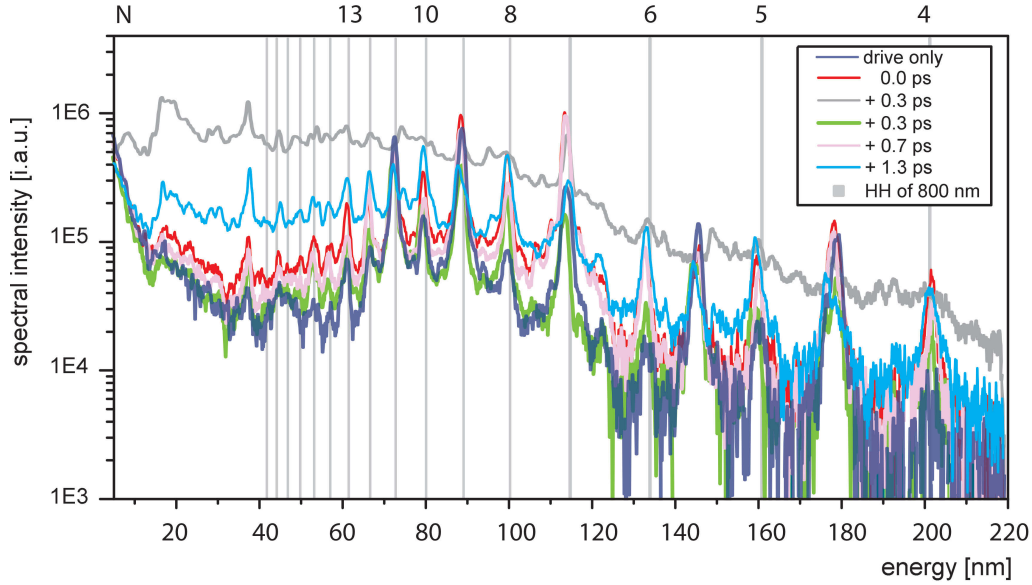


**Figure 8.6:** The high harmonic radiation detected in the propagation direction of the drive pulse, for an interaction of two laser pulses at a  $(35 \pm 2)$  nm PVF foil and close to the temporal overlap of both pulses. For comparison, a reference spectrum detected without applying the P2 pulse is shown.

cus of recent discussions [17, 57, 109, 112, 125]. The time of emission, either sub laser cycle or longer, determines the electron bunch density or even leads to equally spaced electron bunches, as suggested in [57], which could enable a more efficient coherent backscattering from more than one electron bunch. The experiments used PVF foils in a thickness range from 12 nm to 85 nm, which is close to the electron blow out for the laser intensity applied (cf. Equation (3.7) and Sections 6.2, A.2). Hence, on the one hand, the experiments tested the backscattering from the emitted fast electrons. On the other hand, the experiments aimed to find general influences in the HH spectrum by an interaction of both laser pulses close to the temporal overlap.

The experiments were performed with the same setup as above and the P2 pulse was applied with an intensity of  $I_P \leq 7 \times 10^{17}$  W/cm<sup>2</sup>. The intensity of the drive pulse was about  $I_L = 6 \times 10^{19}$  W/cm<sup>2</sup>. The polarization of the drive pulse was linear. The P2 pulse was linearly polarized perpendicular to the drive pulse to enhance the diffraction efficiency for the grating used for backscattered light of the P2 pulse. The experimental campaign consisted of 8 experimental runs with approximately 100 measurements in total. As before, direct comparisons always refer to the same experimental run. When only the P2 pulse interacted with the target, no harmonic content could be measured. A typical comparison of the XUV spectra measured for a single and two laser pulse interaction is depicted in Fig. 8.6 for a 35 nm PVF foil target and the P2 pulse applied at a delay range of  $0 < \Delta t_P < +1.3$  ps. Close to the temporal overlap, at  $\Delta t_P = (0 \pm 0.3)$  ps, a small enhancement of single harmonic lines was observed. With regards to the

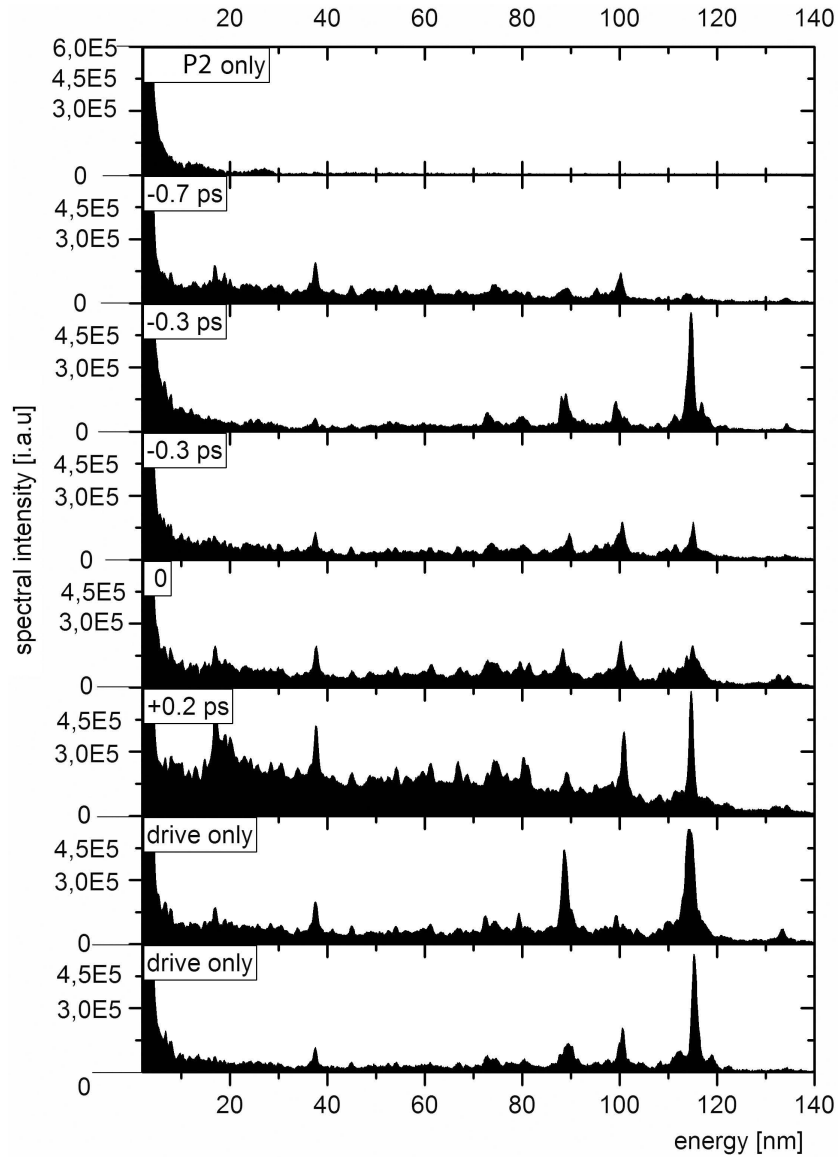


**Figure 8.7:** High harmonic radiation detected from a  $(12 \pm 1)$  nm PVF foil and both laser pulses close to the temporal overlap. Two reference spectra from the single laser pulse interaction are shown for comparison. Note, that the scaling of the y-axis is chosen to be linear.

fluctuations of the HH signal from the single laser pulse interaction (cf. Fig. 8.2), this effect is concluded to be insignificant. At the same delay range, for up to 30% of the measurements at the temporal overlap, no HH radiation could be detected. Instead, an intense and broad XUV background signal (grey line in Fig. 8.6) appeared, which is reminiscent of the XUV spectrum obtained for the HC condition (see Fig. 8.5 and Appendix Section A.3 Fig. A.15)). In Fig. 8.7 an additional example is given for a 12 nm PVF foil and smaller delay times of the P2 pulse. Again, a reduction and even an inhibition of the HH emission can be seen for delay times  $-0.3$  and  $+0.7$  ps. The fluctuating appearance of this effect is depicted in two different measurements for the time delay of  $-0.3$  ps. This observation indicates that in presence of the second laser pulse for a delay close to the temporal overlap, an inhibition of the HH emission occurs, e.g. a perturbation of the collective, oscillatory electron motion. Such a perturbation can be attributed to a time interval, either just before or at the temporal overlap and the fluctuations might be explained by shot to shot variations e.g. spatial beam pointing fluctuations<sup>4</sup>. To illustrate the fluctuation in the HH spectrum for consecutive measurements, two measurements with only using the drive pulse are shown. For longer delay times, of up to a few ps, the incoherent XUV background is found to be raised, similar to the case of the HC condition and two laser pulse interaction in Fig. 8.5 a).

In conclusion, for the chosen parameters, no radiation that could be attributed to a relativistic backscattering process was found, but an indication for a perturbation of the HH emission process was observed, when the second laser pulse was applied close to the temporal overlap. Contrary to the results shown here, the experiment of Ref. [57] showed evidence for a relativistically backscattered radiation. It was performed with a similar experimental setup. And used higher laser intensity ( $I_{peak} = 6 \times 10^{20}$  W/cm<sup>2</sup>)<sup>5</sup> for the drive pulse and a much weaker one for the P2 pulse ( $I_P = 10^{16}$  W/cm<sup>2</sup>). The target thickness was close to the blow out regime (10 nm, 50 nm DLC). The corresponding electron spectra exhibited a spectral maximum at 1.5 MeV and a significantly higher electron number than the ones obtained in the experiment presented here. In the reflected spectrum of Ref. [57], HH like line emission up to  $N_{max} = 15$  was detected for the two laser pulse interaction, which was not observed without using the second laser pulse for this foil thickness. In this experiment, HH radiation with solely using the drive pulse was obtained only for a greater target thickness (150 nm DLC). A limitation due to the foil thickness for the HH emission was already discussed in Section 8.1.2. It can be a consequence of a limitation of the particle numbers and/or the laser contrast condition. A comparison suggests the following interpretation: For the experiments presented here, the electron number was too small to enable sufficient scattering and the intensity of the P2 pulse was high enough to interrupt the HH emission process for an interaction just before or at the temporal overlap. However, both investigations demonstrated that for ultrathin foils and ultrahigh laser contrast, the efficiency of the backscattering process is small,

<sup>4</sup> Beam pointing reaches up to  $\pm 10$   $\mu$ m in x and y direction

<sup>5</sup> There the intensity is given for the peak value, here it is given in average.

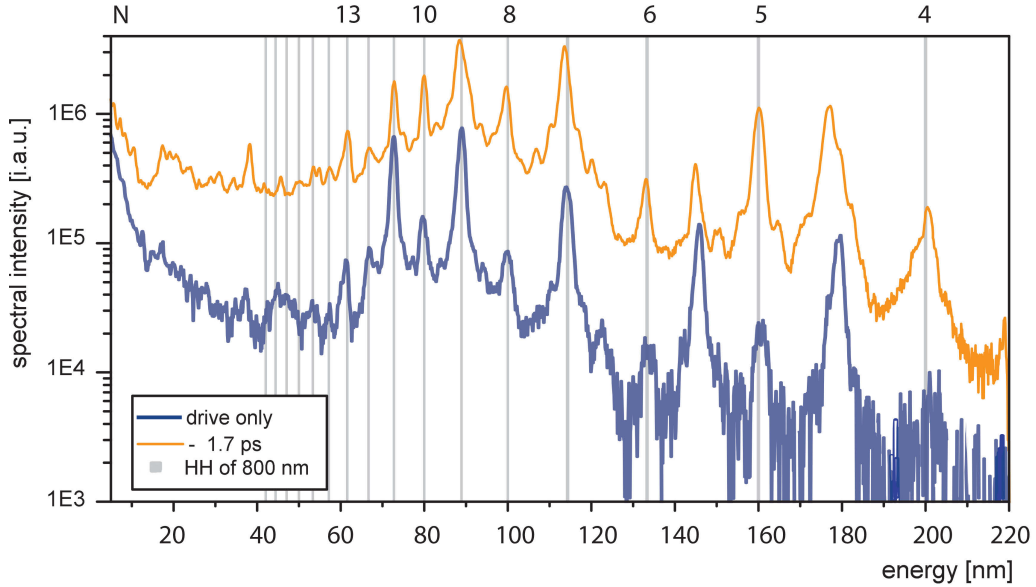


**Figure 8.8:** High harmonic radiation detected in the propagation direction of the drive pulse. The P2 pulse was used as a pre-pulse to manipulate the plasma condition. The P2 pulse irradiated the target at a specific delay time before the stronger drive pulse interacted with it. The target was a  $(35 \pm 2)$  nm PVF foil. The reference spectrum was measured without the P2 pulse in the same experimental run.

which would only be improved with faster and much denser electron bunches.

### 8.3 Enhanced High Harmonic Emission

The experiments in Sections 6.6 and 7.4 found significant differences in the results for ion and electron acceleration, if the target was manipulated by a strong pre-pulse. Although the HH emission processes depend on a sharp plasma boundary, their efficiency depends on a particular raise of the plasma density [24, 68]. In consequence, for a pre-heated and pre-expanded plasma boundary one expects to see a difference. As already discussed in Section 8.1.2, the scale length of the plasma density gradient,  $L(\nabla n_e)$ , differs for either the CWE and ROM model, and for a large pre-expansion of the target, such as given in the case of the HC condition, HH emission is inhibited (see Section 8.1). The experiments tested, for the first time, the influence of an applied pre-pulse on the HH emission process from ultrathin foil targets.

The same experimental setup as in the previous section was used, but now the second, counter-propagating laser pulse served as a strong pre-pulse, by applying it at negative delay times (see definition in Fig. 8.4). The experiment was performed in 7 experimental runs, with a total of 37 measurements.

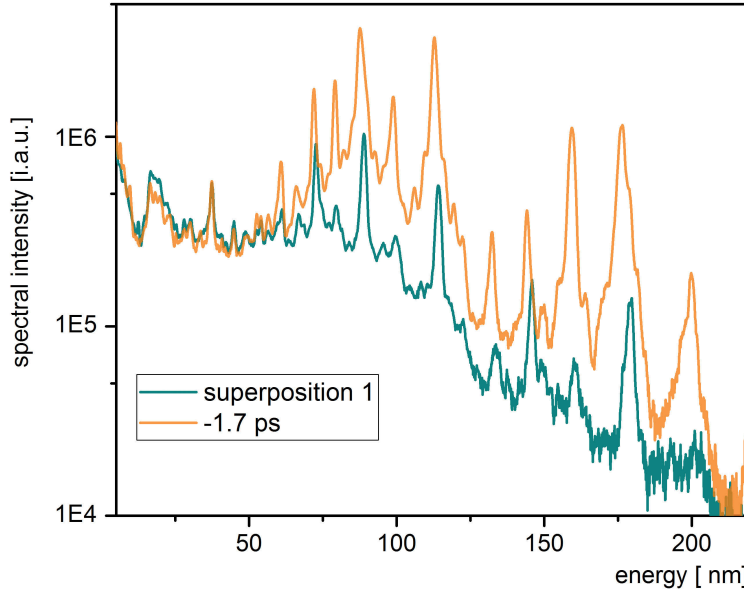


**Figure 8.9:** The superposition of a characteristic incoherent XUV spectrum (grey line in Fig. 8.6) and HH radiation from single laser pulse interaction (Fig. 8.8) is compared to the detected high harmonic spectrum which exhibited an enhanced intensity in Fig. 8.8 due to the pre-plasma manipulation by a pre-pulse. All measurements correspond to the same experimental run. The intensity of the incoherent XUV radiation was scaled to reproduce the XUV background level of the enhanced HH spectrum in the spectral range from 10 nm to 60 nm.

### 8.3.1 A Basic Description of the Effect

The pre-pulse, P2, was applied with  $I_P \leq 1 \times 10^{18} \text{ W/cm}^2$ , the drive pulse with  $I_L = 6 \times 10^{19} \text{ W/cm}^2$ . Both laser pulses were at UHC condition and had a linear field polarization which was set perpendicular to each other. For longer ( $< -1 \text{ ps}$ ) negative delay times, a significant enhancement of the HH signal was observed. This effect was reproducibly measured in all 3 experimental runs and in total 10 measurements that looked for such a long negative delay time. In all of these measurements, the enhanced HH intensity was distinct from the small enhancement seen for positive delay times (cf. last Section). A typical example is depicted in Fig. 8.8. The best measurement from single laser pulse interaction in the same experimental run served as a reference spectrum. In the spectrum chosen, odd harmonic numbers are pronounced. This spectral feature was already discussed in Section 8.1. The ratio between the HH intensity and the incoherent XUV for this reference is comparable to the highest ratio measured in other experimental runs (cf. Fig. 8.2, Fig. 8.1, Fig. 8.7, Fig. 8.6). In a direct comparison between this reference and the measurement with the pre-pulse, a rise of the incoherent XUV background (c.f. Section 8.2) is apparent. Hence, it was necessary to verify if the spectrum shows a true enhancement of the HH signal. A linear superposition between the HH spectrum of the reference measurement of Fig. 8.8 and a charac-

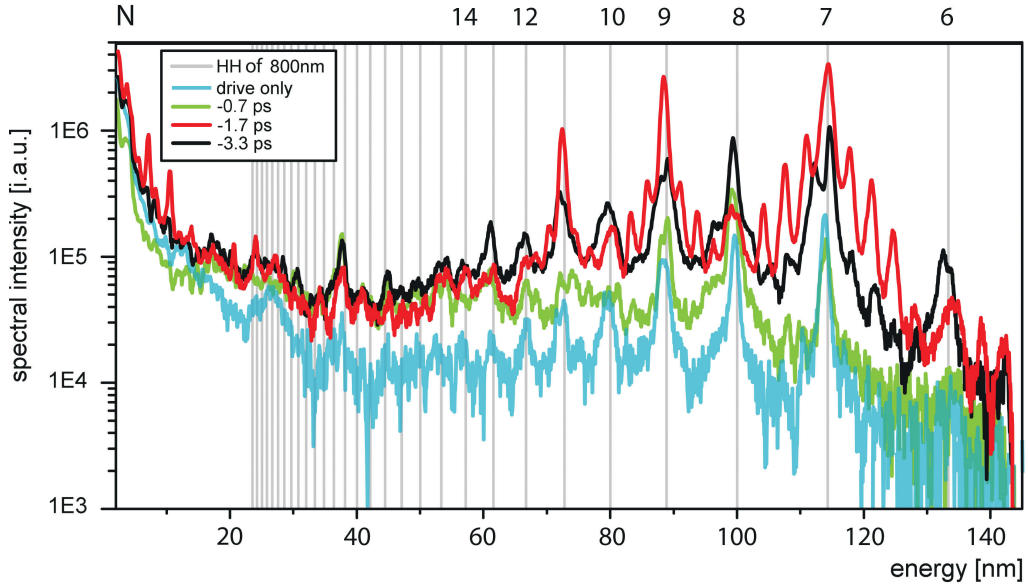


**Figure 8.10:** A selection of high harmonic spectra for the pre-pulse applied at long negative delay times from a  $(35 \pm 2)$  nm PVF foil and detected in the propagation direction of the drive pulse. Further details are given in the text.

teristic incoherent XUV spectrum is shown in Fig. 8.9. The signal strength of the incoherent spectrum was chosen to reproduce the XUV background level of the enhanced HH spectrum of Fig. 8.8 in the spectral range of 10–60 nm. The comparison shows that the method fails to reconstruct the enhanced HH intensity and therefore, reveals that the pre-heating of the target led to a real enhancement of the HH emission. In Fig. 8.9 the HH intensity is enhanced by about approximately one order of magnitude.

### 8.3.2 Dependency on the Delay of the Pre-Pulse

The dependency of the enhanced HH emission on the applied delay time is shown in Fig. 8.10. The measurements were taken for the same experimental conditions as above, except of the detection range of the spectrometer. The corresponding raw images can be found in Appendix Section A.3 in Fig. A.19. For delay times smaller than  $< 0$  ps, the incoherent XUV signal starts to rise in comparison to the reference measurement. With respect to the spectral range from 2 nm to 60 nm the XUV background does not further increase for long negative delay times, e.g.  $\leq -0.7$  ps. The HH radiation is significantly enhanced for delay times  $< -1$  ps. It is maximal at approximately  $-2$  ps and still has a significantly high intensity for the longer negative delay of  $\leq -3$  ps. More spectra referring to the same experimental run and additional negative delay values are shown in the Appendix in Section A.3. These measurements reveal an optimum delay time for the pre-pulse. The pre-pulse manipulates the pre-plasma in accordance with the applied intensity and delay, and hence, either the plasma density gradient and/or the plasma

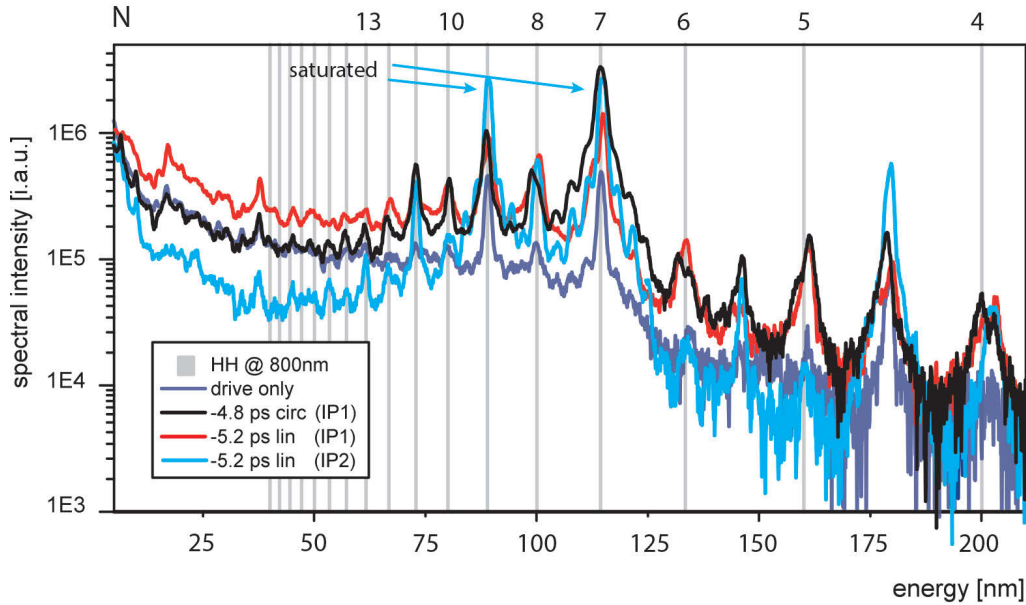


**Figure 8.11:** A comparison of measurements for high harmonic radiation for the pre-pulse at different laser field polarizations (linear or circular) and different delay times. Depicted is the optimal delay time for a maximized HH intensity from the P2 pulse either at linear or circular polarization and its corresponding intensity level. The P2 pulse was applied at different intensity levels:  $I_P(1) = 1 \times 10^{18} \text{ W/cm}^2$  and  $I_P(2) = 3 \times 10^{17} \text{ W/cm}^2$ . The target was a  $(85 \pm 3) \text{ nm}$  PVF foil. A reference spectrum solely from interaction with the drive pulse is given for the same foil thickness. The saturated signal is indicated with arrows.

density optimizes the HH generation process. At this optimum, all harmonic lines are spectrally broadened and odd harmonic numbers are pronounced. Strong side bands appeared at harmonic lines  $N \geq 6$ . These side bands exhibited symmetric maxima with a constant spectral difference for the energy representation in  $\lambda$ . They originate from a diffraction effect from the supporting grid of the grating, which is dependent on the intensity of the particular radiation. The details about this effect can be found in the Appendix Section [A.3](#).

### 8.3.3 The dependency on the Polarization and the Intensity of the Pre-pulse

In general, for the laser field at circular polarization, HH emission is excluded [126]. Hence one can demonstrate that no HH emission originates from the P2 pulse when it is circularly polarized. In the experiments the P2 pulse was applied with circular polarization and an enhancement effect for the HH emission still seen <sup>6</sup>. The HH intensity could be maximized for an applied delay of  $\geq -5 \text{ ps}$ , as shown in Fig. 8.11. At this optimal range both the spectral characteristics and the HH

<sup>6</sup> Circular polarization was realized by moving a  $\lambda/4$  plate of  $\sim 150 \mu\text{m}$  mica in the beam way of P2. It was considered to have a refractive index of 1.6 in the delay calculation.

intensity level are comparable to what was obtained with linear laser polarization for the corresponding optimal delay time in Fig. 8.10. However, in comparison, the optimal delay times differ by about  $\sim 3$  ps. Here, one can consider a dependency of the optimal delay time on the laser field strength of the pre-pulse, which is decreased for circular laser polarization by about a factor of  $1/\sqrt{2}$  [13, 15]. Therefore, the target expansion is smaller and a longer delay is needed to reach the optimum condition of  $L(\nabla n_e)$  or the plasma density for an maximized HH emission. This principle was validated in a measurement for P2 at linear laser polarization, but now for two different intensities:  $I_P(1) = 1 \times 10^{18}$  W/cm<sup>2</sup> and  $I_P(2) = 3 \times 10^{17}$  W/cm<sup>2</sup>. The corresponding measurement is shown in Fig. 8.11. Here, the P2 pulse was applied with a delay time similar to the optimum found for circular polarization at  $\sim -5$  ps. As demonstrated in Fig. 8.10, for the pre-pulse at linear polarization and high intensity  $I_P(1)$ , this delay is too long to reach the maximized HH emission, since the pre-pulse was applied too early. But for a lower intensity ( $I_P(2)$ ) the HH signal could be enhanced for this delay time. The measurement revealed a dependency of the optimum delay time on the intensity level of the pre-pulse. It can be concluded from this that the optimum condition of  $L(\nabla n_e)$  and/or the plasma density for an enhanced HH emission can be controlled with the intensity and the delay of the pre-pulse.

### 8.3.4 Discussion of the Enhanced High Harmonic Emission

In publications about HH emission in forward direction from sub 400 nm foils, the best results for  $N_{max}$  and the intensity of the detected HH signal were reported from laser systems that have small pre-pulses, few ps before and an approximately  $< 10^{-4}$  smaller intensity than the laser peak intensity [63, 112]. In general, pre-pulses introduce longer rise of the plasma density and can even lower the target density for an ultrathin foil. As seen in PIC simulations, the efficiency of the HH emission is strongly dependent on the scale length of the plasma density gradient and on the electron density of the plasma [4, 24, 68]. An optimum plasma gradient length of  $> \lambda_L/5$  was derived from a comparison between experimental results and PIC simulations in [68] for the ROM emission process. In this work an enhancement of up to a factor of about  $\times 4$  in the HH peak intensity was shown, when a slightly lower laser contrast enabled a longer rise of the plasma density. The findings referred to a ROM harmonic emission in the reflection direction with a laser incidence angle of  $45^\circ$  on a solid state bulk target. Since a sufficiently high laser contrast is still needed for an emission of HH, this "medium" laser contrast was realized by using a single instead of a double plasma mirror (cf. Section 5.3). The results presented here revealed a method by which a significantly better access to the control of the pre-plasma is obtained. This is enabled by a strong pre-pulse at an optimized delay time and intensity, which was shown to significantly enhance the HH emission efficiency. The investigation presented here showed that the expansion velocity can be controlled with the applied pre-pulse and intensity, and that for the efficiency of the HH emission, the resulting pre-plasma condition is a highly sensitive parameter.

With applying a similar method to manipulate the rise of the plasma density, an inhibition of the CWE HH emission process was recently reported in Ref. [65]. For a laser incidence angle of  $45^\circ$  at a solid state target, a laser field strength of  $a_0 = 0.7$  and for an XUV detection in specular direction, a suppression of the HH emission was found when a pre-pulse with  $I_P = 10^{14}$  W/cm<sup>2</sup> had heated the target few ps earlier. For the parameters and setup used in that work, an expansion velocity of  $v_{ion} > 1 \times 10^6$  cm/s was assumed that enlarged the scale length of the plasma gradient to  $\geq 0.1\lambda_L$  for a delay of  $-2$  ps and inhibited the CWE emission process. In contrast, the experiments presented here used a significantly higher pre-pulse intensity that should cause a higher expansion velocity, and thus, a longer scale length of the plasma density gradient and/or even a decreased plasma density. The experiments demonstrated an enhancement of the HH peak intensity of about one order of magnitude for a delay time of  $-2$  ps. These findings and the comparison suggest that the CWE model is not the underlying emission process, since the CWE requires a very steep plasma gradient and should become inefficient and/or deliver smaller values of  $N_{max}$  for a decreased target density [5, 24].

In addition, the sensitive dependency of the HH emission efficiency on the properties of the pre-plasma could explain qualitatively the differences that become apparent in a comparative study of Ref. [63, 112] and Ref. [57, 119]). For HH emission from ultrathin foils and in the laser propagation direction, a high HH intensity was only reported from laser systems with a high laser contrast and a pre-pulse(s) at few ps and with regards to the here discussed experimental results ([63, 112] compared to [57, 119]). In the cases where the laser intensities can be compared significant differences in the HH cutoff frequency become apparent. A remarkable higher cutoff frequency seems were detected for laser systems with a longer laser pulse duration and a higher laser energy.

## 8.4 Conclusions on the XUV Emission

### XUV emission at different laser contrast conditions

The XUV radiation emitted in the forward direction from the interaction between a single ultra-intense laser pulse and an ultrathin foil target was characterized for two different laser contrast conditions. The emission of high harmonic radiation from dense laser-plasmas is contingent on a steep plasma boundary. This condition is not fulfilled for the laser at high contrast, since this pre-heats the target with weak pre-pulses some (ns) and continuously with a rising intensity level some ps before the laser peak intensity interacts with it. High harmonic radiation was only detected with the ultrahigh laser contrast condition. Its intensity could be remarkably enhanced when this laser contrast condition was used and an additional strong pre-pulse was applied on the timescale of few ps. This demonstrated that the HH generation is dependent on a specific pre-condition of the plasma.

For the ultrahigh laser contrast condition the detected spectra consisted of high harmonic radiation and an incoherent XUV background. This XUV background spectrum differs from the spectra measured for the high laser contrast

condition by exhibiting a lower intensity level in a specific spectral range. This observation correlates to the difference in the amount of emitted fast electrons for these two different contrast conditions, which was demonstrated in Section 7.2.1. In addition, for the foil thicknesses discussed here ( $< 100$  nm) it also correlates to a discrepancy in the kinetic energies of the accelerated ions and to a much higher laser transmission through the target. Here, interesting questions arise, how do pre-plasma properties influence the laser to plasma absorption and the electron dynamics at the target boundary? In this context, perturbation processes of the laser driven electron dynamics at the plasma boundaries have to be further investigated.

### The Enhanced High Harmonic Emission

In a first approach, a strong pre-pulse was applied at different delay times on the target's back side and for the laser at ultrahigh contrast condition. A second counter-propagating laser pulse at an intensity of up to  $1 \times 10^{18}$  W/cm<sup>2</sup> served as a pre-pulse. It arrived at the target a few ps earlier than the stronger drive pulse. This method showed an enhancement of the HH emission of about one order of magnitude (cf. Section 8.3). The investigation excluded HH emission from the interaction of the applied pre-pulse in a direct measurement and by using a circularly polarized pre-pulse [126]. Hence, the enhanced HH emission is a consequence of a manipulation of the pre-plasma condition, such as enlarging the rise of the plasma density or even reducing the target density. The mechanism is similar as reported for the ROM harmonic emission from solid bulk targets, where a specific scale length of the plasma density gradient is needed for a high emission efficiency [24, 68]. The investigation revealed that maximization of the HH intensity required simultaneous adjustment of both the delay time and the intensity of the pre-pulse. In comparison to Ref. [68], therefore a method was revealed, which enables a controlled alignment of the plasma pre-condition. The enhanced HH emission exhibited a remarkable signal strength and high reproducibility. This stands in contrast to the HH radiation obtained without the second laser pulse, which was observed with high fluctuations in the intensity.

The HH radiation was found to originate from the target front side, since up to a certain harmonic number the HH signal was suppressed, either with the application of the pre-pulse or without. No evidence to definitely attribute the HH generation mechanism to either the CSE, ROM or CWE model was obtained from single laser pulse experiments. However, the CWE model requires a refined theoretical model for the case when the laser illuminates the target at normal incidence. The CWE emission efficiency is dependent on a steeper rise of the plasma density than in the case of the ROM model [24, 65]. In the experiments enlarged the rise of the plasma density and caused with this method a significantly enhancement of the HH emission. This stands in contrast to the CWE model [65] and hence, at least for the enhanced HH emission the CWE model should be excluded as the driving mechanism. However, neither in the enhanced HH emission nor in the HH spectra obtained at different target densities or thicknesses a

definite change in the harmonic cutoff frequency was found. These findings and the comparison to literature for the experimental situation discussed here, point to other parameters, such as, e.g. the laser energy or pulse duration, that affect the HH cutoff frequency.

### Relativistic Backscattering

The principle of relativistic backscattering according to the relativistic mirror model was tested in a two laser pulse experiment. As shown in Section 7.3 one laser pulse accelerated electrons to relativistic velocity from an ultrathin foil target. The second weaker, but still strong laser pulse ( $I_P = 1 \times 10^{16}$  to  $1 \times 10^{18}$  W/cm<sup>2</sup>) propagated in the opposite direction to the electrons, from which it was supposed to be backscattered and shifted in frequency. The backscattering was tested with different approaches, at different laser contrast conditions, different laser intensities, for different target systems. For these various parameter sets the measurements did not observe a clear indication for a backscattered signal which was shifted in frequency. For the UHC condition, instead evidence for a disturbance of the HH emission process was found, close to the temporal overlap of both pulses. To realize the promising idea of relativistic backscattering to obtain a brilliant, coherent and high energetic photon source, a much higher density of the electron bunch is needed, and an affect of the intensity of the second laser pulse has to be considered.



## Part IV

# SUMMARY AND OUTLOOK



---

## 9 Summary and Perspective

This work presented a comprehensive experimental study of the emission of electrons, ions and XUV radiation in laser-plasma experiments using ultrathin foils targets. The laser-plasma dynamics reflect a relativistic, highly nonlinear interaction between coherent laser light and a fully ionized plasma. A variety of physical processes occur simultaneously and the impact of each is highly dependent on the boundary conditions. In this complex interaction, the experimental parameters determine whether a certain process is dominant or suppressed. This thesis examined correlated parametric dependencies and revealed new effects. The findings obtained improved and refined the understanding of the interplay between laser-driven collective electron motions and the ion and electron acceleration schemes. This, in combination with the new experimental methods presented here, introduces a novel approach to the access and control of certain laser-plasma processes, allowing the experimental results to be optimized to a remarkable degree.

### 9.1 Laser Ion Acceleration

Laser plasma ion acceleration in the high intensity range has now been studied for more than two decades accompanied by the rapid development of the laser technology over the same time period. Several parameters have a great impact on the laser-plasma dynamics and hence, on the efficiency of the laser ion acceleration: the laser energy and pulse duration, the laser contrast and the target system. In this work, the attention was paid to the laser contrast and the target system. New methods for manufacturing and characterization of ultrathin foils from different constituents were developed [70]. In particular, this work found a method to produce heavy material foils in the sub 50 nm range and few nm thick double layer foils consisting of a heavy material layer on a low density hydro-carbon substrate foil. With these foils, a new and efficient acceleration of heavy material (gold and silver) into the kinetic energy regime above about 1 MeV/u for high ion charge states ( $Z^{max}/A \leq 0.3$ ) was discovered. In contrast to prior publications and predictions [35, 39, 42, 85], these heavy ions were accelerated in the presence of the contamination layer and even in the presence of a several nanometer thick hydro-carbon layer [74]. This result reduced the demands of the target preparation and the laser intensity required for an efficient heavy ion acceleration. Furthermore, this revealed a new acceleration mechanism with a significantly higher charge to

kinetic energy scaling for heavy ions. The heavy ions' spectra exhibited a characteristic charge to kinetic energy distribution. A detailed analysis was presented here and gave new and fundamental insights into the ion acceleration dynamics for a multi-ion species laser-plasma interaction. The spectral features of the heavy ions and their dependency on specific parameters offer a unique method for the examination of staged acceleration processes and related fundamental questions, e.g., how do the ions separate in the acceleration process, and how does this affect the kinetic energies in a mixed acceleration scheme? These findings pointed to fundamental principles, e.g. to inherent ion recharging processes during the ion acceleration, and to a shock acceleration due to the radiation pressure at the laser illuminated foil side, even for heavy ions.

Moreover, subsequent electron capture was demonstrated for laser-accelerated ions that had passed through a second separated ultrathin foil. The efficiency of this process was found to scale with the charge state and velocity of the ion beam. These observations complemented recent observations [86, 87, 96, 98] on charge transfer processes. The cross-sections for these processes in (ionized) matter are objectives of the most recent investigations [87, 88, 98, 100, 103]. Since electron capture significantly affected ions with the highest charge state and was found to decrease with the velocity of the projectile ion, the final ion distribution is spectrally filtered. This results holds promises as a simple method to obtain a remarkably narrow spectral emittance for ion beams. The spectral emittance is a very important parameter for laser ion acceleration in potential future applications [3].

The highest kinetic ion energies were obtained for a RPA influenced acceleration using the highest laser contrast and an optimized foil thickness and density. The results presented improved prior works [2, 10, 127] and significantly lowered the demands on the target thickness. When using hydrocarbon foils, a benchmark of about 15 MeV/u for the protons and of about  $\sim 7$  MeV/u for the carbon ions was reached applying a laser field strength of  $a_0 = 5$ .

## 9.2 Laser Electron Acceleration

Answering the fundamental question, how can the electrons gain high kinetic energies in the field of a laser pulse? requires the marriage of the single electron picture including relativistic effects with a complex macroscopic model for a laser pulse interaction at an overdense but partly transparent plasma boundary. A complete model, covering all involved dynamics and including the multiple particle interaction with the laser pulse, is still the subject of ongoing research [17, 22, 56, 65, 106, 107]. Since in general, the electron dynamics dominate the laser-plasma interaction and thus determine all subsequent processes, e.g. the ion acceleration, XUV and high harmonic emission, their investigation is important and fundamental. The examination presented here showed how the experimental results of ion acceleration and high harmonic emission correlate to the spectra of the fast electrons with kinetic energies in range 0.2–30 MeV. These correlations

are important for the derivation of the underlying models.

This thesis characterized the spectral distribution of fast electrons emitted in the laser propagation direction from ultrathin foils. The experimental results provided new and important insights into the multi-parametric dependency of the electrons' spectral distribution. The findings complement current discussions about the laser to electron absorption mechanisms and about the electron acceleration and emission in a pulsed laser field and from dense plasmas [17, 56, 65, 107]. The electron spectra measured in this work were discussed in detail in the context of the latest published works. Summarizing briefly, significant differences were found between the results obtained with the experiment setup used here (normal laser incidence angle on an ultrathin foil target and detection of fast electrons normal to the target) and results reported using an oblique laser incidence angle and detecting fast electrons in the specular direction. Hence, the recent models [17, 65, 107] can not be easily transferred to the laser-plasma interaction at ultrathin foil targets. Understanding the underlying physics behind this difference will require further investigation. The acceleration and deceleration of electrons in a transient laser field needs further analysis, within a macroscopic picture, to determine the affect it has on the electron emission efficiency and kinetic energies. The description of how electrons are ejected from the laser field and the plasma potential for the situation discussed here needs further refinement with regards to the emitted spectral distribution, place of emission, ponderomotive effects, and anharmonic plasmon excitations in the plasma skin layer.

Nevertheless, the investigation presented here already demonstrated that the electron spectra, ion acceleration, and XUV emission have mutual parametric dependencies. For example, the amount of fast electrons emitted is determined by the laser contrast condition. Hence, for a steeply rise plasma density at the plasma boundary, the emission of fast electrons is restricted, in contrast to a long pre-expanded one. This observation correlates to a more efficient ion acceleration and the emission of coherent XUV radiation in the case of a steep plasma boundary. The fast electron spectrum could potentially be developed as an additional diagnostic for the laser-plasma interaction since it was shown to be sensitive to many parameters, such as, e.g., the condition of the pre-plasma, the laser energy and laser intensity, the target thickness and even the target holder construction. More investigations and comparison of electron spectra obtained from different laser systems are required in order to derive scaling laws and to fully resolve the interdependencies found in the spectral distribution of the fast electrons.

Moreover, the experiments tested, as suggested by Ref. [109], if the fast electron emission could be enhanced when the electrons are decoupled from the transmitted laser field by the use a second, separated ultrathin foil. This method was predicted to inhibit electron deceleration caused by the decay of the laser field envelope. Experiments have tested this method and revealed an enhancement of the emitted electron numbers in a narrow spectral range. Further investigation examined different parameters in order to extract the mechanism of this effect. The amplification of the electron number could be enhanced to a remarkable ex-

tent when a second, weaker laser pulse pre-heated the second foil at different delay times on a timescale of few picoseconds. So far, the results point to an interpretation that is close to the suggestion of Ref. [109]: The emission efficiency of fast electrons seems to be determined by the deceleration in the light field from the transmitted laser pulse and the emission could be remarkably enhanced when the electrons had been decoupled from the declining transient light field. The effect will be further investigated in cooperation with A. A. Andreev.

### 9.3 XUV Emission From Laser Plasma Interaction

High harmonic emission from the laser-dense plasma interaction holds promise as a brilliant coherent XUV source, and is a hot topic of ongoing research to that end. Depending on the applied laser contrast, the emitted XUV radiation was demonstrated to be either coherent or incoherent plasma emission. High harmonic emission is caused by laser driven coherent collective electron oscillations at a steep plasma boundary. Every laser cycle a single XUV-pulse is emitted with a pulse duration smaller than one laser cycle. According to the ROM [4] or CSE model [128], the harmonic cutoff frequency and the pulse duration of such a single HH pulse is determined by the laser intensity. A remarkably high photon flux is predicted, as this also scales with the laser intensity and can reach an efficiency of up to  $10^{-5}$  [7, 126]. In the case of high harmonic radiation that is emitted in the laser propagation direction at a laser incidence angle of  $0^\circ$ , as examined in this thesis, the underlying theoretical model is disputed [54, 57, 63, 112, 118, 119, 126]. The results obtained here were discussed in the context of the emission models ROM, CSE and CWE. No definite evidence was found to conclude or exclude a particular model. The efficiency of the high harmonic generation depends on a specific length of the plasma gradient [24, 65, 68] or the plasma density [4, 5]. Hence, it can be optimized and distinguished by a careful manipulation of the pre-plasma, for example, by using different laser contrast conditions [65, 68]. The experiments in this thesis demonstrated for the first time, for the high harmonic emission in forward direction, an enhancement of the high harmonic intensity of about one order of magnitude due to a manipulation of the plasma boundary. With a strong second laser pulse the target was pre-heated and pre-expanded on a timescale of few picoseconds. This optimization of the pre-plasma in order to maximize the high harmonic emission was demonstrated to be achievable by controlling the intensity of the pre-pulse and the applied delay time. This method causes a target expansion that introduces a longer scale length of the plasma gradient and could even lead to a decreased target density. In addition, this effect excluded the CWE model for the enhanced HH emission. Although the details of the expansion velocity require further investigation, this method already promises an efficient and controllable way to maximize the high harmonic emission.

## 9.4 A Controlled Manipulation of Plasma Dynamics

Pre-pulses and/or the rise of the laser intensity level have a big impact on the plasma properties leading to significantly different results for the ion, electron and XUV emission. This was observed at least since the development of laser systems capable of achieving the ultrahigh laser contrast. However, little in particular is known about the impact of the pre-plasma properties on the laser plasma dynamics. This lack of knowledge often hinders a direct comparison of the experimental result obtained using different laser systems and to predictions from theoretical models. This thesis characterized differences in the ion, electron acceleration and the XUV emission for two different laser contrast conditions. Since these processes occur simultaneously it is important to understand how the property of the pre-plasma changes their interplay.

This thesis investigated how an artificially applied strong pre-pulse influences the ion, electron and XUV spectrum at ultrahigh laser contrast. The results demonstrated that for a pre-pulse with an intensity of  $< 1 \times 10^{18} \text{ W/cm}^2$  the decrease in the maximum kinetic energies of the ions is proportional to the delay time over a range of a few picoseconds. For the same parameter set, a remarkably enhanced high harmonic emission was detected and when heavy material foils were used an increase in the total number of accelerated ions was found. These findings demonstrated that an artificial pre-pulse at ultrahigh laser contrast is an effective method to change the properties of the pre-plasma. This method gives access to control the laser-plasma dynamics that in consequence significantly causes specific processes to be inhibited or enhanced. In addition, it was shown that the spectrum of laser accelerated ions and electrons are affected by a post-interaction with a second laser pulse. Further investigation using different pre- or post-pulse intensities, longer timescales and different target systems is required, but the latest publication [65] and the findings presented here already demonstrated that this method holds promises to become a new way to control the laser-plasma absorption mechanism and the collective electron dynamics, and hence all other simultaneously occurring processes.



---

# A Appendix

## A.1 Additional Material on Laser Ion Acceleration

In the following additional material for the experiments on laser-ion acceleration is provided and complements Chapter 6. The results were obtained in the same experimental campaigns and with the experimental setup and methods described in Chapter 5.

### Efficient Acceleration of Silver Ions

Laser heavy ion acceleration was demonstrated for ultrathin gold foils in Section 6.3. The experiments used also silver coated PVF foils, and a typical obtained ion spectrum is shown in the following. The same experimental setup as in Section 6.3 was used and the laser illuminated the foil at normal incidence angle with  $a_0 = 5.5$  and the UHC condition. Linear laser polarization was applied. Accelerated silver ions are shown in Fig. A.1 for a measurement using a 13 nm thick PVF foil with a silver coating of 3 nm at its backside. The silver atoms appeared in a bunch of ion traces that corresponds to successive charge states from  $Z \geq 30+$  to  $Z = 38+$ . The silver atoms reached a maximum kinetic energy of  $\leq 1.3$  MeV/u for  $\text{Ag}^{38+}$ .

### High Laser Contrast and Heavy Ion Acceleration

No gold ions were accelerated when the high instead of the ultrahigh laser contrast condition was applied with using gold foils up to a thickness of 50 nm or gold coated plastic foils up to a total thickness of 80 nm. An example is shown in Fig. A.2 for a measurement with using 12 nm gold foil and the high laser contrast condition. The spectrum was obtained in same experimental run and with the same experimental conditions as the results in Fig. 6.4 in Section 6.3.1 ( $a_0 = 5.5$ , linear laser polarization, normal incidence).

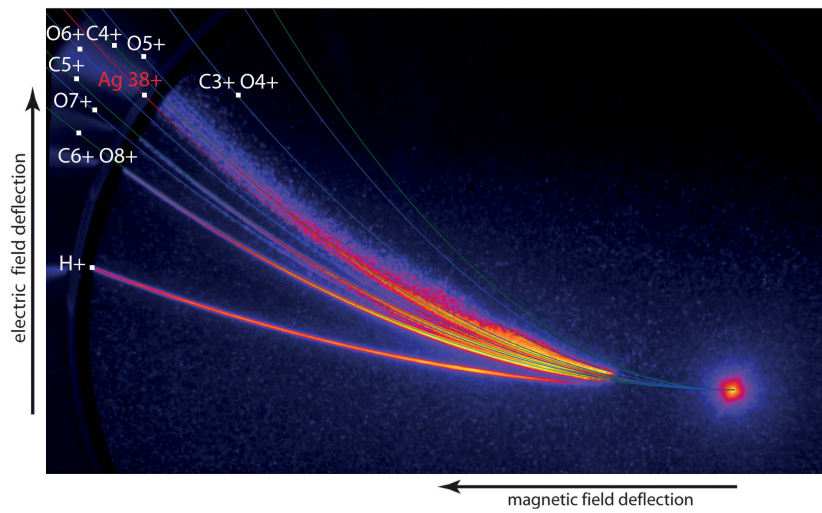


**Figure A.1:** A image of the ion spectra on the detector from laser interaction with a  $(3 \pm 1)$  nm silver backside coated  $(13 \pm 1)$  nm thick PVF foil. Theoretical Thomson parabolas for various charge to mass ratios are shown.

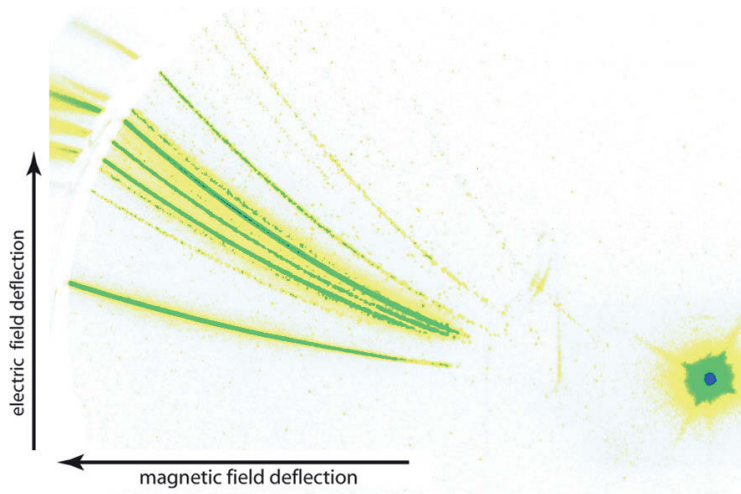


**Figure A.2:** The image of the detector shows the ion traces that were accelerated from a  $(12 \pm 3)$  nm gold foil and with using the HC condition.

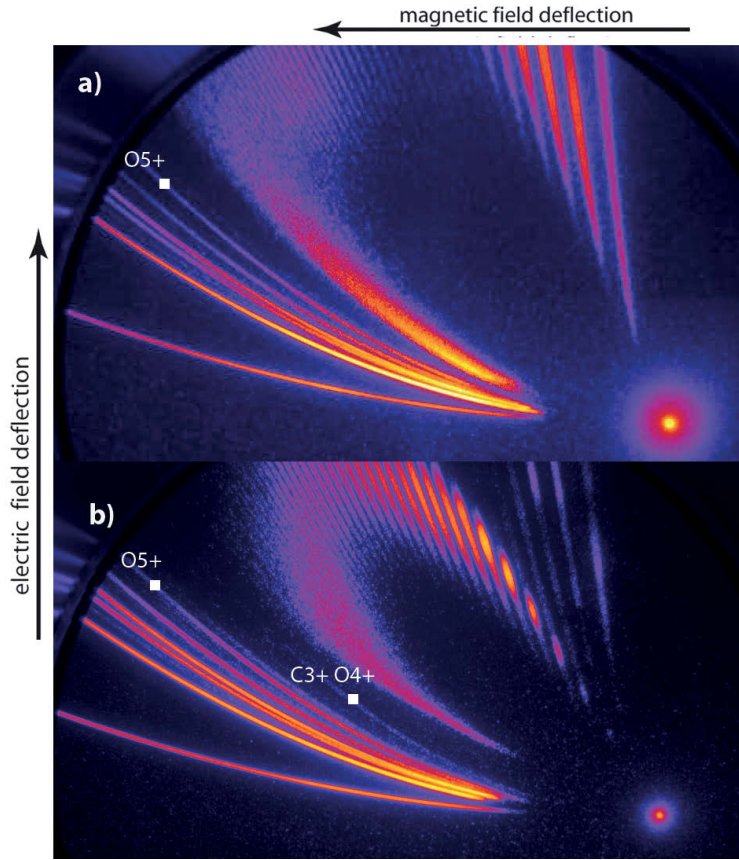


**Figure A.3:** The detector images show accelerated gold ions that passed through the Thomson spectrometer. The measurement used gold coated PVF foils and a circular laser polarization. a): Measurement with a PVF foil thickness of  $(12 \pm 1)$  nm and a  $(6 \pm 2)$  nm thick gold coating at the foil's front side, b): with a PVF foil thickness of  $(23 \pm 1)$  nm with a  $(4 \pm 1)$  nm gold coating at the foil's front side.

### Heavy Ion Acceleration with Circular Laser Polarization

Gold ions were also efficiently accelerated with the laser at circular polarization, shown in Fig. A.3. The laser was applied with an field strength of  $a_0 = 5.5$ , the UHC condition and the experimental setup used in Section 6.3. Here, the gold ions exhibited similar spectral characteristics as in the case of the linear laser polarization. In a direct comparison between both, with circular laser polarization the maximum kinetic energy of the heavy ions were found somewhat lower. When the gold layer faced to the laser illuminated side, the spectral bandwidth of the gold ions was observed significantly decreased, as depicted in Fig. A.3 b).

### Electron Capture with the High Laser Contrast Condition

Experiments used a double foil target configuration. It consisted of two ultrathin foils that were separated about a distance of 500  $\mu\text{m}$ . By this method an efficient

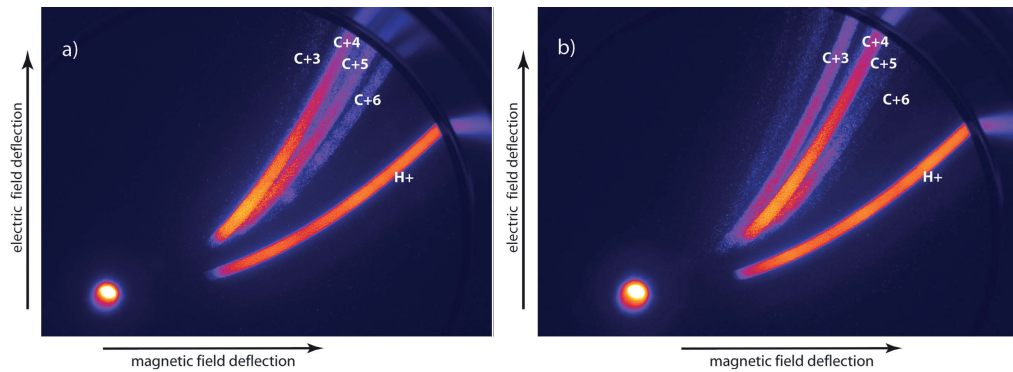


**Figure A.4:** The ion spectra on the detector from laser interaction with a): a single,  $(90 \pm 3)$  nm PVF target and b): the double foil configuration. Both PVF foils had a thickness of  $(90 \pm 3)$  nm. The measurements were taken in the same experimental run and with applying the HC condition.

electron capture in the ion spectrum was observed, as presented in Section 6.5 for the laser at UHC condition. Similar electron capture processes were observed for the lower laser contrast condition and the double foil configuration. An example is shown in Fig. A.4 obtained in the same experimental run and under the same experimental conditions. Carbon ions were detected at charge stages of  $Z=3+$ ,  $2+$  in the case of the double target. These charge states were not present in the ion spectrum obtained from the single foil configuration. The decrease in the charge state correlates to a remarkable smaller particle number of  $C^{6+}$  and  $C^{5+}$ .

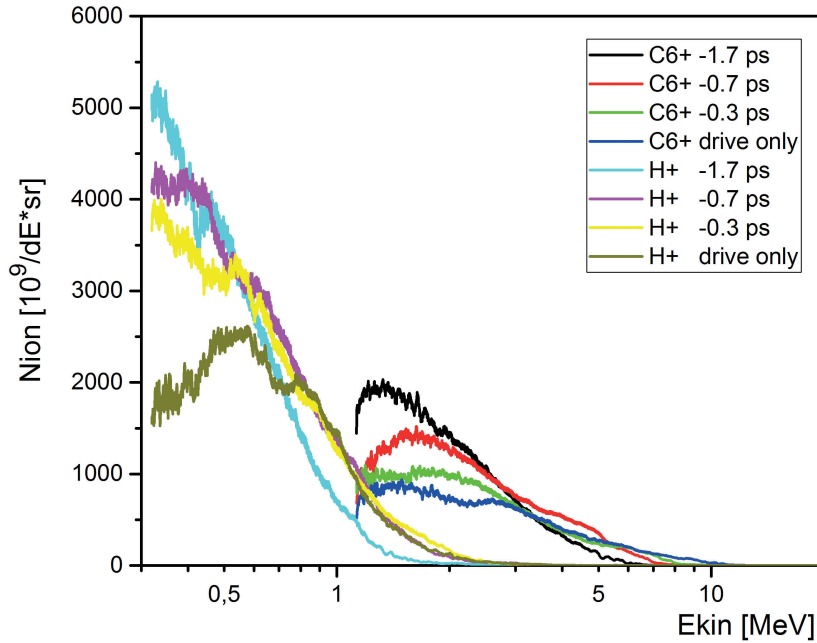


**Figure A.5:** The ion spectra of hydrogen and fully ionized carbon from a  $(50 \pm 4)$  nm gold foil and measured for different delay times of the pre-pulse (P2). For a comparison, a measurement without the P2 pulse is shown. Note, the scaling of the y-axis was chosen linear.

### The Ion Spectrum from a Preheated Gold Foil

A significant enhancement in the overall ion particle number was detected for a 50 nm gold foil target when the foil's backside was pre-heated by a strong ultrashort pre-pulse. The main results were already presented in Section 6.6 and a detailed description of the methods use can be found in Section 5.4. In the following, details of the experiment with a pre-heated gold foil in Section 6.6 are presented. The measurements are taken from the same experimental run as in Fig. 6.17 with the same experimental parameters (linear laser polarization, UHC and  $I_P = 9 \times 10^{17}$  W/cm<sup>2</sup>, 50 nm gold foil). The pre-pulse was applied with linear laser polarization and an intensity of  $9 \times 10^{17}$  W/cm<sup>2</sup>. It heated the target backside few picoseconds before the stronger drive pulse arrived. Fig.A.5 shows the evaluated spectra of C<sup>6+</sup> and H<sup>+</sup> ions for different delays. For the same measurement, Table A.1 gives the relative difference of the integrated particle number to a reference measurement of an un-heated target and with respect to the detection range.

When the P2 pulse was applied at a delay of  $-0.7$  ps, a variety of new ion traces appeared on the detector that otherwise were not detected. This can be seen in Fig. 6.17 of Section 6.6 and the corresponding Z/A were evaluated to derive an identification. For the spectrometer configuration used, the Z/A ratio

delay time	ion species	relative $N_{ion}$
-1.3 ps	H <sup>+</sup>	1.0
-0.7 ps	H <sup>+</sup>	1.3
-0.3 ps	H <sup>+</sup>	1.2
-1.3 ps	C <sup>6+</sup>	1.2
-0.7 ps	C <sup>6+</sup>	1.3
-0.3 ps	C <sup>6+</sup>	1.0

**Table A.1:** The relative increase of the integrated particle number for ion species depicted. The value is given relative to measurement without applying the P2 pulse and for different delay times. The measurement corresponds to the one shown in Fig. A.5.

can be distinguished with an accuracy of up to  $\Delta Z/A \geq 0.0015$ <sup>1</sup>. The charge to mass ratio of these new traces are listed in Table A.2. Next to constituents of the target material and parting agent used (see Section 5.5), other elements were taken into account. Table A.2 depicts elements with charge to mass ratio that matched to the unidentified ion traces in the given accuracy. Since the target was a gold foil with an purity of 99.99%, light elements can originate from contamination by air, water or rests of the parting agent Victawet, which consists of a phosphor-ester. In Section 5.5 the stoichiometry was measured for a gold foil with a 12 nm thickness and determined the content of carbon and oxygen about < 4%, gold about 96% and all other elements below < 1%. Table A.2 shows, that even with considering C,O,N and P, some of detected Z/A ratios are left unidentified. In a following step, some of the natural isotopes were taken into account and delivered some matches, e.g. C<sub>13</sub>. The natural occurrence of C<sub>13</sub> is about 1.1%. An ion trace at the charge to mass ratio of  $Z/A(C_{13}^{6+}) = 0.462$  has been observed earlier in measurements with other experimental conditions, e.g. for pure plastic, gold or Ti targets and for single laser pulse interaction (see Fig. 6.1 in Section 6.1). Natural isotopes of C, N and O have a much smaller probability than C<sub>13</sub>, but even these could still not cover all charge to mass ratios detected<sup>2</sup>. All elements up to the 4. period were assigned in Table A.2 and possible matches with unidentified traces are shown. However, these constituents are unlikely without further validation, since they can originate neither from the parting agent, nor from a contamination according to the purity of the gold foil. Heavier ions, such as e.g. gold, delivered some matches, but with non-sequential (single) charge states, which is unlikely, as discussed in Section 6.3.3. In Section 6.3 it was shown, that light elements are accelerated with successive charge states reaching from full ionization down to a certain Z/A ratio (in Table A.2  $Z/A \geq 0.167$ ). On contrary, heavy elements with  $A > 100$  were detected in the range  $0.250 < Z/A < 0.005$  and always appeared as a multiplet of traces. For this reason, the gold ions at charge states, matching to

<sup>1</sup> The accuracy is not constant for Z/A. It is taken from the deviation of theoretical Thomson parabolas for each Z/A ratio with a minimum separation given on the detector image due to the particle pinhole diameter.

<sup>2</sup> An acceleration of molecule fragments e.g. CH<sub>x</sub> find among the measurement accuracy the same Z/A numbers as the carbon isotopes.

Z/A	contamination	isotopes	elements	signal strength
$1.000 \pm 0.003$	$\text{H}_1^+$			very strong
$0.499 \pm 0.002$	$\text{C}_{12}^{6+}, \text{N}_{14}^{7+}, \text{O}_{16}^{8+}$			very strong
$0.461 \pm 0.002$		$\text{C}_{13}^{6+}, \text{N}_{13}^{6+}$	$\text{B}^{5+}, \text{K}^{18+}, \text{Ti}^{22+}, \text{Cr}^{24+}, \text{Ni}^{27+}$	mid
$0.438 \pm 0.002$	$\text{O}_{16}^{7+}$			strong
$0.428 \pm 0.002$	$\text{N}_{14}^{6+}$	$\text{C}_{14}^{6+}$	$\text{Fe}^{24+}, \text{Zn}^{28+}, \text{Ge}^{31+}, \text{As}^{32+}, \text{Kr}^{36+}$	mid
$0.416 \pm 0.002$	$\text{C}_{12}^{5+}$			strong
$0.405 \pm 0.002$			$\text{S}^{13+}, \text{V}^{21+}, \text{Cr}^{21+}, \text{Se}^{32+}, \text{Kr}^{34+}$	weak
$0.390 \pm 0.003$		$\text{O}_{18}^{7+}$	$\text{Na}^{9+}, \text{P}^{12+}, \text{Co}^{23+}, \text{Ni}^{23+}, \text{Ga}^{27+}, \text{As}^{29+}, \text{Se}^{31+}, \text{Br}^{31+}, \text{Au}^{77+}$	weak
$0.375 \pm 0.0015$	$\text{O}_{16}^{6+}$			strong
$0.357 \pm 0.0015$	$\text{N}_{14}^{5+}$	$\text{C}_{14}^{5+}$	$\text{K}^{14+}, \text{Sc}^{16+}, \text{Fe}^{20+}, \text{Co}^{21+}, \text{Ni}^{21+}, \text{Ge}^{26+}, \text{Kr}^{30+}$	mid
$0.344 \pm 0.0015$			$\text{Si}^{10+}, \text{Ga}^{24+}, \text{Ge}^{25+}, \text{Au}^{68+}$	weak
$0.333 \pm 0.0015$	$\text{C}_{12}^{4+}$	$(\text{N}_{15}^{5+}, \text{O}_{18}^{6+})$		mid
$0.285 \pm 0.0015$	$\text{N}_{14}^{4+}$	$\text{C}_{14}^{4+}$	$\text{Kr}^{24+}, \text{Au}^{56+}$	weak
$0.250 \pm 0.002$	$\text{C}_{12}^{3+}, \text{O}_{16}^{4+}$			mid
$0.214 \pm 0.002$	$\text{N}_{14}^{3+}$	$\text{C}_{14}^{3+}$	$\text{Fe}^{12+}, \text{Zn}^{14+}, \text{Ga}^{15+}, \text{As}^{16+}, \text{Se}^{17+}, \text{Br}^{17+}, \text{Kr}^{18+}, \text{Au}^{42+}$	weak
$0.188 \pm 0.002$	$\text{O}_{16}^{3+}$			weak
$0.167 \pm 0.002$	$\text{C}_{12}^{2+}$			weak

**Table A.2:** Charge over mass ratio of detected ion traces from gold foil 50 nm at  $\Delta t_P = -1.67$  ps. For unidentified Z/A numbers elements are assigned when they match within the accuracy, regardless of the target constituent or natural proportion.

the unidentified charge to mass ratios in Table A.2, might be excluded. In addition it would raise the question, how to explain such a high degree of ionization.

In conclusion, a satisfying explanation or a sufficient identification was not found. Next to a precise determination of the foils contamination e.g. by the target support<sup>3</sup> one might consider nuclear reactions as suggested in [129].

<sup>3</sup>Target support is a steel plate with holes of 0.6 mm diameter on which the freestanding gold foil was placed. Laser was focused in the middle of the foil, monitored by the BRF diagnostic

## A.2 Additional Material on the Fast Electron Spectrum

In the following, experimental results are shown to complement Chapter 7. The same experimental setup and methods were used and measurements were obtained in the same experimental campaign.

### Dependency of the Electron Spectrum on a Displacement of the Focal Plane

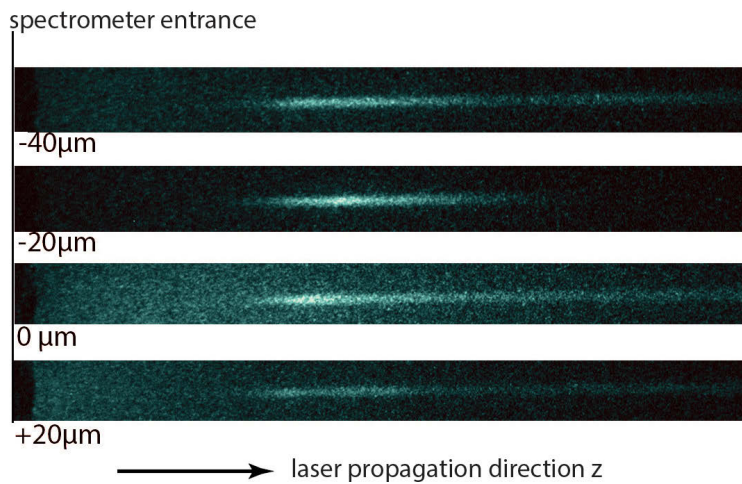


**Figure A.6:** Detector images are shown for the spectra in Fig. 7.2 in Section 7.2.2. The laser interacted at HC condition with a  $(35 \pm 2)$  nm PVF foil and with small displacements of the focal plane in coordinate  $z$  of the laser propagation direction. Electrons were detected in the same direction. The pictures are in a comparable colour scaling and are taken in the same experimental run.

For a small displacement of the laser’s focal plane on the target, the detected fast electron spectra differed, as shown and discussed in Section 7.2.2. Further examples are depicted in Fig. A.6 and Fig. A.7. The displacement refers to the coordinate of the laser propagation direction. Negative values correspond to a focus position before the target, positive values to one inside the target, respectively. Fig. A.6 depicts the detector images in a comparable colour scaling for the electron spectra in Fig. 7.2 (cf. Section 7.2.2). Fig. A.7 summarizes a similar comparison for the single and double foil configuration. Different features appear in the electron spectrum at different displacement positions of the focal plane on the target. Each picture refers to a different experimental run but the measurements of one picture refer to the same experimental run.

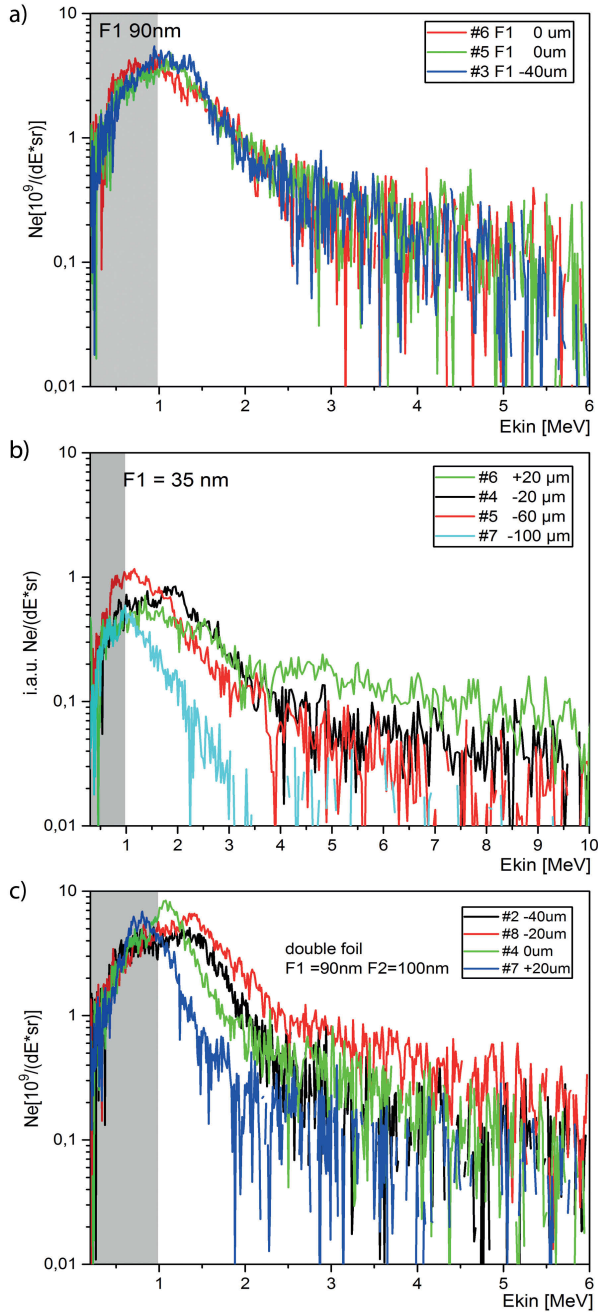


**Figure A.7:** The electron spectra for different positions of the focal plane on the target. a): Single PVF foil,  $(90 \pm 4)$  nm thick with the HC condition,  $a_0 = 6$ , a laser energy of  $1.8 \pm 0.1$  J on the target and spectrometer configuration III, b): single PVF foil, 35 nm thick with HC condition,  $a_0 = 6$  and  $E_L = 1.7 \pm 0.1$  J obtained from spectrometer configuration II. The electron number is given in an arbitrary unit. c): Double PVF foil configuration, foils are separated about  $500 \mu\text{m}$ . F1 has a thickness of  $(90 \pm 4)$  nm and F2 of  $(100 \pm 4)$  nm. The experiment applied the laser with  $a_0 = 6$ , the HC condition and a laser energy of  $1.8 \pm 0.1$  J on the target. The measurement was taken with spectrometer configuration III.

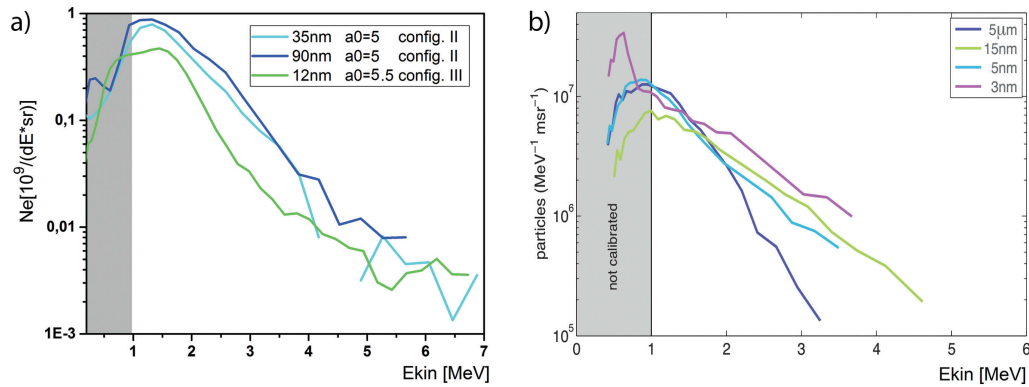


**Figure A.8:** The electron spectra measured with ultrahigh laser contrast for different PVF foil thickness: a): Obtained for PVF foils with a thickness of  $(12 \pm 1)$  nm,  $(35 \pm 2)$  nm and  $(90 \pm 3)$  nm. The measurements relate to different experimental runs and different spectrometer configurations and an applied laser field strengths  $a_0 = 5$  and  $a_0 = 5.5$ , respectively. b): The electron spectra detected in experiments of the MBI laser system in the year 2010 with the laser at ultrahigh contrast condition. The picture is taken out of [56]. The results were obtained with  $a_0 = 3.5$  and diamond like carbon foils at various thickness. Note, the scaling of the particle differs between a) and b).

## Electron Spectra for the Optimized Ion Acceleration

Since the ion acceleration approved a strong dependence of the target thickness (cf. Section 6.2), the experiment investigated if this correlates to changes in the electron spectrum for comparable parameters, as e.g. applied laser field strength  $a_0 \leq 5.5$ , UHC condition and hydrocarbon foils within a thickness range of 12–90 nm. Some measurements are depicted in Fig. A.8 a). They are taken from two different experimental runs. The foil thickness of 12 nm corresponds to the optimum target thickness for the ion acceleration in Section 6.2 where significant higher maximum kinetic energies for the ions were observed. In the electron spectra from this foil thickness no significant change appeared and hence no correlation can be concluded. A similar and earlier experiment is given in Fig. A.8 [56] b). It was performed at the MBI laser system in the year 2010 with using DLC foils and  $a_0 = 3.5$ . In comparison to this measurement, the particle number in a) is significantly smaller. Differences due to uncertainties in the calibration might reach up to 30%<sup>4</sup>. Since the year 2010 great improvements on laser contrast have been made, in particular the basic contrast level could be decreased (cf. Section 5.2). A dependence of  $N_e$  on the laser contrast was demonstrated in Section 7.2.1. Thus, the deviation of the particle number about approximately one order of magnitude can be explained by the higher laser contrast of the MBI laser system in a).

The prior measurements used Diamond like Carbon (DLC) foils with a density of  $\rho \sim 2.5 \text{ g/cm}^3$ . This measurement exhibited a peak bandwidth FWHM

<sup>4</sup>This is due to the lifetime of the used Tritium light source and a well known problem for the used detection screens[79].

of about  $\Delta E/E_{kin} \sim 1.3$  at  $f(E_{kin})^{max} = 0.8$  MeV. For the thinnest foil with a thickness of 3 nm, a steeper distribution  $\Delta E/E_{kin} \sim 0.3$  at  $f(E_{kin})^{max} = 0.6$  MeV was detected and an increase of  $N_e$  about  $\sim 3$  times at the distribution maximum. Considering the RPA model (cf. Section 3.3) and with it, the approach to optimize the target thickness on the laser intensity (cf. Equation (3.7)), this result has been interpreted as an indication of the electron blown out setting in for targets thinner than the optimum foil thickness. Although the used PVF foils have a  $2\times$  smaller density ( $\rho = 1.23$  g/cm<sup>3</sup>), down to a thickness of 12 nm, a remarkable increase of  $N_e$  for the thinnest targets was not observed (see Fig. A.8). Hence, the electron blow out might be assumed for an even thinner target thickness.

### Target Expansion for the High Laser Contrast Condition

An higher number of the fast electrons was demonstrated with using a two foil configuration in Section 7.3. Compared to the case of a single foil target, always an similar or higher electron signal was detected in presence of the second foil for all foil thicknesses discussed before. On contrary, a significant decline in the electron signal was measured for a two foil configuration consisting of a first PVF foil with a thickness of 14 nm and a second PVF foil of 33 nm. The laser parameters were comparable to Section 7.3 ( $a_0 \geq 6$ , linear laser polarization, HC condition). From this foil assembly, the electron signal on the detector was found close to the detection limit. This was observed in two different experimental runs and in total 4 measurements. It is shown in Fig. A.9 and compared to a measurement obtained with a thicker foil arrangement from another experimental run. The measurement gives evidence that there exist a limit in the target thickness for the HC condition. Such a limit corresponds to a strong induced target expansion due to pre-pulses that could cause a significant decrease of the plasma density. The observation correlates to the limit in the target thickness for the ion acceleration found in Section 6.1. Note, that one expected a high electron signal for the case of a too thin foil target in accordance to the electron blown out. This seems to be not the case of a lower laser contrast and a therefore pre-heated and pre-expanded plasma.

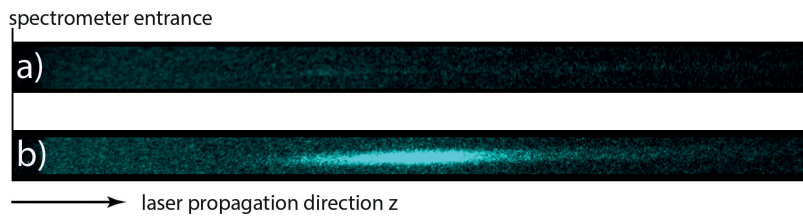


**Figure A.9:** The detector image of the electron spectrometer in configuration II from measurements with applying the laser at the HC condition and a field strength of  $a_0 = 6.5$ . Both pictures are taken at the same exposure conditions and are given in a comparable colour scaling. a): For a two foil configuration with F1 a  $(14 \pm 1)$  nm thick and F2 a  $(33 \pm 2)$  nm thick PVF foil, b): for a two foil configuration with F1 as a  $(104 \pm 4)$  nm thick and F2 a  $(95 \pm 4)$  nm PVF foil. The signal saturated at this exposure value.

## The Fast Electron Spectrum and the Dependency on the Target Holder Arrangement

Experiments using the double foil target configuration were enabled by target holder construction made of two steel hole plates on which the foil targets were attached. The thickness of the steel plates, when put together, introduced the separation between the foils, which was about  $500\ \mu\text{m}$ . This construction is illustrated in Fig. A.10. The target holder was used in two different arrangements by turning it about  $180^\circ$ . A corresponding measurement was presented in Section 7.3 in Fig. 7.8 b). Both arrangements differ in the length of the tunnel that electrons have to pass and which is a consequence of the chosen arrangement. The difference of the tunnel length did not lead to changes in the electron spectrum, as shown in Fig. A.10.

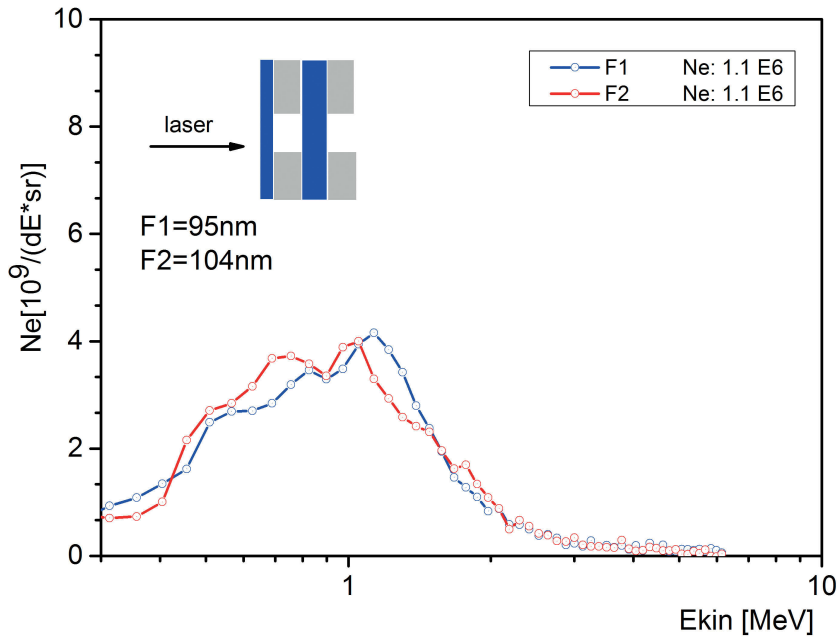


**Figure A.10:** The electron spectrum from either a single foil at position F1 or F2 with using a double foil target holder with hole diameters of  $600\ \mu\text{m}$ . F1 is a  $(95 \pm 4)$  nm and F2 a  $(104 \pm 4)$  nm PVF foil. The measurements were taken in the same experimental run for the same experimental conditions (linear laser polarization, HC condition,  $a_0 = 6$ ). The y-axis was chosen to be in linear scale.

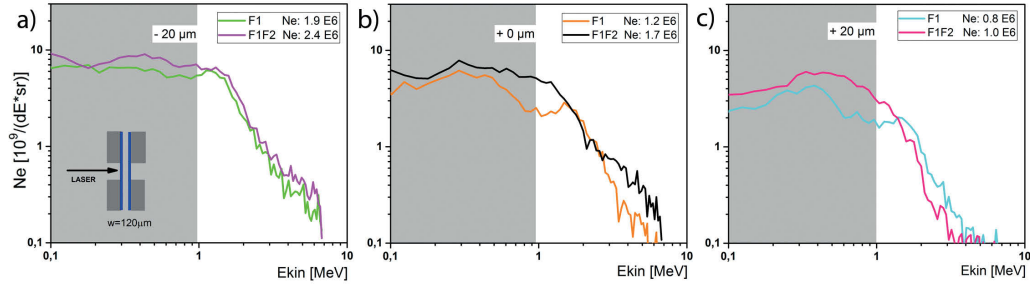


**Figure A.11:** The electron spectra and their integrated  $N_e$  from measurements with using either single or double foil configuration and  $(90 \pm 3)$  nm PVF foils. The foil distance was about  $w = 120 \mu m$  and the target hole diameter was about 0.6 mm. Measurements with different positions of the focal plane on the target are shown in a) - c).

### Electron Amplification for a Smaller Distance in a Double Foil Assembly

According to the theory of Ref. [109], one expects the enhancement of  $N_e$  that is introduced by the presence of a second separated foil, to be dependent on the distance between the two foils. If the effect is attributed to the decoupling between the electrons and the transient laser field, it should be higher for a smaller distance and even could lead to higher velocities than for a larger distance. The experiment used a double foil target system with a distance between the foils of about  $120 \mu m$ . The laser was applied at HC condition linearly polarized and with  $a_0 = 6.5$ . Two PVF foils were used with a thickness of 90 nm. The smaller separation of the foils a modification required a change of the target holder construction. A schematic is depicted in the insert of Fig. A.11 a). Note, that the conducting tunnel, after the first foil, given in the other configuration used by the target support, is now missing for the length of  $w$ . Fig. A.11 shows the electron spectra that was detected from single and two foil configuration and for different displacements of the laser's focal plane on the target. In a direct comparison to the spectrum obtained with distance between the foils of about  $500 \mu m$ , this smaller separation delivered similar results. For example, the amplification between double and single foil configuration is about 1.3 and 1.4. Out of the results no clear dependency of  $A_{N_e}$  on the conducting tunnel or the distance between the two foils can be concluded.

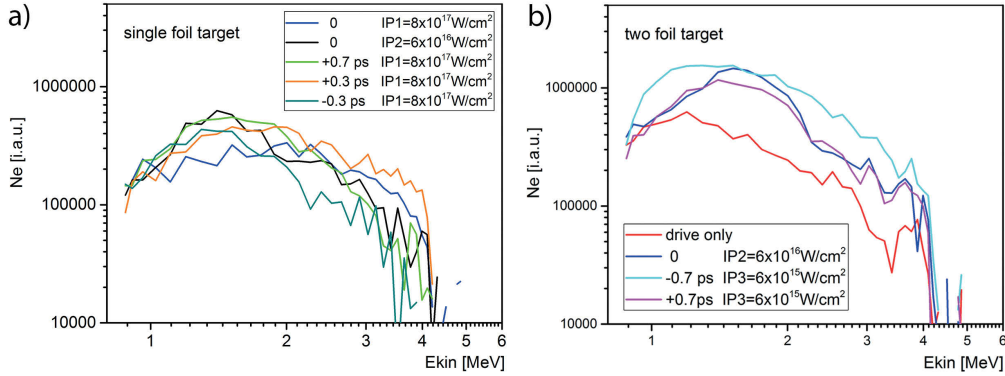


**Figure A.12:** The electron spectra detected from a single or two foil target configuration and with a counter-propagating second laser pulse applied with different intensities and delays. Both PVF foils have a thickness of  $(85 \pm 3)$  nm. a): The electron spectra from the single foil, b): from the double foil configuration. The intensity of the drive pulse was about  $7 \times 10^{19}$  W/cm<sup>2</sup> and both laser pulses were applied at the HC condition.

## Electron Spectra in a Two Counter-Propagating Laser Pulse Experiment

Fig. A.12 shows electron spectra detected for one experimental run with two counter-propagating laser pulses for the single and double foil configuration. This measurement gives additional material for the experiments in Section 7.4. The methods used and the experimental setup was described in Section 5.4. PVF foils with an thickness of 85 nm were separated of about 500  $\mu$ m and free standing on a target holder hole diameter of about 600  $\mu$ m. The second laser pulse was applied at different intensity levels and delays. In the single target configuration in Fig. A.12 a), the electron spectra was affected dependent on the intensity of the P2 pulse. Close to and at the temporal overlap and for a high intensity of the P2 pulse, more electrons with kinetic energies above 1.7 MeV were detected. The total particle number differed little dependent on delay time and an influence of spectral distribution can be concluded.

In Fig.A.12 b), a similar scan is shown for the double foil target configuration taken from the same experimental run. The temporal overlap corresponds to time when both pulses would meet at the fist foil. The travelling time for light for 500  $\mu$ m is about +1.7 ps. In the presence of the P2 pulse, the total electron number was higher than obtained without it or in the case of the single foil configuration. A remarkable peak appeared in the spectral distribution when the P2 pulse was applied with a moderate intensity either at the temporal overlap or at a positive delay. For the same intensity of the P2 pulse, but for negative delay times, the highest particle number was observed and the spectral distribution was enhanced in the whole detection range. Hence, the second laser pulse has significantly changed the electron spectrum and their number in the double foil configuration. The examples show, that the amplification effect that was found

for the double foil configuration, could be further increased when the second foil had been pre-heated at the time before the emitted electrons from the first foil arrived it.

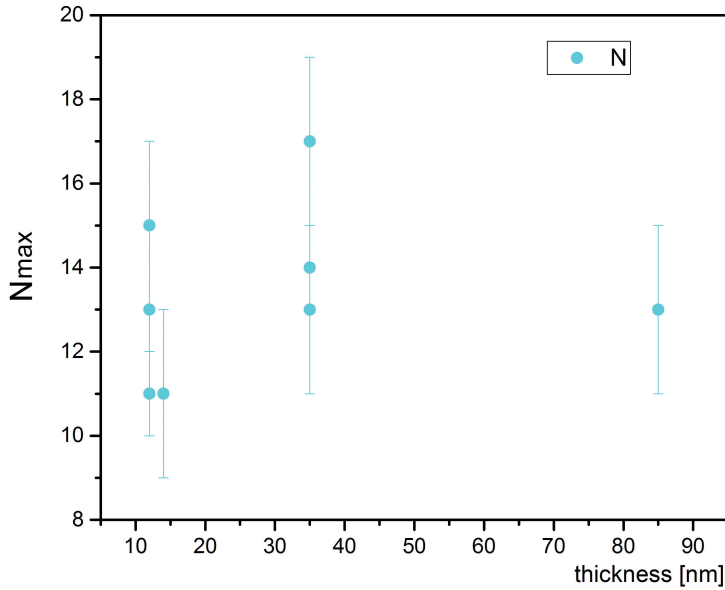


**Figure A.13:** Maximum detected harmonic number  $N_{max}$  in dependence of the PVF foil thickness used.

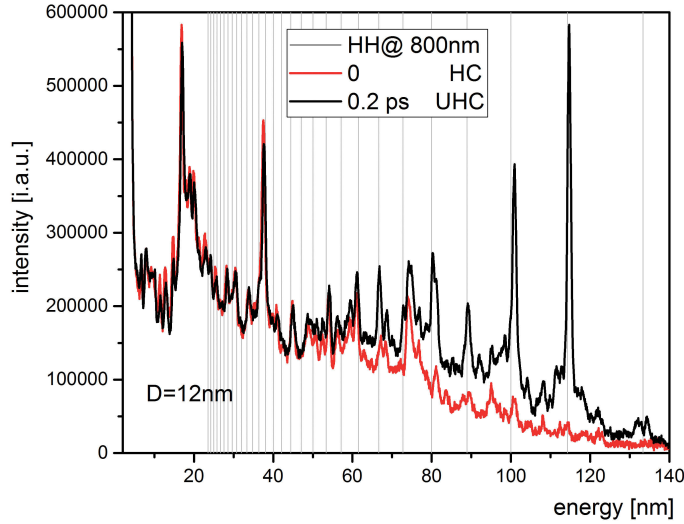
### A.3 Additional Material on the XUV Emission

In the following additional material for Chapter 8 are presented. All results originate from the same experimental campaign and details of the used setup and methods can be found in the named Chapter.

#### High Harmonic Cutoff Frequency and Target Thickness

In order to validate a dependency of the HH cutoff frequency on the target thickness, results of PVF foils at various thicknesses are summarized in Fig. A.13. The comparison only considered the best results from different experimental runs with  $a_0 = 4.5$ , the laser at UHC and a linear laser polarization. The experimental parameters were comparable (laser intensity, laser contrast), but may differ in the daily operational laser condition (focal alignment, laser wavefront). The high variance of  $N^{max}$  is attributed to a fluctuation in the HH emission process, as discussed in Section 8.1.2. The HH radiation can only be identified, when a sufficient ratio of their intensity to the incoherent XUV background is reached. Hence, a slightly higher cutoff frequency could be possible.

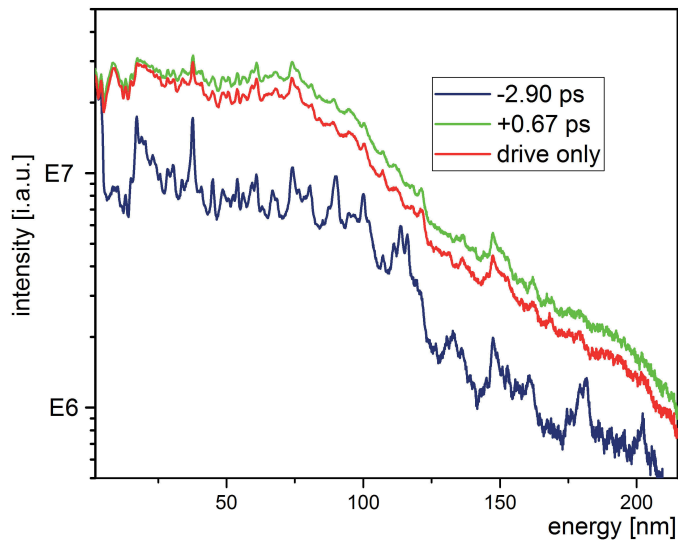
## Incoherent XUV Radiation from Different Laser Contrast Conditions



**Figure A.14:** XUV radiation detected from a two laser pulse experiment for different laser contrast conditions from a  $(12 \pm 1)$  nm PVF foil.

The following results complement the two laser pulse experiments of Sections 8.2.2 and 8.3. XUV radiation was detected from 12 nm PVF foil target in a two laser pulse experiment. The radiation was detected in the propagation direction of the stronger drive pulse, while the second laser pulse propagated to it from the opposite direction. Fig. A.14 provides two examples at different laser contrast conditions and illustrates the similarity of the incoherent XUV radiation. The measurements were taken from the same experimental run with  $a_0 \sim 4.5$  for the UHC condition and  $a_0 \sim 5$  for the HC condition. The laser polarization was linear and the P2 pulse had an intensity of  $I_P \leq 10^{18}$ . In case of the ultrahigh laser contrast, the HH spectrum was superimposed with an incoherent XUV radiation, similar to the one detected at high laser contrast. This observation differed in measurements using thicker foil targets in a single laser pulse interaction and can be seen in Section 8.1. The second laser pulse caused for the ultrahigh laser contrast condition a rise of the incoherent XUV background, which was suppressed without it.

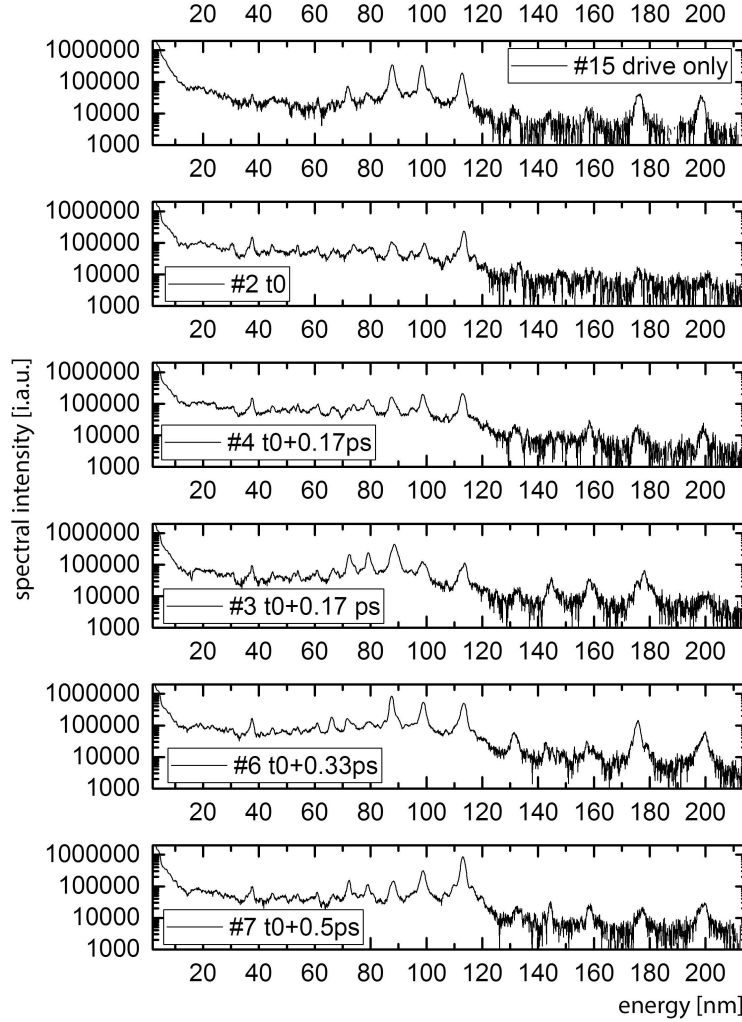
The results for the high laser contrast condition from a single foil interaction with different delay times of the second laser pulse are depicted in Fig A.15. While the drive pulse was applied with an intensity of  $I_L = 7 \times 10^{19}$  for the P2 pulse it was  $I_P = 6 \times 10^{17}$ . Both pulses had a linear laser polarization and illuminated a PVF foil target of 35 nm. For a wide delay range, the spectral characteristics were found comparable to spectrum obtained without the second laser pulse (see Section 8.2.1). A difference was observed for a pre-heated target, which led to a decreased signal strength and remarkably enhanced the characteristic plasma line radiation. This could be explained by the expansion of the pre-plasma due to this



**Figure A.15:** XUV emission from in the two laser pulse experiment using the high laser contrast condition (HC) and a  $(30 \pm 2)$  nm foil. Measurements for different delay times of the P2 pulse and without it are shown.

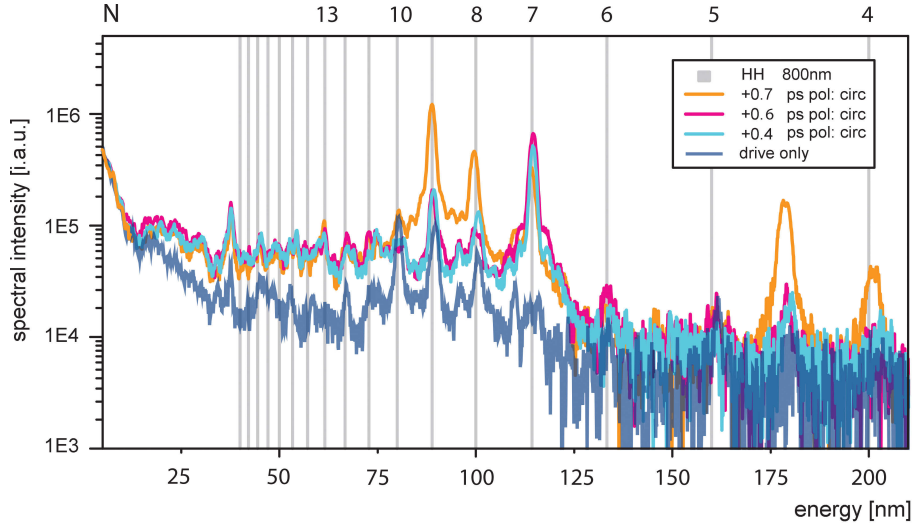
laser contrast condition, that causes a decrease of the plasma density when "too" thin foils were used.

### Backscattering at Ultrahigh Laser Contrast



**Figure A.16:** XUV spectra obtained from a  $(35 \pm 2)$  nm PVF foil and for different delay times of the P2 pulse, close to the temporal overlap between both pulses. The polarization of both laser pulses are linear and perpendicular to each other.

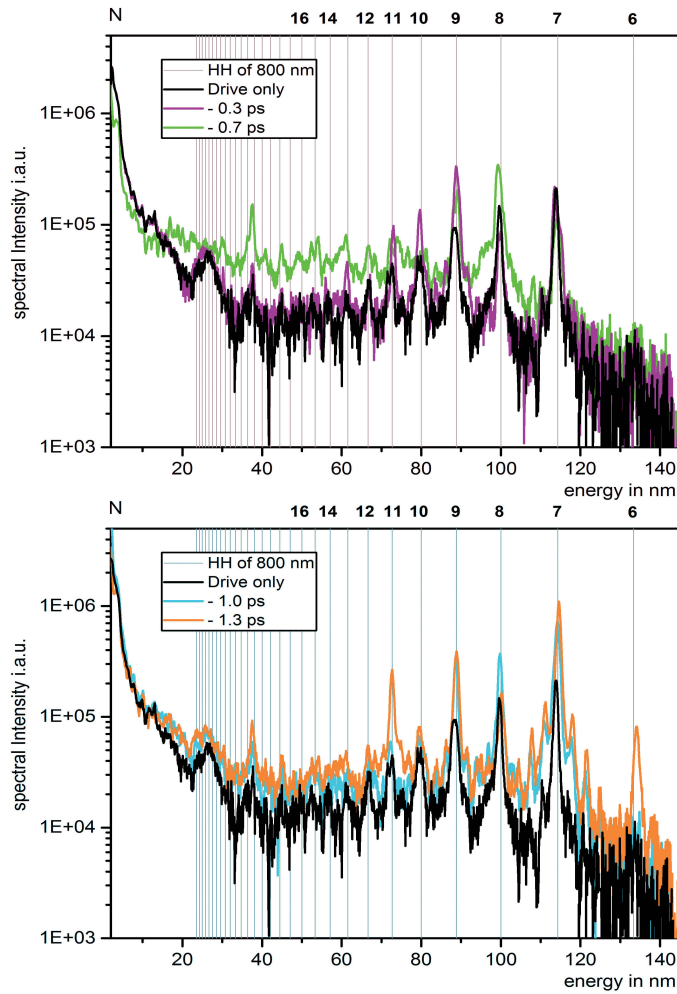
The experiment tested a relativistic backscattering with two laser pulses using the UHC condition for different target thicknesses. The following results complement the experiments presented in Section 8.2.2. The P2 pulse was used with  $I_P = 6 \times 10^{17}$  and was linearly polarized. It propagated in the opposite direction to the stronger drive pulse, which was applied with  $I_L = 5 \times 10^{19}$ . Fig.A.16 shows the XUV radiation that was detected at different delay times and close to the temporal overlap. These results are comparable to the ones in Fig. 8.7 in Section 8.2.2. At the temporal overlap, a disturbance of HH emission process was observed. For the second laser pulse arriving at later times, a raise of the incoherent XUV background was detected. In conclusion, no spectral indication



**Figure A.17:** High harmonic radiation emitted in the forward direction in two laser pulse experiment and with using different laser polarizations. The drive pulse is linear and the P2 pulse was circularly polarized. A PVF target with a thickness of  $(35 \pm 2)$  nm was used.

for a backscattered or up shifted laser light could be found.

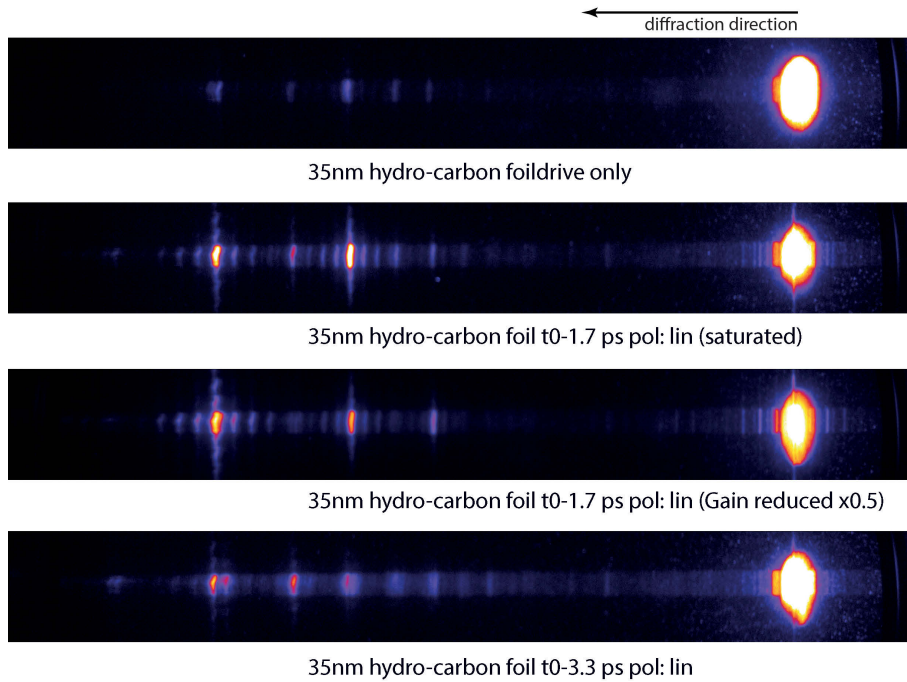
The polarization of the P2 pulse was changed to circular, since this excludes high harmonic emission [126]. Selected spectra that were detected for the P2 pulse applied close to the temporal overlap and for small positive delay times are shown in Fig. A.17. A small enhancement in the intensity of the HH radiation was observed. This observation is similar to the case when the P2 pulse was used at linear laser polarization in Fig. 8.1 (cf. Section 8.2.2). This small enhancement can not be concluded to be significant in comparison to the shot to shot fluctuations in the HH signal strength that were obtained from the single laser pulse interaction (cf. Fig. 8.2).



**Figure A.18:** XUV spectra detected from two laser pulse interaction with a  $(35 \pm 2)$  nm thick PVF foil and for different negative delays of the counter-propagating P2 pulse.

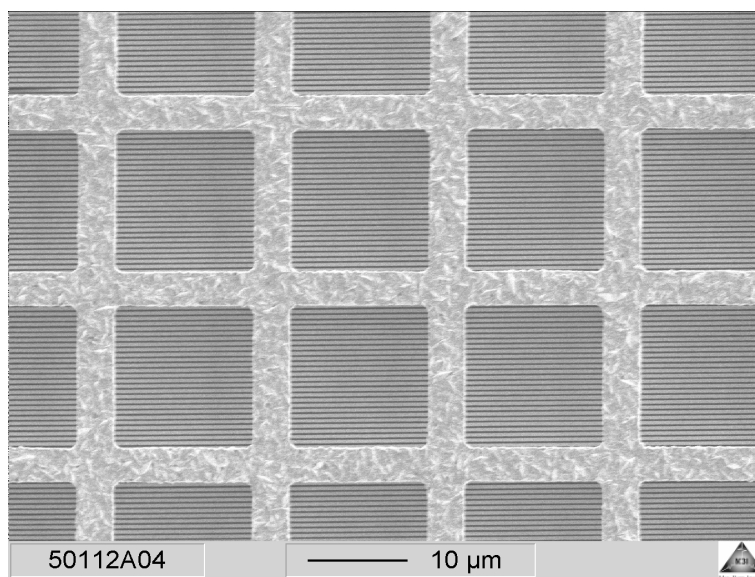
### Enhanced High Harmonic Emission

Fig. A.18 complements the results of Section 8.3.2 with measurements for smaller negative delays of the pre-pulse applied. The P2 pulse serves then as a pre-pulse. The spectra depicted, were detected in the same experimental run of Fig. 8.10. The drive pulse was at  $I_L \times 10^{19} \text{ W/cm}^2$ , the P2 pulse at  $I_P \leq 10^{18} \text{ W/cm}^2$ , both at linear laser polarization and at the UHC condition. It can be seen, that a rise in the incoherent XUV background signal set in for delays  $\leq -0.5 \text{ ps}$ . For even earlier pre-heating an enhanced HH emission was observed. Fig. A.19 depicts images of the XUV detector for the measurement of Fig. 8.10 in Section 8.3.2. A substructure in the HH spectrum can be seen on the detector images exhibiting an echo like line emission which is symmetrical to the particular harmonic lines. The maxima of this pattern are symmetric around the particular harmonic lines and equally spaced in the representation of  $\lambda$ . In this optimized HH inten-



**Figure A.19:** Detector images of the diffracted XUV radiation detected in the counter-propagating experiment at different delay times.

sity spectrum, side bands at specific harmonic numbers appeared in the spectral range between 2 nm and 40 nm. This can be seen in Fig. A.19 close to the image of the source and in Fig. A.18 for longer negative delay times. The pattern is very pronounced in Fig. 8.10 of Section 8.3.2. The spectrometer consisted of a transmission grating of gold with a grating constant of about 1900 lines/mm and the grating was supported by a mesh. The supporting mesh has a structure constant of 17.6  $\mu\text{m}$ , as shown in Fig. A.20. With the spectrometer parameters and the imaging system, the observed side bands can be explained by a diffraction at this support grating. The effect appeared only for coherent light and for a high intensity level.



**Figure A.20:** A image obtained from reflection electron microscopy of the transmission grating used. The grating constant is about 1900 lines/mm and is supported by a mesh structure of about 17.6  $\mu\text{m}$ .

## Bibliography

- [1] H. Daido, M. Nishiuchi, and A. S. Pirozhkov. “Review of laser-driven ion sources and their applications”. In: *Reports on Progress in Physics* **75** (2012), 056401. DOI: [10.1088/0034-4885/75/5/056401](https://doi.org/10.1088/0034-4885/75/5/056401) (cit. on pp. [3](#), [12](#), [23](#), [25–26](#), [51](#), [57](#), [76](#), [84](#), [88](#))
- [2] A. Henig, S. Steinke, M. Schnürer, T. Sokollik, R. Hörlein, D. Kiefer, D. Jung, J. Schreiber, B. M. Hegelich, X. Q. Yan, J. Meyer-ter-Vehn, T. Tajima, P. V. Nickles, W. Sandner, and D. Habs. “Radiation-Pressure Acceleration of Ion Beams Driven by Circularly Polarized Laser Pulses”. In: *Physical Review Letters* **103** (2009), 245003. DOI: [10.1103/PhysRevLett.103.245003](https://doi.org/10.1103/PhysRevLett.103.245003) (cit. on pp. [3–4](#), [25](#), [51–52](#), [54–57](#), [82](#), [136](#))
- [3] G. A. Mourou, G. Korn, W. Sandner, and J. L. Collier. *Extreme Light Infrastructure - White book - Science and Technology with Ultra-Intense Lasers*. ELI PP Publications. 2015. URL: [http://www.eli-beams.eu/wp-content/uploads/2011/08/ELI-Book\\_neues\\_Logo-edited-web.pdf](http://www.eli-beams.eu/wp-content/uploads/2011/08/ELI-Book_neues_Logo-edited-web.pdf) (cit. on pp. [3](#), [136](#))
- [4] R. Lichters, J. Meyer-ter-Vehn, and A. Pukhov. “Short-pulse laser harmonics from oscillating plasma surfaces driven at relativistic intensity”. In: *Physics of Plasmas* **3** (1996), 3425–3437. DOI: [10.1063/1.871619](https://doi.org/10.1063/1.871619) (cit. on pp. [3](#), [28–29](#), [111–112](#), [114](#), [128](#), [138](#))
- [5] F. Quèrè, C. Thaury, P. Monot, S. Dobosz, P. Martin, J. P. Geindre, and P. Audebert. “Coherent Wake Emission of High-Order Harmonics from Overdense Plasmas”. In: *Physical Review Letters* **96** (2006), 125004. DOI: [10.1103/PhysRevLett.96.125004](https://doi.org/10.1103/PhysRevLett.96.125004) (cit. on pp. [3](#), [27–28](#), [87](#), [112](#), [114](#), [129](#), [138](#))
- [6] S. V. Bulanov, F. Califano, T. Z. Esirkepov, K. Mima, N. M. Naumova, K. Nishihara, F. Pegoraro, Y. Sentoku, and V. A. Vshivkov. “Generation of subcycle relativistic solitons by super intense laser pulses in plasmas”. In: *Physica D: Nonlinear Phenomena* **152** (2001), 682–693. DOI: [10.1016/S0167-2789\(01\)00201-9](https://doi.org/10.1016/S0167-2789(01)00201-9) (cit. on pp. [3](#), [111](#))
- [7] P. Heissler, A. Barna, J. M. Mikhailova, G. Ma, K. Khrennikov, S. Karsch, L. Veisz, I. B. Földes, and G. D. Tsakiris. “Multi- $\mu$ J harmonic emission energy from laser-driven plasma”. In: *Applied Physics B* **118** (2014), 195–201. DOI: [10.1007/s00340-014-5968-x](https://doi.org/10.1007/s00340-014-5968-x) (cit. on pp. [3](#), [138](#))

- [8] R. Spitzenpfeil, S. Eyring, C. Kern, C. Ott, J. Lohbreier, J. Henneberger, N. Franke, S. Jung, D. Walter, M. Weger, C. Winterfeldt, T. Pfeifer, and C. Spielmann. “Enhancing the brilliance of high-harmonic generation”. In: *Applied Physics A* **96** (2009), 69–81. DOI: [10.1007/s00339-009-5173-7](https://doi.org/10.1007/s00339-009-5173-7) (cit. on p. 3)
- [9] C. A. J. Palmer, J. Schreiber, S. R. Nagel, N. P. Dover, C. Bellei, F. N. Beg, S. Bott, R. J. Clarke, A. E. Dangor, S. M. Hassan, P. Hilz, D. Jung, S. Kneip, S. P. D. Mangles, K. L. Lancaster, A. Rehman, A. P. L. Robinson, C. Spindloe, J. Szerypo, M. Tatarakis, M. Yeung, M. Zepf, and Z. Najmudin. “Rayleigh-Taylor Instability of an Ultrathin Foil Accelerated by the Radiation Pressure of an Intense Laser”. In: *Physical Review Letters* **108** (2012), 225002. DOI: [10.1103/PhysRevLett.108.225002](https://doi.org/10.1103/PhysRevLett.108.225002) (cit. on pp. 4, 55)
- [10] S. Steinke. “Ion Acceleration in the laser transparency regime”. PhD thesis. TU Berlin, 2010. DOI: [10.14279/depositonce-2693](https://doi.org/10.14279/depositonce-2693) (cit. on pp. 4, 34, 37, 52, 54–55, 57, 72, 136)
- [11] A. Einstein. “Zur Elektrodynamik bewegter Körper”. In: *Annalen der Physik* **322** (1905), 891–921. DOI: [10.1002/andp.19053221004](https://doi.org/10.1002/andp.19053221004) (cit. on pp. 5, 28)
- [12] J. C. Diels and W. Rudolph. *Ultrashort Laser Pulse Phenomena*. Academic Press Elsevier, 2006. ISBN: 978-0-12-215493-5 (cit. on pp. 9–10, 14, 33, 40)
- [13] P. Gibbon. *Short Pulse Laser Interactions with Matter - An Introduction*. Imperial College Press, 2005. ISBN: 1-86094-135-4 (cit. on pp. 9, 11, 15–18, 21, 58, 85–87, 128)
- [14] S. Eliezer. *The Interaction of High-Power Lasers with Plasma*. Ed. by J. Navas. The Institute of Physics, 2002. ISBN: 0-7503-0747-1. DOI: [10.1088/0741-3335/45/2/701](https://doi.org/10.1088/0741-3335/45/2/701) (cit. on pp. 9, 17–18, 21)
- [15] J. D. Jackson. *Classical Electrodynamics, 3rd edition*. Willey, 1998. ISBN: 978-0-471-30932-1 (cit. on pp. 9, 21, 128)
- [16] S. C. Wilks, W. L. Kruer, M. Tabak, and A. B. Langdon. “Absorption of ultra-intense laser pulses”. In: *Physical Review Letters* **69** (1992), 1383–1386. DOI: [10.1103/PhysRevLett.69.1383](https://doi.org/10.1103/PhysRevLett.69.1383) (cit. on pp. 12, 22, 26, 82)
- [17] T. Liseykina, P. Mulser, and M. Murakami. “Collisionless absorption, hot electron generation, and energy scaling in intense laser-target interaction”. In: *Physics of Plasmas* **22**, 033302 (2015), 033302. DOI: [10.1063/1.4914837](https://doi.org/10.1063/1.4914837) (cit. on pp. 12, 17, 76, 85–89, 95–96, 108, 121, 136–137)
- [18] V. A. Vshivkov, N. M. Naumova, F. Pegoraro, and S. V. Bulanov. “Non-linear electrodynamics of the interaction of ultra-intense laser pulses with a thin foil”. In: *Physics of Plasmas* **5** (1998), 2727–2741. DOI: [10.1063/1.872961](https://doi.org/10.1063/1.872961) (cit. on pp. 14, 72, 114)
- [19] M. Ammosov, A. Delone, and V. Krainov. In: *Sov. Phys. JETP* **64** (1986), 1191 (cit. on pp. 15, 61)

- [20] W. L. Kruer. *The Physics of Laser Plasma Interactions*. 1988. ISBN: 0-8133-4083-7. DOI: [10.1017/S0022377800015555](https://doi.org/10.1017/S0022377800015555) (cit. on pp. 16–17)
- [21] B. Hughey, R. Shefer, R. Klinkowstein, X. Zhao, W. Kieser, and A. Litherland. “Experimental investigation of the destruction of 1 MeV 12CH2 molecules in single and double stripping foils”. In: *Nuclear Instruments and Methods B: Beam Interactions with Materials and Atoms* **123** (1997), 186–192. DOI: [10.1016/S0168-583X\(96\)00408-9](https://doi.org/10.1016/S0168-583X(96)00408-9) (cit. on p. 17)
- [22] P. Gibbon, A. A. Andreev, and K. Y. Platonov. “A kinematic model of relativistic laser absorption in an overdense plasma”. In: *Plasma Physics and Controlled Fusion* **54** (2012), 045001. DOI: [10.1088/0741-3335/54/4/045001](https://doi.org/10.1088/0741-3335/54/4/045001) (cit. on pp. 17, 76, 87–88, 136)
- [23] S. C. Wilks, A. B. Langdon, T. E. Cowan, M. Roth, M. Singh, S. Hatchett, M. H. Key, D. Pennington, A. MacKinnon, and R. A. Snavely. “Energetic proton generation in ultra-intense laser-solid interactions”. In: *Physics of Plasmas* **8** (2001), 542–549. DOI: [10.1063/1.1333697](https://doi.org/10.1063/1.1333697) (cit. on pp. 17, 22, 88)
- [24] C. Thaury and F. Quèrè. “High-order harmonic and attosecond pulse generation on plasma mirrors: basic mechanisms”. In: *Journal of Physics B: Atomic, Molecular and Optical Physics* **43** (2010), 213001. DOI: [10.1088/0953-4075/43/21/213001](https://doi.org/10.1088/0953-4075/43/21/213001) (cit. on pp. 18, 27–28, 87–88, 111–114, 117, 124, 128–130, 138)
- [25] J. F. Ziegler. “Stopping of energetic light ions in elemental matter”. In: *Journal of Applied Physics* **85** (1999), 1249–1272. DOI: [10.1063/1.369844](https://doi.org/10.1063/1.369844) (cit. on pp. 19, 70)
- [26] L. C. Northcliffe. “Energy Loss and Effective Charge of Heavy Ions in Aluminum”. In: *Physical Review Letters* **120** (1960), 1744–1757. DOI: [10.1103/PhysRev.120.1744](https://doi.org/10.1103/PhysRev.120.1744) (cit. on p. 19)
- [27] R. C. Webber and C. Hojvat. “Measurement of the Electron Loss Cross Sections for Negative Hydrogen Ions on Carbon at 200 MeV”. In: *IEEE Transactions on Nuclear Science* **NS-2** (1979), 0018–9499 (cit. on p. 20)
- [28] P. Mora. “Plasma Expansion into a Vacuum”. In: *Physical Review Letters* **90** (2003), 185002. DOI: [10.1103/PhysRevLett.90.185002](https://doi.org/10.1103/PhysRevLett.90.185002) (cit. on pp. 22–23, 57)
- [29] J. Schreiber. “Ion Acceleration driven by High-Intensity Laser Pulses”. PhD. LMU Munich, 2006. URL: [https://edoc.ub.uni-muenchen.de/5842/1/Schreiber\\_Joerg.pdf](https://edoc.ub.uni-muenchen.de/5842/1/Schreiber_Joerg.pdf) (cit. on pp. 22–23, 62)
- [30] P. Mora. “Thin-foil expansion into a vacuum”. In: *Physical Review E* **72** (2005), 056401. DOI: [10.1103/PhysRevE.72.056401](https://doi.org/10.1103/PhysRevE.72.056401) (cit. on p. 22)

- [31] J. Schreiber, F. Bell, F. Grüner, U. Schramm, M. Geissler, M. Schnürer, S. Ter-Avetisyan, B. M. Hegelich, J. Cobble, E. Brambrink, J. Fuchs, P. Audebert, and D. Habs. “Analytical Model for Ion Acceleration by High-Intensity Laser Pulses”. In: *Physical Review Letters* **97** (2006), 045005. DOI: [10.1103/PhysRevLett.97.045005](https://doi.org/10.1103/PhysRevLett.97.045005) (cit. on pp. 22–23, 62, 82)
- [32] F. Abicht. “Ultrafast field dynamics in laser ion acceleration”. PhD thesis. TU Berlin, 2015. DOI: [10.14279/depositonce-4584](https://doi.org/10.14279/depositonce-4584) (cit. on pp. 22–23, 34, 38, 40, 57, 68, 76, 84)
- [33] R. Prasad, A. A. Andreev, S. Ter-Avetisyan, D. Doria, K. E. Quinn, L. Rognagnani, C. M. Brenner, D. C. Carroll, N. P. Dover, D. Neely, P. S. Foster, P. Gallegos, J. S. Green, P. McKenna, Z. Najmudin, C. A. J. Palmer, J. Schreiber, M. J. V. Streeter, O. Tresca, M. Zepf, and M. Borghesi. “Fast ion acceleration from thin foils irradiated by ultra-high intensity, ultra-high contrast laser pulses”. In: *Applied Physics Letters* **99**, 121504 (2011). DOI: [10.1063/1.3643133](https://doi.org/10.1063/1.3643133) (cit. on p. 23)
- [34] M. Schnürer, A. A. Andreev, S. Steinke, T. Sokollik, T. Paasch-Colberg, P. V. Nickles, A. Henig, D. Jung, D. Kiefer, R. Hörlein, J. Schreiber, T. Tajima, D. Habs, and W. Sandner. “Comparison of femtosecond laser-driven proton acceleration using nanometer and micrometer thick target foils”. In: *Laser and Particle Beams* **29** (2011), 437–446. DOI: [10.1017/S0263034611000553](https://doi.org/10.1017/S0263034611000553) (cit. on p. 23)
- [35] B. M. Hegelich, B. Albright, P. Audebert, A. Blazevic, E. Brambrink, J. Cobble, T. Cowan, J. Fuchs, J. C. Gauthier, C. Gautier, M. Geissler, D. Habs, R. Johnson, S. Karsch, A. Kemp, S. Letzring, M. Roth, U. Schramm, J. Schreiber, K. J. Witte, and J. C. Fernandez. “Spectral properties of laser-accelerated mid-Z MeV/u ion beams”. In: *Physics of Plasmas* **12** (2005), 056314. DOI: [10.1063/1.1915350](https://doi.org/10.1063/1.1915350) (cit. on pp. 23, 25, 52, 61, 65, 70, 82, 135)
- [36] A. Macchi, A. Sgattoni, S. Sinigardi, M. Borghesi, and M. Passoni. “Advanced strategies for ion acceleration using high-power lasers”. In: *Plasma Physics and Controlled Fusion* **55** (2013), 124020. DOI: [10.1088/0741-3335/55/12/124020](https://doi.org/10.1088/0741-3335/55/12/124020) (cit. on pp. 23–26, 51)
- [37] G. Marx. “Interstellar Vehicle Propelled By Terrestrial Laser Beam”. In: *Nature Physics* **211** (1966), 22–23. DOI: [10.1038/213588a0](https://doi.org/10.1038/213588a0) (cit. on pp. 23, 112)
- [38] A. Macchi, S. Veghini, T. V. Liseykina, and F. Pegoraro. “Radiation pressure acceleration of ultrathin foils”. In: *New Journal of Physics* **12** (2010), 124033. DOI: [10.1088/1367-2630/12/4/045013](https://doi.org/10.1088/1367-2630/12/4/045013) (cit. on pp. 24, 51, 57)
- [39] T. Esirkepov, M. Yamagiwa, and T. Tajima. “Laser Ion-Acceleration Scaling Laws Seen in Multiparametric Particle-in-Cell Simulations”. In: *Physical Review Letters* **96** (2006), 105001. DOI: [10.1103/PhysRevLett.96.105001](https://doi.org/10.1103/PhysRevLett.96.105001) (cit. on pp. 24–26, 29, 51–52, 55–58, 67, 69–70, 135)

- [40] I. J. Kim, K. H. Pae, C. M. Kim, H. T. Kim, J. H. Sung, S. K. Lee, T. J. Yu, I. W. Choi, C.-L. Lee, K. H. Nam, P. V. Nickles, T. M. Jeong, and J. Lee. “Transition of Proton Energy Scaling Using an Ultrathin Target Irradiated by Linearly Polarized Femtosecond Laser Pulses”. In: *Physical Review Letters* **111** (2013), 165003. DOI: [10.1103/PhysRevLett.111.165003](https://doi.org/10.1103/PhysRevLett.111.165003) (cit. on pp. 25, 37, 51–52, 54–55, 58, 82, 111)
- [41] B. Qiao, M. Zepf, M. Borghesi, B. Dromey, M. Geissler, A. Karmakar, and P. Gibbon. “Radiation-Pressure Acceleration of Ion Beams from Nanofoil Targets: The Leaky Light-Sail Regime”. In: *Physical Review Letters* **105** (2010), 155002. DOI: [10.1103/PhysRevLett.105.155002](https://doi.org/10.1103/PhysRevLett.105.155002) (cit. on pp. 25, 55, 57–58, 67, 70–71)
- [42] H. Y. Wang, C. Lin, B. Liu, Z. M. Sheng, H. Y. Lu, W. J. Ma, J. H. Bin, J. Schreiber, X. T. He, J. E. Chen, M. Zepf, and X. Q. Yan. “Laser-driven three-stage heavy-ion acceleration from relativistic laser-plasma interaction”. In: *Physical Review E* **89** (2014), 013107. DOI: [10.1103/PhysRevE.89.013107](https://doi.org/10.1103/PhysRevE.89.013107) (cit. on pp. 25–26, 51, 58, 65, 70–71, 135)
- [43] T. Z. Esirkepov, S. V. Bulanov, K. Nishihara, T. Tajima, F. Pegoraro, V. S. Khoroshkov, K. Mima, H. Daido, Y. Kato, Y. Kitagawa, K. Nagai, and S. Sakabe. “Proposed double-layer target for the generation of high-quality laser-accelerated ion beams”. In: *Physical Review Letters* **89** (2002), 175003. DOI: [10.1103/PhysRevLett.89.175003](https://doi.org/10.1103/PhysRevLett.89.175003) (cit. on pp. 26, 58, 65, 70–71)
- [44] L. O. Silva, M. Marti, J. R. Davies, R. A. Fonseca, C. Ren, F. S. Tsung, and W. B. Mori. “Proton Shock Acceleration in Laser-Plasma Interactions”. In: *Physical Review Letters* **92** (2004), 015002. DOI: [10.1103/PhysRevLett.92.015002](https://doi.org/10.1103/PhysRevLett.92.015002) (cit. on p. 26)
- [45] F. Fiuza, A. Stockem, E. Boella, R. A. Fonseca, L. O. Silva, D. Haberberger, S. Tochitsky, C. Gong, W. B. Mori, and C. Joshi. “Laser-Driven Shock Acceleration of Monoenergetic Ion Beams”. In: *Physical Review Letters* **109** (2012), 215001. DOI: [10.1103/PhysRevLett.109.215001](https://doi.org/10.1103/PhysRevLett.109.215001) (cit. on p. 26)
- [46] M. Behmke, D. an der Brügge, C. Rödel, M. Cerchez, D. Hemmers, M. Heyer, O. Jäckel, M. Kübel, G. G. Paulus, G. Pretzler, A. Pukhov, M. Toncian, T. Toncian, and O. Willi. “Controlling the Spacing of Attosecond Pulse Trains from Relativistic Surface Plasmas”. In: *Physical Review Letters* **106** (2011), 185002. DOI: [10.1103/PhysRevLett.106.185002](https://doi.org/10.1103/PhysRevLett.106.185002) (cit. on pp. 27, 117)
- [47] J. Braenzel, A. Andreev, M. Schnürer, S. Steinke, K. Platonov, G. Priebe, and W. Sandner. “Sub-structure of laser generated harmonics reveals plasma dynamics of a relativistically oscillating mirror”. In: *Physics of Plasmas* **20** (2013), 083109. DOI: [10.1063/1.4817807](https://doi.org/10.1063/1.4817807) (cit. on pp. 27–28, 111, 114, 117)

- [48] Y. Nomura, R. Hörlein, P. Tzallas, B. Dromey, S. Rykovanov, Z. Major, J. Osterhoff, S. Karsch, L. Veisz, M. Zepf, D. Charalambidis, F. Krausz, and G. D. Tsakiris. “Attosecond phase locking of harmonics emitted from laser-produced plasmas”. In: *Nature Physics* **5** (2009), 124–128. DOI: [10.1038/nphys1155](https://doi.org/10.1038/nphys1155) (cit. on p. 27)
- [49] H. Vincenti and F. Quèrè. “Attosecond Lighthouses: How To Use Spatiotemporally Coupled Light Fields To Generate Isolated Attosecond Pulses”. In: *Physical Review Letters* **108** (2012), 113904. DOI: [10.1103/PhysRevLett.108.113904](https://doi.org/10.1103/PhysRevLett.108.113904) (cit. on p. 27)
- [50] J. A. Wheeler, A. Borot, S. Monchoce, H. Vincenti, A. Ricci, A. Malvache, R. Lopez-Martens, and F. Quèrè. “Attosecond lighthouses from plasma mirrors”. In: *Nature Photonics* **6** (2012), 829–833. DOI: [10.1038/nphoton.2012.284](https://doi.org/10.1038/nphoton.2012.284) (cit. on p. 27)
- [51] M. Chini, K. Zhao, and Z. Chang. “The generation, characterization and applications of broadband isolated attosecond pulses”. In: *Nature Photonics* **8** (2014), 178–186. DOI: [10.1038/nphoton.2013.362](https://doi.org/10.1038/nphoton.2013.362) (cit. on p. 27)
- [52] C. Thaury, F. Quèrè, J. P. Geindre, A. Levy, T. Ceccotti, P. Monot, M. Bougeard, F. Reau, P. D’Oliveira, P. Audebert, R. Marjoribanks, and P. H. Martin. “Plasma mirrors for ultrahigh-intensity optics”. In: *Nature Physics* **3** (2007), 424–429. DOI: [10.1038/nphys595](https://doi.org/10.1038/nphys595) (cit. on pp. 28, 36)
- [53] J. Braenzel. “Entwicklung eines VUV-Spektrometers zur Charakterisierung höherer harmonischer bei Laser Plasma Wechselwirkung”. MA thesis. Freie Universität Berlin, 2011 (cit. on pp. 28, 112)
- [54] H. George, F. Quèrè, C. Thaury, G. Bonnaud, and P. Martin. “Mechanisms of forward laser harmonic emission from thin overdense plasmas”. In: *New Journal of Physics* **11** (2009), 113028. DOI: [10.1088/1367-2630/11/11/113028](https://doi.org/10.1088/1367-2630/11/11/113028) (cit. on pp. 28, 114–115, 138)
- [55] S. S. Bulanov, A. Macchi, A. Maksimchuk, T. Matsuoka, J. Nees, and F. Pegoraro. “Electromagnetic pulse reflection at self-generated plasma mirrors: Laser pulse shaping and high order harmonic generation”. In: *Physics of Plasmas* **14** (2007), 093105. DOI: [093105Artn093105](https://doi.org/093105Artn093105) (cit. on pp. 29, 111–112, 114)
- [56] D. Kiefer. “Relativistic Electron Mirror from High Intensity Laser Nanofoil Interactions”. PhD thesis. MPQ Munich, 2012. URL: [www2.mpg.mpg.de/APS/data/dissertationen/KieferDaniel.pdf](http://www2.mpg.mpg.de/APS/data/dissertationen/KieferDaniel.pdf) (cit. on pp. 30, 55, 85–87, 90–96, 108, 136–137, 150)
- [57] D. Kiefer, M. Yeung, T. Dzelzainis, P. S. Foster, S. G. Rykovanov, C. L. Lewis, R. S. Marjoribanks, H. Ruhl, D. Habs, J. Schreiber, M. Zepf, and B. Dromey. “Relativistic electron mirrors from nanoscale foils for coherent frequency upshift to the extreme ultraviolet”. In: *Nature Communications* **4** (2013), 1763. DOI: [10.1038/ncomms2775](https://doi.org/10.1038/ncomms2775) (cit. on pp. 30, 86–87, 111, 114–115, 117, 119–121, 123, 129, 138)

- [58] E. Esarey, S. K. Ride, and P. Sprangle. “Nonlinear Thomson scattering of intense laser pulses from beams and plasmas”. In: *Physical Review E* **48** (1993), 3003–3021. DOI: [10.1103/PhysRevE.48.3003](https://doi.org/10.1103/PhysRevE.48.3003) (cit. on p. 30)
- [59] Y. Y. Lau, F. He, D. P. Umstädter, and R. Kowalczyk. “Nonlinear Thomson scattering: A tutorial”. In: *Physics of Plasmas* **10** (2003), 2155–2162. DOI: [10.1063/1.1565115](https://doi.org/10.1063/1.1565115) (cit. on p. 30)
- [60] M. P. Kalashnikov, H. Schönengel, and W. Sandner. “High temporal contrast front end with a CaF<sub>2</sub>-based XPW temporal filter for high intensity lasers”. In: *AIP Conference Proceedings* **1465** (2012), 13–17. DOI: [10.1063/1.4737531](https://doi.org/10.1063/1.4737531) (cit. on p. 33)
- [61] V. Chvykov, P. Rousseau, S. Reed, G. Kalinchenko, and V. Yanovsky. “Generation of 1011 contrast 50 TW laser pulses”. In: *Optical Letters* **31** (2006), 1456–1458. DOI: [10.1364/OL.31.001456](https://doi.org/10.1364/OL.31.001456) (cit. on p. 33)
- [62] Fastlite. *Dazzler*. Fastlite. 2016. URL: [Acousto-Optic%20Programmable%20Dispersive%20Filter](https://www.fastlite.com/Products/Programmable-Dispersive-Filter) (cit. on p. 34)
- [63] K. Krushelnick, W. Rozmus, U. Wagner, F. N. Beg, S. G. Bochkarev, E. L. Clark, A. E. Dangor, R. G. Evans, A. Gopal, H. Habara, S. P. D. Mangles, P. A. Norreys, A. P. L. Robinson, M. Tatarakis, M. S. Wei, and M. Zepf. “Effect of Relativistic Plasma on Extreme-Ultraviolet Harmonic Emission from Intense Laser-Matter Interactions”. In: *Physical Review Letters* **100** (2008), 125005. DOI: [10.1103/PhysRevLett.100.125005](https://doi.org/10.1103/PhysRevLett.100.125005) (cit. on pp. 36, 53, 76, 88, 111, 114–115, 117, 128–129, 138)
- [64] J. Fuchs, C. A. Cecchetti, M. Borghesi, T. Grismayer, E. d’Humières, P. Antici, S. Atzeni, P. Mora, A. Pipahl, L. Romagnani, A. Schiavi, Y. Sentoku, T. Toncian, P. Audebert, and O. Willi. “Laser-Foil Acceleration of High-Energy Protons in Small-Scale Plasma Gradients”. In: *Physical Review Letters* **99** (2007), 015002. DOI: [10.1103/PhysRevLett.99.015002](https://doi.org/10.1103/PhysRevLett.99.015002) (cit. on pp. 36, 51, 53, 76–77, 81, 84, 89)
- [65] M. Bocoum, M. Thévenet, F. Böhle, B. Beaurepaire, A. Vernier, A. Jullien, J. Faure, and R. Lopez-Martens. “Anticorrelated Emission of High Harmonics and Fast Electron Beams From Plasma Mirrors”. In: *Physical Review Letters* **116** (2016), 185001. DOI: [10.1103/PhysRevLett.116.185001](https://doi.org/10.1103/PhysRevLett.116.185001) (cit. on pp. 36, 53, 76, 85, 87, 89–90, 95–96, 108, 129–130, 136–139)
- [66] C. Ziener, P. S. Foster, E. J. Divall, C. J. Hooker, M. H. R. Hutchinson, A. J. Langley, and D. Neely. “Specular reflectivity of plasma mirrors as a function of intensity, pulse duration, and angle of incidence”. In: *Journal of Applied Physics* **93** (2003), 768–770 (cit. on p. 36)
- [67] S. Steinke. “Entwicklung eines Doppel-Plasmaspiegels zur Erzeugung hoch-energetischer Ionen mit ultra-dünnen Targets”. MA thesis. Freie Universität Berlin, 2007. URL: <http://edocs.fu-berlin.de> (cit. on p. 36)

- [68] C. Rödel, D. an der Brügge, J. Bierbach, M. Yeung, T. Hahn, B. Dromey, S. Herzer, S. Fuchs, A. G. Pour, E. Eckner, M. Behmke, M. Cerchez, O. Jäckel, D. Hemmers, T. Toncian, M. C. Kaluza, A. Belyanin, G. Pretzler, O. Willi, A. Pukhov, M. Zepf, and G. G. Paulus. “Harmonic Generation from Relativistic Plasma Surfaces in Ultrasteep Plasma Density Gradients”. In: *Physical Review Letters* **109** (2012), 125002. DOI: [10.1103/PhysRevLett.109.125002](https://doi.org/10.1103/PhysRevLett.109.125002) (cit. on pp. 37, 53, 76, 88, 111–112, 114–115, 124, 128, 130, 138)
- [69] S. Steinke, P. Hilz, M. Schnürer, G. Priebe, J. Braenzel, F. Abicht, D. Kiefer, C. Kreuzer, T. Ostermayr, J. Schreiber, A. A. Andreev, T. P. Yu, A. Pukhov, and W. Sandner. “Stable laser-ion acceleration in the light sail regime”. In: *Physical Review ST: Acceleration and Beams* **16** (2013), 011303. DOI: [10.1103/PhysRevSTAB.16.011303](https://doi.org/10.1103/PhysRevSTAB.16.011303) (cit. on pp. 37, 52, 54–57, 82, 88)
- [70] J. Braenzel, C. Pratsch, P. Hilz, C. Kreuzer, M. Schnürer, H. Stiel, and W. Sandner. “Note: Thickness determination of freestanding ultra-thin foils using a table top laboratory extreme ultraviolet source”. In: *Review of Scientific Instruments* **84** (2013), 84(5):056109. DOI: [10.1063/1.4807153](https://doi.org/10.1063/1.4807153) (cit. on pp. 41, 43, 113, 135)
- [71] H. Endo, M. Mitsuishi, and T. Miyashita. “Free-standing ultrathin films with universal thickness from nanometer to micrometer by polymer nanosheet assembly”. In: *Journal of Material Chemics* **18** (2008), 1302–1308. DOI: [10.1039/B717080G](https://doi.org/10.1039/B717080G) (cit. on p. 42)
- [72] R. Vendamme, S.-Y. Onoue, A. Nakao, and T. Kunitake. “Robust free-standing nanomembranes of organic inorganic interpenetrating networks”. In: *Nature Materials* **5** (2006), 494–501. DOI: [10.1038/nmat1655](https://doi.org/10.1038/nmat1655) (cit. on p. 42)
- [73] S. supplies. *Victawet 12 Surface Release Agent*. Jan. 2016. URL: <http://www.2spi.com/item/z02473/> (cit. on p. 42)
- [74] J. Braenzel, A. A. Andreev, K. Platonov, M. Klingsporn, L. Ehrentraut, W. Sandner, and M. Schnürer. “Coulomb-Driven Energy Boost of Heavy Ions for Laser-Plasma Acceleration”. In: *Physical Review Letters* **114** (2015), 124801. DOI: [10.1103/PhysRevLett.114.124801](https://doi.org/10.1103/PhysRevLett.114.124801) (cit. on pp. 42, 59–62, 69, 82, 135)
- [75] I. Mantouvalou, R. Jung, J. Tuemmler, H. Legall, T. Bidu, H. Stiel, W. Malzer, B. Kanngießler, and W. Sandner. “Note: Study of extreme ultraviolet and soft x-ray emission of metal targets produced by laser-plasma-interaction”. In: *Review of Scientific Instruments* **82**, 066103 (2011), 066103. DOI: [10.1063/1.3600069](https://doi.org/10.1063/1.3600069) (cit. on pp. 43, 112)
- [76] XROS. *X-Ray Interaction With Matter*. lbl.gov. 2015. URL: [http://henke.lbl.gov/optical\\_constants/](http://henke.lbl.gov/optical_constants/) (cit. on p. 43)
- [77] D. Attwood. *Soft X-Rays and Extreme Ultraviolet Radiation*. Cambridge University Press, 2007. ISBN: 9780521029971 (cit. on pp. 43, 115)

- [78] F. Abicht. *Private communications*. 2015 (cit. on p. 45)
- [79] A. Buck, K. Zeil, A. Popp, K. Schmid, A. Jochmann, S. D. Kraft, B. Hidding, T. Kudyakov, C. M. S. Sears, L. Veisz, S. Karsch, J. Pawelke, R. Sauerbrey, T. Cowan, F. Krausz, and U. Schramm. “Absolute charge calibration of scintillating screens for relativistic electron detection”. In: *Review of Scientific Instruments* **81**, 033301 (2010), 033301. DOI: [10.1063/1.3310275](https://doi.org/10.1063/1.3310275) (cit. on pp. 45, 150)
- [80] K. Nakamura, A. J. Gonsalves, C. Lin, A. Smith, D. Rodgers, R. Donahue, W. Byrne, and W. P. Leemans. “Electron beam charge diagnostics for laser plasma accelerators”. In: *Physics Review ST: Acceleration and Beams* **14** (2011), 062801. DOI: [10.1103/PhysRevSTAB.14.062801](https://doi.org/10.1103/PhysRevSTAB.14.062801) (cit. on p. 45)
- [81] H. Chen, N. L. Back, T. Bartal, F. N. Beg, D. C. Eder, A. J. Link, A. G. MacPhee, Y. Ping, P. M. Song, A. Throop, and L. Van Woerkom. “Absolute calibration of image plates for electrons at energy between 100keV and 4MeV”. In: *Review of Scientific Instruments* **79**, 033301 (2008), 79(3):033301. DOI: <http://dx.doi.org/10.1063/1.2885045> (cit. on pp. 46, 94)
- [82] K. Zeil, S. D. Kraft, A. Jochmann, F. Kroll, W. Jahr, U. Schramm, L. Karsch, J. Pawelke, B. Hidding, and G. Pretzler. “Absolute response of Fuji imaging plate detectors to picosecond-electron bunches”. In: *Review of Scientific Instruments* **81**, 013307 (2010), 013307. DOI: <http://dx.doi.org/10.1063/1.3284524> (cit. on pp. 46, 94)
- [83] I. J. Kim, K. H. Pae, C. M. Kim, H. T. Kim, I. W. Choi, C.-L. Lee, H. Singhal, J. H. Sung, S. K. Lee, H. W. Lee, P. V. Nickles, T. M. Jeong, and C. H. Nam. “Fast scaling of energetic protons generated in the interaction of linearly polarized femtosecond petawatt laser pulses with ultrathin targets”. In: *High Energy Density Physics* **17**, Part A (2015), 203–207. DOI: [10.1016/j.hedp.2014.10.007](https://doi.org/10.1016/j.hedp.2014.10.007) (cit. on pp. 51–52, 54–55, 58, 82)
- [84] T. Grismayer and P. Mora. “Influence of a finite initial ion density gradient on plasma expansion into a vacuum”. In: *Physics of Plasmas* **13**, 032103 (2006). DOI: <http://dx.doi.org/10.1063/1.2178653> (cit. on pp. 51, 53, 76, 81, 84)
- [85] M. Hegelich, S. Karsch, G. Pretzler, D. Habs, K. Witte, W. Guenther, M. Allen, A. Blazevic, J. Fuchs, J. C. Gauthier, M. Geissel, P. Audebert, T. Cowan, and M. Roth. “MeV Ion Jets from Short-Pulse-Laser Interaction with Thin Foils”. In: *Physical Review Letters* **89** (2002), 085002. DOI: [10.1103/PhysRevLett.89.085002](https://doi.org/10.1103/PhysRevLett.89.085002) (cit. on pp. 52, 82, 135)
- [86] S. Ter-Avetisyan, J. Braenzel, M. Schnürer, R. Prasad, M. Borghesi, S. Jequier, and V. Tikhonchuk. “New source of MeV negative ion and neutral atom beams”. In: *Review of Scientific Instruments* **87**, 02B134 (2016). DOI: [10.1063/1.4935234](https://doi.org/10.1063/1.4935234) (cit. on pp. 52, 68, 73, 136)

- [87] F. Mollica, L. Antonelli, A. Flacco, J. Braenzel, B. Vauzour, G. Folpini, G. Birindelli, M. Schnürer, D. Batani, and V. Malka. “Efficient laser production of energetic neutral beams”. In: *Plasma Physics and Controlled Fusion* **58** (2016), 034016. DOI: [10.1088/0741-3335/58/3/034016](https://doi.org/10.1088/0741-3335/58/3/034016) (cit. on pp. [52](#), [68](#), [70](#), [73](#), [76](#), [83](#), [136](#))
- [88] S. Ter-Avetisyan, J. Braenzel, M. Schnürer, R. Prasad, M. Borghesi, S. Jequier, and V. Tikhonchuk. “New source of MeV negative ion and neutral atom beams”. In: *Review of Scientific Instruments* **87**, 02B134 (2016). DOI: [10.1063/1.4935234](https://doi.org/10.1063/1.4935234) (cit. on pp. [52](#), [70](#), [76](#), [83](#), [136](#))
- [89] V. K. Tripathi, C. S. Liu, X. Shao, B. Eliasson, and R. Z. Sagdeev. “Laser acceleration of monoenergetic protons in a self-organized double layer from thin foil”. In: *Plasma Physics and Controlled Fusion* **51** (2009), 024014. DOI: [10.1088/0741-3335/51/2/024014](https://doi.org/10.1088/0741-3335/51/2/024014) (cit. on pp. [55–56](#))
- [90] X. Q. Yan, T. Tajima, M. Hegelich, L. Yin, and D. Habs. “Theory of laser ion acceleration from a foil target of nanometer thickness”. In: *Applied Physics B* **98** (2010). Appl. Phys. B, 711–721. DOI: [10.1007/s00340-009-3707-5](https://doi.org/10.1007/s00340-009-3707-5) (cit. on pp. [55–56](#))
- [91] B. Qiao, M. Zepf, M. Borghesi, and M. Geissler. “Stable GeV Ion-Beam Acceleration from Thin Foils by Circularly Polarized Laser Pulses”. In: *Physical Review Letters* **102** (2009), 145002. DOI: [10.1103/PhysRevLett.102.145002](https://doi.org/10.1103/PhysRevLett.102.145002) (cit. on pp. [55](#), [57](#))
- [92] T. P. Yu, A. Pukhov, G. Shvets, M. Chen, T. H. Ratliff, S. A. Yi, and V. Khudik. “Simulations of stable compact proton beam acceleration from a two-ion-species ultrathin foil”. In: *Physics of Plasmas* **18**, 043110 (2011), 043110. DOI: [10.1063/1.3574351](https://doi.org/10.1063/1.3574351) (cit. on pp. [57–58](#), [67](#), [71](#), [88](#))
- [93] B. Aurand. “Untersuchungen zu Mechanismen der Laser-Teilchenbeschleunigung”. PhD thesis. Johannes Gutenberg Universität Mainz, 2012. URL: <http://ubm.opus.hbz-nrw.de/volltexte/2012/3160/> (cit. on pp. [57](#), [70](#))
- [94] D. Wu, B. Qiao, C. McGuffey, X. T. He, and F. N. Beg. “Generation of high-energy mono-energetic heavy ion beams by radiation pressure acceleration of ultra-intense laser pulses”. In: *Physics of Plasmas* **21**, 123118 (2014), 123118. DOI: [10.1063/1.4904402](https://doi.org/10.1063/1.4904402) (cit. on pp. [58](#), [65](#), [70–71](#))
- [95] Wikipedia. *Lemniscate of Bernoulli*. 2016. URL: [https://en.wikipedia.org/wiki/Lemniscate\\_of\\_Bernoulli](https://en.wikipedia.org/wiki/Lemniscate_of_Bernoulli) (cit. on p. [64](#))
- [96] F. Abicht, R. Prasad, G. Priebe, J. Braenzel, L. Ehrentraut, A. Andreev, P. V. Nickles, M. Schnürer, V. Tikhonchuk, and S. Ter-Avetisyan. “Energetic negative ion and neutral atom beam generation at passage of laser accelerated high energy positive ions through a liquid spray”. In: *SPIE Proceedings* **8779** (2013), 87790M. DOI: [10.1117/12.2019505](https://doi.org/10.1117/12.2019505) (cit. on pp. [68](#), [73](#), [83](#), [136](#))

- [97] S. Ter-Avetisyan, B. Ramakrishna, R. Prasad, M. Borghesi, P. V. Nickles, S. Steinke, M. Schnürer, K. I. Popov, L. Ramunno, N. V. Zmitrenko, and V. Bychenkov. “Generation of a quasi-monoenergetic proton beam from laser-irradiated sub-micron droplets”. In: *Physics of Plasmas* **19** (2012). DOI: [10.1063/1.4731712](https://doi.org/10.1063/1.4731712) (cit. on p. 68)
- [98] M. Gauthier, S. N. Chen, A. Levy, P. Audebert, C. Blancard, T. Ceccotti, M. Cerchez, D. Doria, V. Floquet, E. Lamour, C. Peth, L. Romagnani, J.-P. Rozet, M. Scheinder, R. Shepherd, T. Toncian, D. Vernhet, O. Willi, M. Borghesi, G. Faussurier, and J. Fuchs. “Charge Equilibrium of a Laser-Generated Carbon-Ion Beam in Warm Dense Matter”. In: *Physical Review Letters* **110** (2013), 135003. DOI: [10.1103/PhysRevLett.110.135003](https://doi.org/10.1103/PhysRevLett.110.135003) (cit. on pp. 68, 73, 75, 83, 136)
- [99] B. M. Hegelich, B. J. Albright, J. Cobble, K. Flippo, S. Letzring, M. Paffett, H. Ruhl, J. Schreiber, R. K. Schulze, and J. C. Fernandez. “Laser acceleration of quasi-monoenergetic MeV ion beams”. In: *Nature Physics* **439** (2006), 441–444. DOI: [10.1038/nature04400](https://doi.org/10.1038/nature04400) (cit. on pp. 70, 82)
- [100] S. N. Chen, A. P. L. Robinson, P. Antici, E. Brambrink, E. Humieres, S. Gaillard, T. Grismayer, A. Mancic, P. Mora, L. Romagnani, P. Audebert, H. Pepin, and J. Fuchs. “Passive tailoring of laser-accelerated ion beam cut-off energy by using double foil assembly”. In: *Physics of Plasmas* **21**, 023119 (2014), 023119. DOI: [10.1063/1.4867181](https://doi.org/10.1063/1.4867181) (cit. on pp. 73, 136)
- [101] NIST. *ESTAR*. Nov. 2015. URL: <http://physics.nist.gov/PhysRefData/Star/Text/ESTAR.html> (cit. on pp. 74, 94)
- [102] B. Qiao, S. Kar, M. Geissler, P. Gibbon, M. Zepf, and M. Borghesi. “Dominance of Radiation Pressure in Ion Acceleration with Linearly Polarized Pulses at Intensities of  $10^{21}$  W/cm<sup>2</sup>”. In: *Physical Review Letters* **108** (2012), 115002. DOI: [10.1103/PhysRevLett.108.115002](https://doi.org/10.1103/PhysRevLett.108.115002) (cit. on p. 82)
- [103] M. D. Barriga-Carrasco, D. Casas, and R. Morales. “Calculations on charge state and energy loss of argon ions in partially and fully ionized carbon plasmas”. In: *Physical Review E* **93** (2016), 033204. DOI: [10.1103/PhysRevE.93.033204](https://doi.org/10.1103/PhysRevE.93.033204) (cit. on pp. 83, 136)
- [104] S. Ter-Avetisyan, B. Ramakrishna, M. Borghesi, D. Doria, M. Zepf, G. Sarri, L. Ehrentraut, A. Andreev, P. V. Nickles, S. Steinke, W. Sandner, M. Schnürer, and V. Tikhonchuk. “MeV negative ion generation from ultra intense laser interaction with a water spray”. In: *Applied Physics Letters* **99**, 051501 (2011), 051501. DOI: [10.1063/1.3622664](https://doi.org/10.1063/1.3622664) (cit. on p. 83)
- [105] R. Prasad, M. Borghesi, F. Abicht, P. V. Nickles, H. Stiel, M. Schnürer, and S. Ter-Avetisyan. “Ethanol C<sub>2</sub>H<sub>5</sub>OH spray of sub-micron droplets for laser driven negative ion source”. In: *Review of Scientific Instruments* **83**, 083301 (2012). DOI: [10.1063/1.4747002](https://doi.org/10.1063/1.4747002) (cit. on p. 83)

- [106] L. Fedeli, A. Sgattoni, G. Cantono, D. Garzella, F. Réau, I. Prencipe, M. Passoni, M. Raynaud, M. Kveton, J. Proska, A. Macchi, and T. Ceccotti. “Electron Acceleration by Relativistic Surface Plasmons in Laser-Grating Interaction”. In: *Physical Review Letters* **116** (2016), 015001. DOI: [10.1103/PhysRevLett.116.015001](https://doi.org/10.1103/PhysRevLett.116.015001) (cit. on pp. 85–86, 136)
- [107] M. Thevenet, A. Leblanc, S. Kahaly, H. Vincenti, A. Vernier, F. Quèrè, and J. Faure. “Vacuum laser acceleration of relativistic electrons using plasma mirror injectors”. In: *Nature Physics* **12** (2016), 355–360. DOI: [10.1038/nphys3597](https://doi.org/10.1038/nphys3597) (cit. on pp. 85–88, 90, 95–96, 108, 136–137)
- [108] P. M. Woodward and J. D. Lawson. “The Theoretical Precision with which an Arbitrary Radiation-Pattern may be Obtained from a Source of Finite Size”. In: *Electrical Engineers - Part III: Radio and Communication Engineering, Journal of the Institution of* **95** (1948), 363–370. DOI: [10.1049/ji-3-2.1948.0094](https://doi.org/10.1049/ji-3-2.1948.0094) (cit. on pp. 85, 87, 97)
- [109] A. A. Andreev and K. Y. Platonov. “Double relativistic electron-accelerating mirror”. In: *Quantum Electronics* **43** (2013), 435 (cit. on pp. 86, 88, 95–96, 102, 107–108, 121, 137–138, 154)
- [110] J. D. Lawson. “Lasers and Accelerators”. In: *IEEE Transactions on Nuclear Science* **NS-26** (1979), 4217 (cit. on p. 87)
- [111] F. Brunel. “Not-so-resonant, resonant absorption”. In: *Physical Review Letters* **59** (1987), 52–55. DOI: [10.1103/PhysRevLett.59.52](https://doi.org/10.1103/PhysRevLett.59.52) (cit. on p. 87)
- [112] B. Dromey, S. Rykovanov, M. Yeung, R. Horlein, D. Jung, D. C. Gautier, T. Dzelzainis, D. Kiefer, S. Palaniyppan, R. Shah, J. Schreiber, H. Ruhl, J. C. Fernandez, C. L. S. Lewis, M. Zepf, and B. M. Hegelich. “Coherent synchrotron emission from electron nanobunches formed in relativistic laser-plasma interactions”. In: *Nature Physics* **8** (2012), 804–808. DOI: [10.1038/nphys2439](https://doi.org/10.1038/nphys2439) (cit. on pp. 88, 111, 114–115, 117, 121, 128–129, 138)
- [113] M. Yeung, B. Dromey, S. Cousens, T. Dzelzainis, D. Kiefer, J. Schreiber, J. H. Bin, W. Ma, C. Kreuzer, J. Meyer-ter-Vehn, M. J. V. Streeter, P. S. Foster, S. Rykovanov, and M. Zepf. “Dependence of Laser-Driven Coherent Synchrotron Emission Efficiency on Pulse Ellipticity and Implications for Polarization Gating”. In: *Physical Review Letters* **112** (2014), 123902. DOI: [10.1103/PhysRevLett.112.123902](https://doi.org/10.1103/PhysRevLett.112.123902) (cit. on p. 88)
- [114] W.-M. Wang, Z.-M. Sheng, Y.-T. Li, L.-M. Chen, S. Kawata, and J. Zhang. “Monoenergetic electron bunches generated from thin solid foils irradiated by ultrashort, ultraintense circularly polarized lasers”. In: *Physics Review ST: Acceleration and Beams* **13** (2010), 071301. DOI: [10.1103/PhysRevSTAB.13.071301](https://doi.org/10.1103/PhysRevSTAB.13.071301) (cit. on p. 96)
- [115] F. Quèrè, C. Thauray, J. P. Geindre, G. Bonnaud, P. Monot, and P. Martin. “Phase Properties of Laser High-Order Harmonics Generated on Plasma Mirrors”. In: *Physical Review Letters* **100** (2008), 095004. DOI: [10.1103/PhysRevLett.100.095004](https://doi.org/10.1103/PhysRevLett.100.095004) (cit. on p. 111)

- [116] B. Dromey, S. Kar, C. Bellei, D. C. Carroll, R. J. Clarke, J. S. Green, S. Kneip, K. Markey, S. R. Nagel, P. T. Simpson, L. Willingale, P. McKenna, D. Neely, Z. Najmudin, K. Krushelnick, P. A. Norreys, and M. Zepf. “Bright Multi-keV Harmonic Generation from Relativistically Oscillating Plasma Surfaces”. In: *Physical Review Letters* **99** (2007), 085001. DOI: [10.1103/PhysRevLett.99.085001](https://doi.org/10.1103/PhysRevLett.99.085001) (cit. on pp. 111–112, 114)
- [117] G. D. Tsakiris, K. Eidmann, J. Meyer-ter-Vehn, and F. Krausz. “Route to intense single attosecond pulses”. In: *New Journal of Physics* **8** (2006), 19. DOI: [10.1088/1367-2630/8/1/019](https://doi.org/10.1088/1367-2630/8/1/019) (cit. on p. 111)
- [118] D. an der Brügge and A. Pukhov. “Enhanced relativistic harmonics by electron nanobunching”. In: *Physics of Plasmas* **17**, 033110 (2010), 033110. DOI: [10.1063/1.3353050](https://doi.org/10.1063/1.3353050) (cit. on pp. 111, 115, 138)
- [119] R. Hörlein, S. Steinke, A. Henig, S. G. Rykovanov, M. Schnürer, T. Sokollik, D. Kiefer, D. Jung, X. Q. Yan, T. Tajima, J. Schreiber, M. Hegelich, P. V. Nickles, M. Zepf, G. D. Tsakiris, W. Sandner, and D. Habs. “Dynamics of nanometer-scale foil targets irradiated with relativistically intense laser pulses”. In: *Laser and Particle Beams* **29** (2011), 383–388. DOI: [10.1017/s0263034611000462](https://doi.org/10.1017/s0263034611000462) (cit. on pp. 111, 114–116, 129, 138)
- [120] T. Z. Esirkepov, S. V. Bulanov, M. Kando, A. S. Pirozhkov, and A. G. Zhidkov. “Boosted High-Harmonics Pulse from a Double-Sided Relativistic Mirror”. In: *Physical Review Letters* **103** (2009), 025002. DOI: [10.1103/PhysRevLett.103.025002](https://doi.org/10.1103/PhysRevLett.103.025002) (cit. on pp. 111–112, 120)
- [121] NIST. *NIST Atomic Spectra Database*. lbl.gov. 2015. URL: [http://physics.nist.gov/PhysRefData/ASD/levels\\_form.html](http://physics.nist.gov/PhysRefData/ASD/levels_form.html) (cit. on p. 112)
- [122] F. R. Elder, A. M. Gurewitsch, R. V. Langmuir, and H. C. Pollock. “Radiation from Electrons in a Synchrotron”. In: *Physical Review Letters* **71** (1947), 829–830. DOI: [10.1103/PhysRev.71.829.5](https://doi.org/10.1103/PhysRev.71.829.5) (cit. on p. 115)
- [123] B. Dromey, D. Adams, R. Horlein, Y. Nomura, S. G. Rykovanov, D. C. Carroll, P. S. Foster, S. Kar, K. Markey, P. McKenna, D. Neely, M. Geissler, G. D. Tsakiris, and M. Zepf. “Diffraction-limited performance and focusing of high harmonics from relativistic plasmas”. In: *Nat Phys* **5** (2009), 146–152 (cit. on p. 117)
- [124] D. M. Villeneuve, H. A. Baldis, and C. J. Walsh. “The production of  $(3/2)\omega_0$  light by the two plasmon decay instability”. In: *Physics of Fluids* **28** (1985), 1454–1459. DOI: [http://dx.doi.org/10.1063/1.864980](https://dx.doi.org/10.1063/1.864980) (cit. on p. 117)
- [125] M. Schnürer, A. A. Andreev, F. Abicht, J. Braenzel, C. Koschitzki, K. Y. Platonov, G. Priebe, and W. Sandner. “The beat in laser-accelerated ion beams”. In: *Physics of Plasmas* **20** (2013), 103102. DOI: [10.1063/1.4824115](https://doi.org/10.1063/1.4824115) (cit. on p. 121)

- [126] M. Yeung, B. Dromey, S. Cousens, T. Dzelzainis, D. Kiefer, J. Schreiber, J. H. Bin, W. Ma, C. Kreuzer, J. Meyer-ter-Vehn, M. J. V. Streeter, P. S. Foster, S. Rykovanov, and M. Zepf. “Dependence of Laser-Driven Coherent Synchrotron Emission Efficiency on Pulse Ellipticity and Implications for Polarization Gating”. In: *Physical Review Letters* **112** (2014), 123902. DOI: [10.1103/PhysRevLett.112.123902](https://doi.org/10.1103/PhysRevLett.112.123902) (cit. on pp. 127, 130, 138, 161)
- [127] S. Steinke, A. Henig, M. Schnürer, T. Sokollik, P. V. Nickles, D. Jung, D. Kiefer, R. Hörlein, J. Schreiber, T. Tajima, X. Q. Yan, M. Hegelich, J. Meyer-ter-Vehn, W. Sandner, and D. Habs. “Efficient ion acceleration by collective laser-driven electron dynamics with ultra-thin foil targets”. In: *Laser and Particle Beams* **28** (2010), 215–221. DOI: [10.1017/S0263034610000157](https://doi.org/10.1017/S0263034610000157) (cit. on p. 136)
- [128] D. an der Brügge and A. Pukhov. “Propagation of relativistic surface harmonics radiation in free space”. In: *Physics of Plasmas* **14**, 093104 (2007), 093104. DOI: [10.1063/1.2771519](https://doi.org/10.1063/1.2771519) (cit. on p. 138)
- [129] A. V. Andreev, V. M. Gordienko, and A. B. Savelev. “Nuclear processes in a high-temperature plasma produced by an ultrashort laser pulse”. In: *Quantum Electronics* **31** (2001), 941 (cit. on p. 147)

## Danksagung

- Im Gedenken und mit Dank an meinen Doktorvater Prof. Sandner, der unerwartet plötzlich aus dem Leben geschieden ist. Er hat mir diese Arbeit ermöglicht und mich stets motiviert neue Wege zu ergründen.

Ohne die Hilfe vieler Menschen wäre diese Arbeit nicht möglich gewesen. Ich bedanke mich ganz herzlich bei allen, die mich und diese Arbeit unterstützt haben. Besonderer Dank gilt:

- ganz ausdrücklich der Gruppe B1 des Max Born Instituts für eine außerordentlich gute Zusammenarbeit während der gesamten Zeit. Diese Gruppe schaffte eine sehr produktive und herzliche Arbeitsatmosphäre, die eine äußerst effiziente und erfolgreiche Arbeitsweise ermöglichte, mich stets motivierte und in allen Fragen unterstützte. Zu erwähnen sind in diesem Zusammenhang auch die vielen Messkampagnen die ich begleiten konnte, die mir einen tiefen und vielfältigen Einblick in die Physik der Laserplasmadynamik gaben, von dem diese Arbeit profitieren konnte.
- Dr. Schnürer der alle Experimente betreut, unterstützt und begleitet hat. Besonders bedanken möchte ich mich auch für den inspirierenden wissenschaftlichen Austausch bei der Realisierung und Interpretation der Experimente. Ohne sein wissenschaftliches Engagement, seine Neugierde und seine Unterstützung wäre manches Experiment vielleicht nicht versucht worden.
- Lutz Ehrentraut für sein Engagement und seine große technische Expertise als Lasertechniker des MBI Höchstfeldlasers, der stets für eine ausgezeichnete Laserperformance und damit die Grundlage für das Gelingen einer reproduzierbaren Messreihe sorgte. Ich danke ihm auch für die Einführung in alle technischen Grundlagen und das Vertrauen das er mir entgegenbrachte, welches es mir ermöglichte die Performance des Lasers besser zu verstehen und selbst daran mitzuwirken.
- Prof. Eisebitt für die schnelle und unkomplizierte Übernahme meiner Betreuung.
- Prof. A. Andreev i want to thank for a very inspiring and fruitful collaboration, the huge effort he put into the theoretical explanation and simulation of our/my experimental results. I appreciated his patience in the discussions that enabled us to extract the really important points and that he checked a lot of questions with his PIC simulations.
- Dr. Stiel danke ich für die vielen erhellenden und motivierenden Gespräche im Bereich der XUV-Strahlung. Besonderem Dank gilt ihm für die Bereitstellung der EUV-Quelle mit der ich die Messmethodik zur Bestimmung der Targetdicken entwickeln konnte.
- I want to thank Dr. David Casas for the helpful introduction and discussion on ion recharge processes in plasmas.
- Denni Sommer möchte ich für seine große Unterstützung bei der Herstellung, Entwicklung und Charakterisierung der verwendeten Targetfolien danken.
- Dr. Florian Abicht gilt besonderer Dank für die Computersimulationen zur Kalibrierung des Elektronenspektrometers, sowie wie für die Konzeption desselben. Ich danke ihm auch für viele angenehme, interessante und weiterführende physikalische Diskussionen und sein Interesse an jeglicher physikalischen Fragestellung.

- Petra Friedrich möchte ich für ihre große Unterstützung in allen bürokratischen, vielen technischen Dingen und bei der Goldbeschichtung der dünnen Folien danken. Ihre unzähligen vielen kleinen Gefallen haben mir vieles erleichtert.
- Gerd Kommol danke ich für seine äußerst professionelle Ingenieursarbeit. Er fand immer eine bessere Lösung zur Umsetzung des gewünschten Problems, was für die Fertigung und Installation der experimentellen Aufbauten insbesondere im Zweistrahlexperiment unabdingbar war.
- Dirk Roloff danke ich für die schnelle und professionelle Hilfe in allen IT und elektro-automotiven Fragen.
- Jens Gläsel möchte ich für seine erste Hilfe Einsätze bzgl. aller elektrotechnischen Fragen and labortechnischen Haverien danken.
- Martin Heinecke danke für seine präzise Arbeit beim Fertigen der vielen metallischen Adapter.
- Ich möchte Dr. Gerd Priebe für viele interessante Gespräche, physikalische Diskussionen vor allem im Bereich der nicht-linearen Optik danken.
- Besonderer Dank gilt Peter Hilz für die Einführung in die Herstellung der ultradünnen Plastikfolien und für viele gute, offene physikalische Diskussionen.
- Dr. Sven Steinke danke ich für den gut funktionierenden Doppel Plasma Spiegel und für alles, was er mir am Anfang dieser Arbeit in Bezug auf Labortechnik und Laserplasmabeschleunigung beigebracht hat.
- Max Klingsporn möchte ich für seine aufklärende Gespräche bzgl. der Materialwissenschaften und Festkörperphysik danken und für seine im Rahmen des IHP entstandenen Messungen zur Charakterisierung der benutzten Folientargets.
- Ich danke allen, die diese Arbeit geduldig korrigiert haben. Especially, i want to thank Dr. Harvey for his work and patience to improve my English.
- Für den wunderbaren wissenschaftlichen und technischen Austausch und viele Gespräche möchte ich mich besonders bei Christian Koschitzki, Dr. Andrea Lübcke, Henri Zimmermann, Dr. Daniel Brete bedanken.
- Besonderer Dank gilt meinem Freundeskreis und meiner Familie, insbesondere Käthe Hoevermann, für die Anteilnahme, Unterstützung und Interesse an meinen Zielen.
- Ich danke auch der Agentur für Arbeit, die mir und so vielen anderen Doktoranden einen Einblick in die außerwissenschaftliche Arbeitswelt sowie in das Thema der Selbstverwertung gewährte.